Exploring Ferroptosis as a Novel Liability of High-Risk Neuroblastomas

---

Dissertation

submitted to the
Combined Faculty of Natural Sciences and Mathematics
of the Ruperto Carola University Heidelberg, Germany
for the degree of

Doctor of Natural Sciences

M.Sc. Karolina Aleksandra Garbowicz

Inaugural dissertation

for

obtaining the doctoral degree

of the

Combined Faculty of Mathematics, Engineering and Natural Sciences

of the Ruprecht – Karls – University

Heidelberg

Presented by

M.Sc. Karolina Aleksandra Garbowicz

born in: Międzyrzecz, Poland

Oral examination: 11.05.2023

Exploring Ferroptosis as a Novel Liability of High-Risk Neuroblastomas

Referees: Prof. Dr. Stefan Wölfl

PD Dr. Frank Westermann

Declaration

The work presented in this thesis was carried out from June 2018 until February 2023 in the group of Neuroblastoma Genomics at the German Cancer Research Center (DKFZ) in Heidelberg, Germany. It was supervised by PD Dr. Frank Westermann.

I declare that I have written and submitted this dissertation myself and, in this process, have not used any other sources than those indicated. To the best of my knowledge this thesis, and the research to which it refers, are the product of my own work except where due to acknowledgement is made in the thesis itself.

I hereby declare that I have not applied to be examined at any other institution, nor have I used the dissertation in this or any other form at any other institution as an examination paper, nor submitted it to any other faculty as a dissertation.

Karolina Aleksandra Garbowicz
Heidelberg, February 2023

Table of Contents

1 Summary

Neuroblastoma (NB) represents a malignant neoplasm that arises from precursor cells of the sympathetic nervous system. This disease entity is responsible for a considerable proportion of childhood cancer-related mortalities, emphasizing the pressing need for effective therapeutic interventions. Despite the availability of several therapeutic options for the treatment of high-risk NB, patients frequently experience relapse even after exhibiting an initial positive response to treatment. Moreover, the relapsed tumors in the majority of cases demonstrate a high degree of resistance to alternative therapeutic interventions. Amplified *MYCN* is a defining characteristic of a high-risk subtype of NB, which is often accompanied by advanced metastatic disease and an unfavorable prognosis in terms of overall survival. MYCN is an oncoprotein that broadly reprograms tumor cells, induces proliferation, and blocks neuronal differentiation. Additionally, MYCN plays a crucial role in maintaining redox balance by activating antioxidant responses and significantly affecting cellular metabolism (Alborzinia et al., 2022; Floros et al., 2021; Lu et al., 2021).

Although amplified *MYCN* is a well-known risk factor for NB, direct targeting of MYCN remains challenging. Therefore, researchers are exploring alternative therapeutic strategies that exploit metabolic vulnerabilities related to MYCN. According to recent studies conducted by Alborzinia *et al.* (2022), a functional association has been established between oncogenic *MYCN* and ferroptosis, a form of iron-dependent, regulated cell death. The research suggests that NB cells that have amplified *MYCN* are highly dependent on cysteine, and deprivation of this amino acid from the growth medium resulted in significant lipid peroxidation. However, co-administration of ferrostatin-1, a ferroptosis inhibitor, was found to prevent this effect.

To further understand NB cell lines' sensitivity to ferroptosis induction, this study focused on an extensive characterization of NB cell lines to identify the genetic and molecular mechanisms underlying their addiction to cystine and sensitivity to ferroptotic cell death. Based on the acquired data, it is apparent that the sensitivity to ferroptosis is influenced by the cellular lineage state. Specifically, cell lines with greater mesenchymal characteristics exhibit heightened resistance to the induction of

Summary

ferroptosis. Additionally, by correlating baseline gene expression data to sensitivity to ferroptosis induction, the Q_{10}-related pathways were identified as an important resistance mechanism against ferroptosis. Notably, these pathways were found to be downregulated in *MYCN*-amplified tumors, which suggests their possible sensitivity to ferroptosis.

Moreover, the response of NB cell lines to various ferroptotic stress stimuli was investigated. Transcriptome profiling of NB cells subjected to cystine depletion revealed an upregulation of the ATF4-related stress response, which was more prominent in *MYCN*-amplified cell lines. In contrast, *MYCN*-non-amplified cells exhibited increased cystine uptake, likely due to sufficient levels of glutamate available for exchange with cystine. In addition, decreased glutamate levels were observed in *MYCN*-amplified NB tumors, emphasizing the role of glutamate in thiol metabolism.

Furthermore, the role of the transulfuration pathway in NB sensitivity to ferroptotic cell death was explored. Downregulation of one of the key enzymes in *de novo* cysteine synthesis pathway (CTH) was linked to increased sensitivity to ferroptosis inducers and accumulation of toxic lipid peroxides. On the transcriptome level, CTH downregulation led to the upregulation of cysteine uptake / restoration mechanisms and adrenergic-to-mesenchymal transition. In addition, stable isotope tracing experiments confirmed the involvement of methionine-derived cysteine in glutathione synthesis.

In this study, the significance of glutathione peroxidase 4 (GPX4), a crucial factor in ferroptosis, has also been investigated. Treatment with ferroptosis inducers has demonstrated that the downregulation of GPX4 increases the sensitivity of NB cells to ferroptosis induction. Furthermore, transcriptomic profiling has revealed that GPX4 knockdown results in upregulation of genes implicated in the TNFA signaling pathway and adrenergic-to-mesenchymal transition. These findings suggest that the loss of cellular identity is a potential adaptive response mechanism to the stress imposed by ferroptosis.

Summary

To extend the *in vitro* results to clinically relevant scenarios, a regression model was developed using the data from the cell lines and subsequently applied to a dataset of 600 NB tumors. The results of this model suggest that *MYCN*-amplified NB tumors are more likely to be vulnerable to ferroptosis induction. Interestingly, the expression of *MYCN* and its associated targets were found to be the most differentially expressed genes between tumors predicted to be sensitive or resistant to the ferroptosis-inducing agents.

Taken together, the study's findings suggest that targeting ferroptosis may represent a promising therapeutic strategy for MYCN or c-MYC-driven NB tumors. The study's comprehensive profiling of NB cell lines has contributed significantly to the understanding of ferroptosis regulation, and it allowed to identify specific mechanisms that can serve as vulnerabilities of MYC-driven tumors.

2 Zusammenfassung

Das Neuroblastom ist eine maligne Tumorerkrankung, die von Vorgängerzellen sympathischer Nervenzellen abstammt. Diese Erkrankung ist für eine signifikante Anzahl an Todesfällen durch Krebserkrankungen bei Kindern verantwortlich, was den dringenden Bedarf an effektiven therapeutischen Interventionen verdeutlicht. Obwohl verschiedene Therapieoptionen für die Behandlung von Hochrisiko-Neuroblastomen vorhanden sind, erleiden diese Patienten häufig ein Rezidiv trotz eines initial positiven Ansprechens auf die Therapie. Darüber hinaus weisen diese Rezidive in den meisten Fällen einen hohen Grad der Resistenzbildung gegen alternative Therapieinterventionen auf. Amplifiziertes *MYCN* ist ein Kennzeichen eines der Hochrisiko-Subtypen des Neuroblastoms, das oft mit einem fortgeschrittenen metastatischen Krankheitsgeschehen und einer ungünstigen Prognose bezogen auf das Gesamtüberleben assoziiert ist. MYCN ist ein Onkoprotein, welches Tumorzellen umfangreich umprogrammiert, Proliferation induziert und die neuronale Differenzierung hemmt. Zusätzlich spielt MYCN eine entscheidende Rolle in der Aufrechterhaltung der Redoxbalance durch die Aktivierung antioxidanter, zellulärer Antworten und greift signifikant in die Regulation des zellulären Metabolismus ein (Alborzinia et al., 2022; Floros et al., 2021; Lu et al., 2021).

Obwohl amplifiziertes *MYCN* ein etablierter Risikofaktor für Neuroblastome ist, gestaltet sich die Entwicklung von Therapeutika, die direkt gegen MYCN gerichtet sind, als anspruchsvoll. Aus diesem Grund untersuchen Forscher alternative therapeutische Strategien, die die metabolische Vulnerabilität verursacht durch MYCN ausnutzen. Gemäß jüngster Forschungsarbeit von Alborzina *et al.* (2022), wurde ein funktionaler Zusammenhang zwischen dem Onkogen *MYCN* und Ferroptose etabliert; eine Eisen-abhängige, regulierte Form des Zelltodes. Es wurde gezeigt, dass *MYCN*-amplifizierte Neuroblastom-Zellen hochgradig abhängig von Cystein sind und der Entzug dieser Aminosäure aus dem Zellkulturmedium eine massive Oxidation der Lipide verursacht. Durch die simultane Behandlung mit Ferrostatin-1, einem Ferroptose Hemmer, konnte dieser Effekt verhindert werden.

Zusammenfassung

Um die Sensitivität der Neuroblastom Zellen bezogen auf die Induktion von Ferroptose zu verstehen, fokussierte sich diese Arbeit auf die extensive Charakterisierung verschiedener etablierter Neuroblastomzelllinien, um genetische und molekulare Mechanismen zu identifizieren, welche die Abhängigkeit der Zellen von Cystin und die Ferroptose Sensitivität beschreiben. Basierend auf den akquirierten Daten, scheint die Ferroptose Sensitivität vom zellulären Abstammungsstatus beeinflusst zu werden. Besonders Zelllinien mit hauptsächlich mesenchymalen Charakteristika weisen eine deutlichere Resistenz gegenüber der Induktion von Ferroptose auf. Zusätzlich wurden die Q_{10}-regulierten Signalwege als wichtiger Resistenzmechanismus gegen Ferroptose durch die Korrelation basaler Genexpressionsdaten mit der Ferroptose Sensitivität identifiziert. Darüber hinaus konnte gezeigt werden, dass diese Signalwege in *MYCN*-amplifizierten Tumoren reprimiert werden, wodurch ihre etwaige Ferroptose Sensitivität erklärt werden könnte.

Weiterhin wurde die Reaktion verschiedener Neuroblastom Zelllinien auf unterschiedliche Ferroptose-Stress-Stimuli untersucht. Transkriptom-Profile von Neuroblastom Zellen, die einem Entzug von Cystin ausgesetzt waren, zeigten eine Hochregulation ATF4-regulierter Stress-Antwort, welche prominenter in *MYCN*-amplifizierten Zelllinien war. Im Gegensatz dazu wiesen *MYCN*-nicht amplifizierte Zellen eine erhöhte Cystin Aufnahme auf, wahrscheinlich aufgrund ausreichender Glutamat Level, die zum Austausch mit Cystin zur Verfügung stehen. Außerdem wurden in *MYCN*-amplifizierten Neuroblastom Tumoren verringerte Glutamat Level festgestellt, wodurch die Bedeutung von Glutamat im Thiol-Mechanismus hervorgehoben wird.

Zusätzlich wurde die Rolle des Transsulfuration Signalwegs bezogen auf die Sensitivität zum ferroptotischen Zelltod im Neuroblastom untersucht. Ein Zusammenhang zwischen der Repression eines der Schlüsselenzyme des *de novo* Cystein Synthese Signalwegs (CTH) und der Sensitivität gegenüber Ferroptose induzierenden Substanzen sowie der Akkumulation toxischer Lipidperoxide konnte gezeigt werden. Auf Transkriptom-Ebene führte eine Repression von CTH zur Hochregulation der Cystein Aufnahme / Wiederherstellungsmechanismen und der Transition von adrenerg zu mesenchymal. Weiterhin bestätigten stabile Isotop-

Markierungsexperimente die Beteiligung des Methionin-abstammenden Cystein in der Glutathion Synthese.

In dieser Studie wurde außerdem die Rolle der Glutathionperoxidase 4 (GPX4) untersucht, welche eine entscheidende Rolle in der Ferroptose spielt. Die Behandlung mit Ferroptose induzierenden Substanzen zeigte, dass die Repression von GPX4 die Sensitivität von Neuroblastomzellen zur Induktion von Ferroptose steigerte. Darüber hinaus wurde durch das Profiling des Transkriptoms gezeigt, dass der Knockdown von GPX4 in der Hochregulation von Genen resultiert, welche in den TNFA Signalweg und die Transition von adrenerg zu mesenchymal involviert sind. Diese Ergebnisse deuten darauf hin, dass der Verlust der zellulären Identität einen potentiellen adaptiven Antwortmechanismus auf bestimmte Stresssignale verkörpert, die infolge von Ferroptose der Zelle auferlegt werden.

Um die *in vitro* Ergebnisse auf klinisch relevante Szenarien auszuweiten, wurde ein Regressions-Model entwickelt, das Daten der Zelllinien nutzt und anschließend auf einen Datensatz von 600 Neuroblastom Tumoren angewandt wurde. Die Ergebnisse dieses Models deuten an, dass *MYCN*-amplifizierte Neuroblastom Tumore eher vulnerabel für die Induktion von Ferroptose sind. Interessanterweise konnte gezeigt werden, dass die Expression von *MYCN* und dessen assoziierter Zielgene die am stärksten differentiell exprimierten Gene sind, die eine Vorhersage ermöglichen, welche Tumore sensitiv oder resistent auf Ferroptose induzierende Substanzen reagieren.

Zusammenfassend deuten die Ergebnisse dieser Studie darauf hin, dass auf Ferroptose ausgerichtete Therapien vielversprechende neuartige Behandlungsstrategien für MYCN oder c-MYC getriebene Neuroblastom Tumore darstellen. Das in dieser Studie umfangreiche Profiling von verschiedenen Neuroblastom Zelllinien hat signifikant für das Verständnis der Ferroptose Regulation beigetragen und es wurden Mechanismen identifiziert, die als neue Vulnerabilitäten von MYC(N) getriebenen Tumoren dienen können.

3 Introduction

Introduction

3.1. Neuroblastoma

NB is a common type of solid tumor that primarily affects young children (Brodeur, 2003; Maris et al., 2007). It commonly emerges from developing cells in the sympathetic nervous system, with a frequent occurrence in the adrenal medulla or paraspinal ganglia of the abdomen or chest. Despite being a single disease entity, the molecular and clinical characteristics of NB are highly heterogenous. Some cases may regress spontaneously without treatment, while others progress aggressively despite multiple therapeutic interventions (Brodeur, 2003; Maris et al., 2007). As a result, the outcome for patients with NB varies significantly, with those with low to intermediate risk tumors having a survival rate of up to 90%. However, the prognosis for high-risk patients is poor, with nearly half of the patients relapsing and ding from the disease.

The wide range of clinical presentations seen in NB cannot be solely explained by the molecular spectrum of the disease, making it difficult to understand and predict its course. There is a pressing need for new prognostic factors to accurately classify patients into risk groups and tailor treatment approaches accordingly. This is especially important in low-risk cases, where reducing the side effects of therapy can improve outcomes, while highly aggressive tumors often resist treatment.

3.1.1. Neuroblastoma: staging systems

In 1988 the International Neuroblastoma Staging System (INSS), an internationally recognized system for classifying NB tumors based on their extent of disease, was introduced (Brodeur et al., 1988). It uses surgical and pathological parameters to divide tumors into four stages. Stage 1 tumors are localized and can be completely excised with surgery, while stage 2 tumors are incompletely excised and may or may not involve lymph nodes. Stage 3 and 4 tumors are unresectable and may have disseminations to distant lymph nodes and other organs, including bones, bone marrow, liver, and skin. A subgroup of stage 4 tumors, commonly referred to as 4S, is present in patients under the age of 12 months who exhibit small, localized primary tumors and limited metastases confined to the skin, liver, and/or bone marrow. These

4S tumors have a tendency to regress spontaneously and often have a good outcome despite widespread disease (D'Angio et al., 1971).

Several risk classification systems have been developed based on the INSS to anticipate a patient's risk at the time of diagnosis. The German Neuroblastoma Trial NB2004 resulted in a guideline that is currently used in Germany to stratify the risk of NB patients. It divides patients into three main risk groups: low, intermediate, and high risk (**Figure 1**). This classification is derived from a composite of clinical variables and genomic abnormalities, which include INSS stage, age at the time of diagnosis, *MYCN* gene amplification status, and the status of the short arm of chromosome 1. A high age at diagnosis (greater than 18 months) is associated with a poor prognosis, while younger patients typically have less aggressive tumors (London et al., 2005). Patients with amplified *MYCN* oncogene have a very poor prognosis, even if they have stage 1-3 or 4S tumors. (Brodeur et al., 1984; Seeger et al., 1985). Deletion of the short arm of chromosome 1 (1p) is also linked to an unfavorable prognosis.

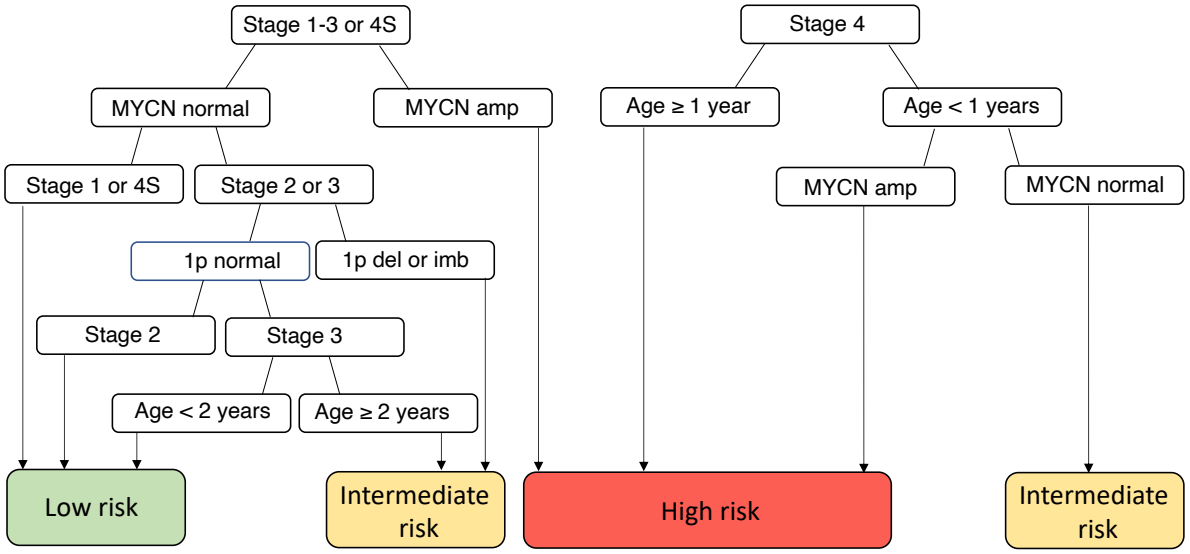

Figure 1: Risk stratification of NB based on the German Neuroblastoma Trial NB2004.
The categorization of patients into low-, intermediate-, and high-risk groups is determined by evaluating both clinical and molecular characteristics of the tumor. amp – amplified, 1p – the short arm of chromosome 1, del – deletion, imb – imbalance. Adapted from (Oberthuer et al., 2009).

3.1.2. Genetic and chromosomal aberrations contributing to neuroblastoma development

Unlike many adult malignancies, pediatric cancers such as NB tend to have a low frequency of mutations that affect the protein sequences, which makes it challenging to identify the oncogenic drivers and develop targeted therapies (Jones et al., 2019; Pugh et al., 2013). However, with the development of next-generation sequencing studies, a few recurrent genetic aberrations, such as gene amplifications, chromosomal alterations, and somatic mutations, could be determined (Molenaar et al., 2012; Pugh et al., 2013; Sausen et al., 2013). Despite these findings, a single genetic or epigenetic event that can independently induce NB formation has not been identified to date.

In contrast to low mutational burden, NB tumors are frequently associated with chromosomal abnormalities that can lead to substantial genomic alterations. Genomic instability, causing segmental chromosome alterations, has a negative impact on the prognosis of patients classified as low- or intermediate-risk and is strongly associated with an increased risk of relapse (Schleiermacher et al., 2010). Conversely, whole chromosome gains triggered by mitotic dysfunction in hyperdiploid or near triploid NB are associated with lower stages of the disease (Schleiermacher et al., 2010). On the other hand, while structural changes are rare in low-risk NB tumors, the majority of high-risk or stage 4 tumors are characterized by segmental chromosome aberrations. These alterations, which are frequently observed in specific regions such as 1p, 1q, 3p, 11q, 14q, and 17p, may contribute to disease progression and have significant implications for disease management and treatment (Caren et al., 2010; Janoueix-Lerosey et al., 2009; Schleiermacher et al., 2010; Schleiermacher et al., 2011).

The transcription factor MYCN was the first oncogenic driver to be identified in NB, and amplification of its gene on chromosome 2p24 remains the most prominent genetic alteration seen in this cancer, detected in up to 25% of NB tumors (Schwab et al., 1983). Regardless the disease stage, amplified *MYCN* is always associated with unfavorable prognosis, affecting both time to tumor progression and overall survival (OS) (Cohn et al., 2009; Schleiermacher et al., 2011). MYCN plays a role in regulating

various gene programs that are associated with the hallmarks of cancer, including malignancy and a stem-like state. Deregulation of MYCN also promotes the progression of the cell cycle through the G1 phase and blocks differentiation leading to the uncontrolled cell proliferation and development of cancer (Tweddle et al., 2001; Wakamatsu et al., 1997). Amplification of *MYCN* often occurs in the form of double minute chromosomes (DMC), which are extrachromosomal circular elements that contain a large region of chromosome 2p24, including the *MYCN* gene (Corvi et al., 1994). An uneven distribution of DMCs during mitosis may result in an accumulation of *MYCN* copies, which can promote the progression of malignancy.

Other genetic mutations that frequently occur in NB include Anaplastic lymphoma kinase receptor (*ALK*), ATRX Chromatin Remodeler (*ATRX*), NRAS Proto-Oncogene, GTPase (NRAS), and Protein Tyrosine Phosphatase Non-Receptor Type 11 (*PTPN11*). Gain-of-function mutations in ALK characterize approximately 9% of sporadic NB, while ALK amplifications are identified in 4% of all the cases (Chen et al., 2008; George et al., 2008; Janoueix-Lerosey et al., 2018). In animal models, co-expression of *ALK* and *MYCN* was shown to drive tumor development, increase the disease penetrance and significantly escalate tumor onset (Berry et al., 2012; Schulte et al., 2013; Zhu et al., 2012). Inactivating mutations of the chromatin remodeling enzyme *ATRX* were identified in 5-25% of NB patients (Cheung et al., 2012; Pugh et al., 2013). It was shown, that *MYCN* amplification and *ATRX* mutations are mutually exclusive, and induction of *MYCN* expression in NB cells with *ATRX* mutation led to metabolic rewiring and increased reactive oxygen species production (Zeineldin et al., 2020).

Another challenge that cancer cells often face is shortened telomeres. Cancer cells have developed ways to interfere with telomere maintenance mechanisms, which helps them to achieve an "immortal" state. For instance, tumors with *ATRX* loss-of-function (LOF) mutation avoid degradation of telomeres using alternative lengthening of telomeres (ALT), and approximately half of ALT-positive cases have *ATRX* LOF mutation (Hartlieb et al., 2021). In addition to ALT, other genetic modifications have been discovered to aid in maintaining telomeres in NB. Recent studies have revealed that certain NB tumors possess rearrangements on chromosome 5p that result in the

translocation of the telomerase reverse transcriptase gene (*TERT*) to potent enhancer elements, leading to its substantial upregulation. (Peifer et al., 2015; Valentijn et al., 2015).

The maintenance of telomeres, which can be achieved through several mechanisms, including ALT, *TERT* rearrangement, or *MYCN* amplification, is a crucial hallmark of high-risk NB and is linked to an unfavorable prognosis (Ackermann et al., 2018), while low-risk NBs lack telomere maintenance mechanism (TMM) (**Figure 2**). It has been shown that mutations in Tumor Protein P53 (*TP53*) or RAS pathway have a particularly negative impact on prognosis when combined with active TMM, but do not affect the prognosis when TMM is not active (Ackermann et al., 2018).

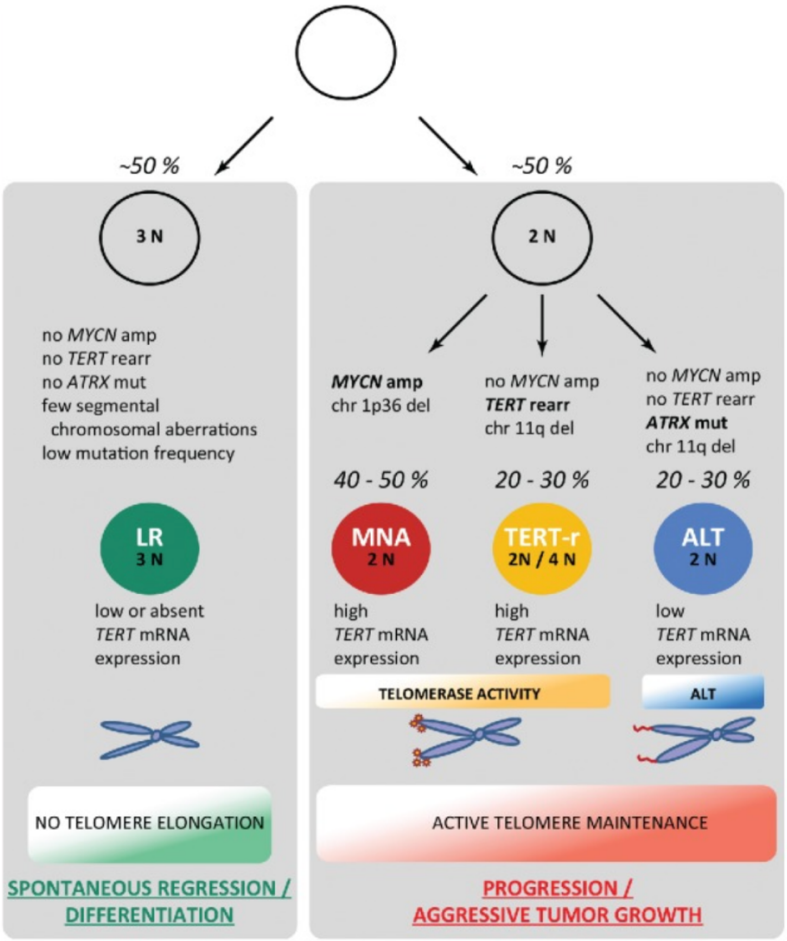

Figure 2: A model of NB development based on genetic alterations.
A diagram showing telomere maintenance mechanism and other recurrent genetic alterations in NB. amp- amplification, rearr – rearrangement, mut – mutation, del – deletion. Adapted from (Hertwig et al., 2016).

3.1.3. Neuroblastoma cell identity

Early in 1950s, Murray and Stout reported on the shared traits of neuroblasts that were sourced from eight sets of primary and secondary tumors (Murray & Stout, 1947). They documented the morphological alterations of these cells, referred to as sympathicoblasts, in a two-dimensional culture environment. The cells generated neurites of different lengths, some of which started to brunch and formed filamentous shapes after culturing for four days. In the following years, Ross et al. uncovered that human NB cell line SK-N-SH consists of two different subtypes that are distinct in terms of their morphological and biochemical characteristics (Ross et al., 1983). These cell types include SH-SY5Y, which exhibit a N-type morphology and possess neuronal characteristics, and SH-EP, a highly adhesive Schwann (S) cell line. Additionally, an intermediate cell type referred to as I-type cells was described (SH-IN), featuring a mixed morphology and properties of both N- and S-type cells (**Figure 3**).

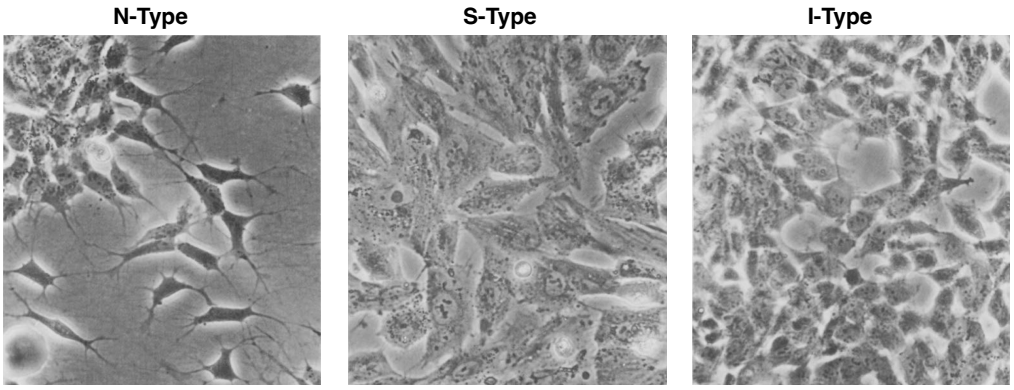

Figure 3: Distinct NB phenotypic states.
Phase-contrast micrograph of distinct SK-N-SH clonal populations: N-type SH-SY5Y cells, S-type SH-EP cells and I-type SH-IN cells. Adapted from (Ross et al., 1983).

Recently published data have shown that super enhancer-associated core transcription factor networks play a crucial role in determining the identity of NB cells (Boeva et al., 2017; van Groningen et al., 2017). In NB, the vast majority of cells display a sympathetic noradrenergic phenotype, characterized by increased activity of adrenergic super enhancers and heightened expression of core regulatory circuitry (CRC) transcription factors such as *HAND2*, *GATA3*, and *PHOX2B*. A subset of NB cell lines, namely SH-EP, GIMEN and GICAN, possess a mesenchymal identity. Meanwhile, SK-N-SH and SK-N-AS cell lines are considered intermediate, exhibiting

both adrenergic and mesenchymal characteristics (Boeva et al., 2017). Mesenchymal NB cells are known for expressing mesenchymal markers like *FN1*, *SNAI2*, and *VIM*, which resemble those found in neural crest cells. These mesenchymal cells are also more resistant to chemotherapy and are commonly found in relapsed tumors. By comparing adrenergic and mesenchymal isogenic cell line pairs, researchers were able to establish expression signatures for both adrenergic and mesenchymal NB cells (van Groningen et al., 2017). An additional investigation that examined the enhancer landscape of NB tumors identified four distinct epigenetic subtypes: high-risk MYCN-amplified NB, high-risk NB lacking *MYCN* amplification, low-risk NB, and mesenchymal NB (Gartlgruber et al., 2021).

3.1.4. Therapy approaches for the treatment of neuroblastoma

Treatment of NB is based on risk assignment. For low-risk patients with a 5-year OS rate around 98% (Irwin et al., 2021), the usual treatment includes either resection or observation without surgery as many tumors spontaneously regress. Patients with intermediate-risk tumors often receive multiagent chemotherapy before definitive resection of the tumor, and the intensity of the treatment is based on clinical and molecular features of the tumor as well as the response to therapy (Twist et al., 2019). Approaches to treat high-risk tumors are the most intensified, and usually include a combination of chemotherapy, surgery, radiation therapy, as well as immunotherapy and stem cell transplant, which results in 5-year OS rates of 62% (Irwin et al., 2021) (**Table 1**).

Table 1: An overview of the treatment approaches available for NB patients.
Treatment strategies are risk based. GM-CSF – granulocyte-macrophage colony-stimulating factor, SCT – stem cell transplant. Adapted from ("Neuroblastoma Treatment (PDQ(R)): Health Professional Version," 2002).

Risk-Group Assignment	Treatment Approaches
Low-risk	**Surgery with observation**
	Observation +/- biopsy
	Chemotherapy +/- surgery
	Radiation therapy (only for emergency therapy)
Intermediate-risk	**Chemotherapy +/- surgery**
	Surgery with observation (in infants)
	Radiation therapy (if needed)

High-risk	**A combination of chemotherapy, surgery, myeloablative therapy and SCT, radiation therapy, immunotherapy, with GM-CSF and isotretinoin**
Stage 4S/MS	**Observation with supportive care** (for asymptomatic patients with favorable tumor biology)
	Chemotherapy (for symptomatic patients, very young infants, or those with unfavorable biology)
	Radiation therapy (rarely for patients with symptoms related to hepatomegaly from metastatic disease)

Development of novel biomarkers that allow better patient risk stratification could improve patients outcome. It was shown that the reduction of aggressive therapy for low- and intermediate-risk patients led to the good response rates with overall survival higher than 90% and minimized side-effects (Baker et al., 2010). However, a large subset of high-risk tumors develops chemo- and radiotherapy resistance that often leads to treatment failures, which, combined with sub-clonal evolution in relapse patients, highlight the necessity for more personalized and targeted therapy approaches (Abbasi et al., 2017).

Amplified *MYCN* is the most prominent tumor-specific aberration that is associated with the most aggressive subtype of NB and is therefore a promising therapeutic target. However, targeting nuclear transcription factors with pharmacological treatments is difficult, and to date there is no molecule that can directly target MYCN. As a result, recent efforts have focused on indirect approaches to interfere with MYCN function, such as suppressing *MYCN* transcription (Shin, 2018; Zimmerman et al., 2018), MYCN protein stability (Muller et al., 2014; Savino et al., 2011; Wang et al., 2007), MYCN target genes (Lewis et al., 2020; Sholler et al., 2018) or exploiting MYCN-dependent synthetic lethality (Z. Liu et al., 2020).

Beside targeting MYCN, other personalized therapy approaches are being developed. For instance, as NB arises from undifferentiated neuronal cells, therapies based on inducing cell differentiation were shown to be associated with more benign phenotypes of the disease (Bayeva et al., 2021). As such, retinoic acid was proven effective to induce differentiation *in vitro* in early 1990s (Melino et al., 1993), and to increase event free survival when administered after chemotherapy (Matthay et al., 1999). Additionally, targeting the Trk family receptors (TRK), which are also controlling differentiation, showed beneficial effects in NB treatment (Minturn et al., 2011), and

several compounds targeting TRKs are currently under clinical evaluation (Pacenta & Macy, 2018).

Therapeutic strategies are also being developed for patients with RAS-MAPK pathway activation or aberration of ALK gene expression. For instance, crizotinib showed positive results in treatment of ALK activated NB (George et al., 2008), while inhibitors of RAS-MAPK pathway inhibited cell growth and xenograft progression (Eleveld et al., 2015). These approaches are especialy valued, as they provide highly needed treatment options for relapse patients.

The application of immunotherapy, which enhances the immune system's function, has exhibited encouraging outcomes in combating various cancer types, including NB. One approach, which involves using monoclonal antibodies to target a protein called G_{D2} on cancer cells, combined with granulocyte-macrophage colony-stimulating factor (GM-CSF) or interleukin-2, has been effective in high-risk NB patients with refractory disease (Furman et al., 2019). While these subgroups have responded well to the therapy, other high-risk patients, who often have advanced cancer at the time of diagnosis and experience rapid progression, have only seen modest improvements. Additional investigation and an enhanced comprehension of the molecular biology underlying NB are imperative in recognizing novel prognostic indicators and establishing more efficacious treatment alternatives.

3.1.5. MYCN transcription factor

Approximately 20% of NB patients harbor amplified *MYCN* oncogene, which is linked with an unfavorable prognosis (**Figure 4**) (Brodeur et al., 1987; Brodeur et al., 1984). Tumors that do not show amplification at diagnosis almost never develop this alteration later on, indicating that amplified *MYCN* is a defining characteristic of aggressive disease (Brodeur et al., 1987).

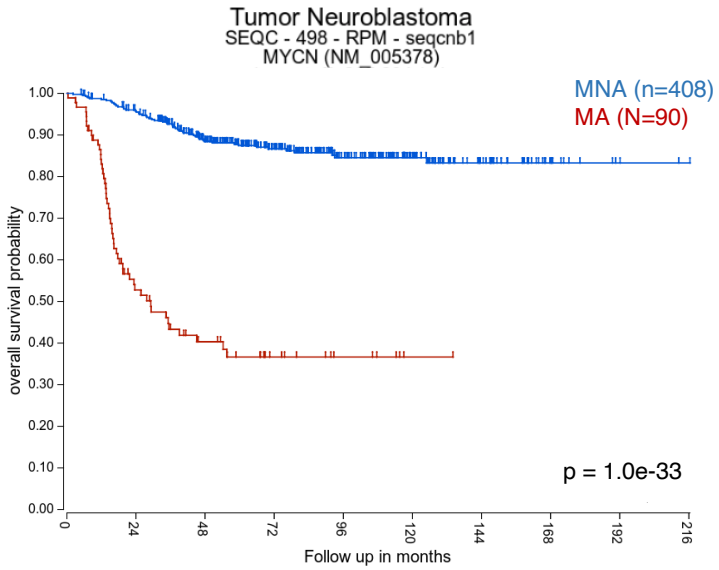

Figure 4: Overall survival probability assessed by *MYCN* status.
Data derived from R2 genomics platform (498 NB primary tumors). MA – *MYCN*-amplified, MNA – *MYCN*-non-amplified. p-value calculated with log rank test.

MYCN belongs to a group of oncogenes known as transcription factors, which also encompasses MYC and MYCL. These oncogenes have high homology in their coding regions, allowing them to function in place of each other in certain experimental conditions (Malynn et al., 2000). In contrast to MYC, which is widely expressed in various tissues, *MYCN* expression is usually limited to the nervous system and mesenchymal tissues during certain developmental stages, and is expressed at low levels in adult tissues (Zimmerman et al., 1986).

NB is thought to originate from fast-proliferating neuroblasts with high *MYCN* expression that are found in the developing adrenal gland and sympathetic ganglia during fetal development (Jansky et al., 2021). High *MYCN* expression in these cells appears to increase the likelihood of acquiring aneuploid karyotypes and genomic MYCN alterations during tumor formation, while genomic alterations that activate MYC or MYCL are relatively rare in NB.

The genetic structure of MYCN includes a basic (b) region that facilitates DNA binding, as well as a helix-loop-helix (HLH) and leucine zipper domain (Zip), which enables it to interact with other bHLH-Zip proteins and bind to DNA (Murre, McCaw, & Baltimore, 1989; Murre, McCaw, Vaessin, et al., 1989). As a part of a protein network with MYC and MAX, it can regulate the transcription of target genes by recruiting chromatin

remodeling co-factors (**Figure 5**). MYC/MAX heterodimers can promote tumor formation and progression, while MAD/MAX or MNT/MAX dimers block cell differentiation by repressing transcription (Laherty et al., 1997). In addition, MYCN can enhance transcriptional elongation, whereas MAX-MAX homodimers are transcriptionally inactive and can repress gene expression by competing with activating MYC-MAX complexes.

The MYC/MAX heterodimer specifically recognizes hexameric CACGTG DNA sequences, known as canonical or classical E-boxes, to activate transcription (Blackwood & Eisenman, 1991). On the other hand, MYCN can also repress target genes independently of initiator elements (INR) or MAX and activate the Polycomb repressive complex 2 (*PRC2*) to set silencing histone marks (Corvetta et al., 2013; Wang et al., 2012). MYCN has also been shown to have a role as a global regulator of euchromatic regions, a function that is in contrast with MYCN's classical role as a transcription factor (Cotterman et al., 2008; Zeid et al., 2018).

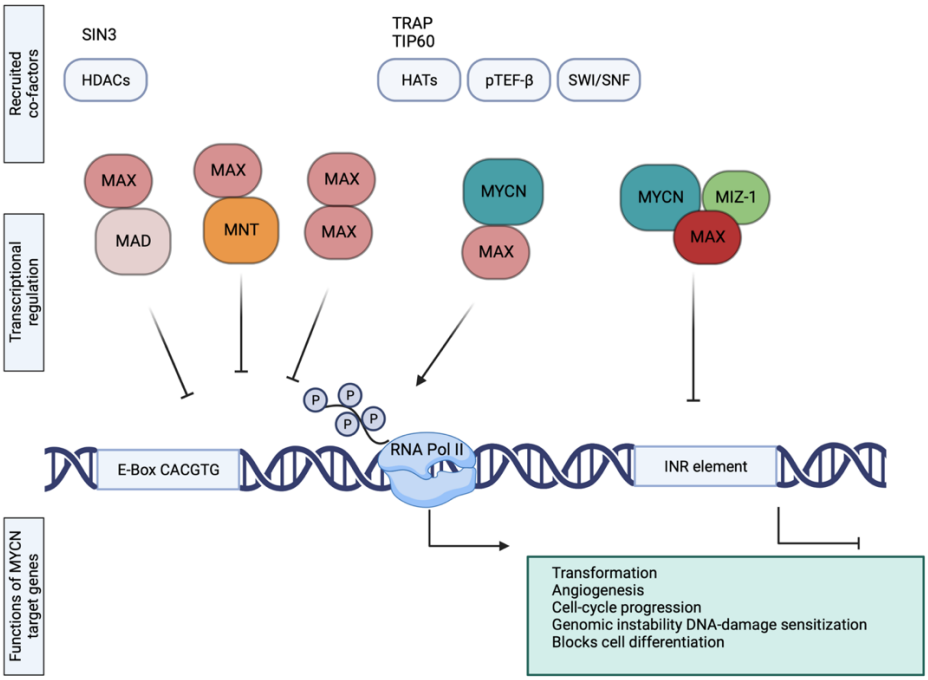

Figure 5: MYCN regulatory network.
MYCN binds DNA with its partner MAX to either activate or repress the transcription. Recruitment of chromatin remodeling factors and pTEF-β phosphorylating RNA Pol II leads to transcription activation, while MYCN-MAX interaction with MIZ-1 at INR elements induces gene repression. There is an ongoing competition of MYCN-MAX complex with other repressive factors that regulate MAX for complex formation. Adapted from (Patel et al., 2004).

3.1.6. MYCN-driven metabolic reprogramming

Cellular metabolism is a complex, dynamic system that enables living cells to meet their bioenergetic and biosynthetic needs. NB cells, like many other cancer cells, often undergo metabolic adaptations to increase the uptake and utilization of nutrients (**Figure 6**). This allows them to fuel the biosynthesis of macromolecules, which are necessary for cancer formation, as well as their rapid growth and proliferation (Martinez-Reyes & Chandel, 2021; Pavlova et al., 2022; Schulze & Harris, 2012). These metabolic transformations concern many aspects of cellular metabolism, including aerobic glycolisis, amino acid, nucleotide as well as fatty acid metabolism, and MYCN role in remodelling these processes will be described in the following chapters.

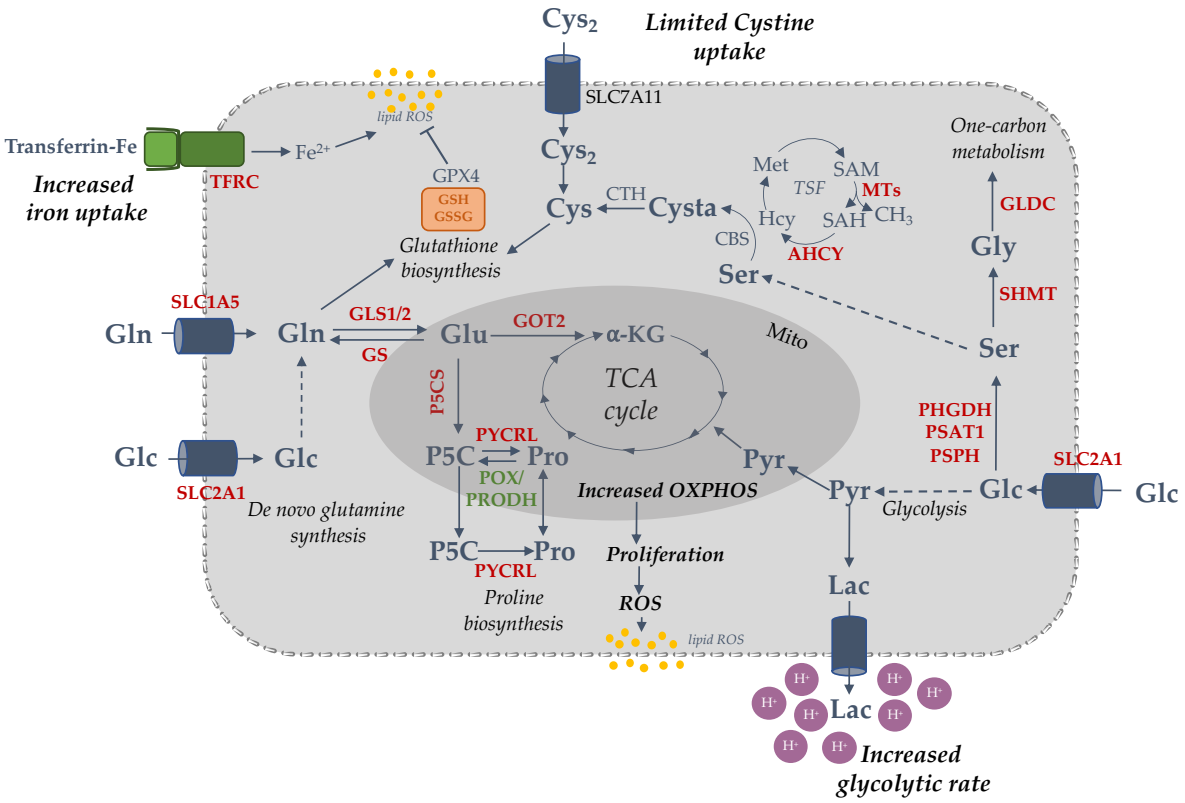

Figure 6: Major metabolic pathways supporting MYCN-driven cancer cell proliferation. Elevated central carbon metabolism is a source for protein, nucleotides, and lipids production. Proteins upregulated by MYCN are indicated in red, while the suppressed ones are indicated in green.

3.1.6.1. Aerobic glycolysis

A well-known characteristic of cancer is the altered metabolic behavior, which involves enhanced glucose consumption and secretion of lactate, despite sufficient oxygen

levels, termed the Warburg effect (Vander Heiden et al., 2009; Warburg, 1956). Studies have demonstrated that increased glycolysis promotes the growth and survival of NB cells both in laboratory settings and in live animal models (Levy et al., 2012; Nile et al., 2021). The transcription factor MYCN and hypoxia-inducible factor 1 α (HIF-1α) have been demonstrated to upregulate the expression of glycolytic enzymes such as hexokinase 2 (*HK2*) and lactate dehydrogenase A (*LDHA*) (Qing et al., 2010). A global -omics analysis of NB cells also revealed a strong correlation between high *MYCN* levels and increased expression of several proteins involved in metabolic pathways, including glycolysis (Oliynyk et al., 2019). In addition, ectotopic expression of *MYCN* in *MYCN*-non-amplified NB SH-EP cells was found to trigger a metabolic switch towards enhanced glycolysis, which was accompanied by increased sensitivity to 2-deoxyglucose, a glycolysis inhibitor (Tjaden et al., 2020).

These findings highlight the important role of MYCN in promoting glycolysis in NB cells.

3.1.6.2. Amino acids metabolism

Metabolic pathways involved in amino acid metabolism play a significant role in the development and progression of cancer. The human body can synthesize a portion of the 20 proteinogenic amino acids, known as non-essential amino acids, which include alanine, arginine, asparagine, aspartate, cysteine, glutamate, glutamine, glycine, proline, serine, and tyrosine. The remaining amino acids cannot be synthesized *de novo* and are considered essential amino acids, which consist of histidine, isoleucine, leucine, lysine, methionine, phenylalanine, threonine, tryptophan, and valine.

It has been demonstrated that MYCN transcriptionally controls the metabolism of essential amino acids by upregulating the expression of genes involved in their transport, namely the solute carrier family (SLC) of genes *SLC7A5* and *SLC43A1* (Yue et al., 2017). In addition, it has been found that reducing the levels of *SLC7A5* or *SLC43A1* can decrease *MYCN* expression by disrupting the translation of *MYCN* mRNA which leads to inhibition of the NB tumor growth *in vitro* and *in vivo* (Yue et al., 2017). This evidence indicates that MYCN and SLC7A5/SLC43A1 work together in a

reinforcing cycle to increase their expression and support the proliferation and cancerous potential of NB cells.

However, reprogramming of cellular metabolism in cancer cells is mainly concerning non-essential amino acids (Choi & Coloff, 2019), which synthesis and transport is controlled by a master regulator – the activating trancription factor 4 (ATF4) (Ameri & Harris, 2008; Kilberg et al., 2009; Pakos-Zebrucka et al., 2016). ATF4, along with the histone lysine demethylase KDM4C, has been shown to upregulate the expression of enzymes responsible for synthesizing several non-essential amino acids, including alanine, arginine, asparagine, aspartate, cysteine, glutamate, glycine, and serine, in NB cells. Moreover, they also enhance the expression of several amino acid transporters, including *SLC1A4, SLC1A5, SLC3A2, SLC6A9, SLC7A1, SLC7A5,* and *SLC7A11* (Zhao et al., 2016). Interestingly, it was shown that *MYCN*-amplified tumors have significantly higher levels of *ATF4* (Xia et al., 2019), and increased *ATF4* expression is linked with poor outcome of NB patients (Ding et al., 2013). Indeed, further studies demonstrated that MYCN increases the *ATF4* expression by binding to its promoter region (Xia et al., 2019).

Taken together, these results imply that the interaction between MYCN and ATF4, along with epigenetic regulators such as KDM4C, plays a crucial role in increasing the availability of amino acids to support the MYCN-driven growth program in NB (Liu et al., 2016; Xia et al., 2019).

3.1.6.3. Glutamine metabolism

Glutamine addiction of cancer cells has already been established for a long time (Eagle et al., 1956; Kovacevic & McGivan, 1983). Cancer cells that rapidly proliferate mainly depend on aerobic glycolysis, a process in which a significant portion of the produced pyruvate is converted into lactate instead of being utilized in the tricarboxylic acid (TCA) cycle. Therefore, these cells must find alternative ways to maintain the TCA cycle to produce ATP and provide intermediates for the synthesis of macromolecules, such as proteins and lipids. For instance, it has been demonstrated that cancer cells with abnormal MYCN levels require tremendous amounts of glutamine to support their fast proliferation (Qing et al., 2012). *MYCN*-amplified NBs depend on the activation of

the glutamine transporter ASCT2/SLC1A5 for the anaplerosis of the TCA cycle (**Figure 6**). This activation is regulated by the ATF4 transcription factor, which directly coordinates with MYCN to increase the expression of *ASCT2* (Qing et al., 2012; Ren et al., 2015). Moreover, MYCN not only elevate the glutamine uptake, but also positively regulates glutaminolysis, a process that enables cells to replenish their energy supply by converting glutamine into α-ketoglutarate (Wang et al., 2018). It has been shown that glutaminolysis was suppressed upon knockdown of *MYCN*, whereas *MYCN* overexpression enhanced it (Wang et al., 2018). In addition, glutaminase 2 (*GLS2*), an enzyme catalyzing the conversion of glutamine to glutamate, is a direct transcriptional target of MYCN, and its expression is significantly elevated in *MYCN*-amplified NBs (Xiao et al., 2015). Several reports also showed that the expression of other genes involved in glutamine metabolism (*GOT1*, *GOT2*, *GPT*, *GPT2* and *PSAT1*) (**Figure 6**) is upregulated by combined activity of MYCN, ATF4 and KDM4C (Liu et al., 2016; Wang et al., 2018; Xia et al., 2019). On the other hand, it was demonstrated that combining glutamine deprivation with radiotherapy, a treatment option for high-risk NBs, led to a selective radio-resistance of *MYCN*-amplified NB cells (Le Grand et al., 2020). This resistance was caused by MYCN's ability to disrupt the DNA repair pathway, maintain glutathione (GSH) and reactive oxygen species (ROS) levels, as well as increase cancer stem cell-like populations.

Overall, these reports indicate that glutamine uptake and metabolism in *MYCN*-amplified NB cells are tightly controlled by combined activity of MYCN, ATF4 and KDM4C to meet their biosynthetic needs for cell growth and division.

3.1.6.4. Serine-glycine-one-carbon (SGOC) metabolism

Higher activity of genes involved in serine and glycine metabolism are a fundamental component of cancer metabolism (Locasale, 2013; Reina-Campos et al., 2020; Yang & Vousden, 2016). The SGOC pathway links the intermediate product of glycolysis, 3- phosphoglycerate (3PG), with the production of serine, glycine, and the one-carbon molecule 5,10-methylenetetrahydrofolate (5,10-MTHF), as well as NADH and α- ketoglutarate (**Figure 7**). These end products are involved in various cellular

processes that are vital for cancer cell growth, including the synthesis of macromolecules, maintaining redox balance, and regulating methylation.

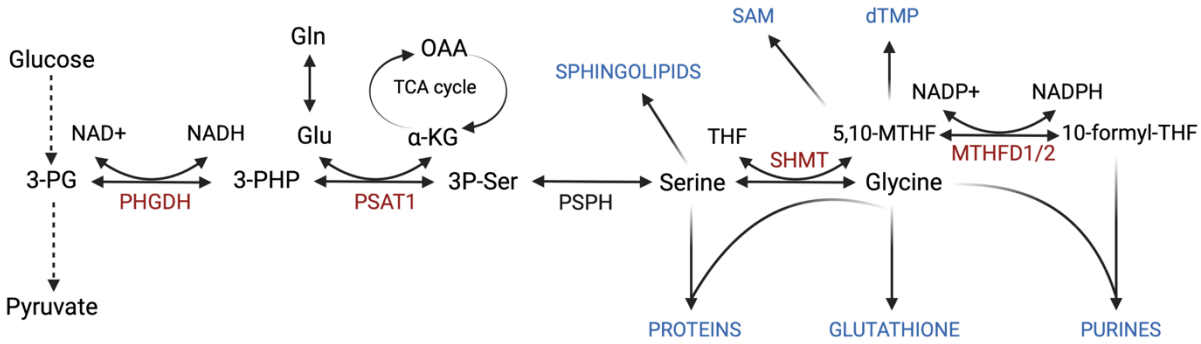

Figure 7: The serine-glycine-one-carbon metabolic pathway.
The intermediates and products of the SGOC metabolic pathway are used as the building blocks for synthesizing other macromolecules, including proteins, nucleotides, lipids, as well as glutathione, reducing equivalents (NADH, NADPH) and components of methionine cycle (SAM). MYCN target genes are indicated in red.

Activation of the SGOC metabolic pathway is also a consequence of transcriptional reprogramming triggered by MYCN oncoprotein (**Figure 7**). Studies have demonstrated that MYCN-amplified NBs often exhibit increased expression of PHGDH, PSAT1, and SHMT2, which is attributed to the transcriptional activation mediated by both MYCN and ATF4 (Arlt et al., 2021; Xia et al., 2019). In addition, MYCN is known to directly increase the transcription of glycine decarboxylase (GLDC), which is an enzyme that catalyzes the initial and crucial step in glycine degradation, resulting in the production of 5,10-MTHF (Alptekin et al., 2019). Elevated levels of *GLDC* were observed in both *MYCN*-amplified NB tumors and cell lines, and siRNA-mediated knockdown inhibited proliferation and tumorigenicity by inducing G1 arrest. Additionally, downregulation of *GLDC* disrupted purine and central carbon metabolism, and reduced citrate production that led to decreased levels of cholesterol and fatty acids (Alptekin et al., 2019).

3.1.6.5. Nucleotides metabolism

The intracellular nucleotide pools are replenished through two main pathways: *de novo* biosynthesis and salvage pathways. While salvage pathways remain the primary source of degraded bases used for nucleotide synthesis in quiescent cells (Fasullo &

Endres, 2015; Pedley & Benkovic, 2017), rapidly proliferating cancer cells have much higher demand on nucleotides, which are necessary for maintaining DNA replication, RNA expression and ATP generation. To meet the heightened demand for nucleotide de novo biosynthesis, cancer cells trigger the activation of multiple metabolic pathways. These pathways encompass the pentose phosphate pathway, amino acid metabolism, one-carbon metabolism, electron transport chain, and oxidative phosphorylation (OXPHOS), which collectively furnish the required building blocks and energy for the process (Lane & Fan, 2015; Pedley & Benkovic, 2017).

In the context of NB, MYCN plays a crucial role in promoting nucleotide biosynthesis. By upregulating enzymes involved in the one-carbon metabolism pathway, it enhances the production of 10-formyl-tetrahydrofolate (10-formyl-THF) and glycine, intermediates of purine biosynthesis (Xia et al., 2019). For instance, the levels of the mitochondrial methylenetetrahydrofolate dehydrogenase 2 (*MTHFD2*) and phosphoribosylaminoimidazole carboxylase (*PAICS*) were simultaneously upregulated in *MYCN*-amplified NB cells and tumors, which were more prone to metastasize (Cheung et al., 2019). MYCN, by directly activating *MTHFD2*, mediates the folate cycle to increase purine synthesis, and further enhance nucleotide production by *PAICS*. Of note, dual knockdown of this gene pair in high-MYCN NB cells synergistically diminishes cell proliferation, colony formation, migration and synthesis of DNA. In addition, MYCN promotes pyrimidine synthesis by transcriptional upregulation of genes involved in that process, such as dihydroorotase (*CAD*) or dihydroorotate dehydrogenase (*DHODH*) (Yu et al., 2021). It also increases substrates for *de novo* pyrimidine biosynthesis through ATF4-mediated transcriptional upregulation of glutamine transporter (*SLC1A5*) (Ren et al., 2015) and by upregulation of enzymes involved in aspartate synthesis (Glutamic-Oxaloacetic Transaminase 1/2; GOT1/2) (Wang et al., 2018). Finally, MYCN also activates the salvage pathway by upregulating the uridine-cytidine kinase 2 (*UCK2*) (Yu et al., 2021).

Collectively, the existing body of evidence suggests that MYCN is essential for promoting nucleotide synthesis in NB cells by stimulating the expression of synthesis enzymes and activating additional metabolic pathways that furnish the requisite substrates for nucleotide production. This process leads to a significant increase in the

intracellular nucleotide pools, highlighting the crucial role of MYCN in the metabolic regulation of NB (Yu et al., 2021).

3.1.6.6. Fatty acids metabolism

With the development of new technologies to study lipids, an emerging role of fatty acids (FAs) and lipids metabolism in cancer development has been reported in recent years (Butler et al., 2020; Matsushita et al., 2021; Santos & Schulze, 2012). FAs play a crucial role in promoting tumor growth and progression as they are necessary for membrane biosynthesis, energy production and storage, as well as their participation in the signal transduction. Recent studies revealed that *MYCN* amplification caused glycerolipid accumulation by activation of fatty acid transport and *de novo* synthesis (Tao et al., 2022). Indeed, Tao et al. showed that FAs uptake is crucial for *MYCN*-amplified NB cells survival.

In the realm of NB, polyunsaturated fatty acids (PUFAs) have garnered significant attention, given their strong activation in neurons. Of particular interest is docosahexaenoic acid (DHA), an omega-3 PUFA with recognized anti-tumor activity. Recent research has shown that MYCN depletion is associated with elevated levels of DHA, pointing to a potential therapeutic avenue for NB treatment (Ding et al., 2019). Based on bioinformatic analysis, it has been demonstrated that MYCN mediates the accumulation of DHA through the PRC1-mediated repression of ELOVL fatty acid elongase 2 (*ELOVL2*), a crucial enzyme involved in cellular DHA synthesis. Moreover, the expression of *ELOVL2* is positively correlated with more favorable biological characteristics and extended patient survival in primary NBs, underscoring the tumor suppressive functions of DHA and ELOVL2, both of which are negatively regulated by the concomitant epigenetic activity of MYCN and PRC1 (Ding et al., 2019).

Moreover, it has been shown that MYCN plays a significant role in regulating fatty acid oxidation (FAO) in *MYCN*-amplified NBs (Zirath et al., 2013). Global proteome analysis upon MYCN inhibition using 10058-F4 agent shows downregulation of several proteins involved in FAO, namely ACADM, DECR1, ECHS1, ECI1, HADHA, HADHB or HSD17B10 (Zirath et al., 2013). Additionally, MYCN inhibition led to accumulation of lipid droplets which was directly caused by a disruption of mitochondrial function.

Overall, these results show that NB growth is enhanced by MYCN-driven FAO, and this phenomenon could be exploited for establishment of new treatment strategies.

3.1.7. MYCN role in regulating cell death

As previously outlined, the metabolic adaptations orchestrated by MYCN facilitate efficient nutrient uptake and the synthesis of requisite building blocks, thereby promoting rapid proliferation in NB. Nonetheless, studies indicate that amplification of MYCN can render NB cells more susceptible to apoptosis in a p53-dependent manner (Petroni et al., 2012; Petroni et al., 2011; Van Maerken et al., 2009; Veschi et al., 2012). Although mutations in the *TP53* gene are rarely found in NB, several mechanisms that lead to its functional inactivation have been identified in this tumor entity. Examination of approximately 80 tumor samples indicated a correlation between high *TP53* expression and the status of MYCN (Chen et al., 2010). Additionally, the presence of MYCN upregulated various p53-regulated genes, such as *MDM2* and *PUMA*. During normal embryonic development, MYCN can trigger p53-dependent apoptosis, which serves to eliminate fast proliferating cells and prevent developmental abnormalities. However, evidence suggests that tumors with amplified-*MYCN* can develop mechanisms to circumvent MYCN-induced apoptosis by modulating the p53/MDM2/p14^{ARF} pathway (Chen et al., 2009). Additionally, co-expression of *MYCN* and *BCL-2*, an anti-apoptotic molecule, is a common feature of NB tumors associated with unfavorable patient outcome (Castle et al., 1993). These findings indicate that MYCN creates a subtle balance between pro- and anti-apoptotic molecules that can be perturbated by various factors, and dysregulation of these processes can eventually trigger apoptosis.

3.2. Ferroptosis as a novel treatment strategy for cancer patients

In addition to heightened nutrient uptake, MYCN-driven rapid proliferation leads to the induction of oxidative stress through increased production of reactive oxygen species (ROS). Consequently, cells become more susceptible to ferroptosis, an iron-dependent and oxidative non-apoptotic form of cell death that can be mitigated by glutathione peroxidase 4 (GPX4). Recent studies revealed that *MYCN*-amplified NB cells are highly addicted to cystine, an oxidized form of cysteine, which deprivation

induced significant lipid peroxidation in high-*MYCN* oncogenic background that eventually leads to ferroptosis execution (**Figure 8**). Cysteine is a sulfur- containing amino acid, which plays a role in numerous important cellular processes (Alborzinia et al., 2022; Floros et al., 2021; Lu et al., 2021). In addition to being a proteinogenic amino acid, cysteine is involved in several essential processes. Cysteine's thiol side chain is an exceptionally reactive group that functions as a nucleophile, which is vital for the catalytic function of numerous enzymes. Moreover, the formation of disulfide bonds between cysteine residues is critical for proper protein folding and stability. The breakdown of cysteine also produces hydrogen sulfide (H_2S) that can be used to generate ATP through the electron transport chain and pyruvate or as a signaling molecule to control cell redox state (Bonifacio et al., 2021). Additionally, cysteine is one of the three amino acids that make up GSH, which helps to neutralize reactive oxygen species (ROS) (Harris et al., 2015).

Cysteine can be either transported inside the cell in its oxidized form via cystine-glutamate antiporter (system x_c^- composed of SLC7A11 and SLC3A2) (Bannai, 1986) or synthesized de novo in the so called transsulfuration pathway. The process of *de novo* cysteine synthesis is mediated by the enzyme cystathionine β-synthase (CBS), which facilitates the condensation of serine and homocysteine, a methionine cycle intermediate, to form cystathionine. This molecule is then further metabolized by cystathionine γ-lyase (CTH) to yield cysteine and α-ketoglutarate (Sbodio et al., 2019).

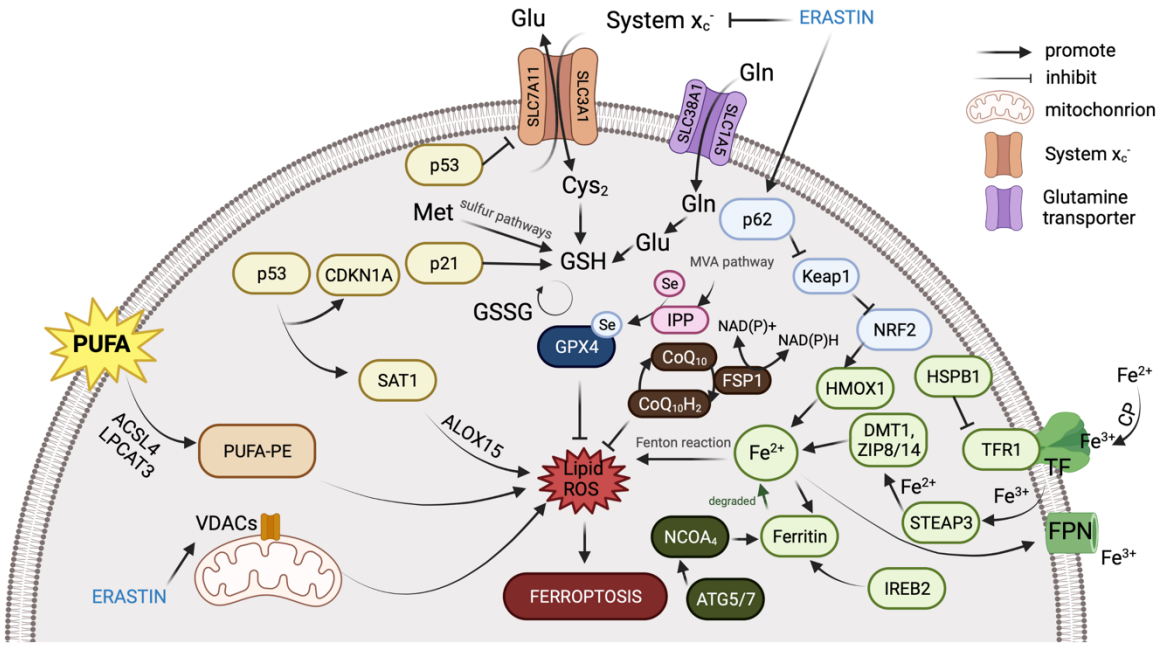

Figure 8: Overview of ferroptosis network.
The ferroptosis network is composed of three major categories. The first and most studied mechanism is controlled by the GSH/GPX4 axis and it involves several components, such as system x_c^- inhibition, mevalonate (MVA) pathway, sulfur transfer pathway (methionine cycle), glutamine metabolism, and p53-regulated pathway. The second major component is related to the iron metabolism, which is heavily regulated by ATG5-ATG7-NCOA$_4$ and p62-Keap1-NRF2 pathways. The third group concerns genes related to lipid metabolism, such as ACSL4, LPCAT3, or P53-SAT1-ALOX15 pathway. Moreover, erastin influence on system x_c^- and mitochondria to induce ferroptosis, as well as the recently discovered anti-ferroptotic pathway (FSP1-CoQ$_{10}$-NDA(P)H) are also depicted. Adapted from (Li et al., 2020)

Studies have shown that NB cells with amplified *MYCN* upregulate the expression of important enzymes involved in cysteine metabolism, such as *CBS*, *CTH*, and *SLC3A2*. This upregulation is achieved through the transcriptional activity of KDM4C and ATF4, leading to increased cysteine levels that are necessary to maintain redox homeostasis. In addition, recent studies revealed that *MYCN*-amplified NB cells show high sensitivity towards GPX4-targeting ferroptosis inducers. Moreover, high *MYCN* levels significantly correlated with upregulated expression of transferrin receptor 1 (*TFRC*), a main cellular iron transporter, thus indicating an increased iron uptake that can potentially lead to enhanced iron-driven lipid peroxidation. Of note, *TFRC* overexpression rendered cells selectively sensitive to GPX4 inhibition. In addition, it has been observed that *MYCN*-amplified NB cells exhibit reduced expression of *SLC7A11*, a transporter protein that facilitates the import of cystine required for the synthesis of GSH, a crucial component in the detoxification of lipid hydroperoxides

GPX4. Therefore, the reduced expression of *SLC7A11* in *MYCN*-amplified cells renders them more susceptible to cystine depletion and underscores their heightened dependence on this amino acid for maintaining redox homeostasis.

The recently published data also showed that *MYCN*-amplified NB cells have low basal levels of intracellular cysteine and GSH, which is most likely caused by reduced cysteine uptake and elevated GSH consumption, rendering cells highly sensitive to oxidative cell death. In addition, cysteine is also utilized for protein synthesis, a process that is heavily activated in rapidly proliferating *MYCN*-amplified NB cells. Indeed, this competing need of cysteine usage for redox homeostasis and protein synthesis can create a vulnerability that eventually lead to ferroptotic cell death.
Taken together, these studies unravel a novel vulnerability of *MYCN*-amplified NBs that could potentially be used for development of novel treatment strategies for high-risk *MYCN*-amplified NB patients.

4 Aims of the thesis

Aims

Neuroblastoma is a highly heterogeneous pediatric cancer that arises from immature nerve cells and accounts for a significant number of childhood cancer-related deaths. Despite multi-modal treatment available for NB, the outcome of patients, especially with amplified *MYCN* is often poor. Although amplified *MYCN* is a well-known risk factor for NB, direct targeting of MYCN remains challenging, which has led researchers to explore alternative therapeutic strategies that focus on exploiting metabolic vulnerabilities related to MYCN.

Recent studies have discovered a functional association between oncogenic *MYCN* and ferroptosis, which is a controlled form of cell death that is dependent on iron. However, previous work has provided only partial insights into the mechanisms of ferroptosis in NB tumors (Alborzinia et al., 2022), and the drivers of sensitivity to ferroptosis were not yet fully described or identified. While the work of Alborzinia et al. focused on the most extreme cases where *MYCN* was either highly amplified or unchanged, NB patients exhibit tumors with a much broader range of clinical presentations. This includes tumors with different genetic backgrounds, such as amplified *MYCN* or *c-MYC*, *MYCN* or *c-MYC* activating translocations, and those with activated telomere lengthening mechanisms without any *MYCN/c-MYC* aberration.

To enhance our knowledge of ferroptosis in NB, this study aims to:

(1) establish and fully characterize the role of MYC(N) in ferroptosis by profiling a large number of NB cell lines with different genetic backgrounds that represent the heterogeneous spectrum of the disease;

(2) investigate the impact of cell identity (adrenergic / mesenchymal) on ferroptosis sensitivity, and identify the mechanisms/factors that contribute to cell resistance to ferroptosis or shape cell response to ferroptosis induction;

(3) study the response of NB cell lines to various ferroptoric stress stimuli to gain a deeper insight into ferroptosis regulation in NB;

(4) translate the *in vitro* findings to a more patient-relevant context by estimating primary tumors' sensitivity to ferroptosis using machine learning approaches.

Ultimately, the findings of this study will contribute to a better understanding of the mechanisms of ferroptosis in NB, paving the way for the development of novel therapeutic strategies that target ferroptotic vulnerabilities.

5 Materials and Methods

Materials and Methods

5.1. Materials

Table 2: Chemicals and reagents

Acetic acid	Sigma Aldrich
Agar agar	Carl Roth
Agarose	Carl Roth
Bacto-tryptone	Carl Roth
Bis- Tris	Sigma Aldrich
Bovine serum albumin (BSA)	Sigma Aldrich
Brilliant Blue R Staining Solution	Sigma Aldrich
Chloroform	Sigma Aldrich
Dimethyl sulfoxide (DMSO)	Carl Roth
Ethanol	Sigma Aldrich
Formaldehyde	AppliChem
Glutaraldehyde	Sigma Aldrich
Isopropanol	Sigma Aldrich
Methanol	Sigma Aldrich
Milk powder	Sigma Aldrich
Sodium chloride	Sigma Aldrich
Sodium dodecyl sulfate (SDS)	AppliChem
Tris base	AppliChem
Tris-HCl	AppliChem
Triton X-100	AppliChem
Trypan Blue	Sigma Aldrich
Tween-20	Sigma Aldrich

Table 3: Amino acids

D-Glucose-$^{13}C_6$	Cambridge Isotope Laboratories, Inc.
L-Cystathionine	Sigma Aldrich
L-Cystine	Sigma Aldrich
L-Cystine-$^{13}C_6$	Cambridge Isotope Laboratories, Inc.
L-Glutamic acid	Sigma Aldrich
L-Glutamic acid-$^{13}C_5$	Cambridge Isotope Laboratories, Inc
L-Glutamine	Thermo Fisher Scientific
L-Glutamine-$^{13}C_5$	Cambridge Isotope Laboratories, Inc.
L-Glycine	Carl Roth
L-Homocysteine	Sigma Aldrich
L-Methionine	Sigma Aldrich
L-Methionine-^{34}S	Toronto Research Chemicals
L-Serine	Sigma Aldrich

Table 4: Others

SOC medium	Takara Bio
Stellar competent cells	Takara Bio
Yeast extract	GERBU

Table 5: Active compounds

Erastin	Biomol
Ferrostatin-1	Sigma Aldrich
Imidazole ketone erastine (IKE)	MedChemExpress
L- Buthionine sulfoximine (BSO)	Santa Cruz Biotechnology, Inc.
ML210	MedChemExpress
RSL-3	MedChemExpress
Sorafenib	Cayman

Table 6: Cell culture reagents

Ampicillin	Serva
Blasticidin S Hydrochloride	Santa Cruz Biotechnology
Custom RPMI Medium 1640 [-] L-Cystine, [-] L-Glutamic Acid, [-] L-Methionine, [-] Glutathione (reduced)	GIBCO, Invitrogen
Dialyzed Fetal bovine serum (FCS)	GIBCO, Invitrogen
Doxycycline	BD Clontech
Fetal bovine serum (FCS)	GIBCO, Invitrogen
Geneticin, G418	Sigma Aldrich
Hank's Balanced Salt Solution	GIBCO, Invitrogen
Opti-MEM	GIBCO, Invitrogen
PBS	GIBCO, Invitrogen
Penicillin/ Streptomycin (10,000 U/ml, 1000 μg/ml)	Bio Whittaker
RPMI 1640	GIBCO, Invitrogen
Zeocin	Thermo Fisher Scientific

Table 7: Molecular biology reagents

Amersham ECL Prime Western Blotting Detection Reagent	GE Healthcare
BM Chemiluminescence Blotting Substrate	Roche
BODIPY™ 581/591 C^{11}	Thermo Fisher Scientific
CellTiter-Blue® Cell Viability Assay	Promega
Clarity Western ECL Substrate	BioRad
EDTA	Carl Roth
EDTA-free Mini Complete Protease Inhibitor Cocktail	Roche
dNTPs	Thermo Fisher Scientific

Effectene Transfection Reagent	Qiagen
EpiTaq HS Polymerase	Takara Bio
MOPS running buffer (20x)	Thermo Fisher Scientific
M-Per lysis buffer	Thermo Fisher Scientific
NuPAGE Sample Buffer	Thermo Fisher Scientific
Oligo(dT)20 Primer	Thermo Fisher Scientific
PhosphoSTOP	Roche
Platinum High Fidelity Taq Polymerase	Thermo Fisher Scientific
Ponceau-S	Sigma Aldrich
PowerUP SYBR Green Mastermix	Thermo Fisher Scientific
Protease inhibitor cocktail, EDTA	Roche
RNAseA	Invitrogen

Table 8: Laboratory materials

12-Strip PCR Tubes, 0.2 ml	Star Lab
Blot 2 Transfer Stacks, nitrocellulose	Invitrogen
Cell culture flasks and plates	TPP
Cell scraper	TPP
Cryotubes	NalgeneNunc
Cuvettes Semi-Micro	Greiner Bio-One
FACS tubes with cell-strainer cap	Corning
Filter tips, graduated (10, 100, 200, 1000 µl)	Star Lab
Luna Cell Counter Slides	Logos Biosystems
NuPAGE Novex 4-12% Bis-Tris-Gels	Thermo Fisher Scientific
Plastic pipettes (5, 10, 25, 50 ml)	Corning
qPCR 96 well plates, white	Biozym
qPCR optical adhesive film	Applied Biosystems
Qubit Tubes	Roche
Reaction tubes (0.5, 1.5, 2.0, 5.0 ml)	Eppendorf
Reaction tubes (15, 20 ml)	Greiner Bio-One
Sonification tubes	Diagenode

Table 9: Research equipment

2100 Bioanalyzer	Agilent Technologies
Analytical Balances PM 4600	Mettler
Biofuge fresco	Thermo Fisher Scientific
Bioruptor Pico	Diagenode
Cell culture hood Hera	Heraeus
ChemiSmart 5100	Vilber Lourmat
CO2 Incubator Steri-Cult	Thermo Fisher Scientific
Gel documentation system (Geldoc)	BioRad
Horizontal mixer RM5	CAT
iBlot 2 Dry Blotting System	Invitrogen
Incubator Function Line	Heraeus
Incubator Shaker, Innova 4300	New Brunswick Scientific
J2-21 M/E	Beckman Coulter

LightCycler 480	Roche
Luna automated cell count	Logos Biosystems
MACSQuant VYB flow cytometer	Miltenyi Biotec
Magnetic Mixers	Heidolph-Elektro
Mini Star	Neolab
NanoDrop Spectrophotometer ND-1000	Peqlab
pH-Meter Ph 540 GLP	WTW
Freezing container, Mr. Frosty	Nalgene
Qubit 2.0 Fluorometer	Invitrogen
SDS-gel electrophoresis chamber	BioRad
Shaking Platform	Heidolf Polymax 2040
Tecan Sparks	Tecan
Thermo water bads	GFL, Hans Bayer, Julabo
Vortex Genie	NeoLab

Table 10: Kits for molecular biology

2-D Quant Kit	VWR
Bradford Protein Assay kit	Thermo Fisher Scientific
High Pure PCR Template Preparation Kit	Sigma Aldrich
miRNeasy Mini Kit	Qiagen
NEBNext Multiplex Oligos for Illumina (Primer Set1)	BioLabs
NEBNext Ultra II Directional RNA Library Prep Kit for Illumina	BioLabs
RNaseOUT Recombinant Ribonuclease Inhibitor	Thermo Fisher Scientific
Qubit dsDNA HS Assay Kit	Qiagen
Qiagen Maxi Plasmid Isolation Kits, Endotoxin free	Qiagen
SuperScript IV Reverse Transcriptase	Thermo Fisher Scientific
TOPO TA cloning kit	Thermo Fisher Scientific

Buffers and customed media

10x PBS (pH 7.4)

137 mM NaCl
10 mM Na2HPO4
2.7 mM KCl

10x TBS-T

50 mM Tris, pH 7.6
150 mM NaCl
5% Tween 20

Lysis buffer

10 ml MPER lysis buffer
1 tbl PhosSTOP Phosphatase Inhibitor Cocktail (Roche)
1 tbl Mini Complete Protease Inhibitor Cocktail EDTA-free (Roche)
40 µl 2mM EDTA

Materials and Methods

LB medium

5 g/l yeast extract
10 g/l bacto tryptone
5 g/l NaCl

RIPA buffer

10 mM Tris-HCl, pH 8.0
1 M EDTA, pH 8.0
140 mM NaCl
1% Triton x-100
0.1% SDS
0.1% DOC

Cystine-free medium

custom RPMI1640 medium
10% dialyzed FCS
0.1 mM L-Methionine
0.136 mM L-Glutamic acid
2.055 mM L-Glutamine

Cystine-low medium

custom RPMI1640 medium
10 % dialyzed FCS
0.1 mM L-Methionine
0.136 mM L-Glutamic acid
2.055 mM L-Glutamine
0.005 mM L-Cystine

Versene (pH 7.0)

10 mM EDTA
1x PBS

FULL medium

custom RPMI1640 medium
10% dialyzed FCS
0.1 mM L-Methionine
0.136 mM L-Glutamic acid
2.055 mM L-Glutamine
0.208 mM L-Cystine

Table 11: Antibodies used for western blotting

Specificity	Host	Supplier	Cat. No.	Dilution
MYCN	Rabbit	Santa Cruz	sc-791	1:200
c-MYC	Rabbit	Abcam	ab32072	1:1000
GPX4	Rabbit	Abcam	ab41787	1:1000
CTH	Mouse	Abcam	ab54573	1:1000
GAPDH	Mouse	Millipore	MAB374	1:1000
Vinculin-HRP	Mouse	Santa Cruz	sc73614	1:2500
Secondary-Mouse-HRP	Goat	Dianova	115-035-003	1:5000
Secondary-Rabbit-HRP	Goat	Dianova	111-035-144	1:5000

Table 12: List of shRNAs (5'-3') used for inducible gene knockdown

shCTH_1		GCATCTGAATTTGGATTAA
shCTH_2		CACTCGGGTTTTGAATATA
shCTH_3		CTATGTATTCTGCAACAAA
shGPX4_1		GGCACATGGTTAACCTGGA
shGPX4_3		AATTCGATATGTTCAGCAA
shMYCN	(Muth et al., 2010)	CTGGACAGTCACTGCCACT

Table 13: Vector used for inducible gene knockdown

pTER+	(van de Wetering et al., 2003)

Table 14: Restriction enzymes

Bg1II (10 μg /μl)	5'…A↓GATCT…3' 3'…TCTAG↑A…5'	Thermo Fisher Scientific
HindIII (10 μg /μl)	5'…A↓AGCTT…3' 3'…TTCGA↑A…5'	Thermo Fisher Scientific

Table 15: NB cell lines
TERT – gene encoding telomerase reverse transcriptase.

Cell line	***MYCN* level**	***TERT* level**	Reference
CHLA-15	LOW	HIGH	(Keshelava et al., 1998)
CHLA-20	LOW	HIGH	(Keshelava et al., 1998)
CHLA-90	LOW	LOW	(Keshelava et al., 1998)
CHP-134	HIGH	HIGH	(Schlesinger et al., 1976)
CLB-GA	LOW	HIGH	(Combaret et al., 1995)
GI-ME-N	LOW	HIGH	(Donti et al., 1988)
HDN-33	LOW	HIGH	Schwab, unpublished
IMR-32	HIGH	HIGH	(Tumilowicz et al., 1970)
IMR-5-75	HIGH	HIGH	(Tumilowicz et al., 1970)

Kelly	HIGH	HIGH	(Schwab et al., 1983)
KP-N-SI9S	LOW	HIGH	(Sugimoto et al., 1991)
KP-N-YN	HIGH	HIGH	(Sugimoto et al., 1991)
Lan-1	HIGH	HIGH	(Seeger et al., 1977)
Lan-2	HIGH	HIGH	(Seeger et al., 1977)
Lan-5	HIGH	HIGH	(Seeger et al., 1982)
Lan-6	LOW	LOW	(Wada et al., 1993)
LS	HIGH	HIGH	(Rudolph et al., 1991)
MHH-NB-11	HIGH	HIGH	(Pietsch et al., 1988)
NB-7	HIGH	HIGH	Westermann, unpublished
NB1	HIGH	HIGH	(Miyake et al., 1973)
NB69	LOW	HIGH	(Mena et al., 1989)
NBL-S	HIGH	HIGH	(Cohn et al., 1990)
NGP	HIGH	HIGH	(Brodeur et al., 1977)
NMB	HIGH	HIGH	(Brodeur et al., 1977)
SH-EP	LOW	HIGH	(Ross et al., 1983)
SH-SY5Y	LOW	HIGH	(Biedler et al., 1978)
SIMA	HIGH	HIGH	(Marini et al., 1999)
SJNB-1	LOW	HIGH	(Van Roy et al., 2006)
SJNB-12	LOW	HIGH	(Van Roy et al., 2006)
SK-N-AS	LOW	HIGH	(El-Badry et al., 1989)
SK-N-BE-2	HIGH	LOW	(Biedler & Spengler, 1976)
SK-N-DZ	HIGH	HIGH	(Sugimoto et al., 1984)
SK-N-FI	LOW	LOW	(Sugimoto et al., 1984)
SK-N-SH	LOW	HIGH	(Biedler et al., 1973)
SMS-KCNR	HIGH	HIGH	(Reynolds et al., 1986)
TR14	HIGH	HIGH	(Cowell & Rupniak, 1983)

Software and databases

Inkscape, version 0.92.4
ChemiCapt 5000
Fiji 1.0
FlowJo 10.5.3
GraphPad Prism 6.0
ImageJ 1.52q
R 4.2.0
R Studio 2022.02.0
Microsoft Office package 2010
LightCycler 480 Software, version 1.5

Addgene https://www.addgene.org
National Center for Biotechnology (NCBI) http://www.ncbi.nlm.nih.gov
R2 https://hgserver1.amc.nl
ShinyGo v0.61 http://bioinformatics.sdstate.edu/go
DepMap https://depmap.org/portal/
GSEA http://www.gsea-msigdb.org/gsea/index.jsp
Biorender https://app.biorender.com
El-Maven https://www.elucidata.io/el-maven
Metaboanalyst https://www.metaboanalyst.ca

5.2. Methods

5.2.1. pTER+ vector cloning for inducible stable gene knockdown

The pTER+ expression vector (van de Wetering et al., 2003) containing shRNA targeting *MYCN* was provided by Dr. Kai-Oliver Henrich.

The other pTER+ vectors containing shRNAs sequences targeting *GPX4* or *CTH* were generated using the following procedure. The pTER+ plasmid was initially subjected to restriction digestion at 37°C in a PCR cycler using a mixture of appropriate enzymes (**Table 16**) for 3.5 hours to linearize it.

Table 16: The pTER+ restriction digestion mix

Volume (μl)	Component
3.5	pTER+ (10 μg/μl)
4.5	Bgl II (10 μg/μl)
4.5	Hind III (10 μg/μl)
10	Buffer R+
77.5	H_2O

The enzymes were deactivated by being incubated at 60 °C for 20 min. Subsequently, the fragments were separated using a 1% agarose gel, and the digested vector was isolated from the 5250 bp band using the Qiagen "QIAquick Gel Extraction Kit" following the manufacturer's instructions. Next, the oligonucleotides annealing reaction was performed by mixing 3 μg of the oligonucleotides encoding for the forward and reverse shRNAs with 5 μL of annealing buffer and 43 μL of H_2O. Samples were incubated in a PCR cycler at 95 °C for 3 min, and then slowly cooled down (0.1 °C/s) to 4 °C. Annealed shRNAs were cloned into pTER+ vector by incubating the mix described in Table 17 overnight at 16 °C.

Table 17: The ligation mix

Volume (μl)	Component
1	annealed oligonucleotides
2.5	linearized pTER+ (250 ng)
1	10X ligation buffer

1	Ligase
4.5	H_2O

Cloned vectors were then transformed into chemically competent Stellar cells (Takara) and plated on the ampicillin (200 μg/ml) agar plates for selection. Amplification of efficiently transformed cells was performed using maxi-culture of bacteria in 300 ml of LB media and DNA was isolated using the endotoxin-free EndoFree Plasmid Maxi Kit (Qiagen).

5.2.2. Cell-based methods

5.2.2.1. Cell culturing

The NB cell lines were maintained in RPMI-1640 medium, supplemented with 10% Fetal Bovine Serum (FBS) and cultured in a cell culture incubator at 37 °C, 80% humidity, and 5% CO_2. Upon reaching approximately 90% confluency, the cells were sub-cultured at ratios ranging from 1:3 to 1:15, depending on the cell line. This was achieved either by incubating the cells with versene at 37 °C for 30 s to 4 min or by gently pipetting the cell culture medium. The cell morphology was monitored under a light microscope.

5.2.2.2. Cryo-preservation and thawing

To preserve the cells, they were detached as described above and centrifuged (800rpm, 5 min, RT). The resulting pellet was resuspended in ice-cold medium containing RPMI-1640 supplemented with 50% FBS and 10% sterile DMSO. Cryogenic vials were cooled down gently with cryo-containers (Mr. Frosty, Nalgene) at -80 °C, and after 48 hours, transferred for long-term storage in a liquid nitrogen tank. To re-culture the cells, they were incubated in a water bath at 37 °C for approximately 1 min and resuspended in RPMI-1640 medium. The cells were then allowed to attach for 24 to 48 h before the medium was substituted to remove DMSO.

5.2.2.3. Ferroptosis inducers/inhibitors treatments

Stock solutions of ferroptosis inducing agents (FINs) were prepared by re-suspending the powder in DMSO.

Cells were seeded in 96-well plates and seeded with density according to the type of cell line: 2.5k cells/well for rapidly proliferating cell lines (NB69, SH-EP, SIMA, NB1, SK-N-DZ, IMR-5-75, IMR-32, Lan-1, Kelly, KP-N-YN, NGP, CHLA-15, CLB-GA, LS, MHH-NB-11, SK-N-BE-2) and 4-6k cells/well for the rest (GI-ME-N, SK-N-AS, SH-SY-5Y, SK-N-FI, NBLS, Lan-2, TR14).

Titration experiments were performed to calculate cell line sensitivity to certain FIN. To do so, NB cell lines were treated for 72 hours with following drugs at different concentration range: erastin: 5-0 μM, ML210: 10-0 μM, RLS3: 0.5-0 μM. For assessment of drug efficacy, cell viability was measured as described in Section 5.2.2.5.

5.2.2.4. Cystine titration

Cystine was solved in 1 M HCl and stored at -20 °C. To perform cystine deprivation experiment lasting 24 h, cells were seeded in 96-well plates with density as follows: GI-ME-N (8k cells/well), NB69 (10k cells/well), SK-N-SH (9k cells/well), SK-N-AS (10k cells/well), HD-N-33 (9k cells/well), CHLA-20 (10k cells/well), CHLA-15 (10k cells/well), Lan-6 (12k cells/well), CLB-GA (15k cells/well), SH-EP (1k cells/well), SH-SY5Y (12k cells/well), SK-N-FI (8k cells/well), NBLS (12k cells/well), SIMA (10k cells/well), NB-1 (8k c/well), LS (10k cells/well), SK-N-DZ (10k cells/well), IMR-5-75 (10k cells/well), IMR-32 (10k cells/well), Lan-1 (10k cells/well), TR14 (12k cells/well), Kelly (10k cells/well), CHP-134 (12k cells/well), MHH-NB-11 (10k cells/well), SK-N-BE-2 (8k cells/well), KP-N-YN (10k cells/well), CHP-126 (12k cells/well), NGP (9k cells/well), SMS-KCNR (12k cells/well) and Lan-5 (12k cells/well). After 24 hours cell medium was discarded and wells were washed with 50 μl PBS. Next, cells were supplied with customized RPMI-1640 medium with ranging concentrations of cystine from 0 μM to 200 μM. Full media was used as a control. Treatment outcome was evaluated with a cell viability assay as described in section 5.2.2.5.

5.2.2.5. Cell viability assay

To quantify the viability of the cells after treatment, CellTiter Blue (CTB) viability assay (Promega) measuring metabolic activity was used. Cells were seeded in a black 96-well plates with densities tailored to the treatment in a way that control cells reached 70-80% confluence at the end of the treatment.

At the end point of each experiment, CTB Reagent was added at 1:10 ratio for 5 h, after which fluorescence was detected using Tecan Sparks (Tecan) with following filter parameters: 540 nm excitation, 580 nm emission wavelength. To correct for a background noise, wells containing only normal growth medium without cells were used as a control. Viability of cells at certain drug/ cystine concentration were calculated as a percentage of fluorescence measured for untreated controls (or solvent controls in case of drug treatment).

5.2.2.6. Colony formation assay

To assess the colony-forming capacity of NB cell lines following drug treatments or cystine deprivation, Giemsa staining-based colony formation assays were carried out. Firstly, cells were fixed in 11% glutaraldehyde for 30 min, washed twice with PBS, and stained with Giemsa solution (10% Giemsa Azure Eosin Methylen Blue solution in PBS) overnight. The next day, cells were washed twice with PBS, followed by a 5-min wash with ddH_2O and left to dry for 24 hours. Imaging of the plates was performed using an EPSON Perfection 2450 Photo scanner and processed using the ColonyArea plugin in ImageJ.

5.2.2.7. Generation of doxycycline-inducible shRNA cell lines

To establish doxycycline-inducible short hairpin mediated knockdown of CTH and GPX4, IMR-5-75 6/TR cells were transfected with pTER+ plasmids against CTH or GPX4 generated as described in section 3.2.1. Plasmids' transfection was carried out using the non-liposomal lipid reagent Effectene (Qiagen) mixed with 1 μg vector DNA following the two-step standard protocol 18-24 h after seeding. After 24 h of

transfection, the transfection medium was replaced with fresh RPMI1640 medium. Stably transfected cells were selected by culturing them in selection media (RPMI1640 medium supplemented with Blasticidin and Zeocin at a final concentration of 5 μg/ml and 50 μg/ml, respectively) for up to 3 weeks. To generate single-cell derived knockdown clones, individual cells were seeded into 96-well plates with density one cell/well and cultured in selection medium until obtaining stable cultures.

5.2.3. Molecular-biology methods

5.2.3.1. Fluorescence-activated cell sorting (FACS)

Lipid hydroperoxides accumulation can be measured using BODIPY™ 581/591 C^{11}. This fluorescent dye allows to estimate oxidative state of lipid environments that can be measured by shift of its excitation maximum from 581 to 500 nm and the emission maximum from 591 to 510 nm upon oxidation.

To perform staining, NB cell lines were seeded at a density of 300,000 cells per well 24 h prior to the experiment. At the time of measurement, the supernatant was discarded, and the cells were washed once with pre-warmed PBS. Meanwhile, a staining solution was prepared by diluting BODIPY™ 581/591 C^{11} in Hank's Balanced Salt Solution (HBSS) to a final concentration of 4 µM. The cells were then incubated with the staining solution for 1 h at 37 °C and harvested using the protocol described in section 5.2.2.1. The data was acquired using the MACSQuant VYB flow cytometer (Miltenyi).

5.2.3.2. Protein assessment by SDS-PAGE and western blotting

Protein lysates

To determine protein levels, NB cell lines were collected and promptly placed on ice, rinsed with ice-cold PBS, and centrifuged. The resulting pellet was resuspended in 20-40 µl of lysis buffer. The cell lysates were then kept on ice for at least 10 min and centrifuged at 13000 rpm for 15 min to isolate soluble proteins from cell debris. The Bradford method using Protein Assay Dye Reagent Concentrate (BioRad) or 2-D

Quant Kit were utilized to quantify protein levels, following the manufacturer's instructions. The protein lysates were stored at -80 °C for long-term preservation.

SDS PAGE

The samples were prepared by combining 25 µg of protein lysates with 4X NuPAGE® Sample Buffer (Thermo Fisher Scientific) and NuPAGE® Reducing Agent (Thermo Fisher Scientific). The mixture was then heated at 70 °C for 10 min in a thermal block, and loaded onto NuPAGE Novex 4-12% Bis-Tris gels (Invitrogen) in a XCell4 SureLock Midi Cell chamber (Invitrogen) filled with 1X MOPS running buffer (Invitrogen).

Western blotting

Following electrophoresis, the proteins were transferred onto nitrocellulose membranes using the iBlot2 Dry Blotting System and Blot 2 Transfer Stacks. To block nonspecific binding, 5% milk was applied and incubated for 2 h at room temperature. After washing the membranes thrice with TBS-T buffer for 15 min each, they were incubated overnight at 4 °C in a primary antibody solution (5% BSA) while shaking. The next day, the membranes were washed again thrice with TBS-T buffer for 15 min each, and protein bands were detected using Enhanced Chemiluminescent (ECL) detection reagents (Bio-Rad) and a CCD camera (Bio-Rad).

5.2.4. Omics methods

5.2.4.1. RNA-sequencing

The transcriptional profiles of a large panel of NB cell lines (n = 36) as well as the SK-N-DZ and IMR-5-75 cells transcriptome profiles upon amino acids deprivation used in this study were previously generated in our group by Elisa Maria Wecht.

The expression data of the 600 NB tumors generated in-house was also used. The *MYCN* oncogene status for all the tumors was estimated at the time of diagnosis.

5.2.4.1.1. Experimental design

Cystine deprivation

SK-N-FI and NBL-S cells were seeded in duplicates in 15 cm dishes at density $4x10^6$ cells/plate in the standard growth medium supplemented with 10% FCS. After 24 h, the growth medium was removed, and the cells were washed with PBS. Subsequently, a customized medium containing low or no cystine was administered to the cells and incubated at 37 °C in a cell incubator. As a control, customized full medium was used (please refer to the Materials section for detailed medium composition). Following 8 or 24 h of incubation, the cells were detached and centrifuged for 5 min at 800 rpm, and the resulting cell pellets were used for RNA extraction and library preparation.

Gene knockdown

IMR-5-75 6/TR cells transfected with pTER+ plasmids against *CTH* or *GPX4* were seeded in the 15 cm dishes in quadruplets in the selection medium supplemented with doxycycline (1 μg/ml) to induce gene knockdown. 48 h and 72 h after seeding, cells were harvested using Versene and centrifuge for 5 min at 800 rpm. Cell pellets were then used for RNA extraction and library preparation.

RNA extraction and library preparation

Cell pellets were carefully resuspended in 700 μl of Qiazol lysis reagent and RNA fragments > 200 bp excluding miRNA were isolated using the miRNAeasy kit from Qiagen following the manufacturer's protocol. Quality of obtained samples was monitored by running the Agilent RNA 6000 Nano chip on the 2100 Bioanalyzer (Agilent technologies) to ensure RNA integrity for library preparation. Prior library preparation, 5 μg of total RNA was used for rRNA depletion reaction using the Ribo-Zero rRNA Removal Kit (Illumina). Libraries were prepared using 45 ng mRNA and the NEBNext® Ultra™ Directional RNA Library Prep Kit for Illumina (NEB) following manufacturer's protocol with two changes: RNA fragmentation was performed at 94 °C for 20 min and the synthesis of the first strand cDNA was extended to 50 min at 42 °C. For library size selection SPRI beads (AmpureXP beads, Beckman Coulter Genomics) were used. Assessment of library quality was performed by running the DNA HS kit

on the 2100 Bioanalyzer (Agilent Technologies). Libraries were sequenced by the DKFZ Sequencing Core Facility using Illumina HiSeq 2000 (paired-end 125 bp).

5.2.4.1.2. Data normalization and analysis

Initial data pre-processing steps, including reads alignment to reference genome, were performed by the DKFZ Sequencing Core Facility following a pipeline implemented in the One Touch Pipeline (OTP) service (Reisinger et al., 2017).

Data was normalized using trimmed mean of M values (TMM) method provided within an edgeR package (Chen et al., 2016; McCarthy et al., 2012; Robinson et al., 2010). To conduct differential gene expression analysis, normalized read counts were utilized, and the likelihood ratio test was applied to assess differential gene expression between samples. Benjamini-Hochberg (FDR) correction was applied to adjust p-values. A p_{FDR}-value threshold of < 0.05 was implemented as a criterion to identify genes with differential expression.

5.2.4.2. Metabolomics

Analysis of the cell lines and tumors metabolic profiles was conducted by the group of Dr. Nicole Bechmann from Universitätsklinikum Carl Custav Carus Dresden, Germany following the procedures described below.

Generation of cell culture samples

Cells were seeded in T75 cell culture flasks with density $4x10^6$ cells/flask and 2 flasks/cell line. After 48 h incubation, flasks were placed on ice, supernatants were collected, and cells were washed twice with PBS. Immediately, ice cold Cell disruption buffer (300 µl) was added, and cells were incubated for 10 min on ice. Cells were scraped of the flask and the lysate was transferred to a sample tube (total volume ~600 µl, including leftover PBS). The lysate was centrifuged (4 °C, 16000 × g), and 20 µl of the clear lysate was transferred to a new sample tube containing 80 µl of methanol. The levels of TCA cycle intermediates were quantified by LC-MS/MS as previously described (Langner et al., 2022; Richter et al., 2019).

NB tissue preparation procedure

A cell disruption buffer (100 µl) from the Invitrogen Paris Kit (AM 1921, ThermoFisher Scientific) was added to sample tubes containing the corresponding tumor tissue (5-20 mg), which were kept on ice. Samples were prepared according to the previously described protocol (Bechmann et al., 2021). 10 µl of the obtained clear lysates was aliquoted in new sample tubes containing 90 µl of methanol. The levels of TCA cycle intermediates were quantified by LC-MS/MS as previously described (Langner et al., 2022; Richter et al., 2019).

5.2.4.3. Thiol tracing analysis

Measurements of label cystine incorporation was conducted at Metabolomics Core Technology Platform, Center for Organismal Studies at University of Heidelberg and coordinated by Dr. Gernot Poschet and Dr. Glynis Klinke. The used methods are described below.

Sample preparation

Cell pellets containing $3x10^6$ cells were extracted with 450 µl ice-cold 0.1 M HCl containing. For protein precipitation of cell culture supernatants, equal volumes of ice-cold 0.2 M HCl were added to supernatants. The quantification of total glutathione was performed by reducing disulfides with DTT and subsequently using the fluorescent dye monobromobimane (Thiolyte, Calbiochem) for thiol derivatization, following a previously described method (Wirtz et al., 2004).

LC-IMS-QTOF

The compounds of interest were separated using a binary Acquity UPLC I-class system (Waters) and a reverse-phase Cortecs T3 column (2.1x100 mm; 1.6 µm, Waters) at a flow rate of 0.45 ml/min. The mobile phases A and B consisted of 0.1% formic acid in water and acetonitrile, respectively. A gradient of 6% B for 1 min, followed by a ramp to 20% B from 1 min to 4 min, a second ramp to 85% B from 4 min to 4.01 min, a hold at 85% B until 5 min, and then a return to 6% B from 5 min to 5.01 min was used. The column temperature was kept constant at 42 °C, and the samples

were maintained at 6 °C. The column eluent was directly introduced into the Vion IMS-QTof mass spectrometer (Waters) via electrospray ionization (ESI) to perform targeted mass spectrometric analysis in positive mode. The capillary voltage was set at 1.2 kV, and the cone voltage was set at 20 V. The desolvation gas flow rate was 900 L/h, and the desolvation temperature was set at 550° C. The cone gas flow rate was 50 L/h, and the source temperature was 120 °C. Accurate mass was ensured using the Lock-Spray interface of Leucine-enkephalin (556.2771 [M+H]+ at a concentration of 100 pg/µL in 50% ACN and a rate of 15 µL/min (scan time 0.3 s, interval 1 min, scans to average 3)). The Unifi software package (Waters) was used to acquire mass signals in continuum mode from 100 to 700 mass-to-charge ratio (m/z) in High Definition MS mode and for data processing. For quantification, ultrapure standards (Sigma) were used to create a 5-point calibration ranging from 10 µM to 100 µM.

Data analysis

Obtained data was normalized using total metabolite normalization method and processed using R software.

6 Results

Results

6.1. Characterization of cell lines sensitivity to ferroptosis induction

Approximately 25% of NB patients are characterized by amplified *MYCN* oncogene, which is associated with a very aggressive tumor subtype that accounts for a high percentage of cancer-related pediatric cell deaths. Since direct targeting of MYCN is not possible, approaches that focus on MYCN-related metabolic vulnerabilities are promising avenues for the development of new therapies. A recently published study from our group (Alborzinia et al., 2022) demonstrated that high levels of the oncogenic *MYCN* can make NB cells more sensitive to limiting cystine supply.

Cysteine is an amino acid that plays a critical role in several important cellular processes, including protein synthesis, enzyme activation, and redox balance. In NB, cysteine has been shown to be particularly important for maintaining the redox balance of cancer cells and promoting their survival (Alborzinia et al., 2022). Studies have shown that limiting cysteine availability can sensitize NB cells to ferroptosis and reduce tumor growth in animal models (Alborzinia et al., 2022), suggesting that targeting cysteine metabolism may be a promising novel therapeutic concept which may lead to improvement of outcomes for a subset of high-risk NB patients.

The goal of this research work is to enhance our understanding of MYCN-mediated metabolic reprogramming in NB through the analysis of a large group of NB cell lines for their sensitivity to cystine deprivation and ferroptosis-inducing agents (FINs).

6.1.1. MYC(N) status of NB cell lines

As a first step, a set of representative cell lines was selected in order to determine MYCN influence on ferroptosis sensitivity. To accomplish this, 36 NB cell lines with different genetic backgrounds (**Table 15**, **Supplementary Table 1**) were tested. For each cell line, MYCN and c-MYC levels were determined using two methods: western blot analysis and transcriptomics sequencing (RNAseq). In our large cell line collection, there were cell lines showing high levels of MYCN due to genetically rearranged *MYCN* (amplified or translocated), or high level of c-MYC protein due to rearranged *c-MYC* (amplified or translocated). Additionally, cells with low levels of MYCN and c-MYC, which is often linked to alternative mechanisms of

telomere lengthening (ALT) or *TERT* activation in absence of rearrangements affecting the *MYCN* or *c-MYC* genes were also included in the analysis (**Figure 9**). It is worth noting that MYCN and c-MYC were mutually exclusive as previously described (Westermann et al., 2008).

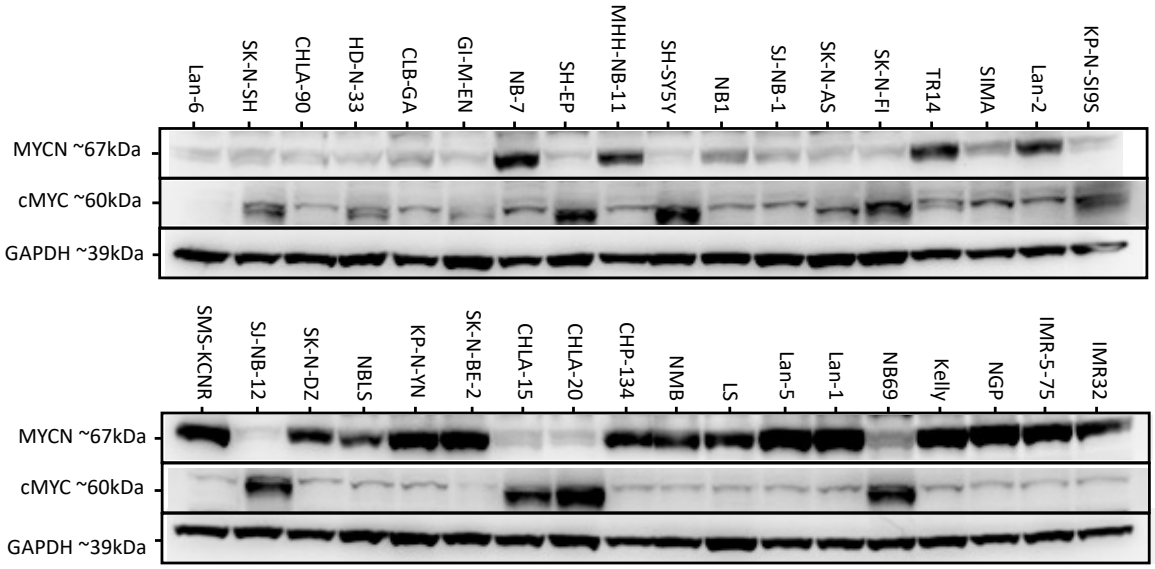

Figure 9: Western blot representing MYCN and cMYC protein levels in a panel of NB cell lines. GAPDH was used as a loading control. Among studied cell line panel there were *MYCN*-amplified (IMR-32, IMR-5-75, NGP, Kelly, Lan-1, Lan-5, LS, NMB, CHP-134, SK-N-BE-2, KP-N-YN, SK-N-DZ, SMS-KCNR, Lan-2, SIMA, TR14, NB1, MHH-NB-11, NB-7), *MYCN*-translocated (NBLS), *c-MYC* amplified (CHLA-20, CHLA-15), c-MYC translocated (NB69, SH-SY5Y, SH-EP, SK-N-AS, SK-N-SH), as well as cells with no genetic *MYCN* or *c-MYC* alterations (ALT positive: Lan-6, CHLA-90, SK-N-FI, and *TERT* positive: HD-N-33, CLB-Ga, KP-N-SI9S, SJ-NB1, SJ-NB12, GI-M-EN).

To quantify MYCN transcriptional activity, the MYC(N) activity score was calculated based on its target gene expression using a previously published MYCN/c-MYC signature gene list (Westermann et al., 2008). To do so, a rank-based single sample gene set scoring method (Foroutan et al., 2018) was applied to the cell line transcriptome dataset containing basic gene expression. In most cases, *MYCN*-amplification overlapped with high MYC(N) activity scores, however there were also non-*MYCN*-amplified cell lines which had a high MYC(N) activity score (**Figure 10**).

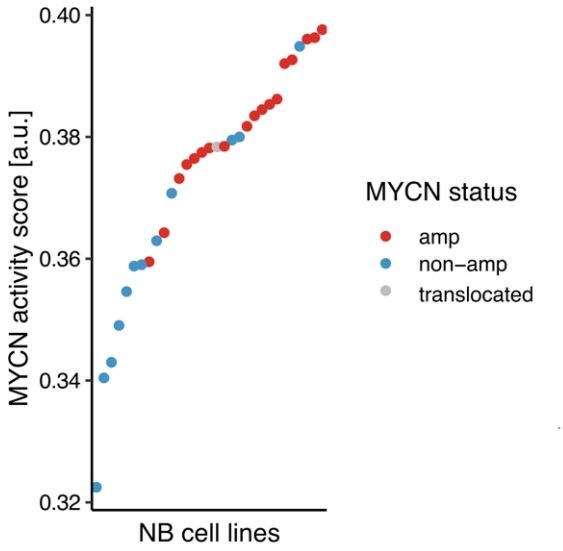

Figure 10: MYC(N) activity scores of NB cell lines.
The activity scores were calculated based on expression data of MYC(N) target genes using Singscore R package. The *MYCN* status of the cell lines is depicted as indicated in the legend.

Since the MYC(N) activity score is represented as positive continuous values, the classification of cell lines into those with low and high MYC(N) activity is not straightforward. This can be modelled as a clustering problem, where the values need to be classified into different subgroups without any prior knowledge on the number of groups or training data. A preliminary visual inspection of the distribution of MYC(N) activity scores in the NB cell lines was conducted by plotting them as a histogram. The resulting plot (**Figure 11**) displayed at least two distinct peaks in the data distribution, which are indicative of cells with low and high MYC(N) activity, respectively.

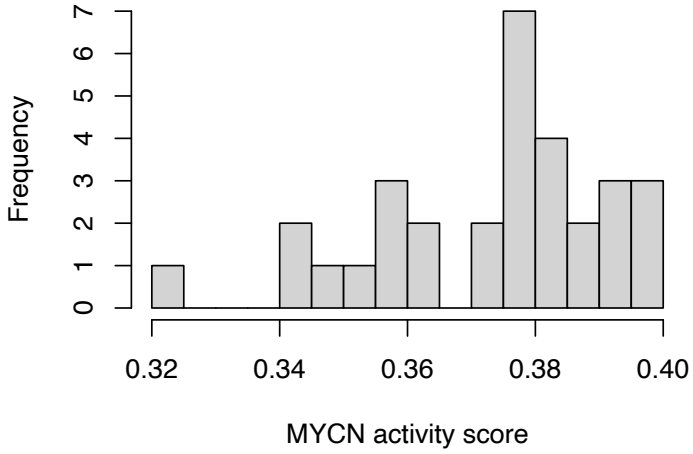

Figure 11: Histogram showing the distribution of MYC(N) activity scores.
Distribution of MYC(N) activity scores obtained for NB cell lines. On x-axis the MYC(N) activity scores are shown.

The data was clustered using Gaussian mixture models, which are used to describe the observed distribution as a combination of multiple normal distributions. It is important to avoid overfitting the data when working with clustering models and machine learning in general, as this can lead to an excessive number of clusters. The Bayesian information criterion (BIC) was used to determine the most probable number of clusters. Due to the limited amount of data available for cell lines, which was also biased towards those with *MYCN*-amplification, the BIC analysis suggested that having only one cluster was the most probable scenario (**Figure 12**). However, when comparing the cell lines grouping using different number of clusters, it was found that the most appropriate separation was obtained with three clusters. Notably, the plot also showed a sharp decline in separation quality with more than three clusters.

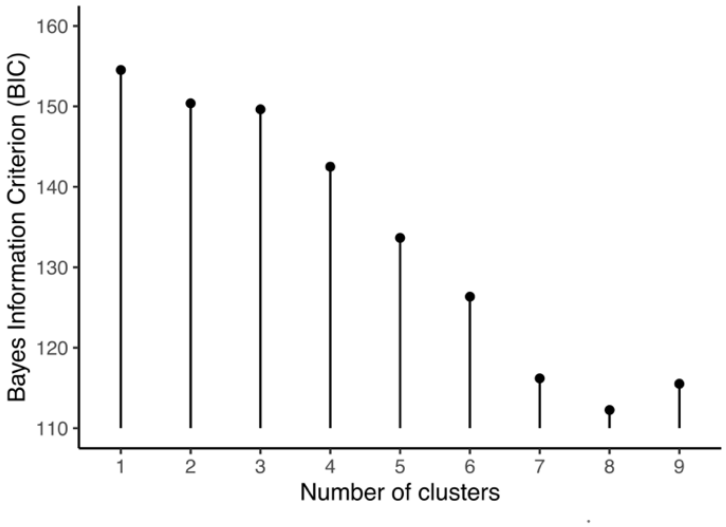

Figure 12: Bayesian information criterion values evaluation to determine the number of clusters that best describes the data.
The BIC obtained for NB cell lines are presented. According to the model the distribution of the obtained MYC(N) activity scores is generated from three gaussian distributions.

In conclusion, regarding the MYC(N) activity scores, cell lines were separated into three groups, and hence they will be further referred to as cell lines with MYCN-low, MYCN-intermediate, and MYCN-high activity (**Figure 13**).

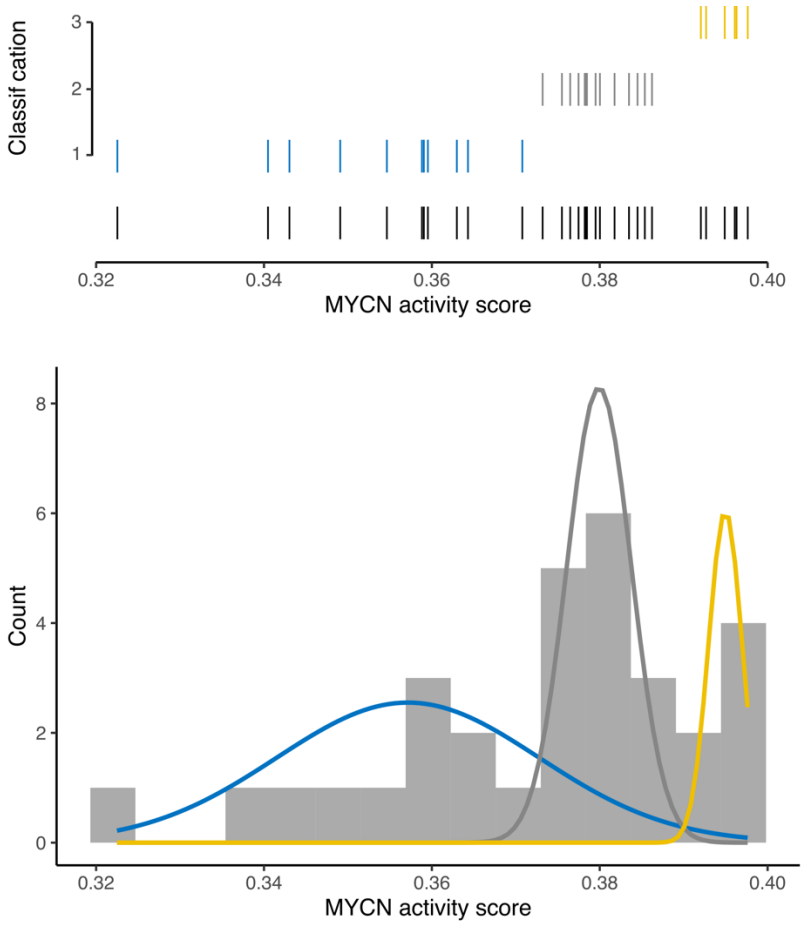

Figure 13: Classification of NB cell lines into different groups based on MYC(N) activity scores. The top plot shows the MYC(N) activity scores of individual cell lines as lines, with the three clusters (yellow, gray, and blue) and the distribution of all values (in black) displayed. The bottom plot presents a histogram of MYC(N) activity score values, with an overlay of the normal distributions identified by the Gaussian mixture model. Cell lines (n = 31) were separated in three groups: low MYC(N)-activity are colored in blue (n = 11), cell lines with the moderate MYC(N) activity are depicted in grey (n = 14), while cell lines with the high MYC(N)-activity are shown in yellow (n = 6).

To ensure the accuracy of the calculated MYC(N) activity scores, comparison was made with MYC(N) protein and expression data to verify their consistency with the MYC(N) status. The analysis showed that high MYC(N) activity score overlapped with high MYCN (IMR-32, IMR-5-75, NGP, Kelly, Lan-1, Lan-5, LS, NMB, CHP-134, SK-N-BE-2, KP-N-YN, SK-N-DZ, SMS-KCNR, Lan-2, SIMA, TR14, NB1, MHH-NB-11, NB-7, NBL-S), or c-MYC protein (CHLA-15, CHLA-20 and NB69) level (**Figure 14**). In addition, an intermediate *c-MYC* expression was observed in most cell lines with translocated *c-MYC* (SH-SY5Y, SH-EP, SK-N-AS, SK-N-SH), while cells immortalized by ALT or high *TERT expression* (Lan-6, SK-N-FI, CLB-Ga) had low *c-MYC* or *MYCN* expression (**Figure 14B**).

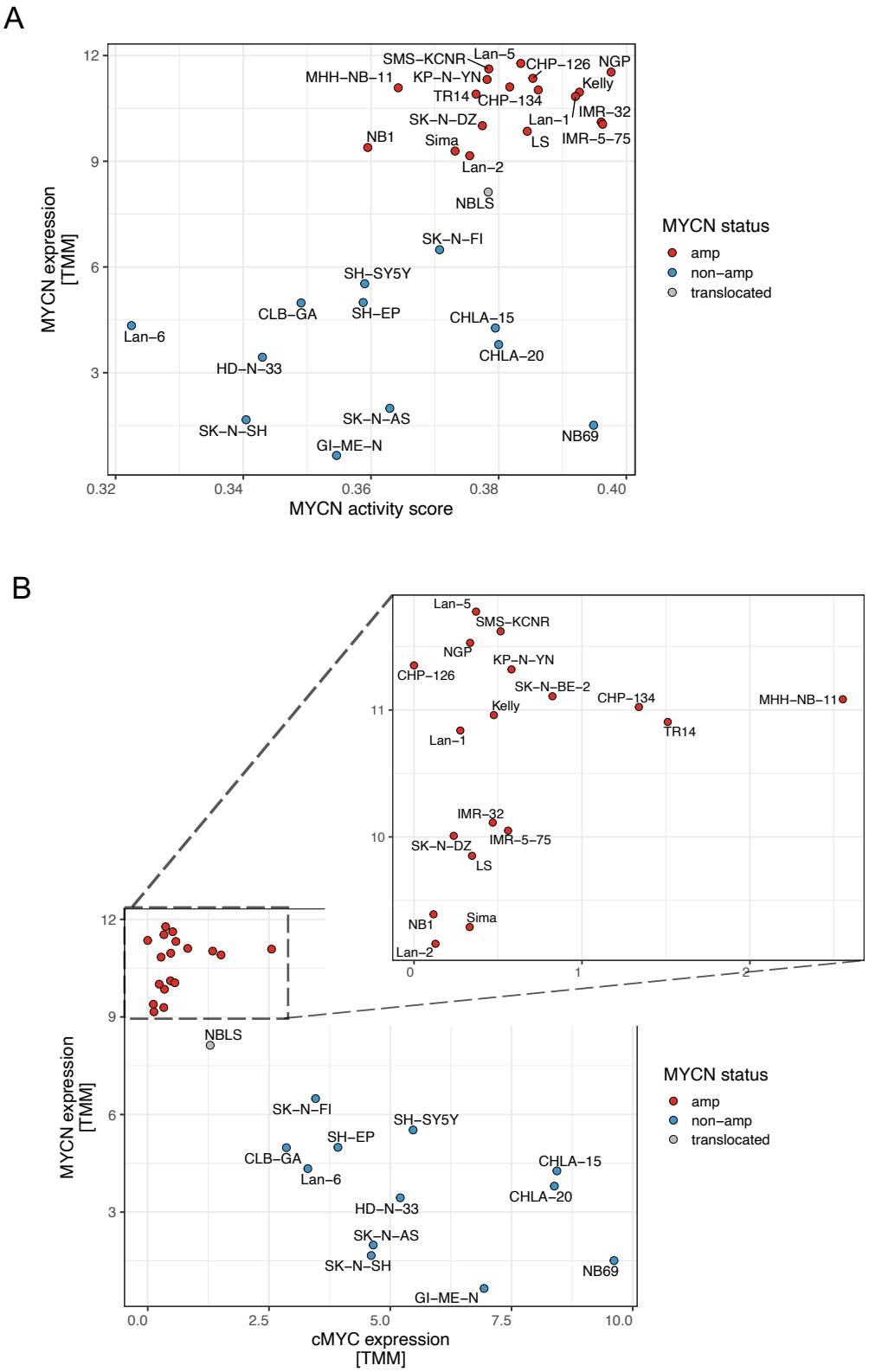

Figure 14: Estimation of the MYCN activity in NB cell lines based on gene expression data. Correlation of (**A)** MYCN expression and MYCN activity scores and (**B)** *MYCN* and *c-MYC* expression across a panel of NB cell lines (n = 31). Cell lines are color-coded according to their MYCN-status as indicated in the legend.

Results

Utilizing the identical methodology, MYC(N) activity scores were also computed for a substantial cohort of primary NB tumors (n = 600) employed in the present study. Consistent with observations in cell lines, the NB tumor data also exhibited the existence of three distinct clusters, delineating tumors exhibiting MYC(N)-low, MYC(N)-moderate, and MYC(N)-high transcriptional activity levels (**Supplementary Figure 1**).

Furthermore, by analyzing both transcriptome and whole genome sequencing (WGS) data, a comprehensive map of the genetic alterations present in our cell line panel was created (**Figure 15**). Amplified *MYCN* oncogene often co-occurs with several chromosomal aberrations such as 1p deletion (White et al., 1995) and 17q gain (Bown et al., 1999), which was nicely recapitulated in our cell line panel. In addition, other common genetic modifications that are characteristics of *de novo* NB were observed, including *ALK*-activating mutations/amplifications (Trigg & Turner, 2018), and *TP53*-inactivating mutations (Imamura et al., 1993), confirming that our cell line panel accurately reflects the diverse range of NB cases with the focus on *MYCN* oncogene amplification.

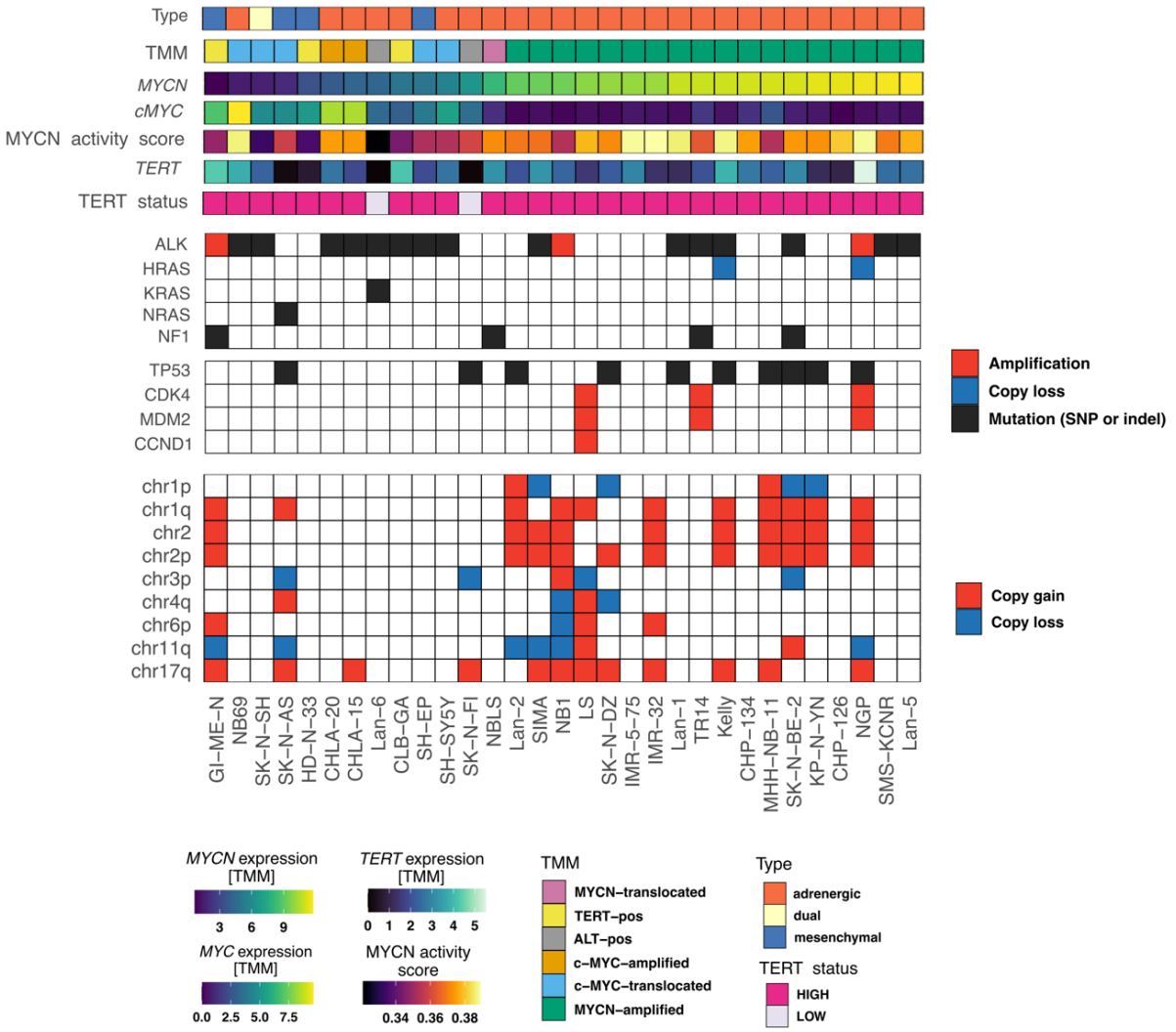

Figure 15: Overview of the characteristics of the NB cell lines studied in the project.
Data used for generating this figure was derived from WES and RNA-seq. Genes and chromosomal aberrations presented are those frequently reported to be associated with NB development. Expression of *MYCN*, *c-MYC,* and *TERT*, as well as MYC(N) activity score, cell type, TERT and telomere maintenance (TMM) status were also depicted.

6.1.2. Assessment of neuroblastoma sensitivity towards ferroptosis

6.1.2.1. Cystine deprivation from culturing medium

Previous experiments showed that amplified *MYCN* strongly sensitizes NB cells to ferroptosis caused by cystine depletion (Alborzinia et al., 2022). To further explore this phenomenon, the cystine dependency was tested in a large panel of NB cell lines (n = 30). To do so, cystine was titrated in range 0-205 µM and cellular viability after 24 h was assessed using CellTiter-Blue Viability Assay. Obtained data was used to

estimate dose-dependent relationships between cystine concentration in the medium and cellular viability (**Figure 16**).

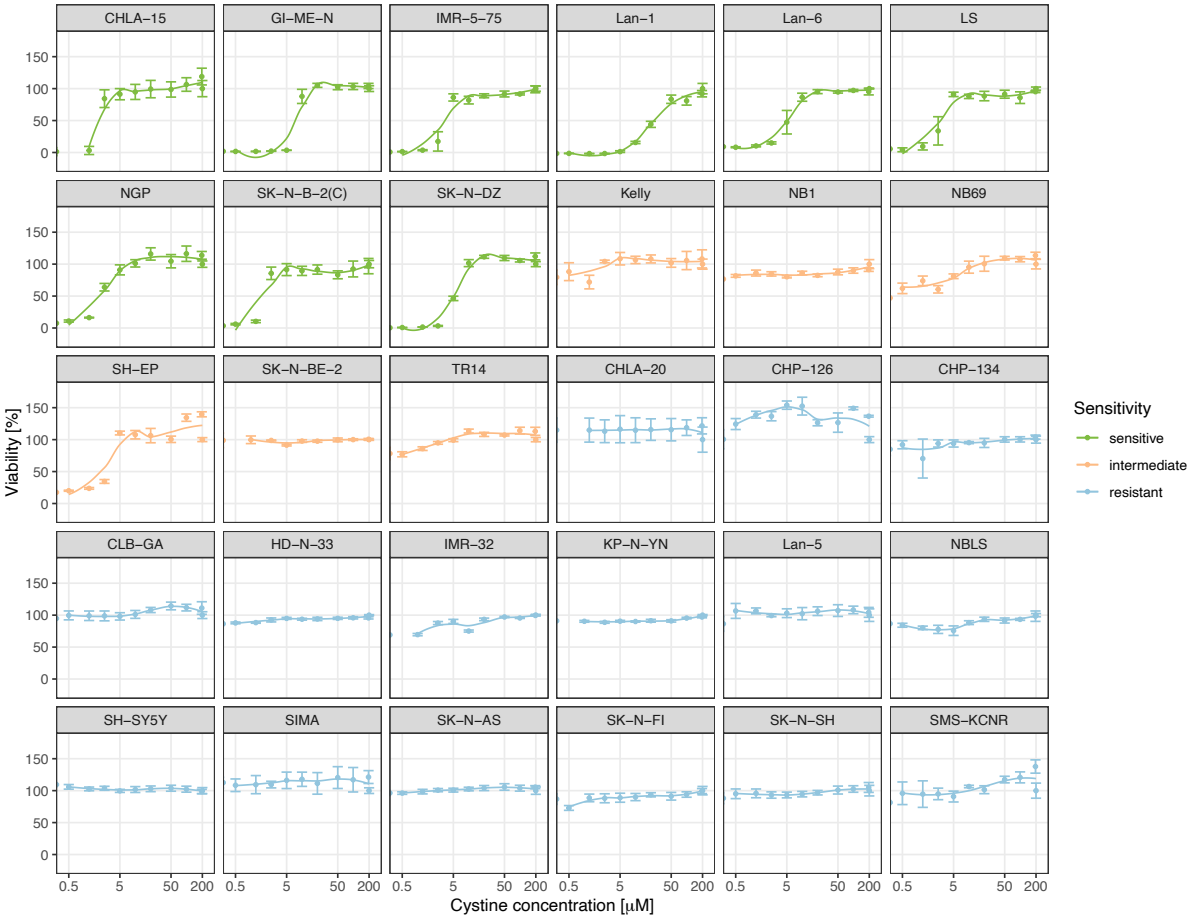

Figure 16: Viability curves obtained from cystine titration expriments performed for a large panel of NB cell lines.
The plots display the viability of different cell lines grown in the customized medium which was supplemented with varying concentrations of cystine. Each cell line is represented by a separate plot. The x-axis represents the concentration of cystine and the y-axis represents the viability of the cells after 1 hour. Cell lines are color-coded based on their sensitivity to cystine deprivation as indicated in the legend. $n_{biol.rep.} = 3$.

Comparison of viability measures upon complete cystine withdrawal at the end point of the treatment (T = 24 h) revealed a wide range of sensitivity across the studied cell lines panel. In depth, there were cell lines which showed more than 80% growth reduction in cystine-free condition (Lan-1, SK-N-DZ, IMR-5-75, CHLA-15, GI-ME-N, SK-N-B-2(C), LS, NGP or Lan-6), as well as those which did not respond to the cystine withdrawal (CHLA-20, CHP-126, CHP-134, CLB-GA, HD-N-33, IMR-32, KP-N-YN, Lan-6, NBLS, SH-SY5Y, SIMA, SK-N-AS, SK-N-FI, SK-N-SH, SMS-KCNR). In addition, a subset of cell lines showed an intermediate response (Kelly, NB1, NB69, SH-EP, SK-N-BE-2, TR14) with cell viability between 20 – 80% (**Figure 17**).

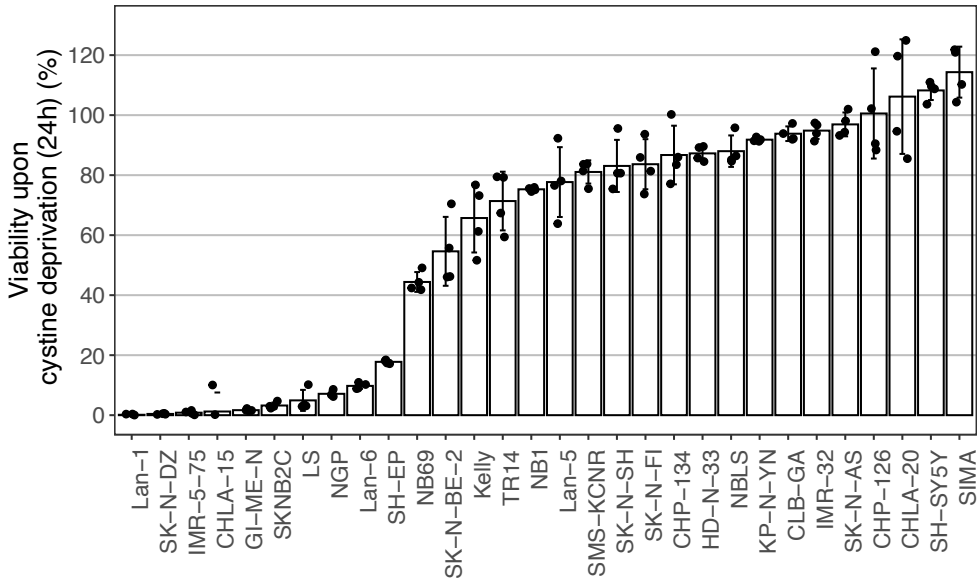

Figure 17: Cell viability of a large panel of NB cell lines upon cystine deprivation at 24 h.
Cell lines (n = 30) were ordered according to mean viability of $n_{biol.rep.}$ = 3. The relative viability (y-axis) was calculated in comparison to viability measured for cells cultivated in the full medium.

In attempt to explain the heterogenous response of NB cell lines to cystine withdrawal from the growth medium (**Figure 18A**), the obtained dose-response curves were used to calculate the area under the curve (AUC) values which corresponded to cell line sensitivity to cystine depletion (the lower AUC value, the more sensitive a given cell line is to the treatment). In the next step, these AUC values were compiled with cell line metadata which included cell line identity (adrenergic or mesenchymal), MYC(N) status (*MYCN*-amplified/translocated, *c-MYC*-amplified/translocated or ALT/*TERT* with no MYC(N) alteration), *TP53*/*MDM2* status (mutations/amplifications in the pathway or wild-type (WT)), *ALK* status (mutations/amplifications or WT), as well as the information if a given cell line was established pre- (primary) or post-therapy (relapse) (**Supplementary Table 1**).

It is commonly known that cancer resistance to the treatment is a major challenge in cancer therapy. This resistance can occur after initial response to the treatment (acquired resistance), or it can be present from the beginning of the treatment (intrinsic resistance). It has been shown that chemo-resistant cancers become well adapted to therapies based on oxidative stress induction by increasing the activity of their antioxidant systems (Mendes & Serpa, 2019; Trachootham et al., 2009).

Results

The comparison of AUC values of cell lines established before or after treatment showed that there was no significant difference between the two groups in terms of high or low sensitivity (**Figure 18B**). However, in cell lines established after initial treatment of the patient, there was a clear distinction between resistant and sensitive cell lines, indicating that certain NB cells may have developed mechanisms to adapt to elevated levels of reactive oxygen species (ROS). It is important to note, however, that without knowledge of the specific treatment given to the patient, it is difficult to make a definitive statement about the cause of the observed variability.

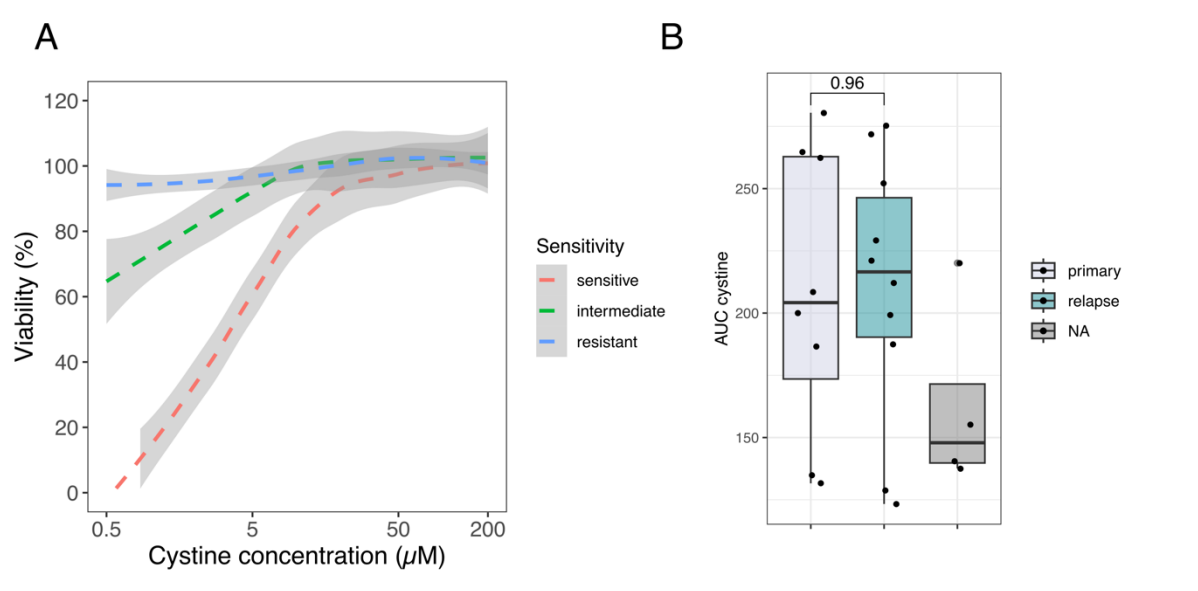

Figure 18: Overview of the sensitivity of NB cell lines to cystine deprivation and its association with the status of the tumor treatment at the time of cell line establishment (pre- or post-treatment).
(**A**) A compilation of dose-response curves representing the heterogeneity of NB cell lines in regard to response to cystine withdrawal from the growth medium. Sensitive (n = 9, red), intermediate (n = 6, green) and resistant (n = 15, blue) cell lines have been depicted. The variation is shown in grey. The relative values were calculated in comparison to cells cultivated in full medium. (**B**) The association of the sensitivity to cystine-withdrawal (represented as AUC values) and the status of the tumor treatment at the time of cell line development (pre-treatment/primary (n = 10) or post-treatment/relapse (n = 16)). NA – unknown origin. The statistical significance was tested using an unpaired t-test.

Next, the influence of MYC(N) on cystine dependency was assessed. The comparison of AUC values between cell lines with amplified or translocated *MYCN*, amplified or translocated *c-MYC* and with no MYC(N) alteration (ALT/TERT) did not show any significant difference. However, in each group the bi-modal sensitivity to cystine depletion was observed, highlighting the complexity of NB cell lines in the context of cystine metabolism (**Figure 19A**). To gain more insight into the relationship between MYC(N) activity and cystine dependency, the calculated MYC(N) activity scores for

each cell line were also used. However, also in this case no significant difference was found between cell lines with high and low MYCN transcriptional activity (**Figure 19B**). These results suggest that while *MYCN*-amplified cell lines are highly sensitive to ferroptosis induction, other cell lines may have adapted to the heightened stress caused by MYCN-driven proliferation, and therefore do not exhibit any response to cystine depletion.

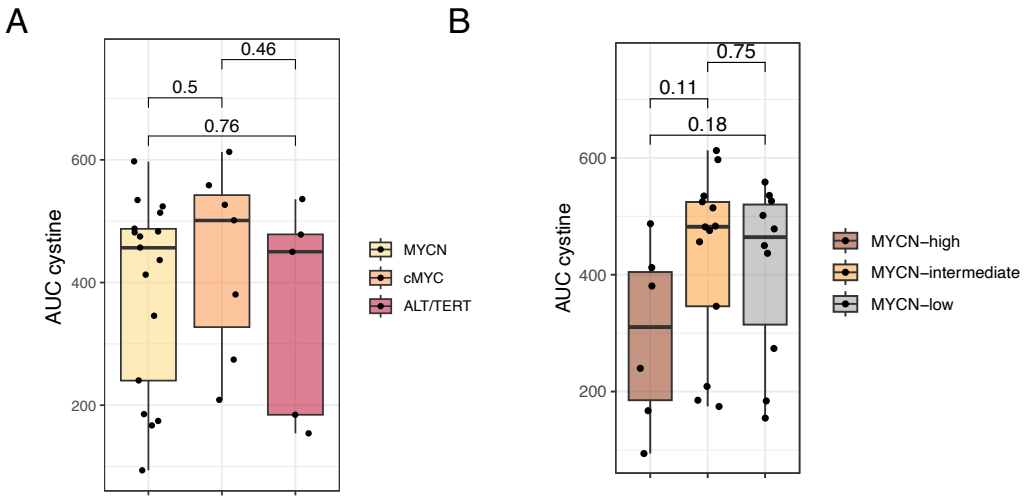

Figure 19: Evaluation of the impact of MYC(N) status and cell identity on cystine withdrawal sensitivity.
(**A**) The association of cystine depletion sensitivity (AUC values) and MYC(N) status of NB cell lines. *MYCN*-amplified/translocated cell lines (n = 17) are shown in red, *c-MYC*-amplified/translocated cell lines (n = 6) in orange, and cells with no MYC(N) alteration (n = 5) are depicted in yellow. (**B**) The comparison of cell lines' dependency on cystine between cells with high (n = 6), intermediate (n = 14) and low (n = 11) MYCN transcriptional activity. The statistical significance was tested using an unpaired t-test.

Furthermore, when comparing the sensitivity to cystine depletion between adrenergic cells (which are predominantly neuronal) and mesenchymal cells (which are more undifferentiated), no significant difference was observed. While the majority of the mesenchymal cells seemed to be less affected by cystine depletion (**Figure 20**), it is necessary to validate whether cell identity truly influences sensitivity to cystine

depletion in a wider range of cell lines that include a higher percentage of mesenchymal cell lines.

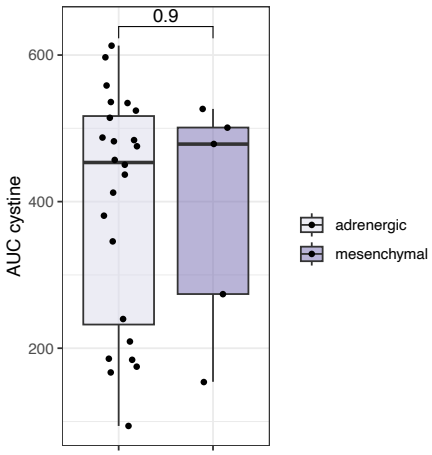

Figure 20: Assessment of cell identity influence on cystine dependency.
Cell identity was defined based on expression of epigenetic markers (Gartlgruber et al., 2021). Adrenergic cell lines (n = 24) are shown in light violet, and mesenchymal cell lines (n = 5) are depicted in dark violet. The statistical significance was tested using an unpaired t-test.

To gain a deeper understanding of NB sensitivity to ferroptosis, the association of cystine dependency with other genomic features relevant to NB biology, such as alterations in *TP53*-related (**Figure 21A**) and *ALK*-related pathways (**Figure 21B**) were investigated. However, no significant differences between the altered and wild-type groups in either case were found, suggesting that cystine dependency is not related to these features. As described in previous comparisons, the cystine dependency displayed a bi-modal distribution, further highlighting the complexity of NB tumor entity. These findings underscore the need for further investigation into NB biology to unravel the intricacies of this disease.

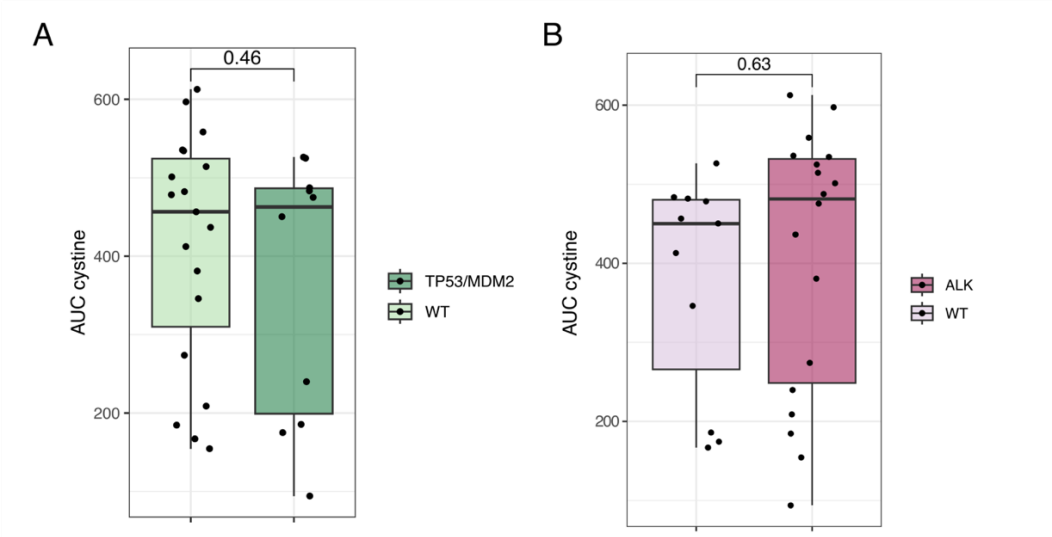

Figure 21: Relationship between the cystine depletion sensitivity and alterations in *TP53/MDM2*- and *ALK*-related pathways.
(**A**) The relationship between alterations in *TP53*/*MDM2*-pathway and cystine dependency. Cell lines with disrupted *TP53*/*MDM2*-pathway (n = 10) are depicted in dark green, whereas WT cells (n = 19) are shown in light green. (**B**) The influence of *ALK* mutation/amplification on the cystine dependency. ALK-altered cell lines (n = 18) are shown in dark pink, while WT cells (n = 11) are colored in light pink. The statistical significance was tested using an unpaired t-test.

To functionally characterize the relationship between MYCN and ferroptosis, a previously developed doxycycline-inducible shRNA-mediated MYCN downregulation model in IMR-5-75 was used in cystine titration experiments (Alborzinia et al., 2022). By reducing MYCN protein expression by ~ 50% (**Figure 22A**), the cystine dependency of the IMR-5-75 cells was completely reversed, providing further evidence of MYCN influence on cystine dependency in the IMR-5-75 ferroptosis sensitive NB cell line model (**Figure 22B**).

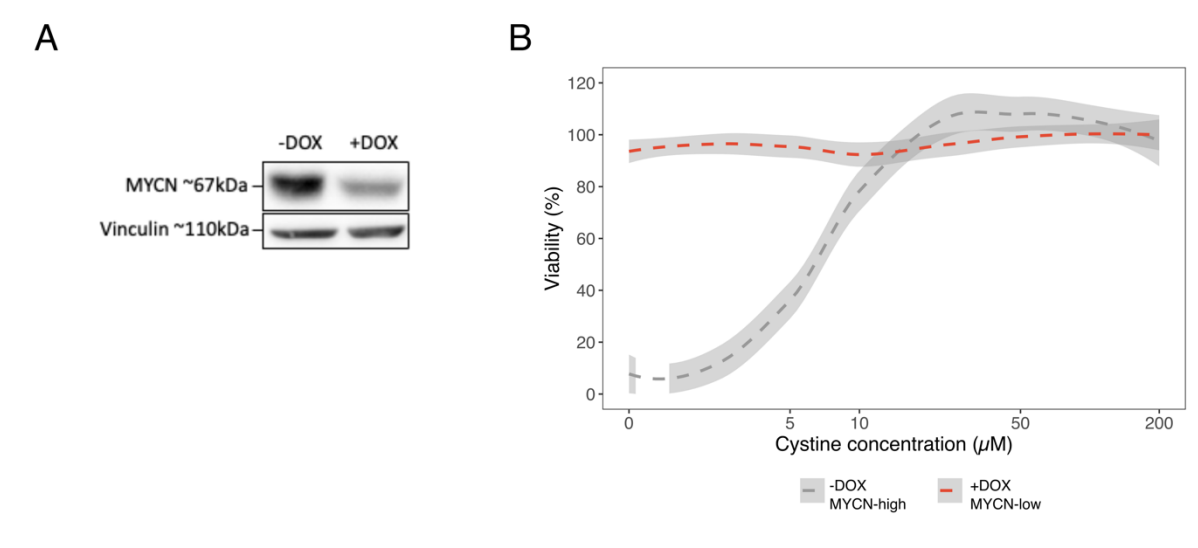

Figure 22: MYCN influence on cystine dependency validated in IMR-5-75 cell line model. (**A**) Western blot analysis representing the efficiency of doxycycline-induced shRNA-mediated MYCN downregulation IMR5-75 cell line model. Vinculin was used as the loading control. (**B**) Cystine titration results upon *MYCN* downregulation in IMR-5-75 cell line (variability of biological replicates are represented in grey; $n_{biol.rep.} = 3$).

Altogether, these findings highlight the intricate regulation of thiol metabolism in NB, and further underscore its complexity, which cannot be directly explained by genetic alterations, MYC(N) status or origin of the cell lines. While some *MYCN*-amplified cell lines exhibit a strong sensitivity to cystine depletion and subsequent ferroptosis induction, there are also other cell lines that do not show any response. This suggests that the high-*MYCN* oncogenic background may trigger the development of additional mechanisms that serve as adaptations to prevent cell death caused by ROS.

6.1.2.2. Treatment with ferroptosis-inducing agents

To further investigate the sensitivity of NB cells to ferroptotic cell death, a series of experiments were conducted using three ferroptosis-inducing agents (FINs) with distinct modes of action: erastin, RSL-3, and ML210. Erastin, a type I FIN, promotes ferroptosis by inhibiting the cystine-glutamate antiporter (system x_c^-) and increasing oxidative phosphorylation and ROS production through regulation of Voltage-Dependent Anion Channels (VDAC) in the mitochondrial outer membrane (Zhao et al., 2020). RSL-3 and ML210, type II FINs, induce ferroptosis by inhibiting the antioxidant enzyme GPX4 and reducing the cell's antioxidative capacity (Eaton et al., 2020; Yang et al., 2014).

To determine the optimal treatment conditions, the compounds were titrated at the following concentrations: erastin 0.1-1 µM, RSL-3 5-500 nM and ML210 0.01-10 µM for 72 h. Cell viability and confluence were quantified using the CellTiter-Blue Viability Assay and Giemsa staining protocol, respectively. Similarly to cystine deprivation experiments, the three response groups could be established, confirming the high heterogeneity of NB cell lines in terms of their sensitivity to ferroptosis induction (**Figure 23**).

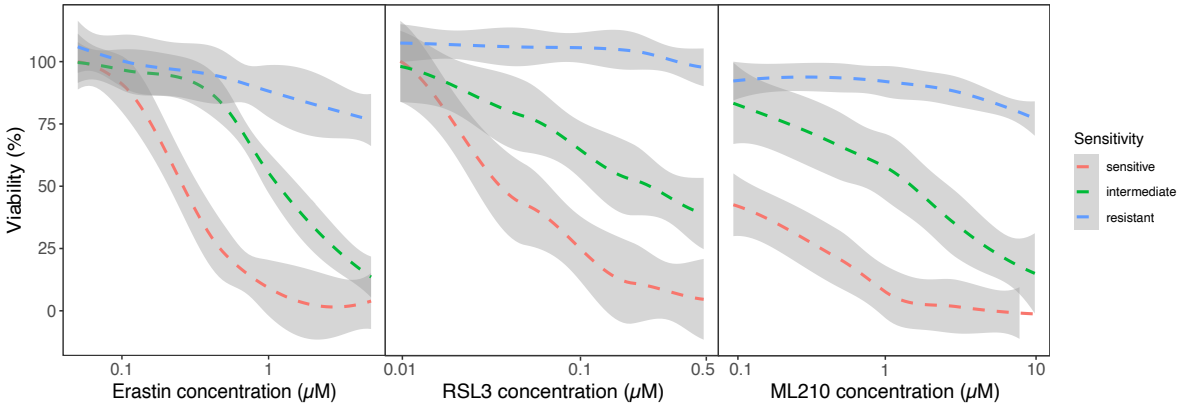

Figure 23: Estimation of NB cell lines sensitivity to ferroptosis induction by FINs.
FINs titration in a large panel of NB CLs allowed to define three subsets: sensitive ($n_{erastin}$ = 8, n_{RSL3} = 10, n_{ML210} = 11) , intermediate ($n_{erastin}$ = 10, n_{RSL3} = 6, n_{ML210} = 5) and resistant ($n_{erastin}$ = , n_{RSL3} = 6, n_{ML210} = 5) to ferroptosis induction driven by a specific ferroptosis-inducer (variability of cell lines viability are represented in gray).

Cell lines were classified as sensitive if more than 80% of the cells died when exposed to the highest tested drug concentration. Conversely, those that showed little response to the treatment (with more than 70% of cells remaining alive at the highest tested concentration) were classified as resistant. Cell lines with viability falling between this threshold (20 – 70% viable cells at the end of the treatment) were classified as intermediate-responders (**Figure 24**). Obtained dose-response curves and AUC values are presented in **Supplementary Figures 2 - 4** and **Supplementary Table 1**, respectively.

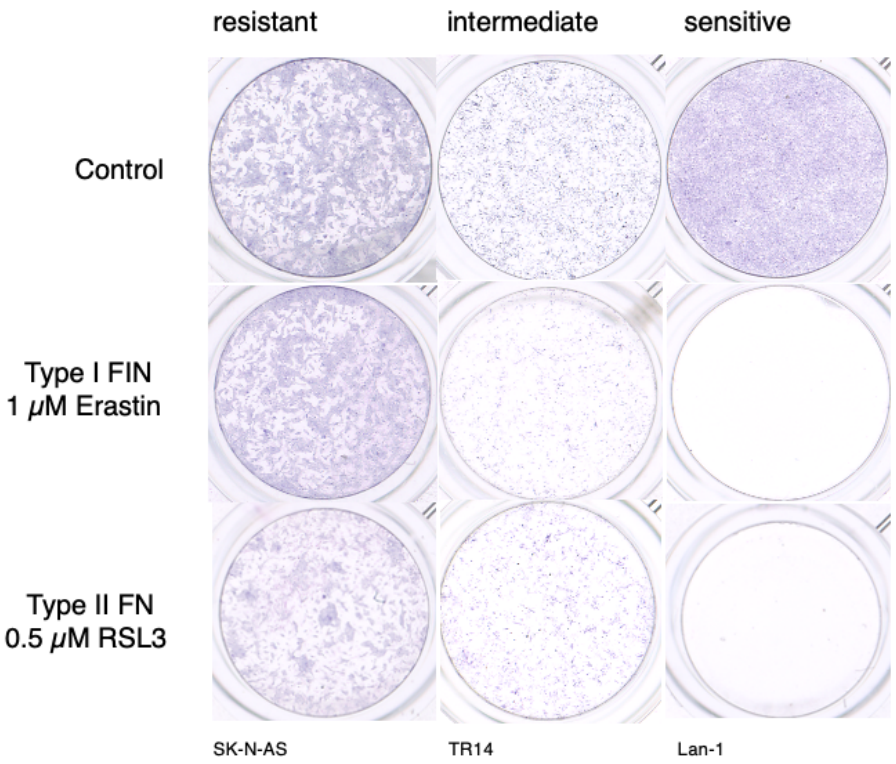

Figure 24: An exemplary image of cell lines response to ferroptosis inducing agents.
Giemsa staining images of three representative cell lines classified as resistant, intermediate, or sensitive to type I and II FINs treatment based on viability curve analysis. Resistant cell lines (e.g. SK-N-AS) showed greater than 80% viability, intermediate cell lines (e.g. TR14) showed 10-80% viability, and sensitive cell lines (e.g. Lan-1) showed less than 10% viability at the end of treatment (bottom row).

Comparison of AUC values between treatments revealed that the response of cell lines to the inhibition of cystine uptake by erastin only partially ($R = 0.5$) reflected their dependence on limiting cystine supply in the medium (**Figure 25A**). This partial correlation may be attributed to erastin's impact on mitochondrial VDAC proteins, as well as the influence of cystine depletion on overall cellular metabolism. Therefore, the response to erastin treatment may not solely reflect cystine dependency and should be interpreted with caution.

In contrast, the response of cells to all three FINs treatments was much more robust (**Figure 25B, C, D**). In particular, the inhibition of GPX4 by RSL3 and ML210 showed a high correlation ($R = 0.91$), indicating a strong and consistent effect of the treatment (**Figure 25D**). This finding highlights the reliability of using these FINs as potent tools for inducing ferroptotic cell death, and suggests that their effects can be accurately measured and compared across different experimental conditions.

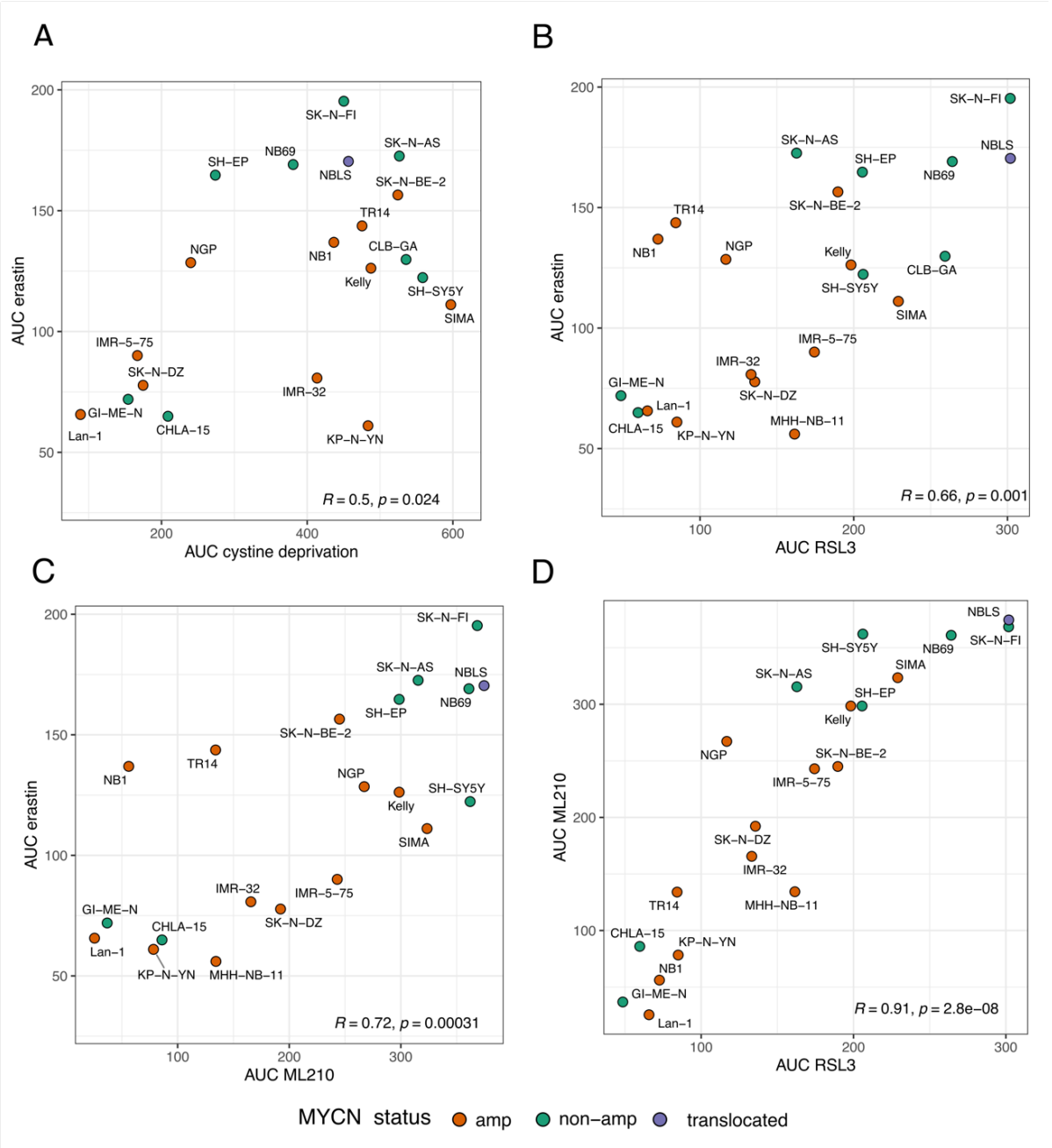

Figure 25: Evaluation of the effect of FINs on NB cell lines.
The correlation of AUC values obtained from (**A**) erastin treatment and cystine deprivation experiments, (**B**) erastin and RSL3 treatments, (**C**) erastin and ML210 treatments and (**D**) GPX4 inhibition using ML210, and RSL-3 are shown. Cell lines are color-coded according to their MYCN status. The correlation coefficient (*R*) and the p-values are depicted in the right bottom corner.

To gain insight into the source of variability that was observed in performed experiments, the influence of several parameters on ferroptosis sensitivity driven by type I and II FINs was compared. The aim was to identify the factors that contribute to the observed differences in treatment response across a large cell line panel. To achieve this, a comparison was made of cell line origin and identity, as well as the mutation status in *TP53*/*ALK* pathways, in a similar manner to the cystine depletion

experiments. No direct and significant correlation between these features and the sensitivity to FINs was found (**Supplementary Figure 5**). Although, the results showed that *MYCN*-amplified/translocated cell lines demonstrated the highest sensitivity to ferroptosis induction, this difference was also not statistically significant when compared to the other telomere maintenance (TMM) groups (**Figure 26**). In addition, cell lines grouping into high- and low-MYC(N) groups based on MYC(N) activities scores also did not improve the correlation (**Supplementary Figure 6**).

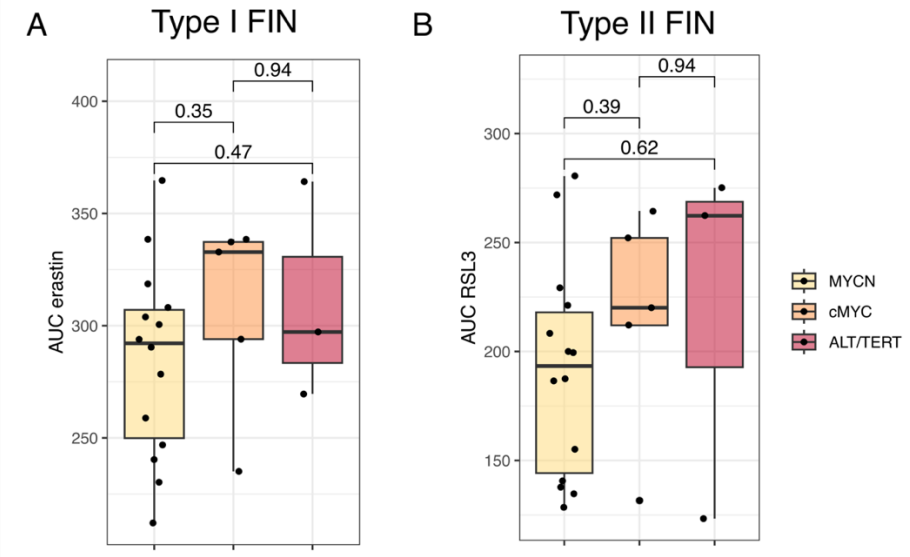

Figure 26: Association of MYC(N) status and cell lines' sensitivity to FINs.
Comparison of cell lines sensitivity to ferroptosis induction by (**A**) type I and (**B**) type II FINs. Cell lines were classified into three groups based on the status of MYC(N). *MYCN*-amplified/ translocated ($n_{erastin}$ = 14, n_{RSL3} = 14) cell lines are colored in red, *c-MYC*-amplified/ translocated ($n_{erastin}$ = 5, n_{RSL3} = 5) cell lines in orange and cell lines with no MYC(N) alteration ($n_{erastin}$ = 3, n_{RSL3} = 3) are shown in yellow. The statistical significance was tested using an unpaired t-test.

Altogether, the results suggest that while MYC(N) may play a role in regulating ferroptosis sensitivity in a subset of NBs, it is not the only factor determining sensitivity. This highlights the need for further research to identify other factors that contribute to the regulation of ferroptosis sensitivity in NB tumors.

6.1.2.3. Correlation of ferroptosis sensitivity to cell lineage state

NB is a type of cancer that arise from progenitor cells of the sympathetic nervous system. These cells can take on different forms and characteristics, ranging from differentiated and adrenergic to undifferentiated and mesenchymal. Malignancy and relapse are often associated with undifferentiated cell states. Although the sensitivity of NB cells to ferroptosis-inducing agents is not explained solely by lineage subtype

(adrenergic or mesenchymal), previous studies have shown that NB cells can interconvert between N-type and S-type states, making it difficult to define their definitive state. In our previous study (Gartlgruber et al., 2021), a method for estimating the mesenchymal score of a given cell line based on its gene expression profile was developed. The sensitivity of cells to certain treatments, such as inhibition of system x_c^- (**Figure 27A**), limiting cystine supply (**Figure 27B**), or inhibiting GPX4 activity (**Figure 27C, D**), was significantly correlated with their cell lineage state, as shown by the correlation analysis. Cells with high mesenchymal scores, including SH-EP, HD-N-33, and SK-N-AS, were largely resistant to ferroptosis induction. This finding is in agreement with previously published data that reported on inactivity of *de novo* cystine synthesis pathway in all tested mesenchymal NB cell lines (Alborzinia et al., 2022). Among adrenergic cell lines, a range of sensitivities was observed, with some cells (e.g., SK-N-DZ, Lan-1, IMR-5-75, LS, NGP) being highly sensitive and others (e.g., IMR-32, NB1, Kelly, TR14, SK-N-FI, CLB-GA, SIMA) being less sensitive. These results suggest that the cell lineage identity of NB cells could indeed contribute to their sensitivity to ferroptosis.

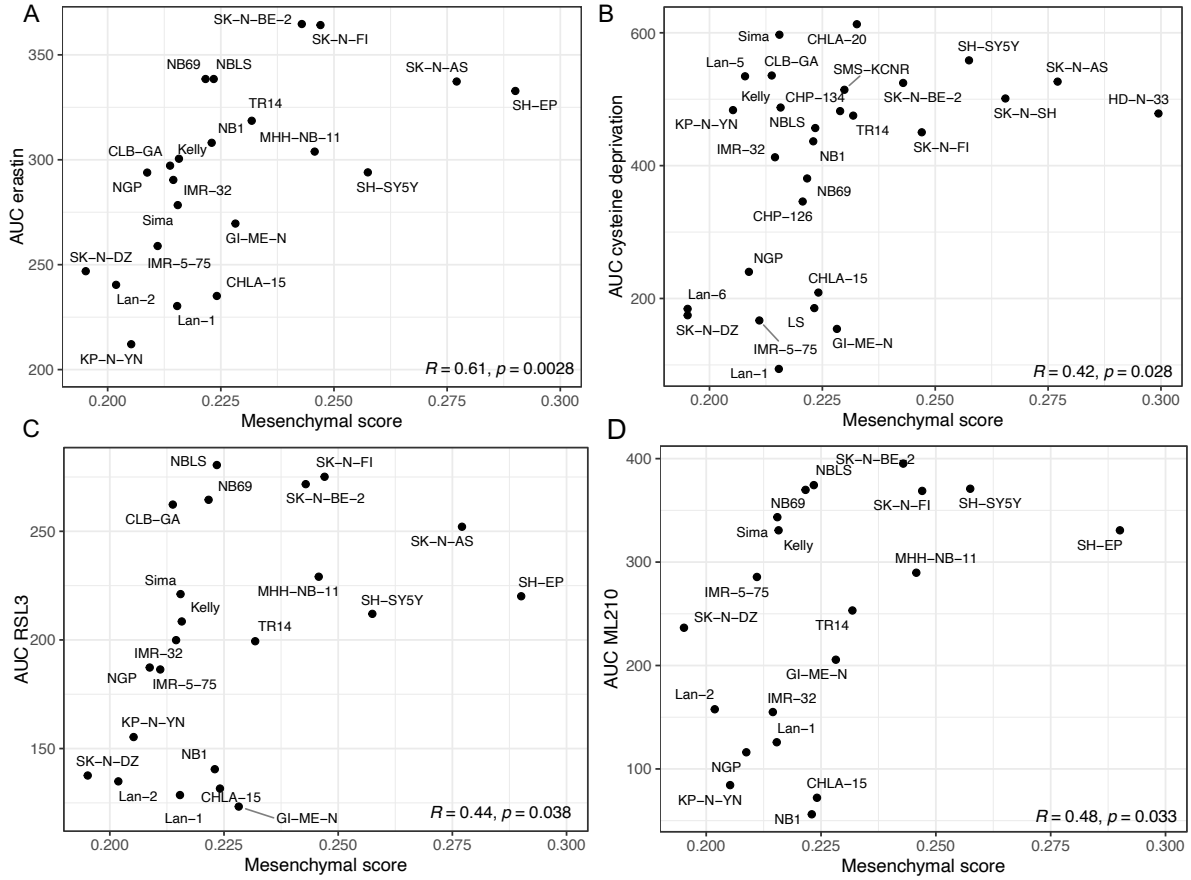

Figure 27: Mesenchymal score is correlated to the cell lines sensitivity to ferroptosis induction. To induce ferroptosis, erastin (**A**), limitation of cystine availability (**B**), RSL3 (**C**) and ML210 (**D**) were used. Mesenchymal score was calculated using signature gene expression (Gartlgruber et al., 2021) and signscore R package (Bhuva et al., 2020; Foroutan et al., 2018).

To gain insight into the factors underlying the differential sensitivity of adrenergic cell lines to treatment, a differential gene expression analysis was conducted comparing sensitive and resistant cell lines. However, only 14 differentially expressed genes (DEGs) significantly upregulated in the sensitive cell lines were identified, possibly due to the high degree of heterogeneity among the studied cell lines (**Figure 28**). Unfortunately, these DEGs did not provide any clear indication of the mechanisms responsible for sensitivity or resistance in these cells.

Figure 28: Differentially expressed genes between cell lines sensitive and resistant to ferroptosis.
Volcano plot summarizes DEGs derived from comparison of transcription profiles of ferroptosis-sensitive (n= 7) and resistant (n= 15) cell lines. In red genes expressed significantly higher in ferroptosis-sensitive cells are indicated. NS – not significant.

6.1.3. Identification of molecular markers of ferroptosis sensitivity

As none of the analyses described above led to the identification of robust drivers of ferroptosis sensitivity in NB cell lines, the search for other genetic or molecular markers needed to be continued. To identify additional factors that may play a role in regulating ferroptosis sensitivity and to gain a better understanding of the complex biology of NB, the drug response data was correlated with a normalized basal gene expression matrix (RNAseq) obtained from the large panel of NB cell lines. A high positive correlation between gene expression and AUC values for a given treatment corresponded to a gene with higher expression in cell lines resistant to that treatment

(see an example in **Figure 29A**), while a high negative correlation identified genes with higher expression in sensitive cell lines (example in **Figure 29B**).

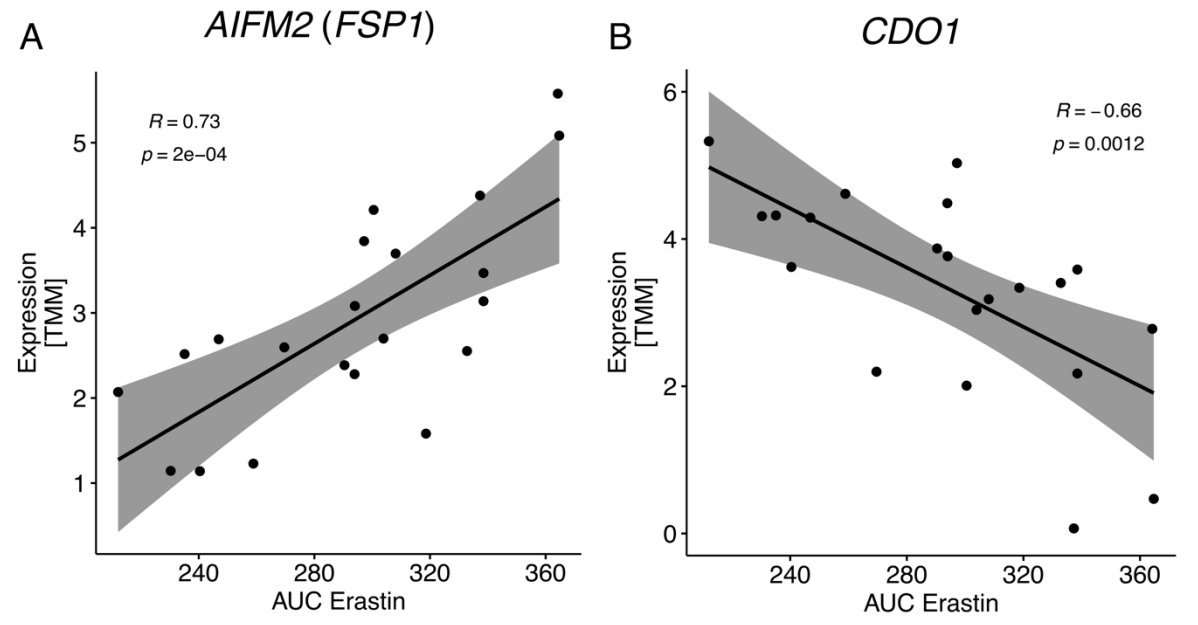

Figure 29: Representation of the two genes with highest positive and negative correlation between expression and sensitivity to ferroptosis.
An example of gene expression positively (**A**) and negatively (**B**) correlated to erastin sensitivity. Each dot corresponds to a specific cell line. The lower AUC value, the more sensitive a cell line is to the treatment. *AIFM2* (*FSP1*) – Apoptosis Inducing Factor Mitochondria Associated 2 (Ferroptosis suppressor protein 1); *CDO1* – Cysteine Dioxygenase Type 1. The Pearson correlation coefficients (R) and p-values are reported on top of the graphs. 95% confidence intervals are represented in grey.

To obtain the most reliable results, the significantly correlated genes across all the treatments (cystine depletion, erastin, RSL3, and ML210) were overlapped. This analysis led to identification of 50 genes that were in common within all the treatments (**Figure 30, Supplementary Table 2**).

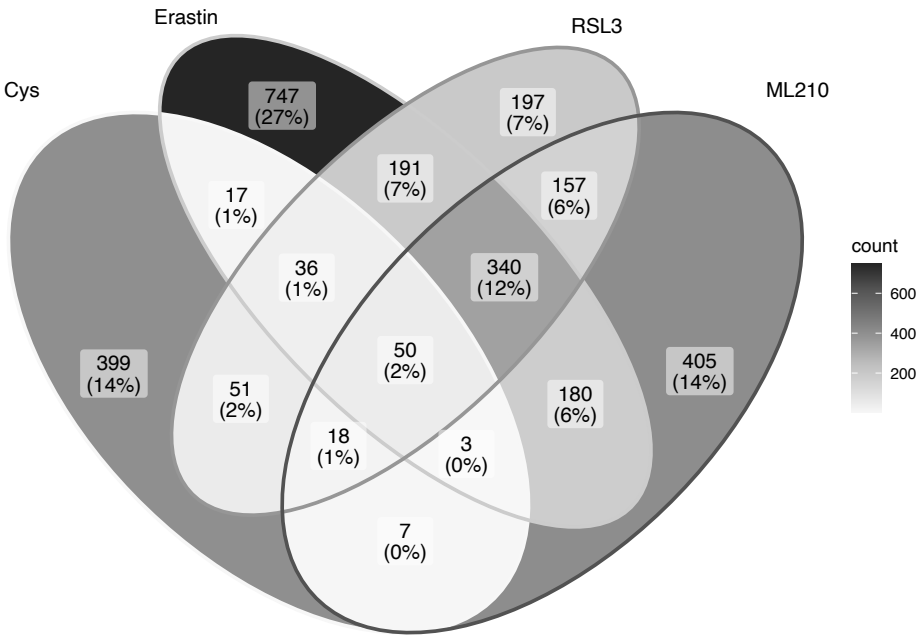

Figure 30: Summary of significantly correlated genes to ferroptosis induction.
Venn plot representing significantly correlated genes for each treatment, with 50 genes being in common across all. Intensity of the color represents the amount of unique genes for a specific comparison.

Among the top-ranked genes was flavoprotein apoptosis-inducing factor mitochondria-associated 2 (*AIFM2*; later renamed to ferroptosis suppressor protein 1 (*FSP1*)), which showed a strong positive correlation with the treatment. Additionally, another ferroptosis suppressor, GTP Cyclohydrolase 1 (*GCH1*), displayed a similar pattern (**Table 18**).

Table 18: The selected genes with the highest positive Pearson's correlation to the ferroptosis sensitivity.
The Pearson correlation coefficients (R*)* representing the association between normalized gene expression data and CLs sensitivity to FINs treatment are presented. Table contains only selected genes.

ENSEMBL ID	Gene Symbol	AUC RSL3	AUC ML210	AUC Cys	AUC Erastin
ENSG00000042286	*AIFM2*	0.65	0.47	0.4	0.73
ENSG00000008283	*CYB561*	0.73	0.7	0.47	0.69
ENSG00000131979	*GCH1*	0.7	0.46	0.54	0.49

FSP1 suppresses ferroptosis by catalyzing the regeneration of CoQ_{10} using NAD(P)H, which is required for the clearance of lipid peroxyl radicals (Doll et al., 2019).

Meanwhile, GCH1 is the major control point for de novo tetrahydrobiopterin (BH_4) synthesis, which under oxidative stress can induce the synthesis of CoQ_{10} to counteract oxidative damage (Kraft et al., 2020). In addition, BH_4/BH_2 synthesis inhibits ferroptosis by depleting phospholipids containing two polyunsaturated fatty acid tails (Kraft et al., 2020).

To determine the clinical relevance of the findings, the expression patterns of the genes identified in the cell line analysis were investigated in a large in-house cohort of NB tumors (n = 600), which consisted mainly of primary NB samples.

The analysis of the expression patterns of two highly correlated genes, *FSP1* and *GCH1*, showed that these genes were significantly less expressed in tumors with high-MYC(N) activity, as opposed to tumors with low or moderate MYC(N) activity, as illustrated in **Figure 31A and B**. Conversely, *MYCN*-amplified tumors exhibited increased expression of *DHFR*, which encodes dihydrofolate reductase and is responsible for BH_4 recycling (**Figure 31C**).

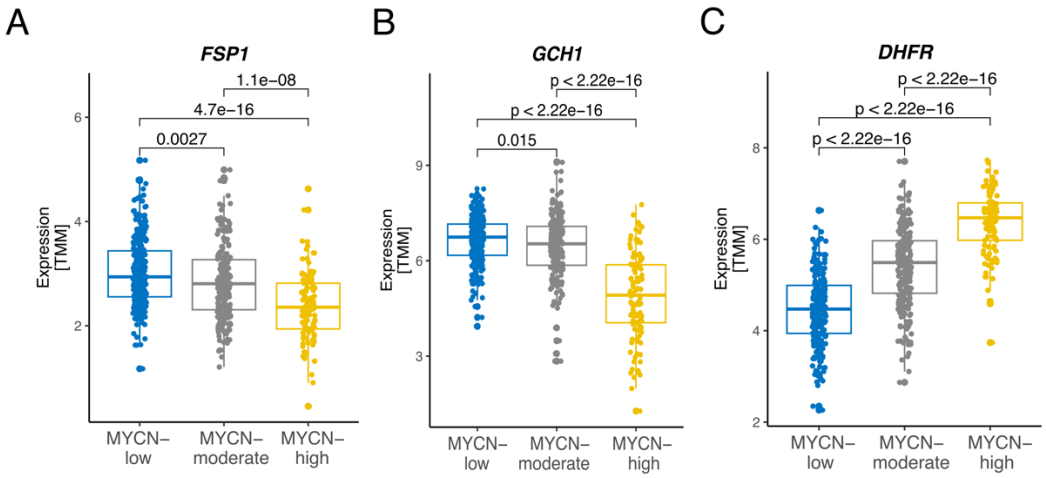

Figure 31: Expression of genes involved in CoQ_{10} pathway.
Expression of (**A**) *FSP1*, (**B**) *GCH1* and (**C**) *DHFR* in a large cohort of NB primary tumors (n= 600). The tumors were classified as MYCN-low (n = 266), MYCN-moderate (n = 221) and MYCN-high (n = 113) based on the MYC(N) activity score. The statistical significance of the expression levels of these genes was assessed using an unpaired t-test.

Taken together, the low expression of genes involved in the CoQ_{10}-related pathways may be a vulnerability of NB cell lines that sensitize them to ferroptosis induction. In addition, the simultaneous downregulation of the FSP1-CoQ_{10}-NAD(P)H and GCH1-

BH_4-CoQ_{10} pathways in NB tumors with high MYC(N) activity suggests that these tumors may be sensitive to ferroptosis induction due to their decreased ability to maintain redox balance. Moreover, the activation of compensatory mechanisms to restore BH_4 levels highlights its importance in *MYCN*-amplified tumors (**Figure 32**).

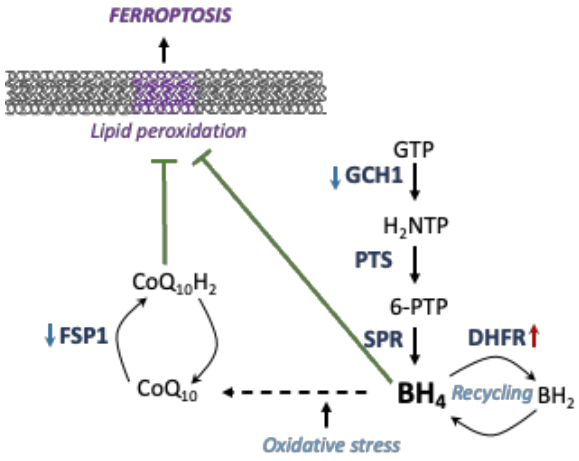

Figure 32: Overview of the FSP1 – CoQ_{10}– GCH1 pathway in the context of ferroptosis.
The reduced form of CoQ_{10} ($CoQ10H_2$) traps radicals that drive lipid peroxidation. FSP1 mediates the regeneration of CoQ_{10} utilizing NAD(P)H. GCH1 is the major controlling point of *de novo* tetrahydrobiopterin (BH_4) synthesis that under oxidative stress induces synthesis of CoQ_{10} to counteract oxidative damage. DHFR can recycle BH_2 and therefore regenerate BH_4 levels. FSP1 - Ferroptosis suppressor protein 1, CoQ_{10} – Coenzyme Q_{10}, PTS - 6-Pyruvoyltetrahydropterin Synthase, SPR - Sepiapterin reductase, H_2NTP- Dihydroneopterin triphosphate, 6-PTP – Pyruovyl tetrahydropterin, BH_2 – dihydrobiopterin.

It is worth noting that the expression pattern of *CYB561* was also positively correlated with drug response values (**Table 18**). *CYB651* encodes Cytochrome B561, a member of the CYB561 transmembrane protein family, which maintains ascorbate recycling and homeostasis (van den Berg et al., 2018). Recent data show that ascorbate promotes iron uptake and modulates its metabolism, supporting the role of CYB651 in maintaining cellular redox state. *MYCN*-amplified tumors showed significantly decreased expression of *CYB651* (**Figure 33**), suggesting dysregulated ascorbate-iron homeostasis that may contribute to ferroptosis execution.

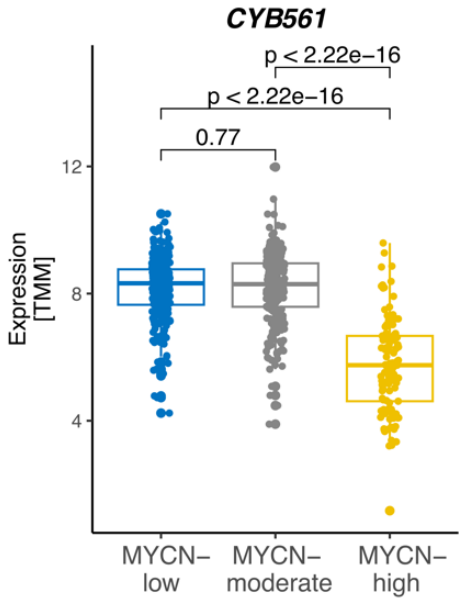

Figure 33: Cytochrome *B561* expression in a large cohort of primary NB.
CYB561 expression is shown in the MYCN-low (n = 266), MYCN-moderate (n = 221) and MYCN-high (n = 113) NB tumors. The statistical significance of the expression levels of these genes was assessed using an unpaired t-test.

6.1.4. Summary I

In this study, an extensive characterization of NB cell lines was conducted, with a focus on identifying the genetic and molecular mechanisms underlying their addiction to cystine and sensitivity to ferroptotic cell death.

The status of several genetic aberrations, including *MYCN* (status and transcriptional activity), *c-MYC*, *TP53*, and *ALK* pathways, was established using various methods such as western blotting, transcriptome, and whole genome sequencing data. Additionally, cystine titration experiments were performed which led to identification of NB cell lines that were strongly addicted to cystine, as well as those that were largely independent of cystine withdrawal from the growth medium. The dependency on cystine was not directly linked to MYC(N) status or alterations in *TP53* or *ALK* pathways, suggesting the involvement of other molecular mechanisms. Interestingly, cell lineage state seems to play a role in ferroptosis sensitivity, with more mesenchymal cell lines being more resistant to the ferroptosis induction. To further investigate NB sensitivity to ferroptotic cell death, three ferroptosis-inducing agents (erastin, RSL-3, and ML210) were tested. Surprisingly, no significant correlation was

observed between the genetic background of cell lines and sensitivity to these treatments, indicating the complex nature of NB response to ferroptosis.

To further understand the mechanisms underlying NB sensitivity to ferroptosis, the Pearson's correlation analysis of baseline gene expression data to cell lines' sensitivity to ferroptosis induction was performed. This analysis led to the identification of coenzyme Q_{10}-related pathways as an important resistance mechanism against ferroptosis. These pathways were found to be downregulated in *MYCN*-amplified tumors, which suggests their possible sensitivity to ferroptosis.

Taken together, these findings provide new insights into the genetic and molecular mechanisms underlying NB addiction to cystine and sensitivity to ferroptosis, and suggest potential biomarkers for the development of novel therapeutic strategies targeting these pathways in NB.

6.2. Characterization of ferroptotic stress

The first part of the thesis was dedicated to determining the ferroptosis sensitivity of a large panel of NB cell lines induced by cystine depletion, as well as type I or type II FINs. However, the direct drivers of ferroptosis sensitivity remained unidentified. To obtain a more comprehensive understanding of the mechanisms underlying ferroptosis in NB, the transcriptome profiles of cells experiencing ferroptotic stress from cystine deprivation or knockdown of key players in the ferroptosis pathway (GPX4, CTH) were compared. Additionally, stable isotope tracing experiments were conducted to functionally validate the findings. The results of these investigations offer new insights into the regulation of ferroptosis in NB.

6.2.1. Cystine limitation-related stress response

To investigate the differences between ferroptosis-sensitive and resistant NB cell lines, four cell lines with different levels of ferroptosis sensitivity were selected (SK-N-DZ, IMR-5-75, NBL-S, and SK-N-FI) to perform transcriptome analysis after partial and full cysteine deprivation. Obtained results showed that the initial response to reduced cysteine concentration in the medium (5 µM) was much stronger in the *MYCN*-

amplified IMR-5-75 and SK-N-DZ cell lines (29 DEGs and 12 DEGs, respectively) compared to the *MYCN*-translocated NBL-S cells (3 DEGs) and *MYCN*-normal SK-N-FI cells (0 DEGs) (**Figure 34A**). Further cultivation in low cysteine conditions led to additional transcriptome dysregulation in SK-N-DZ cells (291 DEGs) and NBL-S cells (9 DEGs), while IMR-5-75 and SK-N-FI did not show any significant transcriptome changes (**Figure 34B**). Interestingly, complete cysteine deprivation from the culturing medium caused a massive stress response activation in the ferroptosis-sensitive SK-N-DZ and IMR-5-75 cells, while there were only a few differentially expressed genes in NBL-S and SK-N-FI cells, and no DEGs that were common among all four cell lines at T24h (**Figure 34C, D**). These results suggest that *MYCN*-amplified cells have a much lower capacity to overcome cystine starvation-induced stress.

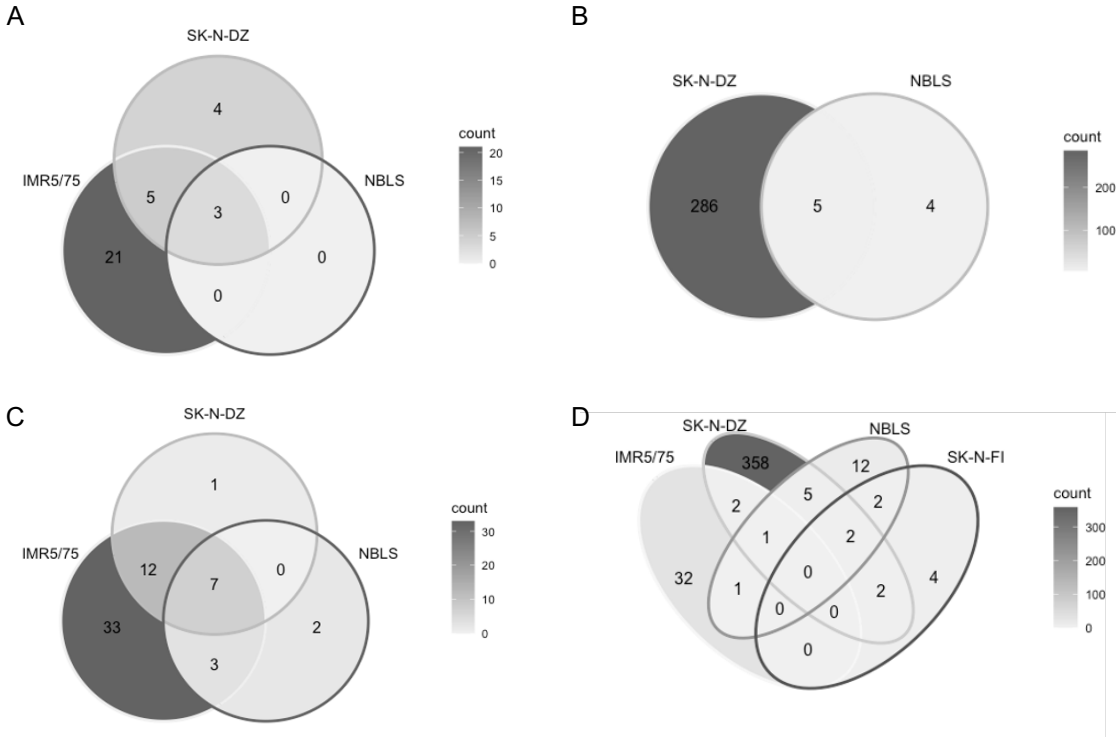

Figure 34: Differentially expressed genes upon cystine limitation.
Venn diagrams representing results from DE analysis comparing transcription profiles of four NB cell lines (IMR-5-75, SK-N-DZ, NBLS and SK-N-FI) cultivated in low cystine medium (5 μM) vs full medium at 8h (**A**) and 24h (**B**), and in cystine deprived medium at 8h (**C**) and 24h (**D**).

Mechanistically, cystine deprivation triggered a stress response mediated by activating transcription factor (ATF) family (Wortel et al., 2017) in all cell lines. However, this response was much weaker and delayed in ferroptosis-resistant cells. Among the most upregulated genes at 8 h were these related to cellular responses to amino acid starvation, such as *adrenomedullin 2* (*ADM2*), *sestrin 2* (*SESN2*),

stanniocalcin 2 (*STC2*), *DNA damage-inducible transcript 4* (*DDIT4*), and *asparagine synthetase* (*ASNS*), which confirm the induction of oxidative stress and mitochondrial dysfunction upon cystine depletion from the growth medium (**Figure 35, Figure 36**).

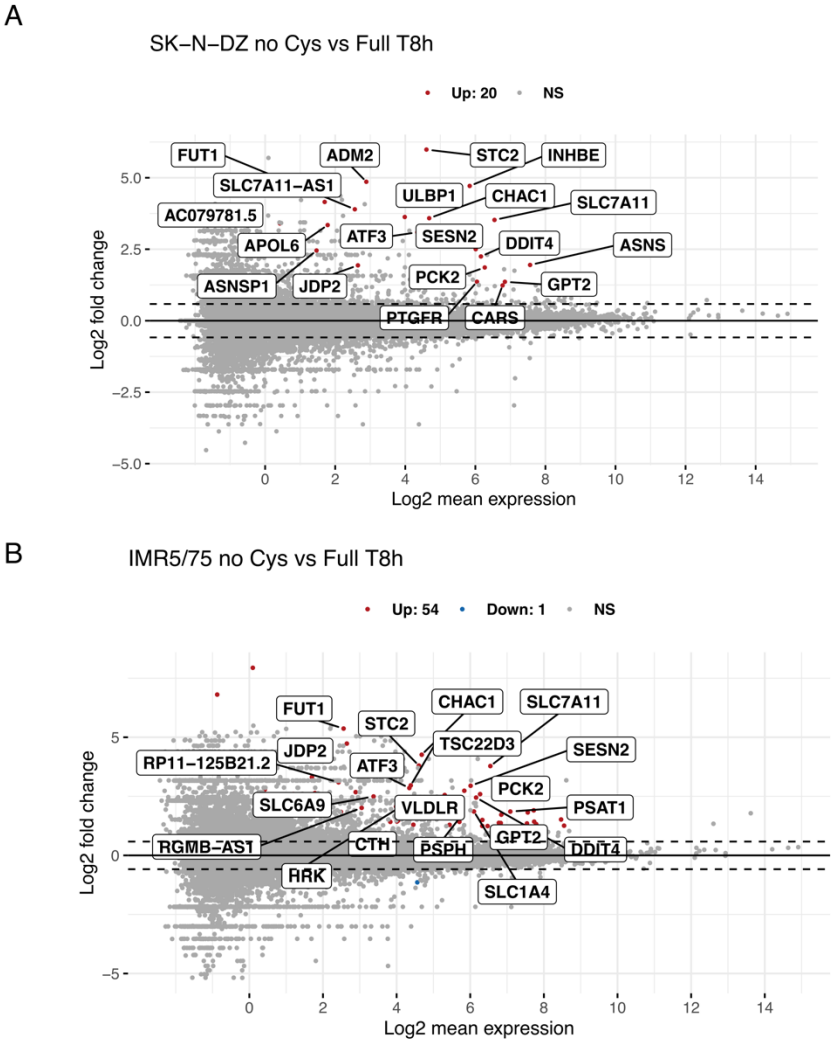

Figure 35: Differentially expressed genes upon cystine deprivation in ferroptosis-sensitive cell lines at 8h.
Volcano plots represents DEGs between two NB cell lines: (**A**) SK-N-DZ and (**B**) IMR-5-75, cultivated in cystine deprived medium and full medium at 8h. Genes which were significantly up- or downregulated are colored in red or blue, respectively. NS – not significant.

In addition, depending on the cell line, the lack of cystine in the growth medium led to upregulation of genes involved in cysteine restoration (*SLC7A11*, *CHAC1*), cysteine *de novo* synthesis (*CTH*, *CBS*, *CARS*), and one-carbon and serine/glycine metabolism (*MTHFD2*, *ALDH1L2*, *PHGDH*, *PSAT1*, *SHMT2*, *SLC6A9*, *PSPH*) (**Figure 35, 36**).

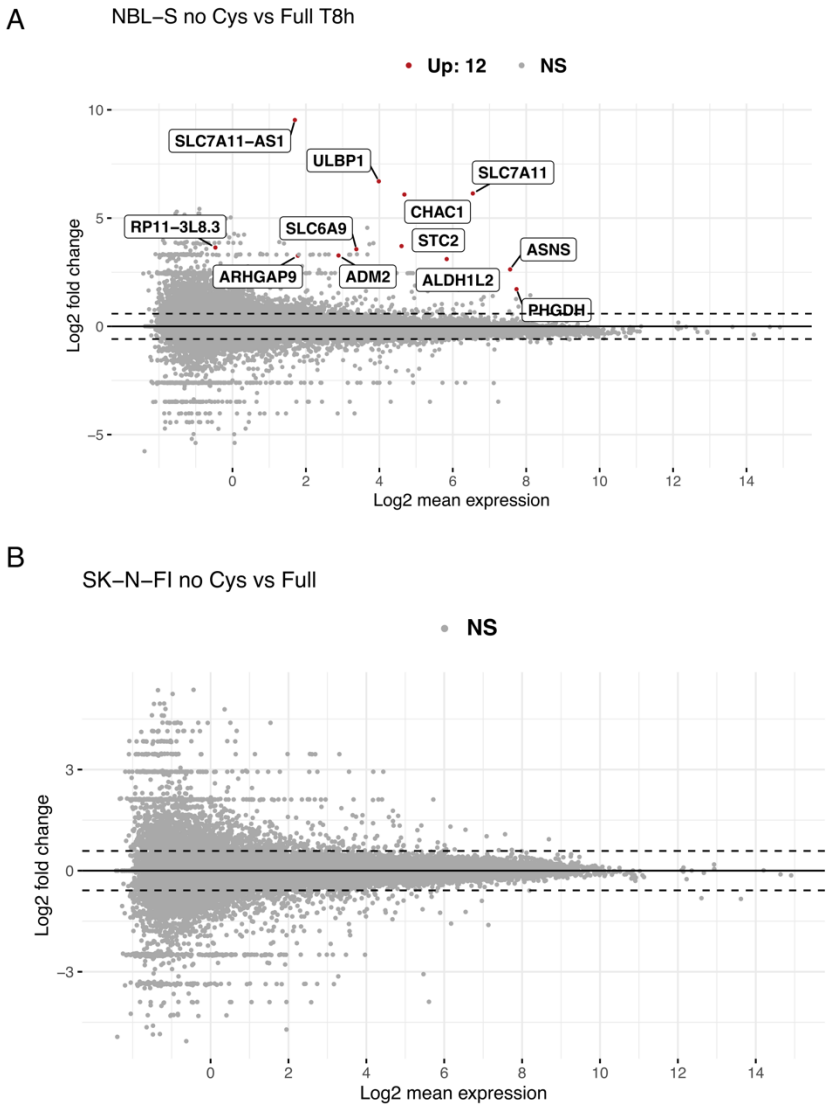

Figure 36: Differentially expressed genes upon cystine deprivation in ferroptosis-resistant cell lines at 8h.
Volcano plots represents DEGs between two NB cell lines: (**A**) NBL-S and (**B**) SK-N-FI, cultivated in cystine deprived medium and full medium at 8h. Genes which were significantly up- or downregulated are colored in red or blue, respectively. NS – not significant.

When comparing the ATF-controlled transcriptional response to cystine starvation at 24h, *MYCN*-amplified cell lines showed a massive transcriptional dysregulation, with hundreds of genes being upregulated (**Figure 37**), which is ultimately leading to the cell death.

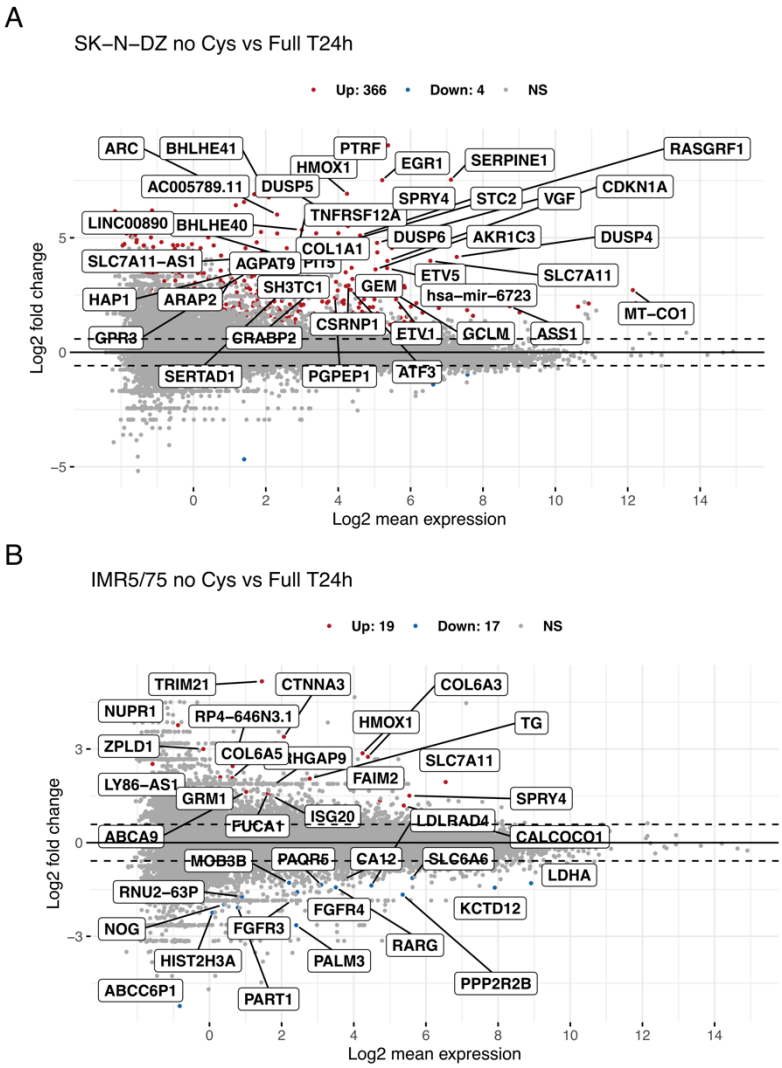

Figure 37: Differentially expressed genes upon cystine deprivation in ferroptosis-sensitive cell lines at 24h.
Volcano plots represents DEGs between two NB cell lines: (**A**) SK-N-DZ and (**B**) IMR-5-75, cultivated in cystine deprived medium and full medium at 24h. Genes which were significantly up- or downregulated are colored in red or blue, respectively. NS – not significant.

In contrast, *MYCN*-non-amplified cells were able to maintain low and steady levels of stress, which helped them to survive in nutrient-deprived conditions (**Figure 38**). These results suggest that *MYCN*-amplified cells are more vulnerable to stress-induced cell death, while *MYCN*-non-amplified cells are better able to withstand such stress.

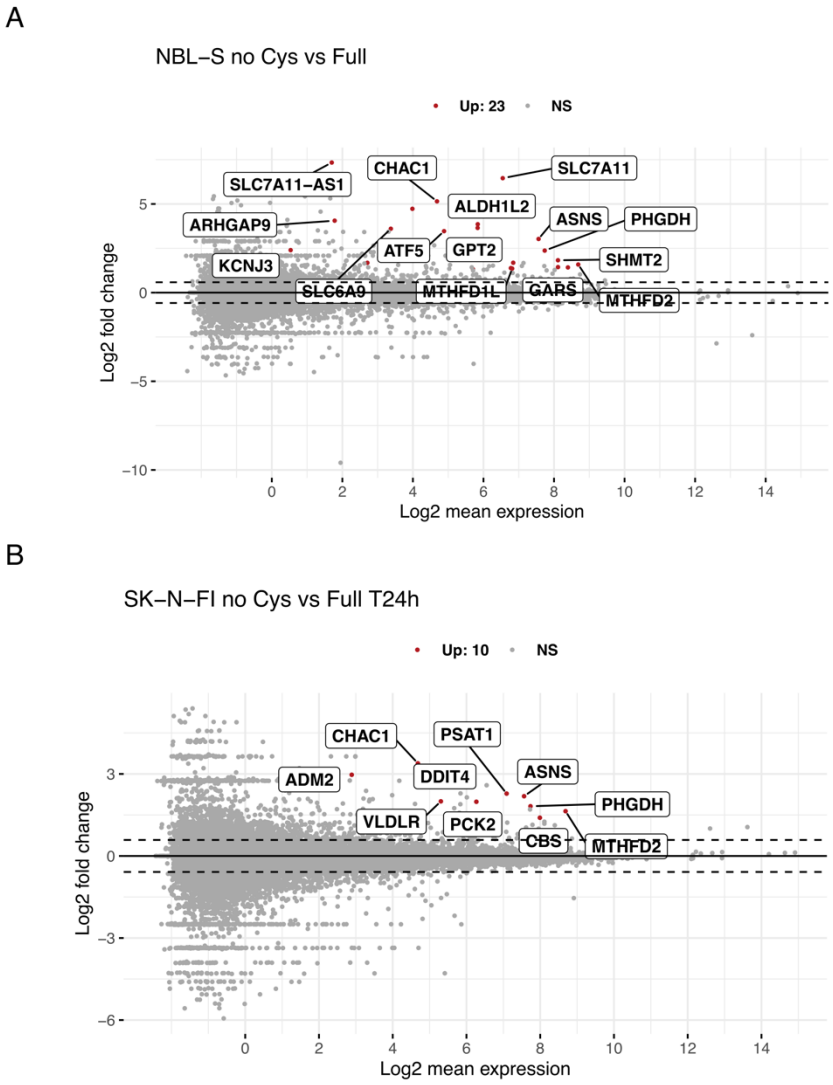

Figure 38: Differentially expressed genes upon cystine deprivation in ferroptosis-resistant cell lines at 24h.
Volcano plots represents DEGs between two NB cell lines: (**A**) NBL-S and (**B**) SK-N-FI, cultivated in cystine deprived medium and full medium at 24h. Genes which were significantly up- or downregulated are colored in red or blue, respectively. NS – not significant.

6.2.1.1. Metabolic profiling of selected NB cell lines

As described in the previous section, the *MYCN*-non-amplified ferroptosis resistant cell lines (NBL-S and SK-N-FI) exhibited a comparatively weaker transcriptomic response to the induced stress resulting from cystine deprivation. In order to uncover the source of this differential regulation, stable isotope tracing experiments were employed in which two NB cell lines with different MYCN levels (**Figure 39A**): IMR-5-75 (*MYCN*-amplified) and SK-N-FI (*MYCN*-normal) were fed with stably labeled $^{13}C_6$-

$^{15}N_2$-cystine (**Figure 39B**). The comparison of baseline thiol levels between the two cell lines revealed that MYCN-high cells had significantly lower levels of cysteine and glutathione compared to SK-N-FI cells (**Figure 39C**). This difference could potentially be attributed to the increased demand for these thiols in MYCN-high cells due to their rapid proliferation, or it could be caused by an inefficient mechanism for cysteine uptake that leaves these cells vulnerable to ferroptosis.

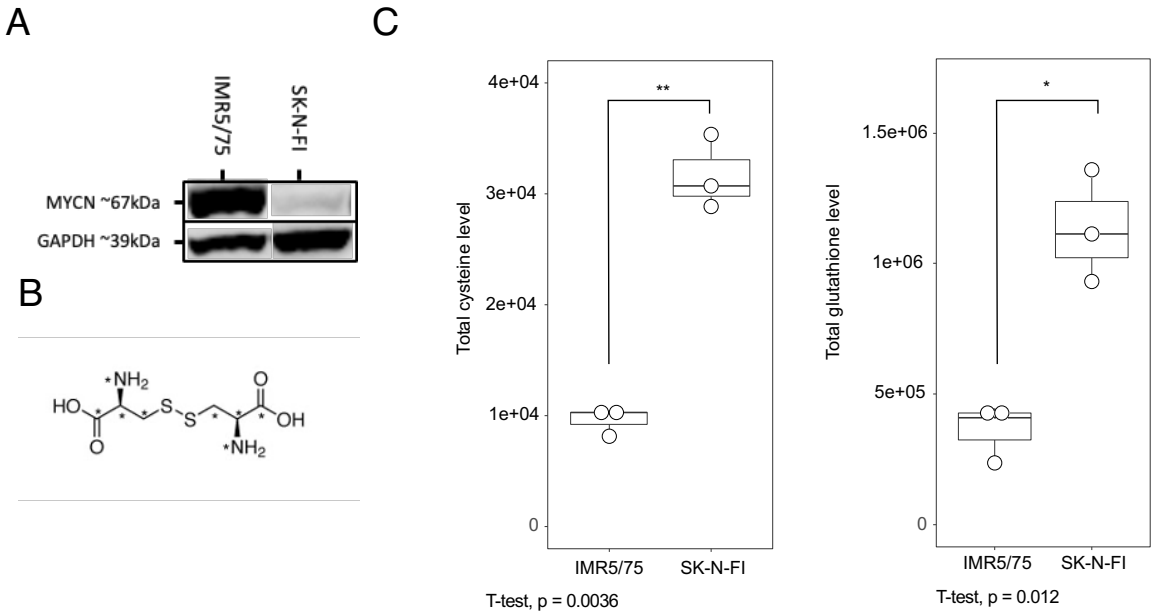

Figure 39: Stably labelled cystine tracing experiments in two NB models.
(**A**) Western Blot image depicting MYCN levels in IMR5/75 and SK-N-FI cells. GAPDH was used as a loading control. (**B**) Schematic representation of the structure of stably labelled cystine used in this study. (**C)** Total level of cysteine and glutathione in MYCN-amplified IMR5/75 cells and non-amplified SK-N-FI cells. n = 3. P-value was calculated using an unpaired t-test.

To evaluate the efficiency of the cystine uptake mechanism in both cell lines, the ratio of labeled to unlabeled cysteine was calculated in the cell pellet of both cell lines after 24 hours from introducing the label cystine in the growth medium. The results showed that SK-N-FI cells were able to uptake cystine more efficiently (about 90% of labeled cysteine) compared to IMR-5-75 cells (about 50% labeled cysteine) (**Figure 40A**). However, the incorporation of labeled cysteine into glutathione was similar for both cell lines (**Figure 40B**), indicating that *MYCN*-amplified cells may have activated compensatory mechanisms (such as MYCN-driven Glutamate-Cysteine Ligase Catalytic Subunit (*GCLC*) upregulation) that effectively incorporate cysteine into GSH.

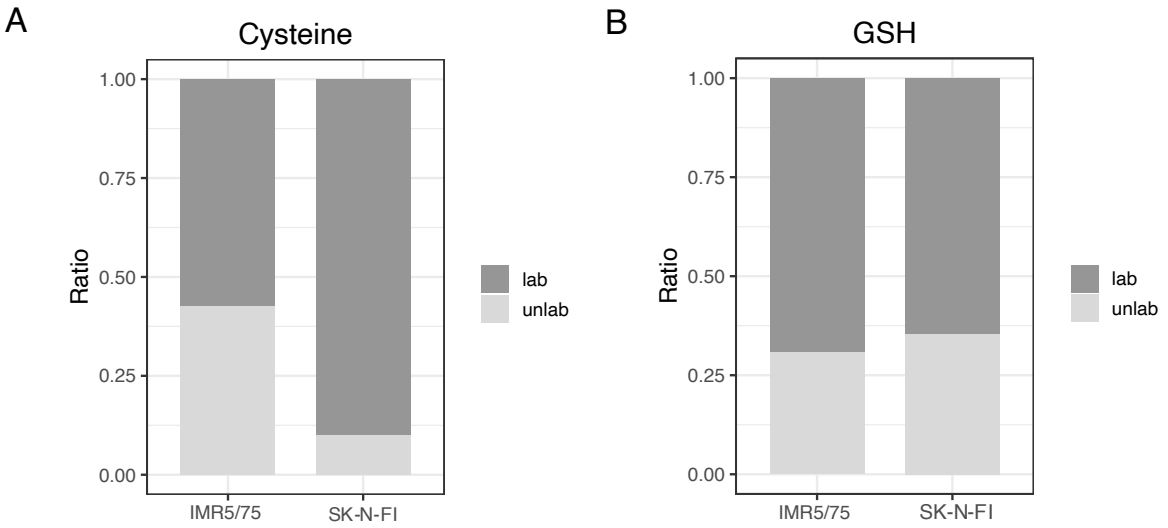

Figure 40: Label distribution in cysteine and glutathione in IMR-5-75 and SK-N-FI cell pellet.
The ratio between label and unlabeled (A) cystine and (B) glutathione. Measurement was performed at 24 h after introducing labelled amino acid in the growth medium. Dark grey – labeled cysteine; light grey – unlabeled cystine. n = 3.

As cystine is transported to the cell with exchange for glutamate, another way to study the functionality of system x_c^- is to estimate the levels of glutamate intra- and extracellularly. In fact, the levels of glutamate in the growth media of SK-N-FI cells increased over time (**Figure 41A**), while at 24 hours, glutamate was barely detected in the supernatant of IMR-5-75 cells. Furthermore, the intracellular glutamate levels in *MYCN*-amplified cells were not only much lower, but also decreased over time (**Figure 41B**), suggesting that competing pathways that heavily utilize glutamate may be activated in these cells, making it unavailable for exchange with cystine.

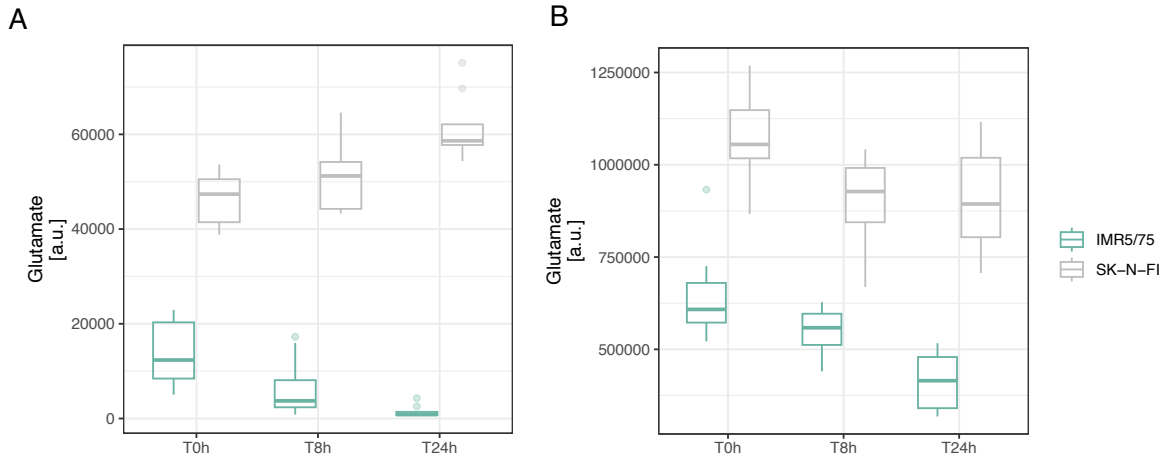

Figure 41: Over-time comparison of extra- and intracellular glutamate levels in IMR-5-75 and SK-N-FI cells.
Cell lines are color-coded as indicated in the figure legend. (**A**) Glutamate levels in cell medium, (**B**) glutamate levels in cell pellet. n = 5.

It is worth noting that additional stable isotope labeling experiments using $^{13}C_5$-glutamine and $^{13}C_5$-glutamate showed that the glutamate that was taken up was not a source for either glutathione synthesis (**Figure 42A**) or the TCA cycle (**Figure 42B**). In contrast, glutamine, via glutaminolysis, contributed to the homeostasis of glutathione and thus to the maintenance of redox balance.

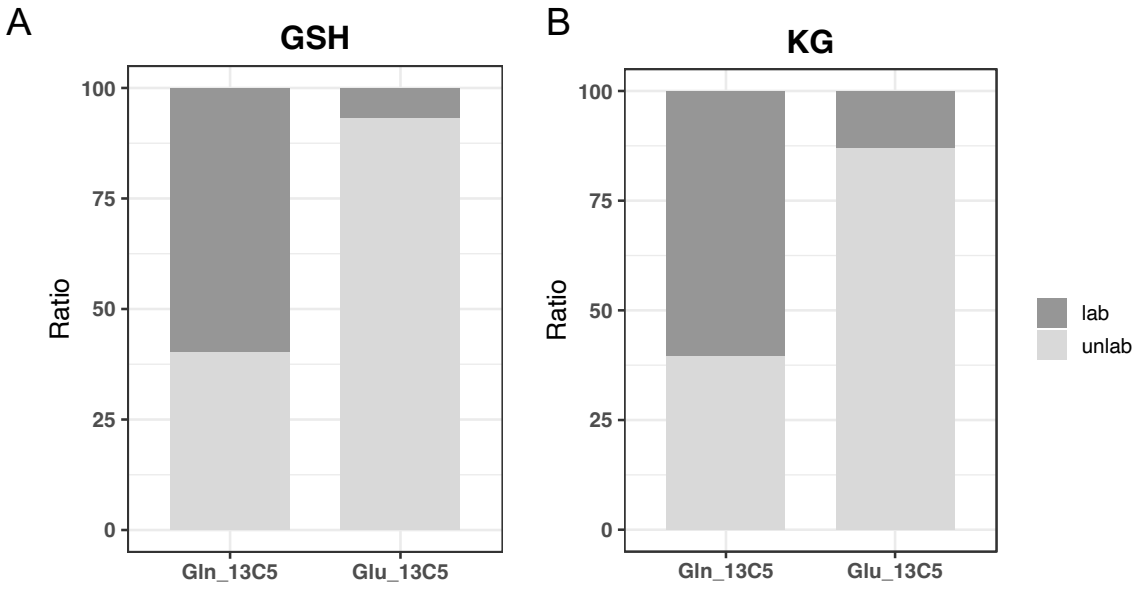

Figure 42: Comparison of glutamate and glutamine uptake of *MYCN*-amplified NB cells.
Label distribution in (**A**) glutathione (GSH) and (**B**) a-ketoglutarate (KG) in cell pellet of IMR-5-75 cells fed with labeled glutamine (Gln_13C5) or glutamate (Glu_135). n = 3.

Finally, a metabolomic analysis of a cohort of 20 patient-derived NB samples showed significantly lower levels of glutamate (**Figure 43**) and glutamine (**Figure 43B**) in *MYCN*-amplified tumors. Combined with low *SLC7A11* expression (as reported in (Alborzinia et al., 2022), these low levels may create a bottleneck for efficient cystine uptake, potentially increasing the risk of ferroptosis induction in rapidly proliferating *MYCN*-amplified NB cells.

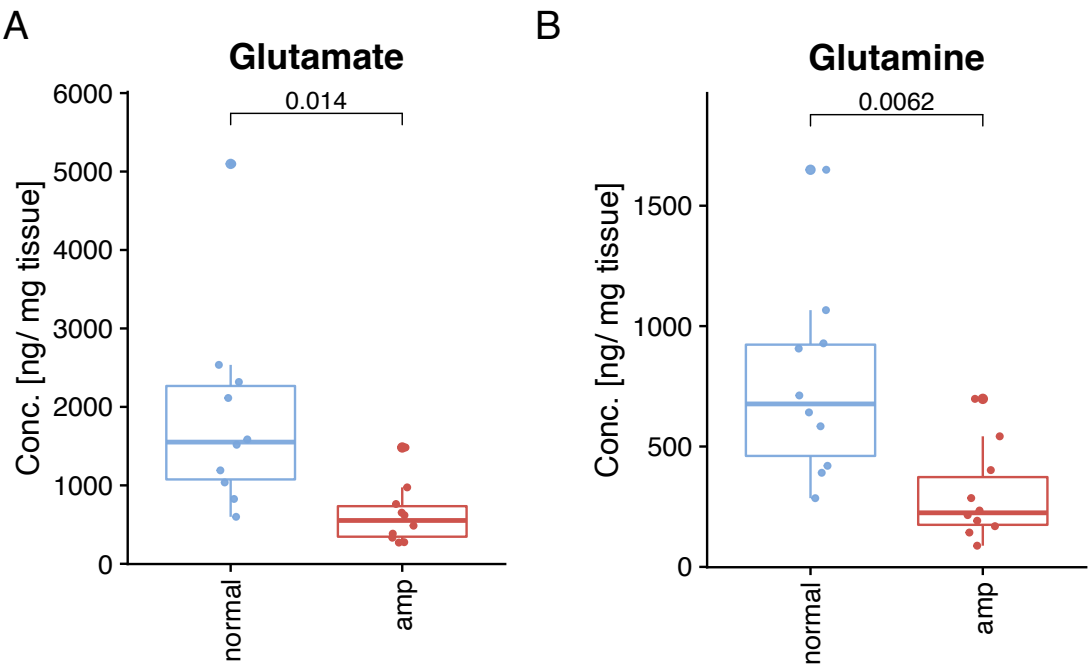

Figure 43: Glutamate and glutamine abundance in NB primary tumors.
Levels of (**A**) glutamate and (**B**) glutamine in patient derived NB tumors were quantified using MS-based techniques. Tumors were classified in two groups based on their MYCN status: normal – *MYCN*-non amplified (n = 10), and amp – *MYCN*-amplified (n = 10). P-values were calculated using an unpaired t-test.

6.2.2. Characterization of the transsulfuration pathway in MYCN-driven neuroblastoma

Cystine uptake is a major source of cysteine in mammalian cells. However, some cells have acquired the ability to synthesize cysteine *de novo* via the transsulfuration pathway, in which homocysteine (an intermediate of the methionine cycle) and serine are combined by the enzyme cystathionine-β-synthase (CBS) to form cystathionine, which is then converted to cysteine by the enzyme cystathionine-γ-lyase (CTH/CSE) (Sbodio et al., 2019).These reactions also lead to the production of a signaling molecule called hydrogen sulfide (H_2S).

6.2.2.1. Inhibition of de novo cysteine synthesis

To investigate the importance of *de novo* cysteine production for NB development, IMR-5-75 cells were transfected with a doxycycline-inducible short hairpin RNA (shRNA) construct against CTH, which resulted in almost complete (>95%) downregulation of CTH at the protein level (**Figure 44A**). Despite no alterations in sensitivity to erastin-induced ferroptosis, co-administration of homocysteine, an

intermediate in the methionine cycle, failed to inhibit cell death only in cells exhibiting reduced CTH (**Figure 44B**). Conversely, ferrostatin-1, a potent ferroptosis inhibitor that scavenges radicals, was effective in preventing cell death in both cases. These findings suggest that cells with decreased CTH levels are incapable of utilizing the transsulfuration pathway as a supplementary source of cysteine to mitigate ferroptotic cell death.

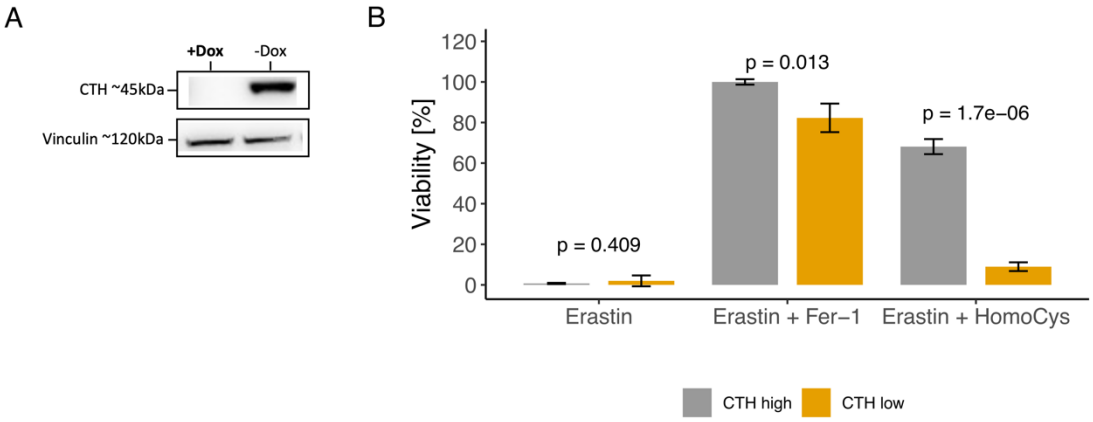

Figure 44: Characterization of CTH knockdown clones in the context of ferroptsis.
(**A)** Western blot analysis of doxycycline-induced shRNA-mediated CTH knockdown model in IMR-5-75 NB cells. Vinculin was used as a loading control. (**B**) Bar plot representing reduced capability of ferrostatin-1 and homocysteine to avert erastin-induced cell death in CTH knockdown cells. grey – CTH high cells, yellow – CTH low cells. P-value was calculated using an unpaired t-test. n = 3.

To further test the impact of transsulfuration pathway downregulation on ferroptosis sensitivity, the cystine titration experiments were performed. A stronger dependence on cystine upon CTH knockdown was observed (**Figure 45A**), which was associated with increased lipid peroxidation (**Figure 45B**). Additionally, cystine reduction in the growth medium to 5 μM elevated lipid peroxides accumulation in CTH-low cells (**Figure 45B**), highlighting the importance of transsulfuration-derived cysteine in maintaining redox homeostasis.

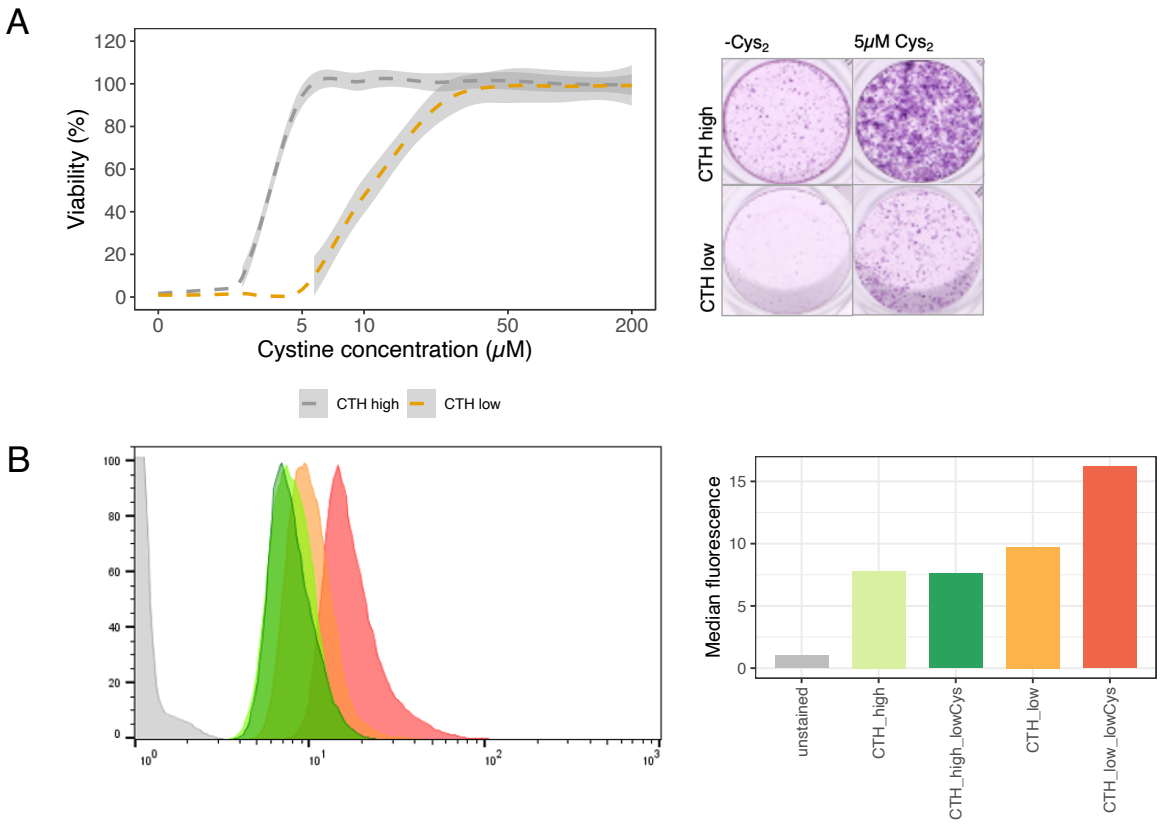

Figure 45: Estimation of cystine-limitation induced lipid peroxidation in CTH knockdown cells. (**A**) Cystine titration experiments in CTH high and low cells (left) and comparison of colony formation capacity in reduced (5 mM) or total cystine withdrawal (-Cys_2) from the growth medium. (**B**) Quantification of lipid peroxidation upon CTH knockdown in full and reduced cystine conditions using C11-Bodipy and flow cytometry.

To study the functional role of CTH, transcriptome analysis was performed on cells with high and low CTH levels. To determine the optimal time point for analysis, the efficiency of *CTH* knockdown was evaluated at 24, 48 and 72 h after doxycycline supplementation using western blot analysis (**Figure 46**). The results showed significant reduction of CTH protein levels at 48 and 72 hours, so these two time points were selected for RNA sequencing (RNAseq) profiling.

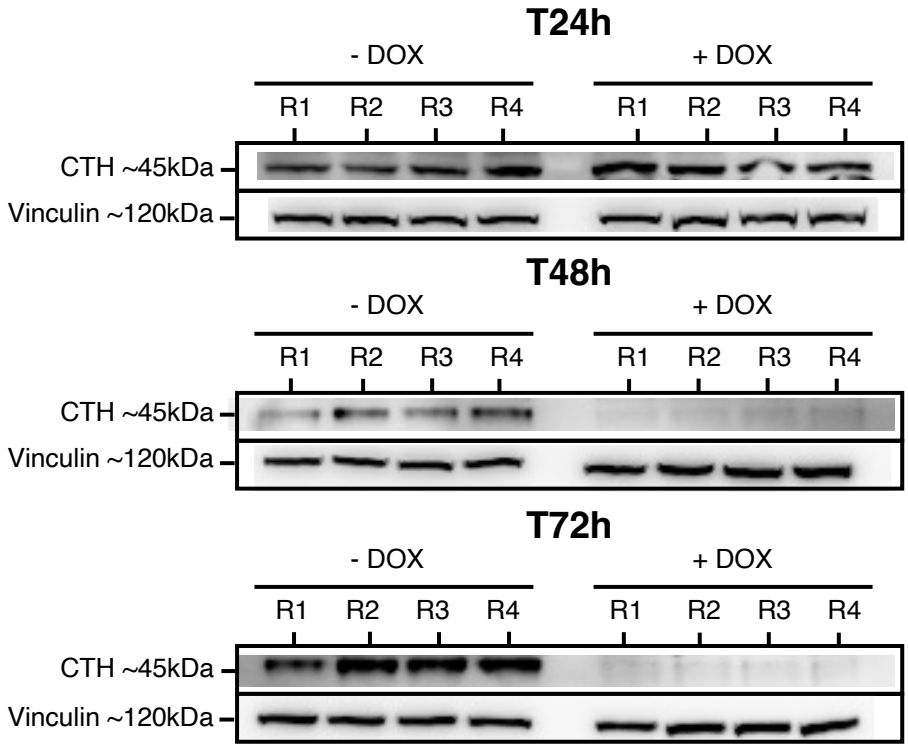

Figure 46: Quantification of CTH protein levels using western blot analysis at 24, 48 and 72 h after the addition of doxycycline to the growth medium.
Vinculin was used as a loading control. R – replicate, -DOX – without doxycycline, +DOX – with doxycycline. $n_{biol.rep.} = 4$

The RNAseq data (n = 4) was normalized using the edgeR normalization protocol, and then the principal component analysis (PCA) was applied to reduce the dimensionality of the data. The PCA analysis showed that the majority of the variance in the data was captured by principal components 1 and 2, which explained more than 70% of the variance (**Figure 47A**). Samples were separated based on doxycycline supplementation (which caused CTH downregulation) in principal component 1 (**Figure 47B**) and on time point in principal component 2 (**Figure 47B**), with 48h samples on top and 72 h samples on the bottom. As a result, these time points were analyzed separately.

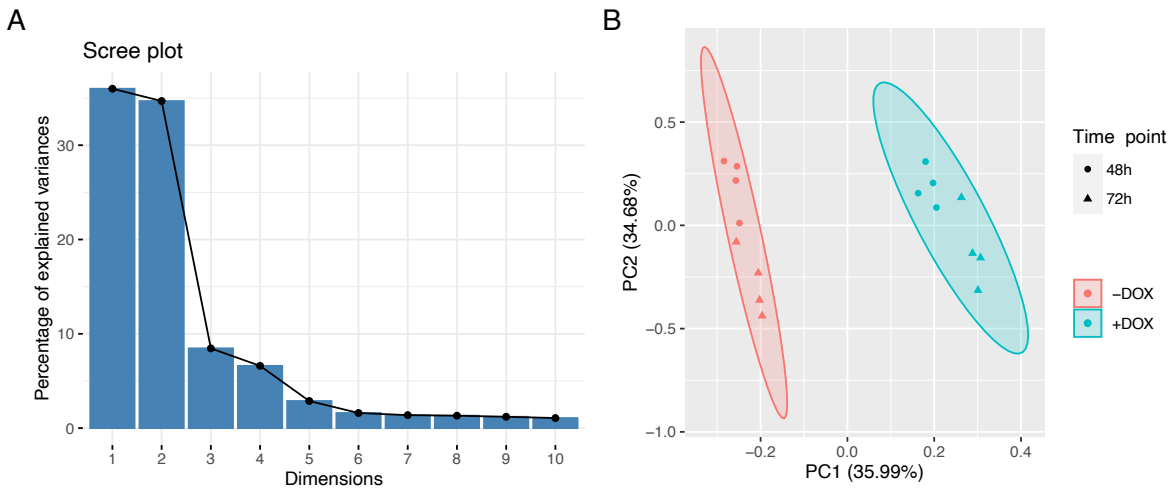

Figure 47: The principal component analysis of the transcriptome data upon *CTH* knockdown. (**A**) A Scree plot graphically representing the eigenvalues obtained from a PCA of *CTH* downregulation model at 48h and 72h after knockdown induction, used to identify the number of significant principal components (PCs) in the dataset. (**B**) Visualization of first two principal components showing that samples clustered based on CTH levels and time from knockdown induction.

Differential expression analysis revealed that CTH downregulation caused strong transcriptional dysregulation as early as 48 hours after knockdown induction, with 253 differentially expressed genes (DEGs) observed at that time point. This dysregulation further progressed at 72 hours, leading to the identification of 403 DEGs (**Figure 48A, Supplementary Table 3**). These results suggest that CTH plays a significant role in transcriptional regulation and its downregulation leads to widespread changes in gene expression. Of note, *CTH* was one of the most differentially expressed genes, with nearly a 2-fold decrease at both time points (**Figure 48B**).

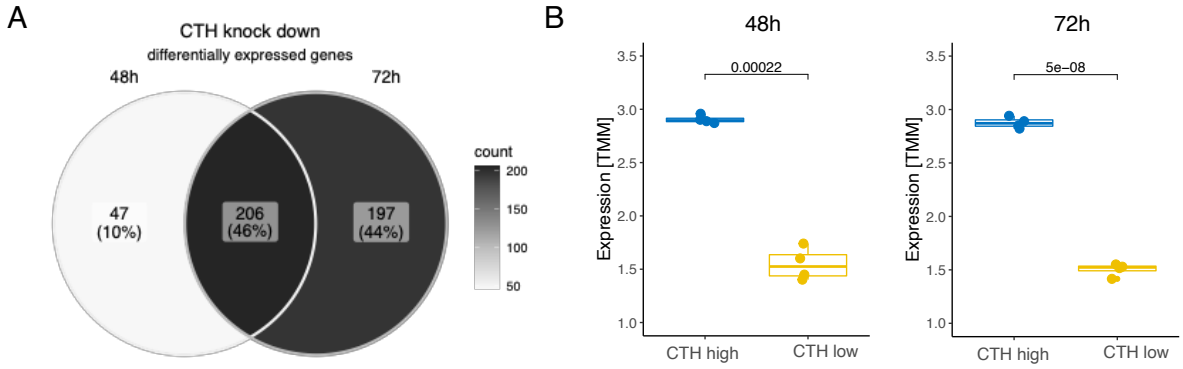

Figure 48: Overview of transcriptomic changes upon *CTH* knockdown. (**A**) Venn plot summarizing differentially expressed genes upon CTH downregulation at 48 h and 72 h after knockdown induction. (**B**) *CTH* expression levels at 48 h and 72 h after knockdown induction. n = 4, p-value was calculated using the Wilcoxon test.

Upon CTH downregulation, NB cells upregulated the expression of genes involved in cysteine uptake (*SLC7A11*) and recycling from glutathione (*ChaC Glutathione Specific Gamma-Glutamylcyclotransferase 1, CHAC1*), confirming that the transsulfuration pathway is an important source of cysteine in these cells (**Figure 49A, B**). Additionally, CTH inhibition led to downregulation of two mitochondrial genes: *Mitochondrial Fission Regulator 1* (*MTFR1*), which regulates mitochondrial organization and fission, and *Methylenetetrahydrofolate Dehydrogenase* (*NADP+ Dependent) 2* (*MTHFD2*), which is involved in *de novo* serine production. Downregulation of these mitochondrial genes could be a sign of mitochondrial dysfunction caused by CTH downregulation (**Figure 49A**).

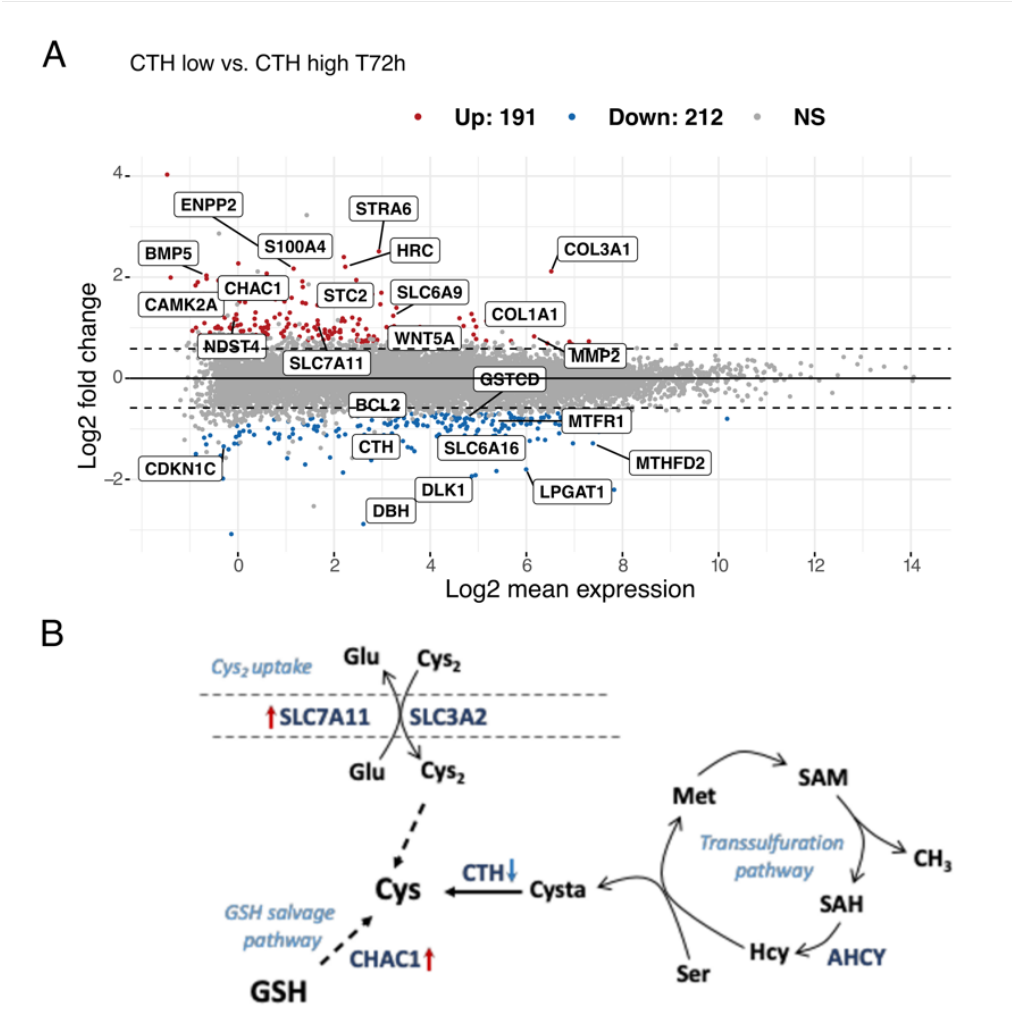

Figure 49: Differentially expressed genes upon *CTH* knockdown.
(**A**) Volcano plot showing differentially expressed genes between CTH low and high cells. Red points represent significantly upregulated genes, while blue points represent significantly downregulated genes. Only a selection of genes have been labeled. NS – not significant. (**B**) Schematic representation of changes induced by CTH downregulation: induction of cystine uptake (SLC7A11) and recycling from GSH (CHAC1). Blue arrow – genes downregulated upon *CTH* knockdown, red arrow – genes upregulated upon *CTH* knockdown.

Results

Gene set enrichment analysis (GSEA) showed that *CTH* knockdown induced epithelial (or in this case adrenergic) to mesenchymal transition, hypoxia, and affected the cell cycle by reducing the expression of genes involved in the G2M checkpoint and E2F target genes (**Figure 50A, Supplementary Table 4, Supplementary Figure 7**).

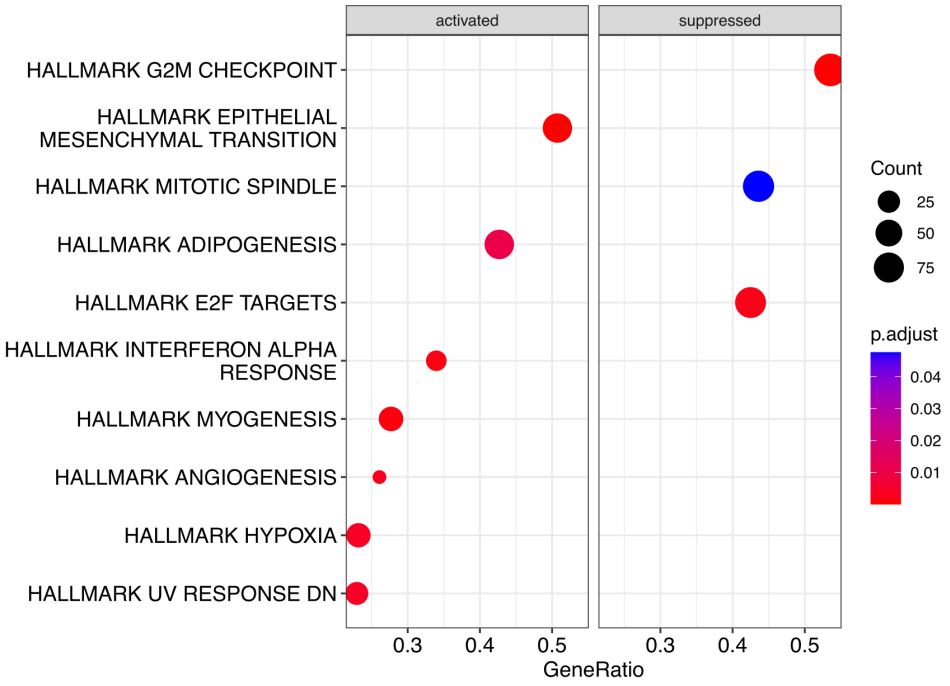

Figure 50: Gene set enrichment analysis highlighting pathways dysregulated upon *CTH* knockdown.
GSEA analysis of DEG upon CTH knockdown was performed using the Hallmark gene set from the Human MSigDB Collections (Liberzon et al., 2015)

To investigate the transcriptomic changes observed upon *CTH* knockdown, a transcriptomic profiling of IMR-5-75 cell line with inducible adenosylhomocysteinase (*AHCY*) knockdown was performed. AHCY is an enzyme that plays a crucial role in methionine cycle by breaking down S-adenosylhomocysteine (SAH) (**Figure 50B**), a potent inhibitor of methyltransferases activity and a by-product of many cellular processes (Turner et al., 1998). AHCY's activity is thought to be regulated by its precise subcellular localization, which helps facilitate local transmethylation reactions and control levels of SAH (Vizan et al., 2021). AHCY is a key player in the one-carbon metabolic cycle, a fundamental metabolic pathway that facilitates the transfer of one-carbon units for a variety of essential cellular processes. These processes include biosynthesis of important molecules such as purines and thymidine, maintenance of

amino acid levels (cysteine, serine, and methionine), regulation of cellular redox balance, and modulation of epigenetic mechanisms (Ducker & Rabinowitz, 2017). The shRNA-mediated *AHCY* knockdown led to ~ 50% reduction of AHCY protein level (**Figure 51A**). The GSEA analysis performed on differentially expressed genes upon AHCY downregulation (**Supplementary Table 5)** showed not only cell cycle dysregulation, but also downregulated MYCN activity and the mTOR signaling pathway (**Figure 51B, Supplementary Table 6, Supplementary Figure 8**).

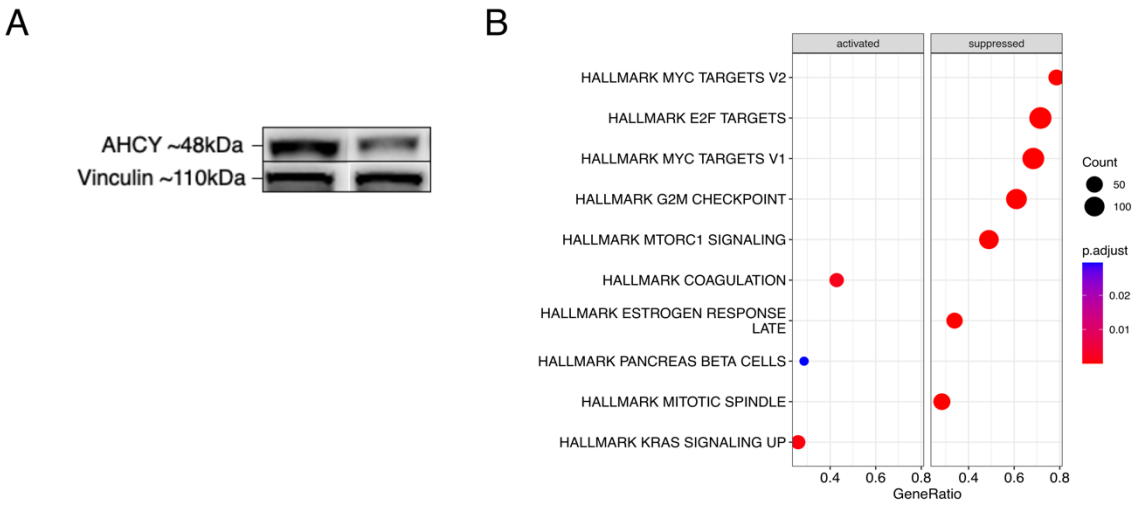

Figure 51: Analysis of transcriptomic changes upon *AHCY* downregulation.
(**A**) Western blot analysis of doxycycline-induced shRNA-mediated *AHCY* knockdown model in IMR-5-75 NB cells. Vinculin was used as a loading control. (**B**) GSEA highlighting pathways dysregulated upon AHCY knockdown. The analysis of DEG upon AHCY knockdown was performed using the Hallmark gene set from the Human MSigDB Collections (Liberzon et al., 2015)

To examine if the expression pattern observed upon *CTH* knockdown is related to cellular identity, the CTH knockdown score derived from transcriptomic profiling was calculated for NB cell lines using the same approach as for estimating MYC(N) activity scores (**Supplementary Figure 9A, C, E**) (see Section 6.1.1.). Comparison of the cell identity type and the obtained CTH knockdown scores revealed that the mesenchymal cell lines exhibited similar expression pattern as NB cells with downregulated CTH levels (**Figure 52A**). In addition, the *MYCN*-amplified cell lines were characterized by much lower CTH knockdown score, indicating that the transsulfuration pathway is more active in these cells (**Figure 52B**).

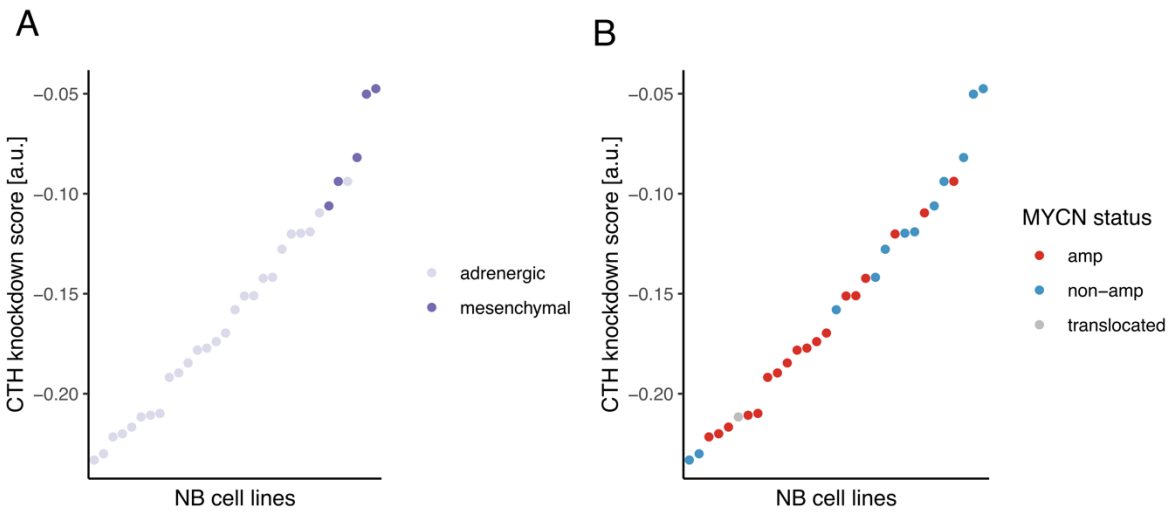

Figure 52: Overview of CTH knockdown score in the panel of NB cell lines.
The relationship between CTH activity and (**A**) cell identity and (**B**) MYCN has been depicted. Cell lines are color-coded according to (**A**) cell identity and (**B**) MYCN status as indicated in the legend.

The CTH knockdown scores were also calculated for previously mentioned 600 NB primary tumors (**Supplementary Figure 9B, D, F)**. Tumors with high MYC(N) activity scores had lower CTH knockdown scores (**Figure 53**), indicating that these cells much more rely on CTH activity and thus *de novo* cystine synthesis, which confirms the results obtained for NB cell lines.

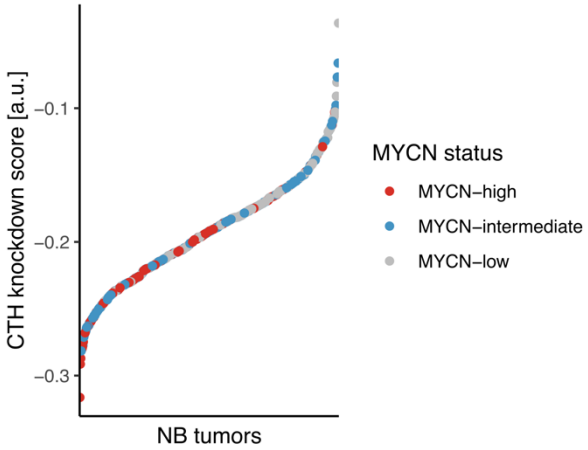

Figure 53: Overview of CTH knockdown score across NB tumors.
The association of CTH knockdown signature and MYCN status of NB tumors is shown. Samples are color-coded as described in the legend.

These results strongly suggest that CTH metabolic activity, in contrast to AHCY transcriptional regulatory effect, is necessary for maintaining the noradrenergic cell identity of NB *MYCN*-amplified cells, which may be related to its role in maintaining cysteine levels or producing the H_2S signaling molecule. However, further experiments are needed to fully characterize the role of CTH in these processes.

6.2.2.2. ^{34}S-methionine as a source for glutathione synthesis

To additionally validate the contribution of transsulfuration pathway into cysteine metabolism, a stable isotope tracing experiments using ^{34}S-methionine were performed.

Stable isotope tracers are commonly used to evaluate interconversions of metabolites within the metabolic network. By measuring the shift in the natural isotopic abundance, the degree of label incorporation into specific metabolites can be quantified. This mass shift can be detected using mass spectrometry (MS) techniques, which allow for the precise measurement of the mass-to-charge ratio of ions in a sample.

To assess whether *MYCN*-amplified NBs can redirect intermediates of the methionine cycle towards glutathione synthesis, IMR-5-75 cells were treated with stably labeled ^{34}S-methionine for 24 hours. If the naturally occurring ^{32}S is exchanged for labeled ^{34}S-methionine, a mass shift of 2 Da between differentially labeled metabolites should be observed in the mass spectra, resulting in an increased intensity of the M+2 peak.

The relative isotope abundance in natural glutathione spectra was distributed in the ratio 100 / 25.05/ **8.77** / **1.49**, corresponding to mass-to-charge (m/z) values 498.2 / 499.2 / 500.2 / 501.2 (**Figure 54A**). The substitution of methionine containing a "light" sulfur atom with one carrying a "heavy" atom in the growth media caused a shift in the isotope ratio distribution to 100 / 25.08 / **18.11** / **3.69** (M+2; **Figure 54B**), indicating that methionine-derived ^{34}S was incorporated into GSH and supporting the role of the transsulfuration pathway as an additional source of cysteine that is used for GSH biosynthesis. However, when comparing the results obtained for labeled methionine-fed cells to the label incorporation derived from $^{13}C_6$-^{15}N-cystine, the latter showed a clear shift of the most abundant isotope to M+4 (m/z = 502.2), indicating that under normal conditions GSH biosynthesis mostly depends on cystine uptake (**Figure 54C**).

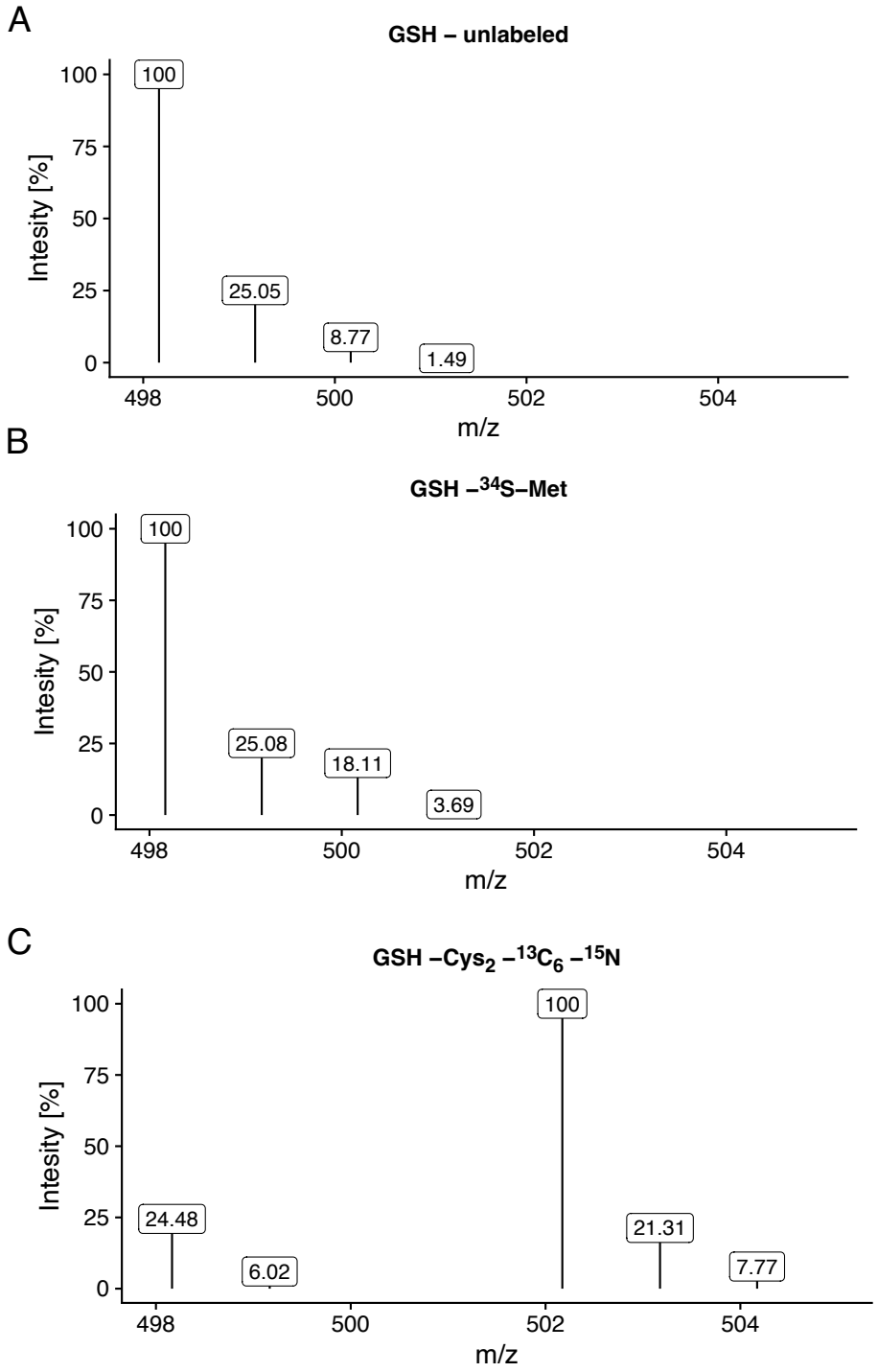

Figure 54: The shift in the distribution of relative isotope abundances in glutathione after supplying cells with labeled isotopes.
Glutathione composition derived from cells grown in the (**A**) standard growth medium, (**B**) medium supplemented with labeled methionine or (**C**), medium supplemented with labeled cysteine is shown. The relative abundance is presented as a percentage of the abundance of the certain isotope. The most abundant isotope is presented as 100%.

6.2.3. Neuroblastoma dependency on GPX4 activity

In terms of redox balance, imported cystine is used as a building block for intracellular glutathione, which serves as a cofactor for glutathione peroxidase 4 (GPX4), the main machinery to detoxify cells from lipid hydroperoxides, which otherwise would accumulate and lead to ferroptosis. To determine the importance of GPX4 activity for NB cells, their dependency on the *GPX4* gene was evaluated using the Cancer Dependency Map Portal (RRID:SCR_017655), containing the results from large-scale CRISPR and shRNA screens. These screens were performed to evaluate the impact of gene knockout/knockdown on cell growth and to determine the selectivity of this effect among different cell lines. Across a large cell lines panel which includes various pediatric and adult cancer entities, GPX4 was considered a strongly selective gene, having a growth-reducing effect only in a subset of cancer cell lines (**Figure 55**).

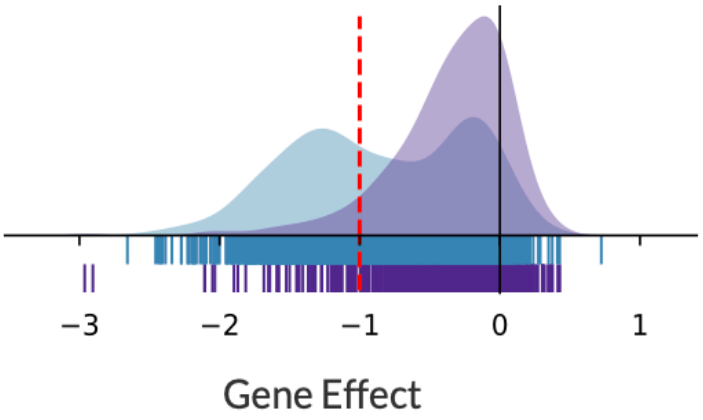

Figure 55: Cancer cell lines dependency on GPX4.
The graph represents the outcome from RNAi (in purple; Achilles + DRIVE + Marcotte, DEMETER2; 699 out of 1078 cell lines are dependent on GPX4) or Chronos (in blue; DepMap Public 22Q4+Score, Chronos; 171 out of 710 cell lines are dependent on GPX4). A lower score of a gene effect indicates a higher probability that the gene is dependent in a given cell line. A score = 0 means that the gene is not essential, whereas score = -1 reflects the median of all common essential genes. Figure adapter from DepMap portal (https://depmap.org/).

Focusing only on pediatric cancer entities, the dependency distribution revealed that most childhood tumors heavily rely on GPX4 activity, but when focusing only on NB cell lines, a bi-modal distribution of dependency was observed: some cell lines were highly dependent on GPX4 activity, while others showed much weaker dependence (**Figure 56A**). Furthermore, NB cell lines that were highly dependent on limiting cystine supply in the culturing medium (LS, SK-N-DZ, NGP) showed high dependency on

Results

GPX4 antioxidant activity, while cell lines resistant to cystine withdrawal (SIMA, SK-N-BE-2, IMR-32) were not affected by GPX4 knockdown (**Figure 56B**). In addition, the analysis also identified a subset of *MYCN*-amplified cell lines resistant to cystine depletion (NB1, Kelly, KP-N-YN) from the growth medium that were dependent on GPX4, once more highlighting the heterogeneity of MYCN-driven tumors.

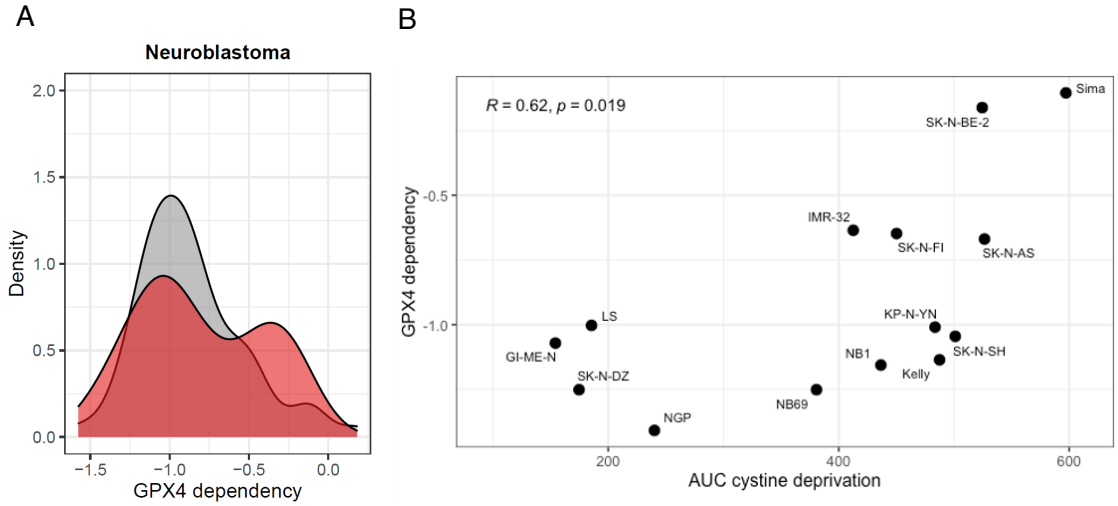

Figure 56: The bi-modal distribution of NB cell lines dependency on *GPX4*.
(**A**) Distribution of *GPX4* dependency of NB cell lines (in red) derived from DepMap database in comparison to other pediatric cancer entities: rhabdomyosarcoma, synovial sarcoma, osteosarcoma, medulloblastoma, malignant rhabdoid tumor, Ewing sarcoma and ATRT (in grey). (**B**) Pearson's correlation of GPX4 dependency to cystine-limitation sensitivity of NB cell lines (n = 14), *R* = 0.62, p-value = 0.019.

To assess the relevance of GPX4 for NB cell lines, an inducible short-hairpin RNA (shRNA)-mediated GPX4 knockdown model in the IMR-5-75 *MYCN*-amplified cell line was created. By addition of doxycycline to the growth medium, the protein level of GPX4 was reduced by ~90% which made it a very robust model to study GPX4 function (**Figure 57A**). Measurement of lipid peroxide levels in cells with high and low GPX4 levels using C11-BODIPY showed that GPX4 knockdown cells were much less capable of clearing lipid peroxides under normal (**Figure 57B**) conditions, however in the cystine-deprived setting this difference was much less pronounced (**Figure 57C**).

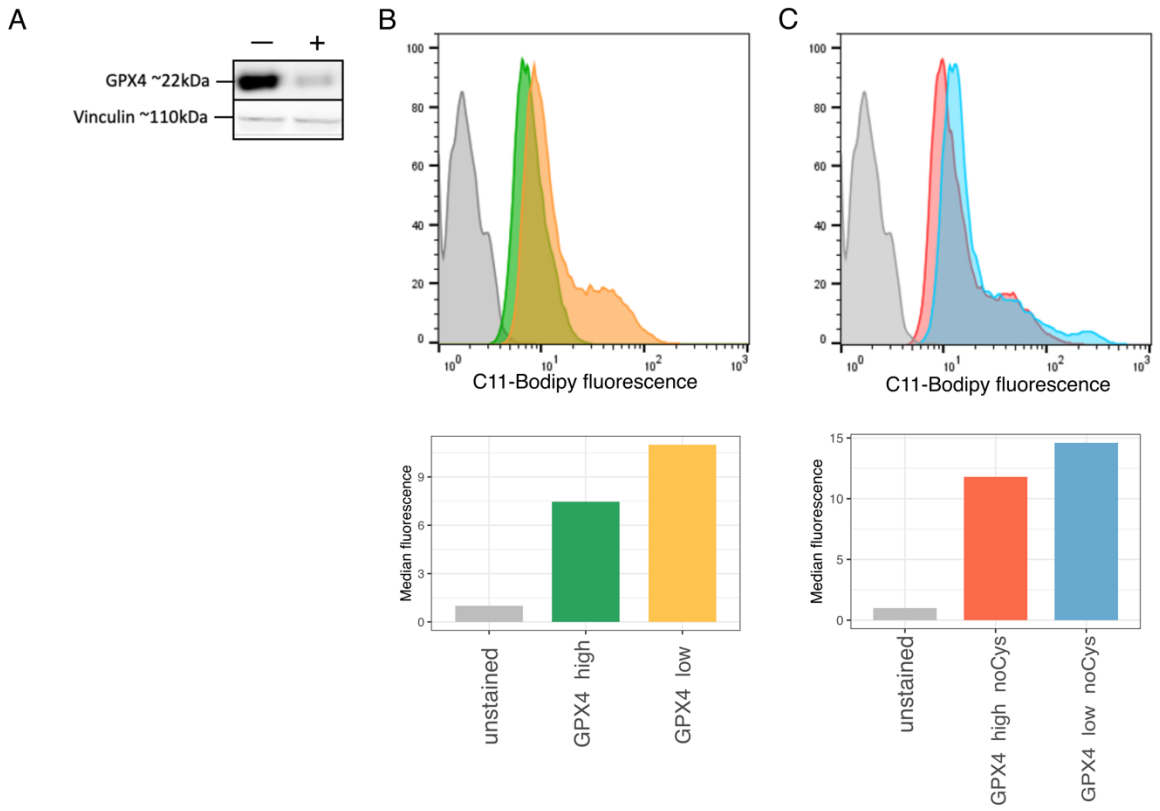

Figure 57: Estimation of lipid peroxidation upon *GPX4* knockdown.
(**A**) GPX4 protein level upon doxycycline inducible shRNA-mediated knockdown induction. "—"without doxycycline, "+"with doxycycline. Vinculin was used as a loading control. **B** and **C** Quantification of lipid peroxides accumulation upon GPX4 downregulation (grey – unstained control; green – GPX4 high; yellow – GPX4 low) at normal (**B**) and cystine-deprived (**C**) growth conditions (orange – GPX4 high, no cystine; blue – GPX4 low, no cystine).

Additionally, *GPX4* knockdown rendered cells highly sensitive to cystine deprivation from the growth medium (**Figure 58A**), highlighting the importance of GPX4 for NB survival. To further study the effect of *GPX4* knockdown on *MYCN*-amplified NB cells, two ferroptosis inducers were used, namely erastin and imidazole ketone erastin (IKE). IKE is an erastin analog with better pharmacokinetics and pharmacodynamics, potentially suitable for *in vivo* studies (Zhang et al., 2019). Treatment of *GPX4* knockdown cells with these type I FINs showed increased sensitivity of GPX4 low cells to ferroptosis induction (**Figure 58B, C**). In addition, cells showed increased sensitivity to sorafenib which potentially induce ferroptosis by blocking cystine uptake through inhibition of system x_c^- (**Figure 58D**). However, it has to be noted, that there are contradictory reports regarding sorafenib, as it primary functions as a protein kinase inhibitor and its role in ferroptosis execution is still under evaluation (Zheng et al., 2021). Furthermore, inhibiting the glutathione synthesis pathway using buthionine

sulfoximine (BSO), an analog of the glutamine synthetase that inhibit glutathione synthesis, in combination with low GPX4 levels caused massive cell death (**Figure 58E**), highlighting the importance of the GPX4 dependent lipid peroxide-detoxifying machinery for *MYCN*-amplified NB cells.

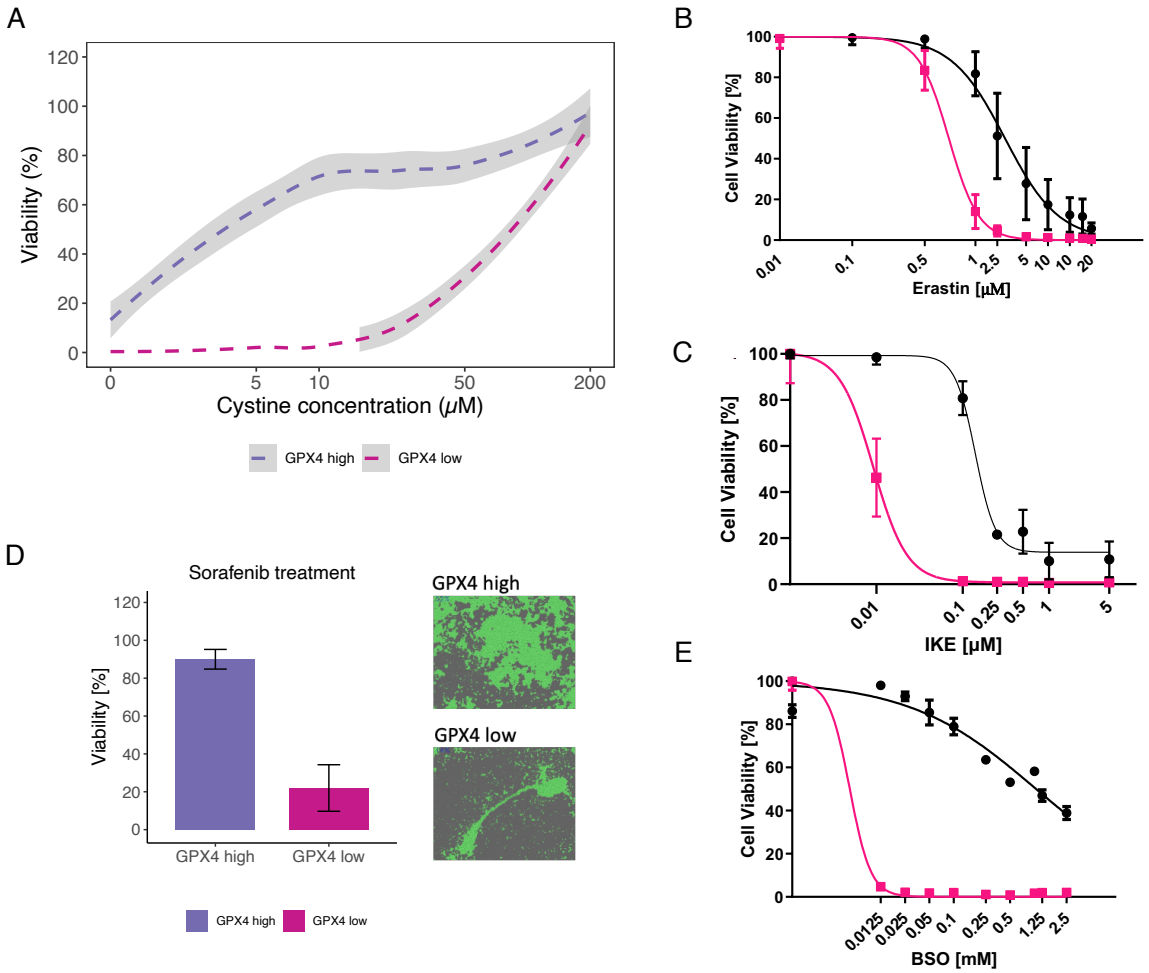

Figure 58: Sensitivity of *GPX4* knockdown cells to ferroptosis induction.
(**A**) Cystine titration experiments in IMR5/75 cells with doxycycline inducible shRNA mediated GPX4 downregulation (in gray variation of biological replicates are presented). CellTiter-Blue Viability Assay was used to assess cell response to the treatment. $n_{biol.rep} = 3$. (**B, C**) Titration of type I FINs (erastin (**B**) and IKE (**C**)) using GPX4 knockdown clones ($n_{biol.rep} = 3$). In black GPX4 high cells are represented, in pink GPX4 low cells. (**D**) Cell viability (left) and cell confluence (right) of GPX4 knockdown clones after treatment with 12.5 μM sorafenib ($n_{biol.rep} = 3$). (**E**) Inhibition of GSH synthesis pathway using BSO in GPX4 high and low cells ($n_{biol.rep} = 3$). In black GPX4 high cells are represented, in pink GPX4 low cells.

To gain a deeper understanding of the role of GPX4 in NB, a transcriptional profiling of the GPX4 knockdown model was performed. First, GPX4 protein levels at 24, 48 and 72 h after adding doxycycline to the growth medium was assessed using western blot analysis. Since approximately 85% downregulation of GPX4 protein levels was achieved at 72 hours, this time point was selected for RNA sequencing (**Figure 59**).

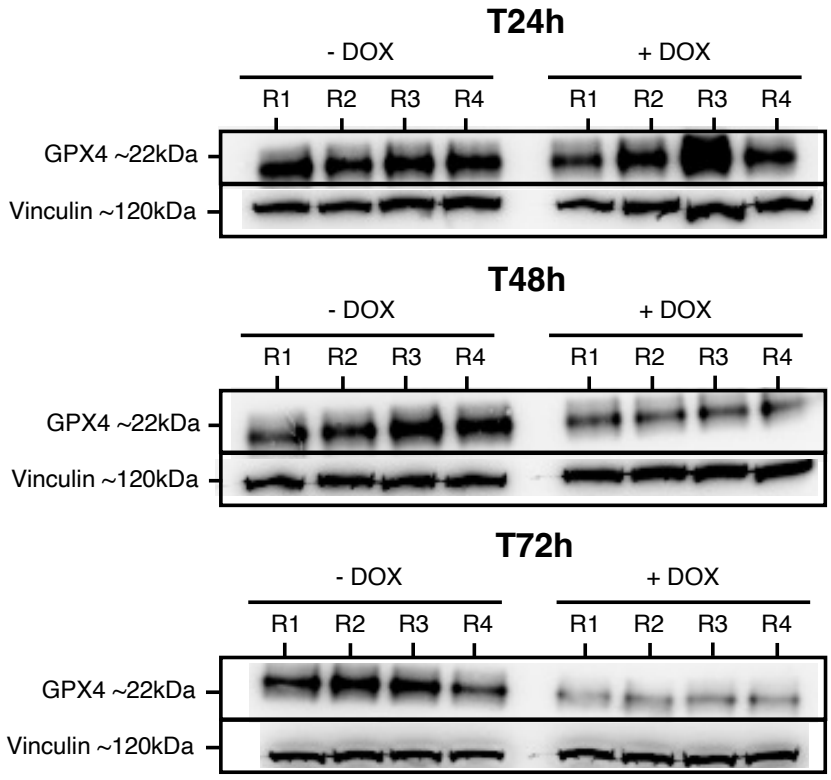

Figure 59: Quantification of GPX4 protein levels upon knockdown induction using western blot analysis.
GPX4 protein levels at 24, 48 and 72 h after addition of doxycycline to the growth medium are depicted. Vinculin was used as a loading control. R – replicate, – DOX = without doxycycline (high GPX4), +DOX = with doxycycline (low GPX4). $n_{biol.rep.} = 4$.

Comparison of the transcriptome profiles (n = 4) of cells with high and low GPX4 levels at 48h and 72 h showed that the significant difference in transcriptome regulation was only observed at 72 h (**Figure 60A**), thus this time point was considered for further analysis. Of note, *GPX4* was among the most differentially expressed genes at both time points, which confirms the efficiency of our model (**Figure 60B**).

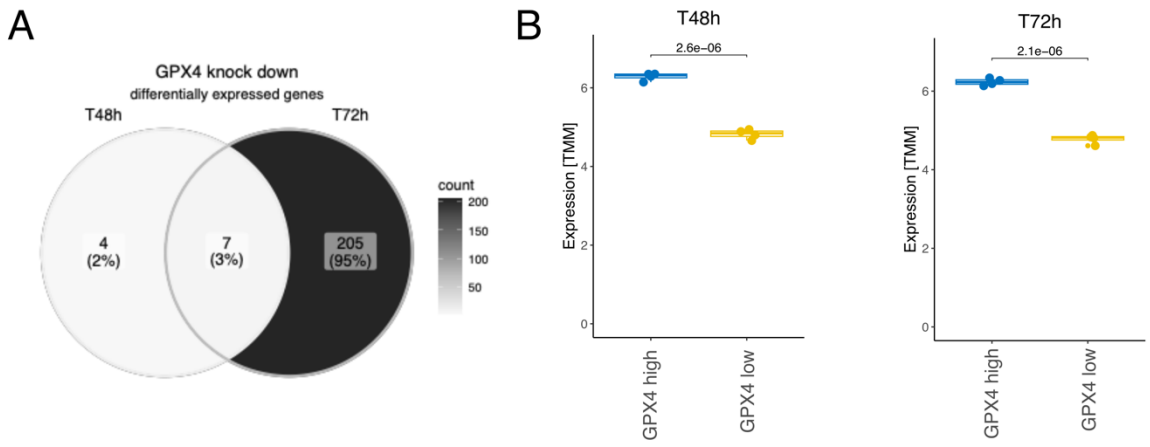

Figure 60: Overview of transcriptomic changes upon *GPX4* knockdown.
(**A**) Venn plot summarizing differentially expressed genes upon GPX4 downregulation at 48h and 72h after knockdown induction. (**B**) *GPX4* expression levels at 48h and 72h after knockdown induction. n = 4, p-value was calculated with Wilcoxon test.

The evaluation of the data revealed that GPX4 inhibition caused differential expression of 212 genes (48 upregulated and 164 downregulated genes) (**Figure 60A, Figure 61**). Among the most upregulated genes there were *ETV4* and *ETV5* transcription factors (**Figure 61**), which are specifically expressed in embryonic stem (ES) cells (Akagi et al., 2015), suggesting an induction of epithelial-to-mesenchymal (or in this case adrenergic to mesenchymal - AM) transition (EMT) upon GPX4 downregulation. Additionally, several p53 target genes were also upregulated (*IGFBP3*, *DUSP5*, *DUSP6*, *DKK1*), which, together with the downregulation of the nerve growth factor (*NGF*) and its receptor (*NGFR*), a negative p53 regulator (Zhou et al., 2016), indicates activation of tumor suppressor mechanisms upon *GPX4* knockdown.

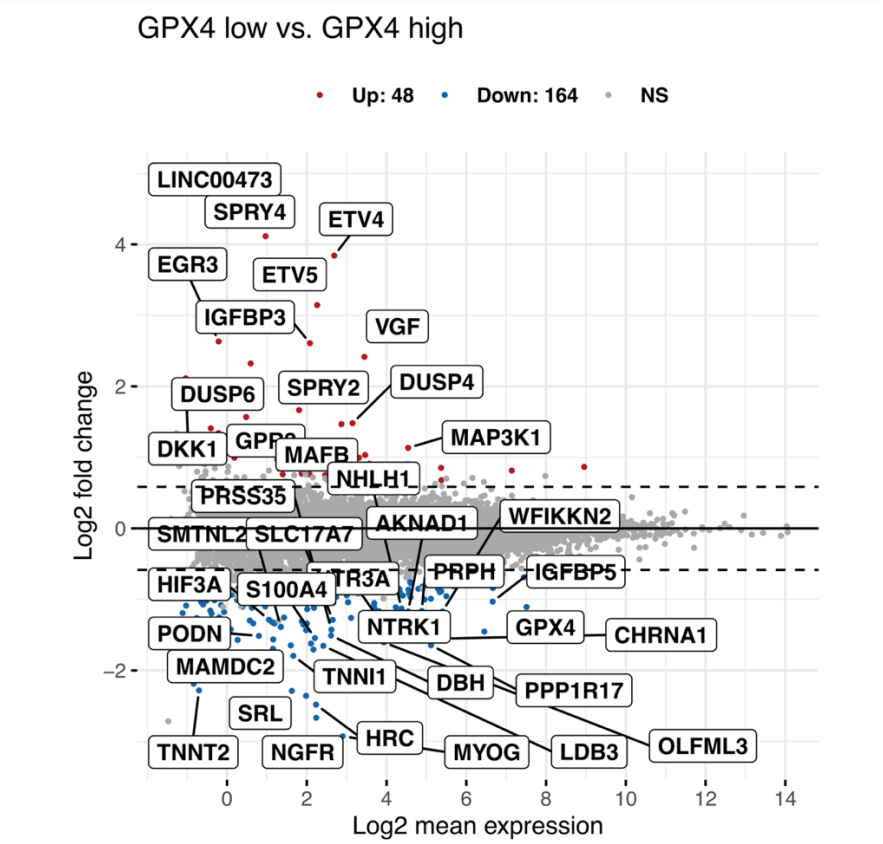

Figure 61: Differentially expressed genes upon *GPX4* knockdown.
Volcano plot illustrating differentially expressed genes upon *GPX4* knockdown. 48 genes were upregulated, and 164 genes were downregulated in GPX4 low cells. Red points represent significantly upregulated genes, while blue points represent significantly downregulated genes. Only a selection of genes have been labeled. NS – not significant.

To further investigate the data, GSEA was performed, which confirmed a significant upregulation of genes associated with adrenergic-to-mesenchymal transition (AMT) in GPX4 low cells (**Figure 62A, Supplementary Table 8, Supplementary Figure 10)**. To explore whether GPX4 downregulation correlates with more undifferentiated phenotype, the gene expression pattern following GPX4 downregulation (hereafter referred to as GPX4 knockdown signature) was calculated using the approach described in the Section 6.1.1 (**Supplementary Figure 11A, C, E**). The obtained signatures were then cross-referenced with the mesenchymal score of NB cell lines. The results of this analysis showed a significant similarity between the transcriptome profile of cell lines with a higher mesenchymal score and cells with low GPX4 levels (**Figure 62B**). This similarity ($R = 0.41$, $p = 0.01$) may indicate that the stress induced by GPX4 knockdown leads to NB cell de-differentiation.

Interestingly, activation of *MYC* target genes and KRAS signaling pathways was also observed upon GPX4 downregulation, however these findings require further investigation.

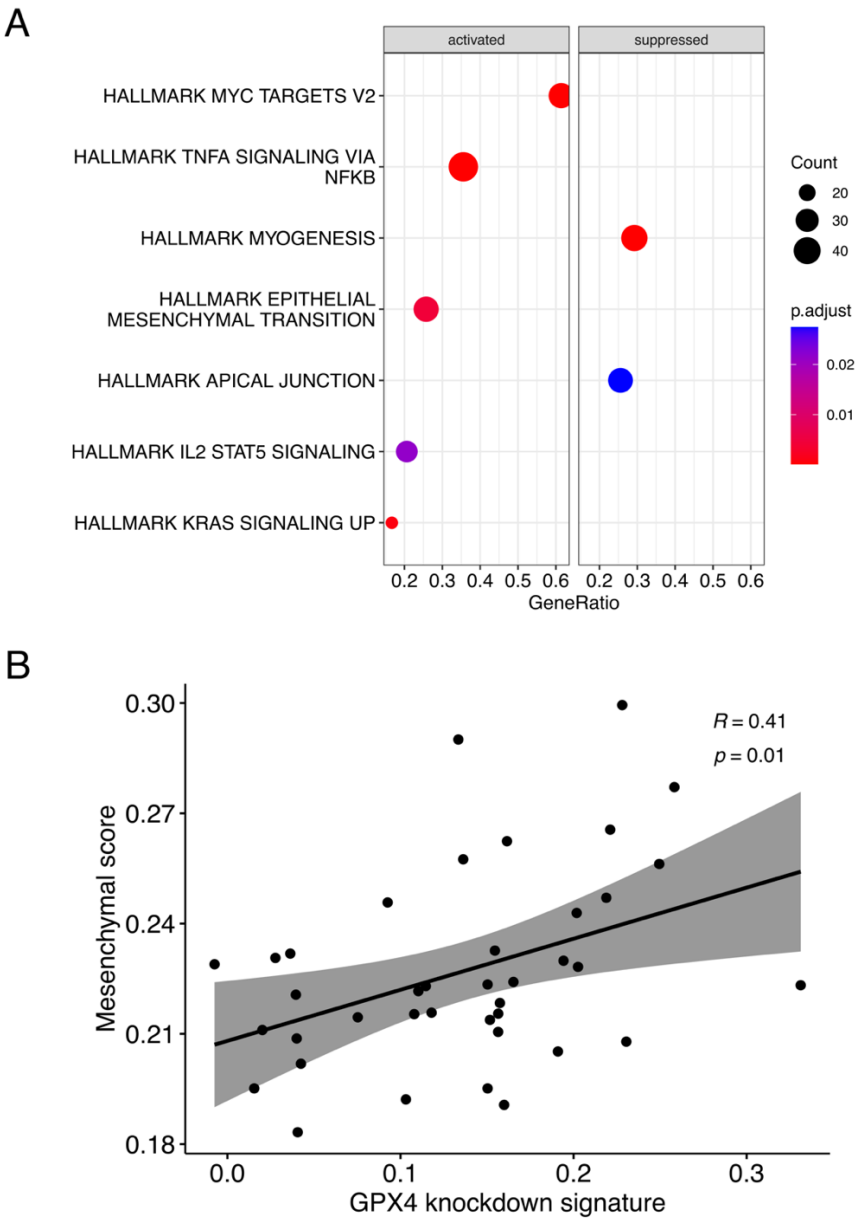

Figure 62: Characterization of GPX4 knockdown signature.
(**A**) GSEA highlighting pathways dysregulated upon GPX4 knockdown. GSEA analysis of DEG upon GPX4 knockdown was performed using the Hallmark gene set from the Human MSigDB Collections (Liberzon et al., 2015). (**B**) The link between GPX4 knockdown signature and cell line lineage state. The Pearson correlation coefficients (R) and p-values are reported in the top-right corner of the graph. 95% confidence intervals are represented in grey.

Furthermore, the study assessed the GPX4 activity in 600 primary NB tumors (**Supplementary Figure 11B, D, F**), revealing a noteworthy association between high-MYC(N) activity score and increased GPX4 knockdown signature in these tumors (**Figure 63**). These findings are consistent with prior research indicating that amplified *MYCN* triggers compensatory mechanisms, such as upregulation of GLS, CBS, GSR, GCLC, or GSS, to counteract insufficient GPX4 activity and cope with the elevated oxidative stress associated with MYCN-driven rapid proliferation (Alborzinia et al., 2022).

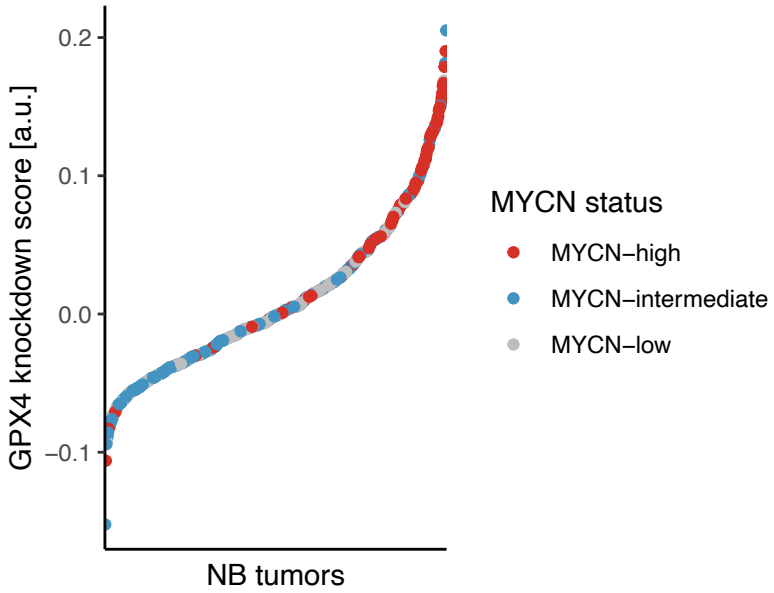

Figure 63: Overview of GPX4 knockdown score across NB tumors.
The association of GPX4 knockdown signature and MYCN status of 600 NB tumors is shown. Samples are color-coded as described in the legend.

6.2.4. Gene expression patterns as a novel way to estimate neuroblastoma sensitivity to ferroptosis induction

As described in the previous chapter, the known factors which are commonly used to classify NB could not fully predict the sensitivity to ferroptosis induction. In attempt to discover the underlying cause for this sensitivity, the comparison of the signatures obtained from the knockdown of the crucial players in ferroptosis and AUC values representing the sensitivity to the ferroptosis induction was performed. Cells that exhibited low GPX4 knockdown signature were further considered as GPX4-high cells, while cell lines with elevated GPX4 knockdown signature were considered GPX4-low

cells. Although the obtained results were not significant, the usage of GPX4 knockdown signature was much more accurate in predicting the cell lines' response to the ferroptosis induction than any of the other previously described factors (**Figure 64**).

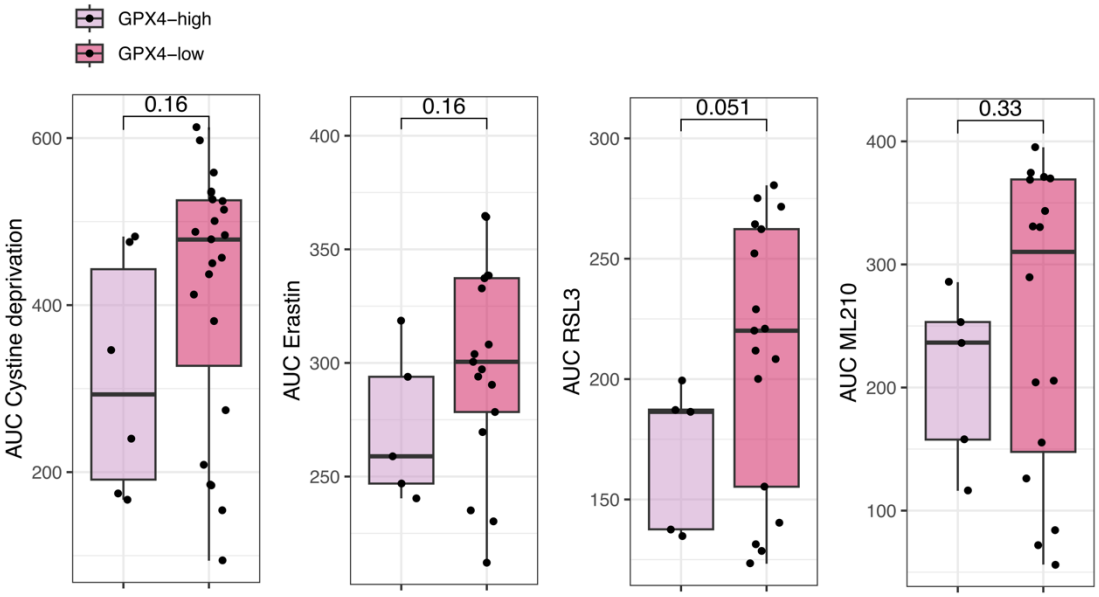

Figure 64: Assessment of the relationship between the GPX4 knockdown signature and the response to ferroptosis inducing agents.
Cell lines with high GPX4 knockdown signature (GPX4-low cells) were colored in dark pink ($n_{cystine}$ = 17, $n_{erastin}$ = 17 , n_{RSL3} = 17 = , n_{ML210} = 16) and these with the low score (GPX4-high) (n = 5) in light pink. P-values were calculated using an unpaired t-test.

In addition, the correlation between the GPX4 knockdown signature and sensitivity to ferroptosis type II inducers was investigated. Interestingly, for the majority of the cell lines the calculated GPX4 knockdown signature could predict the sensitivity to ferroptosis induction (**Figure 65**), indicating that the calculated signature is a good predictive measure for ferroptosis sensitivity. However, there was a subset of cell lines (CHLA-15, GI-ME-N, KP-N-YN, NB1) which showed a high sensitivity to GPX4 inhibition and a high GPX4 knockdown signature. This result could not be explained by any other known genetic alterations, therefore further research is needed to explain the observed phenotype.

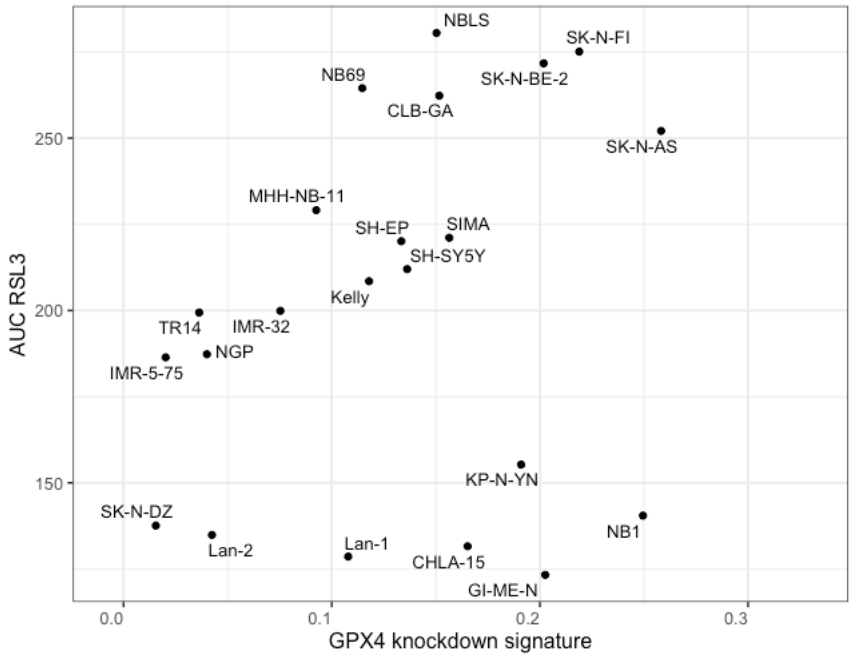

Figure 65: Association between the GPX4 knockdown signature and the response of NB cell lines to type II ferroptosis inducer, RSL3.
The GPX4 knockdown signature for all NB cell lines was calculated using the gene expression pattern obtained after GPX4 downregulation.

In the next step the CTH knockdown signature was evaluated as the prediction marker of the ferroptosis sensitivity. Cell lines that were characterized by decreased CTH knockdown signature were considered as CTH-high, while increased CTH knockdown score corresponded to CTH-low cells. The obtained results revealed that CTH knockdown signature significantly correlated with the cell lines' dependency on cystine availability in the medium (**Figure 66**), and this correlation was not observed for any other ferroptosis inducer. This finding suggests that cell lines exhibiting an active *de novo* cysteine synthesis pathway (adrenergic *MYCN*-amplified cell lines) are better equipped to effectively manage cystine depletion from the growth medium.

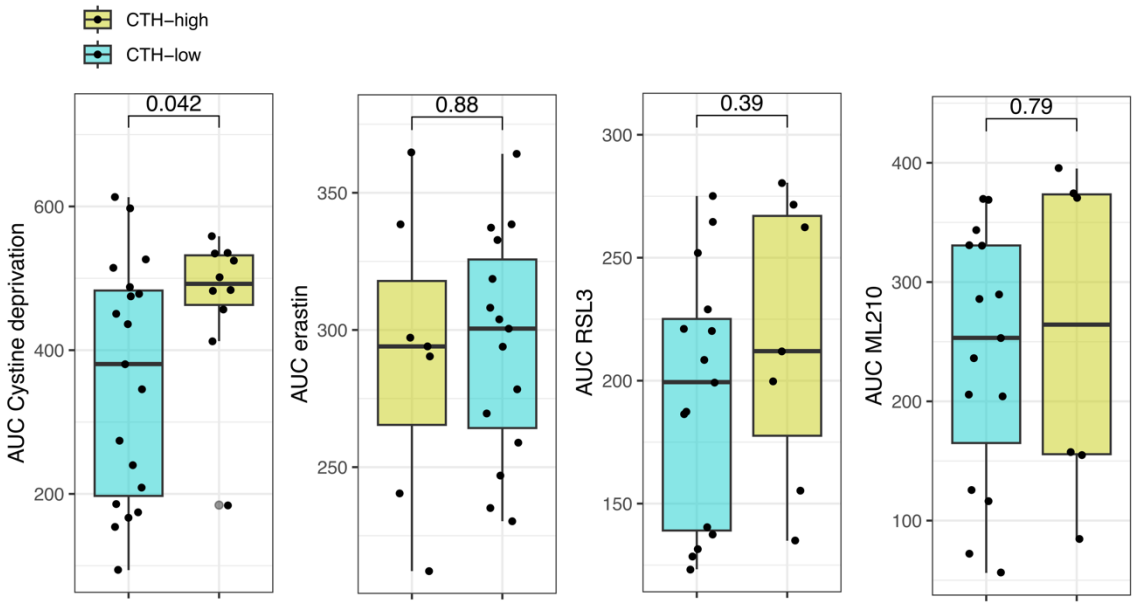

Figure 66: Relationship between the CTH knockdown signature and the response to ferroptosis inducing agents.
Cell lines with high CTH knockdown signature (CTH-low) were colored in blue ($n_{cystine}$ = 17, $n_{erastin}$ = 17, n_{RSL3} = 17, n_{ML210} = 16) and these with the low score (CTH-high) (n = 5) in green. P-values were calculated using an unpaired t-test.

Altogether, the obtained results suggest that utilization of expressions patterns, rather than singular gene expression, can improve the prediction of the cell lines' response to the ferroptosis induction. However, the sensitivity to the FINs could not be explained by CTH knockdown signature, highlighting the need of further research to unravel the basis of the observed sensitivity.

6.2.5. Summary II

In this chapter the response of NB cell lines to various ferroptotic stress stimuli was investigated. Transcriptome profiling of NB cells with high and low MYCN oncogenic background subjected to cystine depletion revealed an upregulation of the ATF4-related stress response, which was more prominent in *MYCN*-amplified cell lines. In contrast, *MYCN*-non-amplified cells exhibited increased cystine uptake, likely due to sufficient levels of glutamate available for exchange with cystine. In addition, decreased glutamate levels were observed in *MYCN*-amplified NB tumors, emphasizing the role of glutamate in thiol metabolism.

Furthermore, the role of the transsulfuration pathway in NB sensitivity to ferroptotic cell death was explored using shRNA mediated CTH downregulation. Decreased CTH

levels were linked to increased sensitivity to ferroptosis inducers and accumulation of toxic lipid peroxides. Transcriptome profiling revealed that CTH downregulation led to upregulation of cysteine uptake/restoration mechanisms and adrenergic-to-mesenchymal transition. In addition, stable isotope tracing experiments confirmed the involvement of methionine-derived cysteine in glutathione synthesis. Together, these findings highlight the importance of *in vivo* cysteine synthesis in NB development and ferroptosis regulation.

In addition, the role of GPX4 in NB cell lines has been studied using shRNA mediated knockdown cells. Treatment with ferroptosis inducers showed that GPX4 downregulation rendered NB cells more sensitive to ferroptosis induction. Moreover, transcriptomic profiling showed that GPX4 knockdown led to upregulation of genes involved in TNFA signaling pathway and AMT-transition. By estimation of GPX4 knockdown signature across NB cell line panel, the positive association between mesenchymal cell identity and GPX4 knockdown signature was observed, highlighting the role of GPX4 in maintaining the NB cell identity.

Moreover, to discover the underlying causes of sensitivity to ferroptosis induction in NB cells, the knockdown signatures of GPX4 and CTH calculated. The correlation between GPX4 knockdown signature and sensitivity to ferroptosis type II shown that the calculated GPX4 signature is a good predictive measure for ferroptosis sensitivity in most cell lines, except for a subset of cell lines that showed a high sensitivity to GPX4 inhibition and a high GPX4 knockdown signature. However, further research is needed to explain the phenotype of these cell lines.

Finally, the CTH knockdown signature as a prediction marker of ferroptosis sensitivity was also evaluated. The results suggested that cell lines exhibiting an active *de novo* cysteine synthesis pathway were better equipped to manage cystine depletion from the growth medium. However, the sensitivity to the ferroptosis inducer could not be explained by the CTH knockdown signature, indicating that this phenotype is strictly related to cystine metabolism.

6.3. Predicting neuroblastoma tumor response to ferroptosis therapy

In vitro findings can be very promising, but it is important to translate these discoveries into clinically relevant applications that can ultimately improve patient outcomes.
To determine which NB patients are most likely to benefit from ferroptosis induction therapy, a linear regression model was implemented to estimate the sensitivity of 600 NB tumors to ferroptosis inducers based on their gene expression profiles. To ensure the accuracy of the prediction analysis, the model was trained using gene expression data from cell lines with known responses to FINs (**Figure 67**).

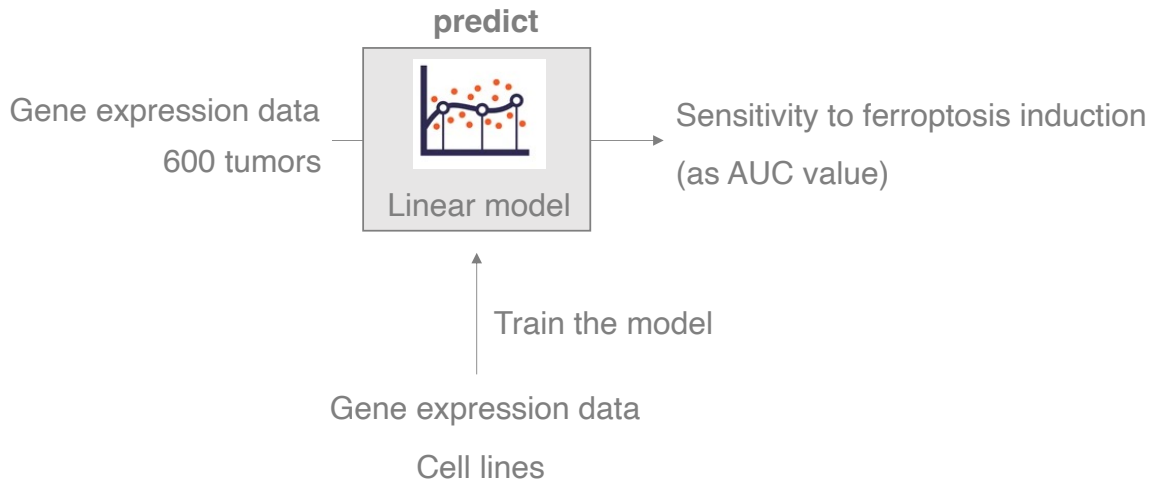

Figure 67: Schematic representation of the prediction analysis for 600 NB tumors.
A linear regression model was used to estimate the sensitivity of tumors to ferroptosis induction therapy. The model was trained using the gene expression dataset derived from cell lines, for which the sensitivity to FINs has been empirically acquired.

In the process of analyzing gene expression data from both cell lines and tumors, it is important to take into account potential differences in the data that may arise from their different sources. In this case, a principal component analysis of the cell line and tumor expression datasets revealed that the two datasets clustered separately based on their source, as expected (**Figure 68A**).

To address this issue, a statistical method called "limma batch correction" was applied to the data. This method is designed to adjust for systematic differences between datasets that may arise from factors such as differences in experimental conditions or measurement technologies. The application of limma batch correction resulted in a more uniform data distribution (**Figure 68B**). This correction allowed for a more accurate comparison of the gene expression profiles of cell lines and primary tumors,

as it helped to minimize the impact of differences in the datasets that were not related to the biology of the samples.

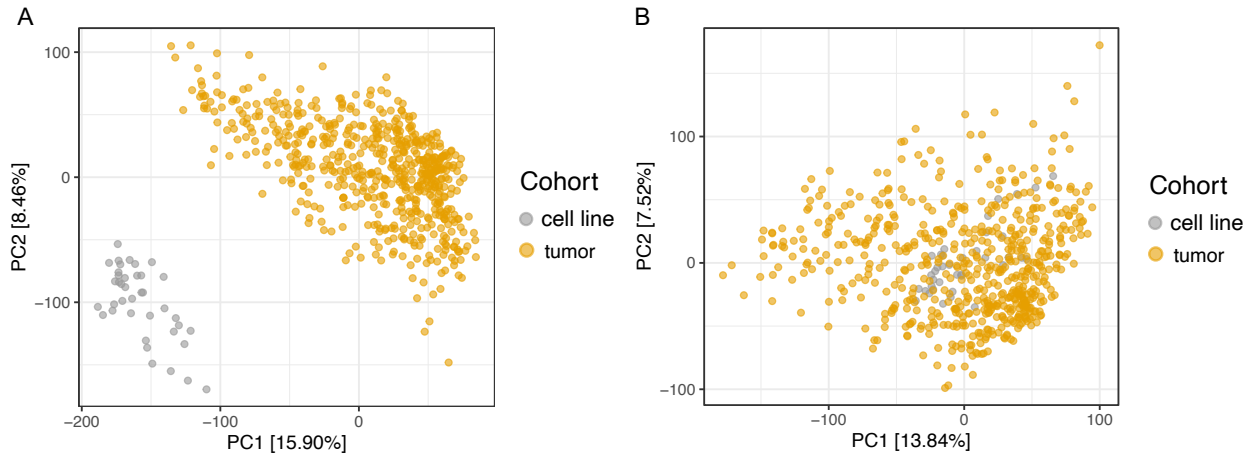

Figure 68: Principal component analysis plot representing cell lines and tumors expression data distribution before and after batch correction.
The first two components of PCA before (**A)** and after (**B**) limma batch correction are shown. Data points are color-coded based on their origin (grey – cell line, yellow – tumor.

To accurately predict the sensitivity of 600 NB tumors to FINs, a linear regression model for each drug was developed using the normalized expression data of NB cell lines ($n_{RSL3/Erastin}$ = 23, n_{ML210} = 21, n_{Cys} = 29). To prevent overfitting of the model, a ridge penalty was applied. A ridge penalty is a type of regularization technique used in linear regression to prevent overfitting by adding a penalty term to the cost function that is minimized during the training of the model.

To assess the performance of the models, a leave-one-out cross-validation method was used. In this method, the model is trained on all but one of the data points and then the model is used to predict the value of the left-out data point. This process is repeated for each data point in the dataset, and the performance of the model is evaluated based on how well it predicts the left-out data points. The correlation between predicted and experimentally obtained AUC values was statistically significant for all drugs except for models built using data from cystine titration experiments (**Figure 69**).

As a result, only the data that had a significant predictive power was used for further analysis. This means that for the cystine titration experiments, the models did not perform well enough to be used for further predictions.

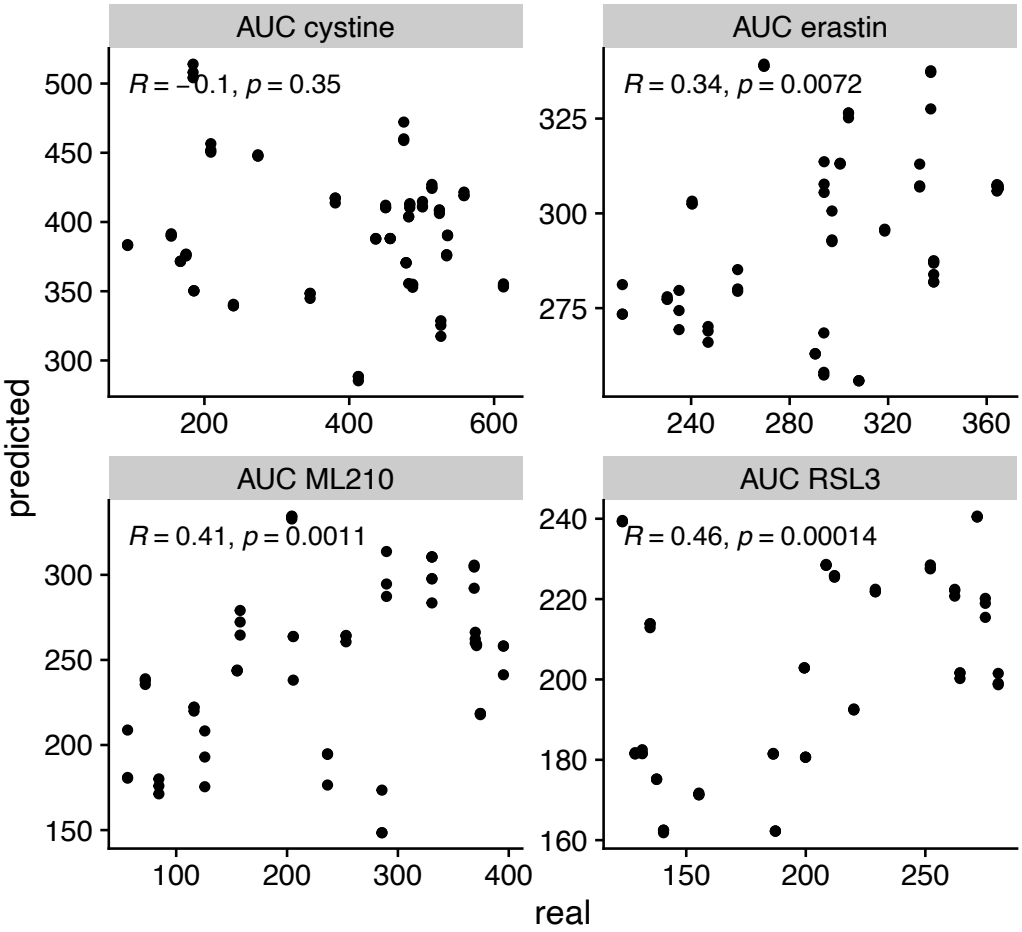

Figure 69: Evaluation of the performance of the model to predict the response to ferroptosis induction.
The learning algorithm was applied once for each cell line, using all other cell lines as a training set and the selected cell lines as a single-item test set. The Pearson correlation coefficients (R) and p-values are reported on top of the graphs.

After developing and evaluating linear regression models for each FIN, these models were then used to predict the sensitivity of 600 NB tumors to ferroptosis. To do this, a normalized expression dataset of the NB tumors was used as input for the models. Interestingly, *MYCN*-amplified tumors (n = 116) were predicted to have significantly smaller AUC values for each drug compared to tumors that lacked *MYCN* amplification (**Figure 70**). This result implies that *MYCN*-amplified tumors are more sensitive to ferroptosis induction compared to tumors without *MYCN* amplification.

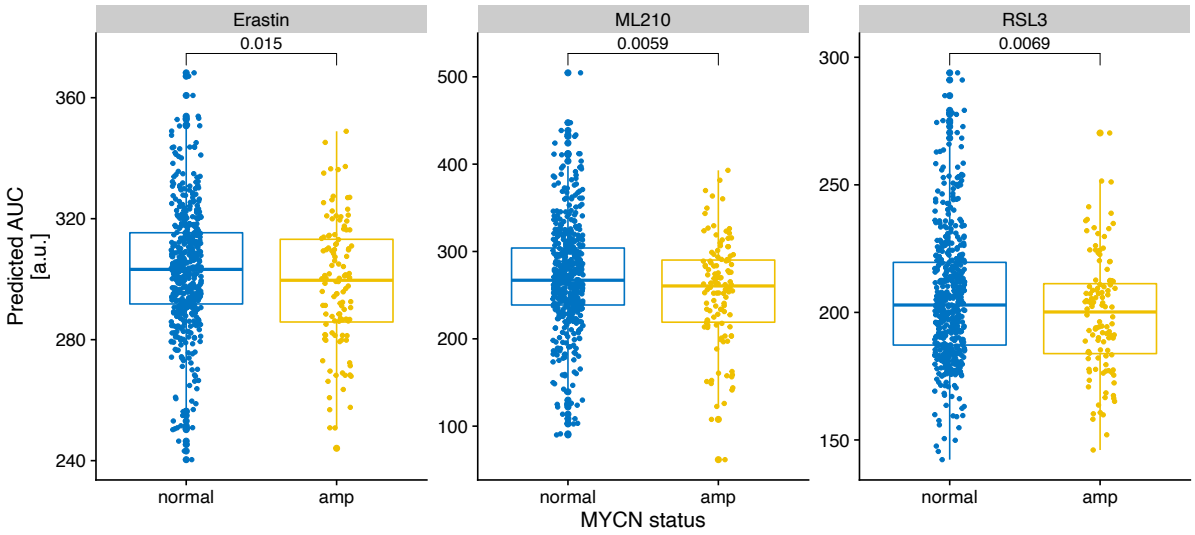

Figure 70: Predicted AUC values for 600 NB primary tumors.
Prediction analysis was performed using models train on data derived from CLs treatment with erastin, ML210 and RSL3 (amp – *MYCN*-amplified; normal – *MYCN*-non-amplified). p-value was calculated *using the* Wilcoxon test.

Next, to identify transcriptomic differences between tumors predicted to be sensitive or resistant to FINs treatment, the differential gene expression analysis was performed. However, the significant batch effect between the cell line and tumor data presented a challenge and could lead to noisy predictions. Therefore, the focus was laid on the extreme of the predictions (1st and 4th quartile) to reduce this noise (**Table 19**).

Table 19: Comparison of significance levels calculated for predicted AUC values between *MYCN*-amplified and non-amplified tumors.
P-values were calculated using all tumor samples (p-val - all) or focusing only on 150 most sensitive (lowest AUC values) vs. 150 most resistant tumors (highest AUC values) regardless of the MYCN-status (p-val 1st and 4th quartile).

	p-val (all)	p-val (1st & 4th quartile)
Erastin	0.0149	0.0095
ML210	0.0059	0.0019
RSL3	0.0069	0.0108

The results of this analysis showed that the sensitivity of NB tumors to ML210 was the most significantly associated with the *MYCN* status of the tumors. The analysis was performed by comparing the transcriptomic profiles of the tumors with the lowest AUC values (n = 150, sensitive to ferroptosis) to these with the highest AUC values (n = 150, resistant to ferroptosis) with respect to ML210. The aim was to identify the differential gene expression patterns that might account for the observed differences

in ferroptosis sensitivity. Differential expression analysis identified *MYCN* and its target genes (*TWIST1*, *ODC1*, *MDM4*, *LINC00839*) as some of the most differentially expressed genes, with higher expression observed in tumors predicted to be more sensitive to the treatment (**Figure 71A**). Furthermore, genes involved in serine/glycine metabolism (*PHGDH*, *PSAT1*, *GLDC*), cysteine and methionine metabolism (*CBS*, *DNMT1*, *DNMT3B*, *MTHFD2*, *EZH2*), and transmembrane transport (*SLC38A5*, *SLC6A11*, *SLCO4A1*, *SLCO5A1*, *SLC30A3*) were significantly upregulated in these tumors, suggesting that MYCN-related metabolic changes may make tumors more vulnerable to ferroptotic cell death.Interestingly, ML210-resistant tumors displayed increased expression of anti-ferroptotic genes related to CoQ_{10} (*AIFM2/FSP1*, *GCH1*), iron homeostasis (*FTH1*, *SLC11A1*, *SLC25A37*), or redox state (*CYB561*, *GPX3*). These genes may provide resistance to ferroptosis induction by counteracting the accumulation of lipid peroxides or depletion of GSH levels in response to GPX4 inhibition. Overall, the results suggest that *MYCN* amplification and MYCN-regulated metabolic changes may play a crucial role in determining the sensitivity of NB tumors to ferroptosis induction.

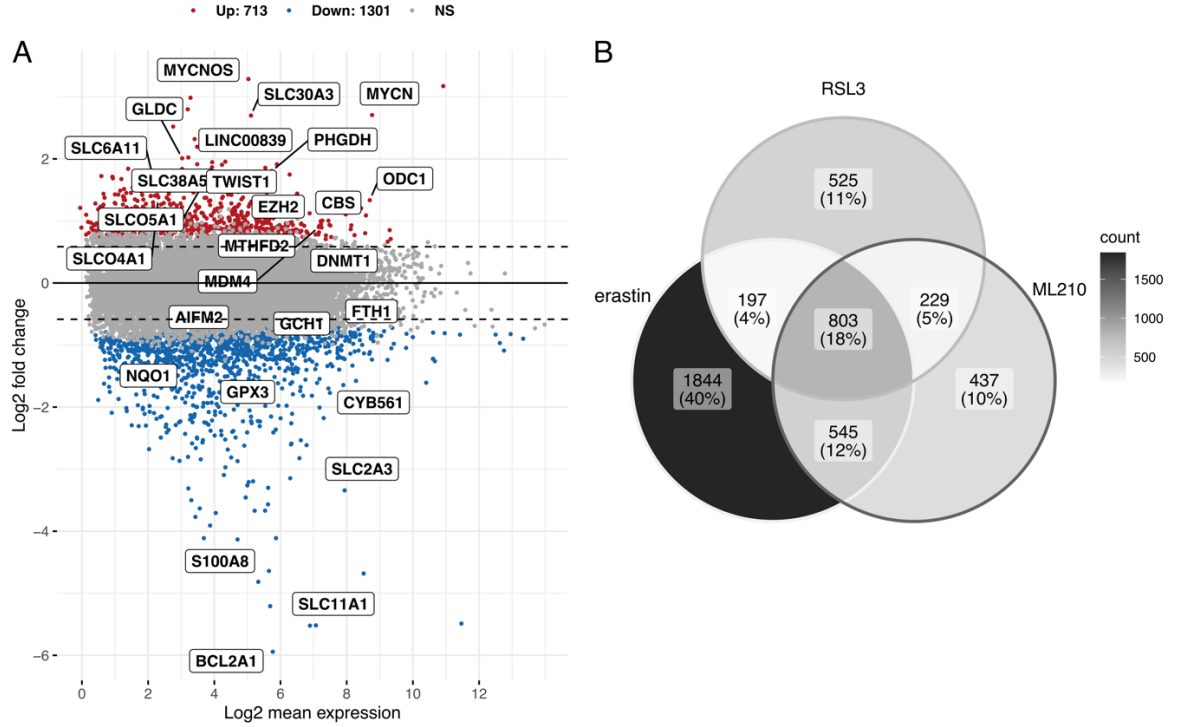

Figure 71: Results of differential gene expression analysis between ferroptosis-sensitive and ferroptosis-resistant tumors.
(**A**) Volcano plot summarizing the results of the differential gene expression analysis performed between 150 most-sensitive and 150 most-resistant tumors predicted using data obtained for ML210. In red genes expressed significantly higher in most-sensitive tumors are indicated, in blue these expressed higher in most-resistant tumors. Only selected genes are labeled. NS – not significant. (**B**) Venn plot representing the results of DE analysis using predicted data obtained for each drug.

To refine the results obtained for ML210, differential gene expression analysis was performed in a similar manner for RSL3 and erastin, and the outcomes were integrated to select only the most robust gene signature. The analysis revealed that 803 DEGs (18%) were common to all treatments, with 140 genes upregulated in sensitive tumors and 663 genes upregulated in resistant ones (**Figure 71B**). While *MYCN* remained the most differentially expressed gene associated with FINs sensitivity, several genes identified as ferroptosis inhibitors were preferentially expressed in resistant tumors, such as *NQO1*, *AIFM2*, *MGST2*, *GPX3*, *CYB561*, *FTH1*, *SLC2A3*, *S100A8*, and *AKR1C3*.

It has been reported that the decreased expression of NAD(P)H quinone dehydrogenase 1 (*NQO1*) was associated with increased sensitivity to ferroptosis induction (Bersuker et al., 2019). NQO1 is a known ferroptosis inhibitor that plays a key role in regulating the redox balance in cells. Additionally, the expression patterns

of the aldosterone reductase family (AKR1) members have been linked to ferroptosis sensitivity (Dixon et al., 2014; Gagliardi et al., 2019). This family of enzymes plays a key role in reducing the end products of lipid peroxides to their nontoxic alcohols, thus preventing their accumulation and the subsequent induction of ferroptosis. Moreover, the upregulation of ferritin heavy chain 1 (FTH1) has also been linked to ferroptosis insensitivity in hepatocellular carcinoma (Hu et al., 2021).

Further exploration of the identified pro- and anti-ferroptotic genes may lead to the development of new biomarkers for the ferroptosis sensitivity of NB tumors.

Overall, the findings of this study are highly significant in the field of cancer research, as they demonstrate the potential of machine learning approaches to predict the sensitivity of individual tumors to specific therapies. By analyzing the genetic and molecular characteristics of tumors, it may be possible to identify patients who are most likely to benefit from particular treatments, leading to improved outcomes for those with a wide range of cancers, including NB. The integration of gene expression data with machine learning algorithms can provide a comprehensive understanding of the underlying biological mechanisms that regulate ferroptosis and its role in cancer development.

6.4. Summary III

The final section of this thesis delved into exploring the sensitivity of 600 NB tumors to ferroptosis inducers which was estimated through the application of a linear regression model. The model was developed based on gene expression data from cell lines with known responses to ferroptosis inducers to ensure the accuracy of the prediction analysis. The study identified *MYCN*-amplified tumors as more sensitive to ferroptosis induction compared to tumors without amplified *MYCN*. *MYCN* and its target genes were found to be some of the most differentially expressed genes, with higher expression observed in tumors predicted to be more sensitive to ferroptosis treatment. In addition, genes involved in metabolic changes, such as serine/glycine metabolism, cysteine and methionine metabolism, and transmembrane transport, were significantly upregulated in these tumors.

This study provide insights into the molecular mechanisms underlying the sensitivity of NB tumors to ferroptosis inducers. This knowledge can help develop novel personalized treatment options for *MYCN*-amplified high-risk NB tumors. It also sheds light on the genes and metabolic pathways that contribute to the sensitivity of tumors to ferroptosis induction, which could be potential targets for therapeutic interventions.

Additionally, increased expression of anti-ferroptotic genes related to CoQ_{10}, iron homeostasis, or redox state was observed in ML210-resistant tumors, which counteracted the accumulation of lipid peroxides or depletion of GSH levels in response to GPX4 inhibition. This knowledge could be helpful in developing strategies to overcome resistance to ferroptosis inducers in tumors that show resistance to treatment.

Overall, this research offers a comprehensive analysis of the molecular mechanisms that determine the sensitivity of NB tumors to ferroptosis inducers, providing insight into potential targets for the development of personalized treatment options for high-risk tumors.

Finally, the regression analysis identified *MYCN* and its downstream targets as the most differentially expressed genes between tumors predicted to be sensitive or resistant to ferroptosis induction. This finding suggests that MYCN plays a critical role in regulating the sensitivity of NB tumors to ferroptosis, and that amplified *MYCN* may serve as a predictive biomarker for NB patients who are likely to benefit from ferroptosis-inducing therapies.

7 Discussion

Discussion

Childhood neuroblastoma shows high diversity in both its clinical characteristics and underlying biology. Patients with NB have a wide range of biological characteristics, which results in varying responses to the treatment. Despite significant progress in recent years, high-risk NB continues to have a poor prognosis and rapidly progresses, with only a 50% chance of survival over a 5- year period. This is primarily due to the low efficacy and high toxicity of current treatment strategies.

While various factors play a role in determining high-risk condition, MYCN status is widely recognized as the primary determinant in pathology diagnosis (Bartolucci et al., 2022). Even though amplified *MYCN* was the first genetic mechanism identified in NB (Brodeur, 2003; Brodeur et al., 1984), its precise role in causing the pathogenesis of the disease is not yet fully understood. In fact, amplified *MYCN* causes extensive changes in cancer cells, including the increased resistance to cell death, an undifferentiated state, evasion of the immune system, and altered metabolism.

In particular, MYCN-driven tumors heavily depend on glutamine for cancer growth and proliferation (Wahlstrom & Henriksson, 2015). MYCN also enhances the glycolysis and fatty acids uptake, which can result in mitochondria alteration (Tao et al., 2022). Furthermore, recent studies have established a novel link between MYCN and ferroptosis, an iron-dependent cell death caused by massive accumulation of toxic lipid peroxides (Alborzinia et al., 2022; Floros et al., 2021; Lu et al., 2021), disclosing a yet unknown metabolic vulnerability that can be exploited therapeutically.

7.1. Diverse response of neuroblastoma cell lines to ferroptosis inducers

In a recent study of our group, Alborzinia *et al.* has described the interplay between MYCN and cysteine metabolism, which levels where strongly reduced in high *MYCN* oncogenic background. By systematical depletion of individual amino acids from the growth medium, the authors established that *MYCN*-amplified cells showed strong dependency on cystine. Deprivation of cysteine caused a massive cell death, which could be largely prevented through downregulation of MYCN or the use of ferroptosis inhibitors (Alborzinia et al., 2022). Cystine can contribute to tumor development and

progression by maintaining redox homeostasis, either on its own or as part of the glutathione synthesis (Stipanuk et al., 2006). Additionally, cysteine metabolism can influence cellular metabolism through interactions with other metabolic pathways, including glucose and glutamine metabolism, as well as the pentose phosphate pathway (Combs & DeNicola, 2019; Koppula et al., 2017; X. Liu et al., 2020).

To understand the underlying cause of cystine addiction, titration experiments were conducted where the effect of varying levels of cystine on a wide range of NB cell lines viability was measured. The results revealed that the cell lines' response to cystine depletion from the growth medium is highly heterogenous, ranging from very sensitive to completely resistant phenotypes. Similar results were obtained when cell lines were treated with type I (erastin) and type II (RSL-3, ML210) FINs, further highlighting the complex nature of NB in the context of ferroptosis.

Surprisingly, the MYC(N) status (expressed as either *MYCN* amplification status or MYC(N) activity sore) did not significantly correlate with ferroptosis sensitivity as previously described (Alborzinia et al., 2022). Although a subset of *MYCN*-amplified cell lines (such as SK-N-DZ, IMR-5-75 or Lan-1) showed a high sensitivity to FINs, there were also cases of complete resistance within high-MYC(N) cell lines (such as SIMA, KP-N-YN or IMR-32). In addition, the observed variability in sensitivity was not directly linked to alterations in other genomic features relevant to NB biology (such as alteration in *TP53* or *ALK* pathways), indicating the involvement of other molecular mechanisms in ferroptosis regulation.

It has been suggested that the recently identified adrenergic and mesenchymal subtypes (van Groningen et al., 2017) may impact cysteine metabolism in NB cells (Alborzinia et al., 2022). To investigate the potential influence of cell identity on ferroptosis sensitivity, the mesenchymal scores of NB cell lines was correlated with cell lines' response to FINs. This analysis indicated a significant association between cell lineage state and ferroptosis sensitivity, with mesenchymal cells exhibiting greater resistance to ferroptosis induction. Alborzinia *et al.* proposed that differences in the regulation of cysteine metabolism between adrenergic and mesenchymal cell types could be responsible for this observed phenomenon. Their research indicated that

mesenchymal cells have higher levels of intracellular cysteine and glutathione due to the upregulated expression of *SLC7A11*, a cystine-glutamate antiporter, which is only expressed at low levels in *MYCN*-amplified adrenergic cells. Moreover, they also found that the transsulfuration pathway's *de novo* cysteine production is suppressed in mesenchymal cells, as opposed to *MYCN*-amplified adrenergic cells, suggesting that mesenchymal cells preferentially use the uptake mechanism to maintain sufficient cystine levels.

The observed differences in cysteine metabolism regulation between adrenergic and mesenchymal NB subtypes may also stem from the slower proliferation rate and stronger substrate adherence of mesenchymal cells, leading to lower production of ROS molecules which can trigger ferroptosis. However, the scarcity of mesenchymal NB tumors is reflected in the limited number of cell lines with this phenotype available for study. The development of new mesenchymal models could provide a more comprehensive understanding of the regulation of ferroptosis in these cell types.

7.2. Association of ferroptosis inducer susceptibility and CoQ_{10}-related pathway suppression

In recent years the significance of ferroptosis induction-based therapies has been increasingly recognized. These approaches include already existing chemotherapeutic drugs with potential to promote ferroptosis, such as sorafenib or artemisinin, as well as iron-based nanoparticles that have been developed more recently. These nanoparticles can deliver and release iron directly into cancer cells, effectively triggering ferroptosis (Nie et al., 2022). However, identification of patients who could potentially benefit from such treatment remains a major obstacle due to the insufficient number of biomarkers that could identify cancers susceptible to ferroptosis, especially among childhood tumors.

Thus, to uncover the genes that are strongly associated with ferroptosis in NB the drug sensitivity data obtained for *in vitro* models were correlated to base-line gene expression data derived from the same cell lines. By overlapping the results obtained for each ferroptosis inducer, a set of genes significantly associated with ferroptosis induction was identified.

Among the top-ranked genes lower expressed in ferroptosis sensitive cells were those involved in CoQ_{10} metabolic pathway, namely *FSP1* and *GCH1*. In fact, both genes have already been associated with ferroptosis. It was shown that FSP1 can counteract lipid peroxidation by restoring the levels of reduced CoQ_{10} (Doll et al., 2019), while GCH1 is a key regulator of *de novo* tetrahydrobiopterin (BH_4) synthesis, which was shown to induce CoQ_{10} upon oxidative stress (Kraft et al., 2020). What is more, the synthesis of BH_4/BH_2 can suppress ferroptosis through depletion of phospholipids containing two polyunsaturated fatty acid tails (Kraft et al., 2020). To validate the relevance of these findings *in vivo*, the expressions patterns of these genes were analyzed in the transcriptome data derived from a large cohort of NB tumors (n = 600). Interestingly, the expression of both genes was significantly lower in tumors with high MYC(N) activity score in comparison to tumors with low MYC(N) activity score. In addition, the elevated expression of another member of this pathway, namely *DHFR* which is responsible for BH_4 recycling, was identified in these *MYCN*-amplified tumors.

These results indicate that the simultaneous downregulation of the FSP1-CoQ_{10}-NAD(P)H and GCH1-BH_4-CoQ_{10} pathways in *MYCN*-amplified NBs could sensitize them to ferroptosis due to the decreased ability of these cells to maintain a redox balance. Moreover, the activation of different compensatory mechanisms to restore BH_4 levels highlights its importance for *MYCN*-amplified tumors biology. In addition, another member of the redox machinery was strongly correlated with ferroptosis inducers, namely CYB561. Similarly to previously described genes, its expression was significantly lower in *MYCN*-amplified NB tumors. These findings strongly suggest that disrupted redox homeostasis may endanger *MYCN*-amplified tumor cells to ferroptosis induction, creating a new treatment opportunity for NB patients. Finally, these findings also highlight the benefits of utilizing computational approaches to unravel biomarkers that could help tailoring patients' treatment.

7.3. A comprehensive overview of neuroblastoma response to ferroptotic stress

The primary objective of the first phase of this study was to evaluate the susceptibility of a repertoire of NB cell lines to ferroptosis induced by cystine deprivation and type I

or type II FINs. However, the exact determinants of ferroptosis sensitivity in this context remained unclear. To gain a more comprehensive understanding of the molecular mechanisms underlying ferroptosis in NB, transcriptome analysis of cells exposed to different ferroptotic stimuli was performed. At first, the transcription profiles of four NB cell lines with different sensitivity to ferroptosis induction subjected to cystine depletion were assessed. Based on the initial analysis, it was found that cells with amplified *MYCN* (IMR-5-75 and SK-N-DZ) were more vulnerable to stress caused by cystine starvation compared to cells without amplified *MYCN* (NBL-S and SK-N-FI). This was supported by the observation of a higher number of genes being differentially expressed in *MYCN*-amplified cells upon cystine depletion.

Upon further analysis of the transcriptomic data, it was found that the stress response activated by cystine deprivation was mediated through the activating transcription factor (ATF) gene family in all cell lines. However, it was found to be weaker and slower in ferroptosis-resistant cells. The ATF family plays a dual role in controlling the cellular response to stress (Wortel et al., 2017). On one hand, it inhibits translation by phosphorylating eukaryotic initiation factor 2 alpha (p-eIF2α), thereby preserving nutrients, reducing equivalents, and endoplasmic reticulum (ER) chaperones. This results in a temporary respite from metabolic, oxidative, and ER stress. On the other hand, to ensure the long-term survival, cells need to activate adaptive genes, which are controlled by transcription factors like ATF4. These genes play a crucial role in maintaining protein and redox homeostasis, amino acid transport, and metabolism (Harding et al., 2003; Novoa et al., 2003). However, excessive, and prolonged stress can cause ATF transcription factors to initiate cell-cycle arrest, senescence, or cell death. As a result, the upregulation of ATF transcription factors can have both positive and negative effects on the development and progression of tumors. On one side, it can help tumors to survive and proliferate, while on the other side, under certain circumstances, it may also sensitize tumors to therapy-induced cell death. For instance, in *MYCN*-amplified cell lines, cystine withdrawal led to extensive transcriptional disruption with upregulation of many genes that ultimately resulted in cell death. In contrast, *MYCN*-non-amplified cells were able to withstand stress and survive in nutrient-deprived conditions. These observations suggest that *MYCN*-

amplified cells are more susceptible to stress-induced cell death, while *MYCN*-non-amplified cells are better adapted to handle such stress.

7.3.1. MYCN-driven metabolic rearrangements

To further elucidate the origin of the differential stress regulation between *MYCN*-amplified and non-amplified NB cells, stable isotope tracing experiments were performed using two NB cell lines exhibiting different levels of MYCN. As previous studies (Alborzinia et al., 2022; Floros et al., 2021) and data obtained from this thesis suggest that cysteine metabolism is a crucial factor in the ferroptosis sensitivity of NB cell lines, the base-line thiols' levels were assessed first. Notably, *MYCN*-amplified IMR-5-75 cells had significantly reduced levels of cysteine and glutathione compared to *MYCN*-normal SK-N-FI cells. This may be due to increased thiol usage to maintain redox balance, which would be jeopardized by MYCN-accelerated proliferation. Alternatively, it could result from an inadequate mechanism for cysteine uptake, leaving these cells susceptible to ferroptosis. The comparison of labeled versus unlabeled cysteine in the cell lines revealed that SK-N-FI cells had a higher cysteine uptake efficiency, with over 90% of labeled cysteine, while IMR-5-75 cells had just around 50% of labeled cysteine. Nevertheless, both cell lines had similar levels of labeled cysteine incorporation into glutathione, highlighting that *MYCN*-amplified cells activated compensatory mechanisms, such as upregulation of *GCLC* expression, to efficiently channel cysteine into glutathione biosynthesis.

Cystine is transported into the cell in exchange for glutamate, therefore an alternative way to examine the functionality of the system x_c^- is to measure the levels of glutamate intra- and extra-cellularly. The levels of glutamate in the growth media of SK-N-FI cells rose over time, while at 24 hours, glutamate was barely present in the supernatant of IMR-5-75 cells. In addition, *MYCN*-amplified cells exhibited significantly lower intracellular glutamate levels that decreased over time, suggesting that alternative pathways that extensively rely on glutamate may be engaged in these cells, thereby reducing its availability for cystine exchange (Yi et al., 2019). It is noteworthy that further stable isotope labeling experiments using $^{13}C_5$-glutamine and $^{13}C_5$-glutamate showed that the absorbed glutamate did not contribute to either glutathione synthesis

or the TCA cycle. On the other hand, glutamine, via glutaminolysis, played a role in maintaining glutathione homeostasis and thus in preserving redox balance. To validate these findings *in vivo*, a metabolomic analysis of 20 patient-derived NB samples was performed. The results showed that *MYCN*-amplified tumors had significantly lower levels of glutamate and glutamine. The low glutamate levels determined in metabolomic analysis, combined with the previously reported low expression of *SLC7A11* (Alborzinia et al., 2022), could represent a potential vulnerability of *MYCN*-amplified NB that limits efficient cystine uptake and increases the risk of ferroptosis in rapidly proliferating cells.

7.4. Relevance of *de novo* cysteine synthesis pathway for *MYCN*-amplified neuroblastoma tumors

Malignant cells encounter various unfavorable circumstances of both intrinsic and extrinsic nature, including scarcities of oxygen and nutrients. As a consequence, they have evolved mechanisms to modify their metabolism and endure these conditions. In particular, the availability of cysteine within cancer cells can affect their metabolic fitness and their potential to develop resistance to therapy (Bonifacio et al., 2021). While cystine acquired from dietary intake constitutes the primary source of cellular cysteine (Bannai, 1986), it can also be obtained through other means, such as the breakdown of extracellular glutathione (Hanigan & Ricketts, 1993), protein catabolism (Davidson et al., 2017), or *de novo* synthesis from intermediates of methionine cycle, in the so called transsulfuration pathway (Mosharov et al., 2000; Sbodio et al., 2019). The transsulfuration pathway is important for maintaining cellular homeostasis, as it allows cells to produce cysteine when it is not available through other means (Sbodio et al., 2019). It also plays a role in the detoxification of harmful substances, such as heavy metals (Kaczor-Kaminska et al., 2020) and in the regulation of blood pressure. H_2S, the end product of the transsulfuration pathway, has various physiological functions, including the modulation of blood flow (Morales-Loredo et al., 2019), the regulation of smooth muscle tone (Hosoki et al., 1997), and the protection against oxidative stress (Xiao et al., 2018). Dysregulation of the transsulfuration pathway has been implicated in various diseases, including cancer, cardiovascular diseases and neurological disorders (Xiao et al., 2018). Alborzinia *et al.* recently reported that MYCN

upregulates the expression of key enzymes in the transsulfuration pathway, namely *CBS* and *AHCY*, in NB cell lines and primary tumors. In addition, in *MYCN*-amplified cells *CBS* expression is epigenetically regulated by the increased levels of activating histone marks (H3K27ac, H3K4me3), and decreased levels of silencing modifications in the gene locus (H3K27me3), highlighting the relevance of *de novo* cysteine production in MYCN-high NB (Alborzinia et al., 2022).

To investigate the relevance of the transsulfuration pathway in *MYCN*-amplified NB, stably labelled amino acids (cystine, methionine) tracing experiments were performed. The results of the experiments showed that cysteine derived from methionine accounted for approximately 10-15% of the total GSH in NB cells, while cystine uptake remained the primary source of cysteine for GSH synthesis in normal growth conditions, accounting for around 80% of total GSH.

Further experiments revealed that inhibition of transulfuration pathway through downregulation of cystathionine γ-lyase (CTH), the enzyme converting cystathionine to cysteine, increased NB dependency on cystine availability in the growth medium and led to elevated levels of lipid peroxides in low cystine conditions. Transcriptomic analysis of cells with regulated CTH levels showed that downregulation of the transsulfuration pathway upregulated the expression of genes involved in cysteine uptake (*SLC7A11*) and recycling from glutathione (*CHAC1*). These findings confirmed that the transsulfuration pathway is a significant source of cysteine in NB cells. In addition, the suppression of CTH resulted in a decreased expression of two mitochondrial genes (*MTFR1* and *MTHFD2*), which may indicate that downregulation of the methionine cycle leads to mitochondrial dysfunction. Additionally, in-depth analysis using GSEA uncovered that silencing CTH led to a shift from adrenergic to mesenchymal characteristics, as well as hypoxia, and disrupted the cell cycle by suppressing the expression of genes involved in the G2M checkpoint and those regulated by E2F. In contrast, inhibiting the transsulfuration pathway through AHCY knockdown not only resulted in cell cycle dysregulation, but it also decreased MYCN activity and mTOR signaling pathway. These findings strongly suggest that the metabolic activity of CTH is vital in preserving the noradrenergic cell identity in NB cell lines and may be linked to its role in maintaining cysteine levels and producing H_2S

signaling molecules. Nonetheless, further research is necessary to fully comprehend the precise role of CTH in these processes.

7.5. GPX4 detoxifying activity is crucial for a subset of high-risk neuroblastomas

Intracellular cysteine acts as the precursor for the production of hydrogen sulfide, taurine, and GSH - molecules known for their strong antioxidant properties. GSH, the prevailing antioxidant in mammalian cells, is composed of cysteine, glutamate, and glycine. Since intracellular cysteine concentration is by far in lower concentration range when compared to glutamate or glycine, cysteine is considered the limiting factor in the production of GSH (McBean, 2017).

By performing an unbiased genome wide MYCN synthetic lethal small interfering (siRNA) screen, Alborzinia *et al.* showed that genes involved in cysteine and GSH metabolism are crucial for *MYCN*-amplified cancer cell survival. Top hits of this screen included members of glutathione peroxidase family, namely *GPX4* and *GPX6*. Additionally, Lu *et al.* showed that *MYCN* amplification increased sensitivity of NB cell lines to GPX4 inhibition and high *GPX4* expression was linked with poor prognosis of NB patients (Lu et al., 2021). The selenoprotein GPX4 has been shown to be the primary control point for ferroptosis (Seibt et al., 2019). Its role as a master regulator of ferroptotic cell death is mostly related to the reduction of lipid hydroperoxides to their corresponding alcohols using GSH as its main cofactor (Seibt et al., 2019). Of note, GPX4 can also utilize other low molecular thiols or even protein thiols as substrates for preventing peroxidative chain reactions (Maiorino et al., 2018).

In this study, the reliance of NB cell lines on GPX4 detoxifying activity was further evaluated. Downregulation of GPX4 in a high *MYCN* oncogenic background led to accumulation of lipid peroxides and sensitized NB cells to ferroptosis inducing agents, which is consistent with previous reports (Floros et al., 2021; Lu et al., 2021). Transcriptome profiling of GPX4-low cells revealed an induction of adrenergic to mesenchymal transition upon GPX4 downregulation driven by *ETV4/5* transcription factors, specifically expressed in embryonic stem cells (Akagi et al., 2015). In fact, the loss of adrenergic characteristics upon GPX4 downregulation was confirmed in a

range of NB cell lines, as evidenced by the significantly increased GPX4 knockdown signature that was correlated with the heightened mesenchymal state of these cell lines. This similarity in gene expression suggests that the stress induced by GPX4 knockdown could be a contributing factor to the undifferentiated phenotype of NB cells. Additionally, GPX4 downregulation led to upregulation of several p53 target genes, which, alongside with downregulation of *NGFR* (Zhou et al., 2016), a p53 negative regulator, may indicate an activation of tumor suppressor mechanisms when GPX4 activity is not maintained.

In this study, the dependency data derived from DepMap database were also integrated (Behan et al., 2019; Tsherniak et al., 2017). The analysis revealed a bi-modal distribution of NB dependency on GPX4: a subset of cell lines showed a very strong dependency, while for others it was much weaker. In fact, *MYCN*-amplified cell lines, which were sensitive to cystine depletion, were also heavily depending on GPX4 activity, while cell lines resistant to cystine withdrawal were much less dependent on GPX4. These results indicate that only the subset of *MYCN*-amplified NB cell lines heavily rely on GPX4, and thus cysteine and GSH metabolism for tumor growth progression. Therefore, stratifying patients based on these factors appears to be critical for leveraging ferroptosis as a therapeutic strategy.

7.6. Enhancing the sensitivity prediction of neuroblastoma cell lines to ferroptosis induction through gene expression patterns

As demonstrated in this thesis, the previously identified factors contributing to NB biology were inadequate in predicting the sensitivity of NB cells to ferroptosis induction. To identify potential predictive markers, the knockdown signatures of key players in ferroptosis, namely CTH and GPX4 were compared with ferroptosis sensitivity values (AUCs). Despite lacking statistical significance, the knockdown signature of GPX4 has proven to be a more precise predictor of ferroptosis sensitivity than previously identified factors. Notably, the GPX4 knockdown signature showed strong correlation with sensitivity to ferroptosis type II inducers in most cell lines. However, the analysis also identified a subset of cell lines that displayed heightened sensitivity to GPX4 inhibition despite exhibiting a high GPX4 knockdown signature, but

to resolve this inconsistency, additional research is required. Furthermore, a notable association between the CTH knockdown signature and the cell lines' reliance on cystine availability in the medium was identified. This suggests that cell lines with an active *de novo* cysteine synthesis pathway are more adept at managing cystine depletion. However, the sensitivity to FINs could not be accounted for by the CTH knockdown signature, which indicates that this phenotype is exclusively linked to cystine metabolism.

Incorporating data obtained from functional characterization of crucial components of the ferroptosis mechanism has resulted in enhanced prediction of cell line sensitivity to this mode of cell death. Nevertheless, these findings also emphasize the need for additional functional data from diverse NB models. This is because the calculated signatures are solely based on transcriptome data obtained from a single cell line, and therefore may not be entirely predictive of the behavior of all cell lines. To enhance the accuracy of this approach, it would be beneficial to perform functional characterization of knockdown models from various parental cell lines. This would allow for the identification of a robust gene signature that can effectively identify both cell lines and tumors that could benefit from the induction of ferroptosis as a treatment strategy.

7.7. Linear regression model predicts *MYCN*-amplified neuroblastoma tumors to be more susceptible to ferroptosis induction

Profiling the cancer cell lines in context to their sensitivity to drugs gives an important insight not only into drugs mechanism of action and their potential for treatment, but also for selecting target group for development of personalized therapies. The primary objective of these studies is to translate *in vitro* findings into real-world cancer treatment and improve patient care. Several reports have demonstrated the effectiveness of this approach in enhancing preclinical drug testing and optimizing clinical trial designs (Garnett et al., 2012; Li et al., 2021; Nguyen et al., 2016; Rees et al., 2016).

In this thesis, three models have been built to predict the sensitivity to three ferroptosis inducing agents and cystine deprivation using base-line gene expression data as predictors. To train these models, the sensitivity data (AUC values) obtained from the

in vitro NB models was used. The transcriptome profiles could significantly predict cell lines sensitivity to all three drugs, with a correlation between predicted and observed AUC values $R > 0.3$. On the other hand, the base-line gene expression data was not able to predict the response to cystine deprivation ($R = -0.1$), therefore this model was not used for further analysis. Since erastin blocks cystine uptake by inhibiting the main cystine transporter, system x_c^-, it was surprising that the results obtained for cystine depletion did not correspond to those derived from erastin treatment. One way to explain this phenomenon could be that NB cells upregulate additional mechanisms to uptake cystine when system x_c^- is not functional, however they are still not efficient enough to prevent ferroptosis induction.

Next, to translate the cell line-based data to real patients scenario, the models with significant predictive power were applied to 600 bulk RNA-seq NB primary tumor samples to predict their sensitivity to ferroptosis induction. Comparing cell lines to tumor samples is a significant challenge due to the heterogeneous composition of tumor samples, which typically contain various cell types, including tumor, stromal, and immune cells. In contrast, cell lines consist solely of cancer cells, which additionally may undergo transcriptional changes during *in vitro* culturing. To overcome these difficulties, a batch correction tool was used to eliminate systematic variations between cell lines and tumors. This led to a more uniform distribution of data across different batches, suggesting that the developmental state of the cell lines was reasonably well-maintained despite the limitations of prolonged culture in the laboratory. After joint normalization, previously described linear regression models were used to estimate tumors susceptibility to the treatments expressed as AUC values based on their expression profiles. Interestingly, *MYCN*-amplified NBs were predicted to be significantly more sensitive to ferroptosis induction when comparing to non-*MYCN*-amplified tumors. Additionally, differential gene expression analysis performed between tumors predicted to be the most sensitive and the most resistant showed that *MYCN* and its target genes were among the top most differentially expressed genes, which were upregulated in the sensitive group. Moreover, the expression of genes involved in various metabolic pathways, such as serine/glycine or cysteine/methionine metabolism as well as transmembrane transporters was increased in *MYCN*-amplified tumors. This strongly indicates that the MYCN-driven

metabolic rewiring may play a crucial role in driving tumors sensitivity to ferroptotic cell death.

Altogether, these results highlight the potential of machine learning approaches to translate data obtained on *in vitro* models to patient's material, which is often unavailable for preclinical drug testing. In addition, to obtain more robust results, it would also be necessary to increase both the number of cell lines and drugs used to train the models. It is also worth noting that this approach could be applied to cell line transcriptome data derived from other cancer entities to identify other tumors that could benefit from ferroptosis induction as a treatment strategy. In fact, there have been some instances where findings from cell lines have been successfully translated to tumors (Barretina et al., 2012; Geeleher et al., 2017; Reinhold et al., 2012). However, one needs to keep in mind that without direct evidence linking the expression of predictive genes to the sensitivity of cell lines to drugs, using transcriptome data to inform clinical practice will remain problematic.

8 Conclusions and Perspectives

Conclusions and Perspectives

Neuroblastoma, a type of cancer that affects nerve cells in the body, is particularly aggressive when it involves amplification of the *MYCN* gene. This genetic alteration is the most significant cancer-related change associated with the most severe form of neuroblastoma, and thus represents a promising target for therapeutic interventions aimed at improving patient outcomes. However, targeting nuclear transcription factors, such as MYCN, with drugs is a challenging task, and as a result, no direct-acting molecule for MYCN has been developed yet. Nevertheless, recent research has shown that ferroptosis may be a potential way to suppress tumors, opening up new avenues for cancer treatment. To investigate this, a comprehensive profiling of a large panel of NB cell lines was performed in this study. The results indicated that commonly used genetic markers to characterize neuroblastoma biology were insufficient in predicting the sensitivity to ferroptosis induction. While the amplification status of *MYCN* or its transcriptional activity could not be used as a definitive predictor of a cell line's sensitivity to ferroptosis induction, a subset of *MYCN*-amplified cell lines showed a strong sensitivity to ferroptosis induction. This observation suggests that cancer cells with a high *MYCN* oncogenic background may exhibit heightened sensitivity to ferroptosis induction initially but are able to rapidly develop adaptive mechanisms to counteract the increased levels of ROS resulting from the rapid cell proliferation.

The findings derived from this study validate the importance of cellular identity in predicting susceptibility to ferroptosis induction. The mesenchymal NB cells, which are a rare subset, demonstrated a comparatively higher resistance to ferroptosis inducers than the adrenergic cell lines. This resistance can be attributed to their unique metabolic regulation, which is primarily dependent on cystine uptake, as opposed to *de novo* cystine biosynthesis. This distinction in metabolic regulation could be due to their slower proliferation rate in comparison to *MYCN*-amplified NB cells, which suggests a possible correlation between cell growth rate and thiol metabolism regulation.

A thorough examination of cell line transcriptome following ferroptotic stress induction revealed a distinctive regulation of stress response mechanisms in *MYCN*-amplified ferroptosis-sensitive cells in comparison to *MYCN*-non-amplified resistant cell lines.

The data obtained from this analysis demonstrated that cells with heightened *MYCN* expression are unable to withstand the stress caused by cystine deprivation, as evidenced by significant transcriptional deregulation in these cells. Additionally, an isotope tracing experiment was performed, revealing that *MYCN*-amplified cells exhibit a less efficient mechanism for cystine uptake compared to non-amplified cells. This inefficiency is potentially caused by the limited availability of glutamate required for the exchange process. It is worth noting that a comparable trend was observed in *MYCN*-amplified NB tumors, which also exhibited significantly lower levels of glutamate. Nonetheless, a more in-depth understanding of the metabolic regulation of NB tumors is imperative and requires further analysis of their metabolome data, as it is highly probable that it differs significantly from the observed metabolic regulation in cell lines.

This study also developed inducible knockdown models targeting key ferroptosis players. Comprehensive profiling of changes resulting from knockdown of either CTH or GPX4 showed that the induced stress sensitized cells to ferroptosis induction and caused their de-differentiation. This finding is particularly noteworthy because previous studies have demonstrated that many tumors undergo EMT transition after chemotherapy, which enables them to acquire resistance to standard therapies. However, the current study suggests that such cells may be more susceptible to ferroptosis, offering a promising therapeutic approach for patients that could be treated with ferroptosis-inducing agents. This thesis demonstrates that utilizing gene expression patterns following gene knockdown proved to be a more effective method for predicting the sensitivity of NB cell lines to ferroptosis induction. However, the transcriptome data utilized in this study was obtained solely from one cell line, significantly limiting its potential for making broader assumptions, particularly due to the observed heterogeneity of cell lines. Therefore, the NB community would greatly benefit from the development of a more diverse panel of cell line models that would enable targeted gene knockdown. This could lead to the development of a robust ferroptotic signature that could be utilized to identify patients who would benefit from ferroptosis induction therapy.

To bridge the gap between information derived from cell lines and the actual behaviour of tumors, a machine learning approach was utilized to predict tumor sensitivity to

ferroptosis induction, using data from *in vitro* models. Results revealed that *MYCN*-amplified tumors were more sensitive compared to non-amplified tumors. Differential gene expression analysis indicated that MYCN activity and its target genes were among the most differentially expressed genes between sensitive and resistant groups of tumors. However, it is important to exercise caution when using computational methods, especially when attempting to translate *in vitro* results to *in vivo* settings due to confounding factors. Integrating data from different cellular models as a training set used for model development could improve prediction accuracy. Additionally, methods for validating these results need further development.

Finally, to identify mechanisms specifically enriched within the high-risk tumor cohort and their potential for pharmacological targeting, it is necessary to obtain more patient-derived tumor material, including low-risk cases that are currently limited or unavailable.

9 References

References

Abbasi, M. R., Rifatbegovic, F., Brunner, C., Mann, G., Ziegler, A., Potschger, U., Crazzolara, R., Ussowicz, M., Benesch, M., Ebetsberger-Dachs, G., Chan, G. C. F., Jones, N., Ladenstein, R., Ambros, I. M., & Ambros, P. F. (2017). Impact of Disseminated Neuroblastoma Cells on the Identification of the Relapse-Seeding Clone. *Clin Cancer Res*, *23*(15), 4224-4232. https://doi.org/10.1158/1078-0432.CCR-16-2082

Ackermann, S., Cartolano, M., Hero, B., Welte, A., Kahlert, Y., Roderwieser, A., Bartenhagen, C., Walter, E., Gecht, J., Kerschke, L., Volland, R., Menon, R., Heuckmann, J. M., Gartlgruber, M., Hartlieb, S., Henrich, K. O., Okonechnikov, K., Altmuller, J., Nurnberg, P., . . . Fischer, M. (2018). A mechanistic classification of clinical phenotypes in neuroblastoma. *Science*, *362*(6419), 1165-1170. https://doi.org/10.1126/science.aat6768

Akagi, T., Kuure, S., Uranishi, K., Koide, H., Costantini, F., & Yokota, T. (2015). ETS-related transcription factors ETV4 and ETV5 are involved in proliferation and induction of differentiation-associated genes in embryonic stem (ES) cells. *J Biol Chem*, *290*(37), 22460-22473. https://doi.org/10.1074/jbc.M115.675595

Alborzinia, H., Florez, A. F., Kreth, S., Bruckner, L. M., Yildiz, U., Gartlgruber, M., Odoni, D. I., Poschet, G., Garbowicz, K., Shao, C., Klein, C., Meier, J., Zeisberger, P., Nadler-Holly, M., Ziehm, M., Paul, F., Burhenne, J., Bell, E., Shaikhkarami, M., . . . Westermann, F. (2022). MYCN mediates cysteine addiction and sensitizes neuroblastoma to ferroptosis. *Nat Cancer*, *3*(4), 471-485. https://doi.org/10.1038/s43018-022-00355-4

Alptekin, A., Ye, B., Yu, Y., Poole, C. J., van Riggelen, J., Zha, Y., & Ding, H. F. (2019). Glycine decarboxylase is a transcriptional target of MYCN required for neuroblastoma cell proliferation and tumorigenicity. *Oncogene*, *38*(50), 7504-7520. https://doi.org/10.1038/s41388-019-0967-3

Ameri, K., & Harris, A. L. (2008). Activating transcription factor 4. *Int J Biochem Cell Biol*, *40*(1), 14-21. https://doi.org/10.1016/j.biocel.2007.01.020

Arlt, B., Zasada, C., Baum, K., Wuenschel, J., Mastrobuoni, G., Lodrini, M., Astrahantseff, K., Winkler, A., Schulte, J. H., Finkler, S., Forbes, M., Hundsdoerfer, P., Guergen, D., Hoffmann, J., Wolf, J., Eggert, A., Kempa, S., & Deubzer, H. E. (2021). Inhibiting phosphoglycerate dehydrogenase counteracts chemotherapeutic efficacy against MYCN-amplified neuroblastoma. *Int J Cancer*, *148*(5), 1219-1232. https://doi.org/10.1002/ijc.33423

Baker, D. L., Schmidt, M. L., Cohn, S. L., Maris, J. M., London, W. B., Buxton, A., Stram, D., Castleberry, R. P., Shimada, H., Sandler, A., Shamberger, R. C., Look, A. T., Reynolds, C. P., Seeger, R. C., Matthay, K. K., & Children's Oncology, G. (2010). Outcome after reduced chemotherapy for intermediate-risk neuroblastoma. *N Engl J Med*, *363*(14), 1313-1323. https://doi.org/10.1056/NEJMoa1001527

Bannai, S. (1986). Exchange of cystine and glutamate across plasma membrane of human fibroblasts. *J Biol Chem*, *261*(5), 2256-2263. https://www.ncbi.nlm.nih.gov/pubmed/2868011

Barretina, J., Caponigro, G., Stransky, N., Venkatesan, K., Margolin, A. A., Kim, S., Wilson, C. J., Lehar, J., Kryukov, G. V., Sonkin, D., Reddy, A., Liu, M., Murray, L., Berger, M. F., Monahan, J. E., Morais, P., Meltzer, J., Korejwa, A., Jane-Valbuena, J., . . . Garraway, L. A. (2012). The Cancer Cell Line Encyclopedia enables predictive modelling of anticancer drug sensitivity. *Nature*, *483*(7391), 603-607. https://doi.org/10.1038/nature11003

Bartolucci, D., Montemurro, L., Raieli, S., Lampis, S., Pession, A., Hrelia, P., & Tonelli, R. (2022). MYCN Impact on High-Risk Neuroblastoma: From Diagnosis and Prognosis to Targeted Treatment. *Cancers (Basel)*, *14*(18). https://doi.org/10.3390/cancers14184421

Bayeva, N., Coll, E., & Piskareva, O. (2021). Differentiating Neuroblastoma: A Systematic Review of the Retinoic Acid, Its Derivatives, and Synergistic Interactions. *J Pers Med*, *11*(3). https://doi.org/10.3390/jpm11030211

Bechmann, N., Watts, D., Steenblock, C., Wallace, P. W., Schurmann, A., Bornstein, S. R., Wielockx, B., Eisenhofer, G., & Peitzsch, M. (2021). Adrenal Hormone Interactions and Metabolism: A Single Sample Multi-Omics Approach. *Horm Metab Res*, *53*(5), 326-334. https://doi.org/10.1055/a-1440-0278

Behan, F. M., Iorio, F., Picco, G., Goncalves, E., Beaver, C. M., Migliardi, G., Santos, R., Rao, Y., Sassi, F., Pinnelli, M., Ansari, R., Harper, S., Jackson, D. A., McRae, R., Pooley, R., Wilkinson, P., van der Meer, D., Dow, D., Buser-Doepner, C., . . . Garnett, M. J. (2019). Prioritization of cancer therapeutic targets using CRISPR-Cas9 screens. *Nature*, *568*(7753), 511-516. https://doi.org/10.1038/s41586-019-1103-9

Berry, T., Luther, W., Bhatnagar, N., Jamin, Y., Poon, E., Sanda, T., Pei, D., Sharma, B., Vetharoy, W. R., Hallsworth, A., Ahmad, Z., Barker, K., Moreau, L., Webber, H., Wang, W., Liu, Q., Perez-Atayde, A., Rodig, S., Cheung, N. K., . . . George, R. E. (2012). The ALK(F1174L) mutation potentiates the oncogenic activity of MYCN in neuroblastoma. *Cancer Cell*, *22*(1), 117-130. https://doi.org/10.1016/j.ccr.2012.06.001

Bersuker, K., Hendricks, J. M., Li, Z., Magtanong, L., Ford, B., Tang, P. H., Roberts, M. A., Tong, B., Maimone, T. J., Zoncu, R., Bassik, M. C., Nomura, D. K., Dixon, S. J., & Olzmann, J. A. (2019). The CoQ oxidoreductase FSP1 acts parallel to GPX4 to inhibit ferroptosis. *Nature*, *575*(7784), 688-692. https://doi.org/10.1038/s41586-019-1705-2

Bhuva, D. D., Cursons, J., & Davis, M. J. (2020). Stable gene expression for normalisation and single-sample scoring. *Nucleic Acids Res*, *48*(19), e113. https://doi.org/10.1093/nar/gkaa802

Biedler, J. L., Helson, L., & Spengler, B. A. (1973). Morphology and growth, tumorigenicity, and cytogenetics of human neuroblastoma cells in continuous culture. *Cancer Res*, *33*(11), 2643-2652. https://www.ncbi.nlm.nih.gov/pubmed/4748425

Biedler, J. L., Roffler-Tarlov, S., Schachner, M., & Freedman, L. S. (1978). Multiple neurotransmitter synthesis by human neuroblastoma cell lines and clones. *Cancer Res*, *38*(11 Pt 1), 3751-3757. https://www.ncbi.nlm.nih.gov/pubmed/29704

Biedler, J. L., & Spengler, B. A. (1976). A novel chromosome abnormality in human neuroblastoma and antifolate-resistant Chinese hamster cell lives in culture. *J Natl Cancer Inst*, *57*(3), 683-695. https://doi.org/10.1093/jnci/57.3.683

Blackwood, E. M., & Eisenman, R. N. (1991). Max: a helix-loop-helix zipper protein that forms a sequence-specific DNA-binding complex with Myc. *Science*, *251*(4998), 1211-1217. https://doi.org/10.1126/science.2006410

Boeva, V., Louis-Brennetot, C., Peltier, A., Durand, S., Pierre-Eugene, C., Raynal, V., Etchevers, H. C., Thomas, S., Lermine, A., Daudigeos-Dubus, E., Geoerger, B., Orth, M. F., Grunewald, T. G. P., Diaz, E., Ducos, B., Surdez, D., Carcaboso, A. M., Medvedeva, I., Deller, T., . . . Janoueix-Lerosey, I. (2017). Heterogeneity of neuroblastoma cell identity defined by transcriptional circuitries. *Nat Genet*, *49*(9), 1408-1413. https://doi.org/10.1038/ng.3921

References

Bonifacio, V. D. B., Pereira, S. A., Serpa, J., & Vicente, J. B. (2021). Cysteine metabolic circuitries: druggable targets in cancer. *Br J Cancer*, *124*(5), 862-879. https://doi.org/10.1038/s41416-020-01156-1

Bown, N., Cotterill, S., Lastowska, M., O'Neill, S., Pearson, A. D., Plantaz, D., Meddeb, M., Danglot, G., Brinkschmidt, C., Christiansen, H., Laureys, G., Speleman, F., Nicholson, J., Bernheim, A., Betts, D. R., Vandesompele, J., & Van Roy, N. (1999). Gain of chromosome arm 17q and adverse outcome in patients with neuroblastoma. *N Engl J Med*, *340*(25), 1954-1961. https://doi.org/10.1056/NEJM199906243402504

Brodeur, G. M. (2003). Neuroblastoma: biological insights into a clinical enigma. *Nature Reviews Cancer*, *3*(3), 203-216. https://doi.org/10.1038/nrc1014

Brodeur, G. M., Hayes, F. A., Green, A. A., Casper, J. T., Wasson, J., Wallach, S., & Seeger, R. C. (1987). Consistent N-myc copy number in simultaneous or consecutive neuroblastoma samples from sixty individual patients. *Cancer Res*, *47*(16), 4248-4253. https://www.ncbi.nlm.nih.gov/pubmed/2440561

Brodeur, G. M., Seeger, R. C., Barrett, A., Berthold, F., Castleberry, R. P., D'Angio, G., De Bernardi, B., Evans, A. E., Favrot, M., Freeman, A. I., & et al. (1988). International criteria for diagnosis, staging, and response to treatment in patients with neuroblastoma. *J Clin Oncol*, *6*(12), 1874-1881. https://doi.org/10.1200/JCO.1988.6.12.1874

Brodeur, G. M., Seeger, R. C., Schwab, M., Varmus, H. E., & Bishop, J. M. (1984). Amplification of N-myc in untreated human neuroblastomas correlates with advanced disease stage. *Science*, *224*(4653), 1121-1124. https://doi.org/10.1126/science.6719137

Brodeur, G. M., Sekhon, G., & Goldstein, M. N. (1977). Chromosomal aberrations in human neuroblastomas. *Cancer*, *40*(5), 2256-2263. https://doi.org/10.1002/1097-0142(197711)40:5<2256::aid-cncr2820400536>3.0.co;2-1

Butler, L. M., Perone, Y., Dehairs, J., Lupien, L. E., de Laat, V., Talebi, A., Loda, M., Kinlaw, W. B., & Swinnen, J. V. (2020). Lipids and cancer: Emerging roles in pathogenesis, diagnosis and therapeutic intervention. *Adv Drug Deliv Rev*, *159*, 245-293. https://doi.org/10.1016/j.addr.2020.07.013

Caren, H., Kryh, H., Nethander, M., Sjoberg, R. M., Trager, C., Nilsson, S., Abrahamsson, J., Kogner, P., & Martinsson, T. (2010). High-risk neuroblastoma tumors with 11q-deletion display a poor prognostic, chromosome instability phenotype with later onset. *Proc Natl Acad Sci U S A*, *107*(9), 4323-4328. https://doi.org/10.1073/pnas.0910684107

Castle, V. P., Heidelberger, K. P., Bromberg, J., Ou, X., Dole, M., & Nunez, G. (1993). Expression of the apoptosis-suppressing protein bcl-2, in neuroblastoma is associated with unfavorable histology and N-myc amplification. *Am J Pathol*, *143*(6), 1543-1550. https://www.ncbi.nlm.nih.gov/pubmed/8256847

Chen, L., Iraci, N., Gherardi, S., Gamble, L. D., Wood, K. M., Perini, G., Lunec, J., & Tweddle, D. A. (2010). p53 is a direct transcriptional target of MYCN in neuroblastoma. *Cancer Res*, *70*(4), 1377-1388. https://doi.org/10.1158/0008-5472.CAN-09-2598

Chen, Y., Lun, A. T., & Smyth, G. K. (2016). From reads to genes to pathways: differential expression analysis of RNA-Seq experiments using Rsubread and the edgeR quasi-likelihood pipeline. *F1000Res*, *5*, 1438. https://doi.org/10.12688/f1000research.8987.2

Chen, Y., Takita, J., Choi, Y. L., Kato, M., Ohira, M., Sanada, M., Wang, L., Soda, M., Kikuchi, A., Igarashi, T., Nakagawara, A., Hayashi, Y., Mano, H., & Ogawa, S. (2008). Oncogenic mutations of ALK kinase in neuroblastoma. *Nature*, *455*(7215), 971-974. https://doi.org/10.1038/nature07399

Chen, Z., Lin, Y., Barbieri, E., Burlingame, S., Hicks, J., Ludwig, A., & Shohet, J. M. (2009). Mdm2 deficiency suppresses MYCN-Driven neuroblastoma tumorigenesis in vivo. *Neoplasia*, *11*(8), 753-762. https://doi.org/10.1593/neo.09466

Cheung, C. H. Y., Hsu, C. L., Tsuei, C. Y., Kuo, T. T., Huang, C. T., Hsu, W. M., Chung, Y. H., Wu, H. Y., Hsu, C. C., Huang, H. C., & Juan, H. F. (2019). Combinatorial targeting of MTHFD2 and PAICS in purine synthesis as a novel therapeutic strategy. *Cell Death Dis*, *10*(11), 786. https://doi.org/10.1038/s41419-019-2033-z

Cheung, N. K., Zhang, J., Lu, C., Parker, M., Bahrami, A., Tickoo, S. K., Heguy, A., Pappo, A. S., Federico, S., Dalton, J., Cheung, I. Y., Ding, L., Fulton, R., Wang, J., Chen, X., Becksfort, J., Wu, J., Billups, C. A., Ellison, D., . . . St Jude Children's Research Hospital-Washington University Pediatric Cancer Genome, P. (2012). Association of age at diagnosis and genetic mutations in patients with neuroblastoma. *JAMA*, *307*(10), 1062-1071. https://doi.org/10.1001/jama.2012.228

Choi, B. H., & Coloff, J. L. (2019). The Diverse Functions of Non-Essential Amino Acids in Cancer. *Cancers (Basel)*, *11*(5). https://doi.org/10.3390/cancers11050675

Cohn, S. L., Pearson, A. D., London, W. B., Monclair, T., Ambros, P. F., Brodeur, G. M., Faldum, A., Hero, B., Iehara, T., Machin, D., Mosseri, V., Simon, T., Garaventa, A., Castel, V., Matthay, K. K., & Force, I. T. (2009). The International Neuroblastoma Risk Group (INRG) classification system: an INRG Task Force report. *J Clin Oncol*, *27*(2), 289-297. https://doi.org/10.1200/JCO.2008.16.6785

Cohn, S. L., Salwen, H., Quasney, M. W., Ikegaki, N., Cowan, J. M., Herst, C. V., Kennett, R. H., Rosen, S. T., DiGiuseppe, J. A., & Brodeur, G. M. (1990). Prolonged N-myc protein half-life in a neuroblastoma cell line lacking N-myc amplification. *Oncogene*, *5*(12), 1821-1827. https://www.ncbi.nlm.nih.gov/pubmed/2284101

Combaret, V., Turc-Carel, C., Thiesse, P., Rebillard, A. C., Frappaz, D., Haus, O., Philip, T., & Favrot, M. C. (1995). Sensitive detection of numerical and structural aberrations of chromosome 1 in neuroblastoma by interphase fluorescence in situ hybridization. Comparison with restriction fragment length polymorphism and conventional cytogenetic analyses. *Int J Cancer*, *61*(2), 185-191. https://doi.org/10.1002/ijc.2910610208

Combs, J. A., & DeNicola, G. M. (2019). The Non-Essential Amino Acid Cysteine Becomes Essential for Tumor Proliferation and Survival. *Cancers (Basel)*, *11*(5). https://doi.org/10.3390/cancers11050678

Corvetta, D., Chayka, O., Gherardi, S., D'Acunto, C. W., Cantilena, S., Valli, E., Piotrowska, I., Perini, G., & Sala, A. (2013). Physical interaction between MYCN oncogene and polycomb repressive complex 2 (PRC2) in neuroblastoma: functional and therapeutic implications. *J Biol Chem*, *288*(12), 8332-8341. https://doi.org/10.1074/jbc.M113.454280

Corvi, R., Amler, L. C., Savelyeva, L., Gehring, M., & Schwab, M. (1994). MYCN is retained in single copy at chromosome 2 band p23-24 during amplification in human neuroblastoma cells. *Proc Natl Acad Sci U S A*, *91*(12), 5523-5527. https://doi.org/10.1073/pnas.91.12.5523

References

Cotterman, R., Jin, V. X., Krig, S. R., Lemen, J. M., Wey, A., Farnham, P. J., & Knoepfler, P. S. (2008). N-Myc regulates a widespread euchromatic program in the human genome partially independent of its role as a classical transcription factor. *Cancer Res*, *68*(23), 9654-9662. https://doi.org/10.1158/0008-5472.CAN-08-1961

Cowell, J. K., & Rupniak, H. T. (1983). Chromosome analysis of human neuroblastoma cell line TR14 showing double minutes and an aberration involving chromosome 1. *Cancer Genet Cytogenet*, *9*(3), 273-280. https://doi.org/10.1016/0165-4608(83)90011-0

D'Angio, G. J., Evans, A. E., & Koop, C. E. (1971). Special pattern of widespread neuroblastoma with a favourable prognosis. *Lancet*, *1*(7708), 1046-1049. https://doi.org/10.1016/s0140-6736(71)91606-0

Davidson, S. M., Jonas, O., Keibler, M. A., Hou, H. W., Luengo, A., Mayers, J. R., Wyckoff, J., Del Rosario, A. M., Whitman, M., Chin, C. R., Condon, K. J., Lammers, A., Kellersberger, K. A., Stall, B. K., Stephanopoulos, G., Bar-Sagi, D., Han, J., Rabinowitz, J. D., Cima, M. J., . . . Vander Heiden, M. G. (2017). Direct evidence for cancer-cell-autonomous extracellular protein catabolism in pancreatic tumors. *Nat Med*, *23*(2), 235-241. https://doi.org/10.1038/nm.4256

Ding, J., Li, T., Wang, X., Zhao, E., Choi, J. H., Yang, L., Zha, Y., Dong, Z., Huang, S., Asara, J. M., Cui, H., & Ding, H. F. (2013). The histone H3 methyltransferase G9A epigenetically activates the serine-glycine synthesis pathway to sustain cancer cell survival and proliferation. *Cell Metab*, *18*(6), 896-907. https://doi.org/10.1016/j.cmet.2013.11.004

Ding, Y., Yang, J., Ma, Y., Yao, T., Chen, X., Ge, S., Wang, L., & Fan, X. (2019). MYCN and PRC1 cooperatively repress docosahexaenoic acid synthesis in neuroblastoma via ELOVL2. *J Exp Clin Cancer Res*, *38*(1), 498. https://doi.org/10.1186/s13046-019-1492-5

Dixon, S. J., Patel, D. N., Welsch, M., Skouta, R., Lee, E. D., Hayano, M., Thomas, A. G., Gleason, C. E., Tatonetti, N. P., Slusher, B. S., & Stockwell, B. R. (2014). Pharmacological inhibition of cystine-glutamate exchange induces endoplasmic reticulum stress and ferroptosis. *Elife*, *3*, e02523. https://doi.org/10.7554/eLife.02523

Doll, S., Freitas, F. P., Shah, R., Aldrovandi, M., da Silva, M. C., Ingold, I., Goya Grocin, A., Xavier da Silva, T. N., Panzilius, E., Scheel, C. H., Mourao, A., Buday, K., Sato, M., Wanninger, J., Vignane, T., Mohana, V., Rehberg, M., Flatley, A., Schepers, A., . . . Conrad, M. (2019). FSP1 is a glutathione-independent ferroptosis suppressor. *Nature*, *575*(7784), 693-698. https://doi.org/10.1038/s41586-019-1707-0

Donti, E., Longo, L., Tonini, G. P., Verdona, G., Melodia, A., Lanino, E., & Cornaglia-Ferraris, P. (1988). Cytogenetic and molecular study of two human neuroblastoma cell lines. *Cancer Genet Cytogenet*, *30*(2), 225-231. https://doi.org/10.1016/0165-4608(88)90188-4

Ducker, G. S., & Rabinowitz, J. D. (2017). One-Carbon Metabolism in Health and Disease. *Cell Metab*, *25*(1), 27-42. https://doi.org/10.1016/j.cmet.2016.08.009

Eagle, H., Oyama, V. I., Levy, M., Horton, C. L., & Fleischman, R. (1956). The growth response of mammalian cells in tissue culture to L-glutamine and L-glutamic acid. *J Biol Chem*, *218*(2), 607-616. https://www.ncbi.nlm.nih.gov/pubmed/13295214

Eaton, J. K., Furst, L., Ruberto, R. A., Moosmayer, D., Hilpmann, A., Ryan, M. J., Zimmermann, K., Cai, L. L., Niehues, M., Badock, V., Kramm, A., Chen, S., Hillig, R. C., Clemons, P. A., Gradl, S., Montagnon, C., Lazarski, K. E., Christian, S., Bajrami, B., . . .

Schreiber, S. L. (2020). Selective covalent targeting of GPX4 using masked nitrile-oxide electrophiles. *Nat Chem Biol*, *16*(5), 497-506. https://doi.org/10.1038/s41589-020-0501-5

El-Badry, O. M., Romanus, J. A., Helman, L. J., Cooper, M. J., Rechler, M. M., & Israel, M. A. (1989). Autonomous growth of a human neuroblastoma cell line is mediated by insulin-like growth factor II. *J Clin Invest*, *84*(3), 829-839. https://doi.org/10.1172/JCI114243

Eleveld, T. F., Oldridge, D. A., Bernard, V., Koster, J., Colmet Daage, L., Diskin, S. J., Schild, L., Bentahar, N. B., Bellini, A., Chicard, M., Lapouble, E., Combaret, V., Legoix-Ne, P., Michon, J., Pugh, T. J., Hart, L. S., Rader, J., Attiyeh, E. F., Wei, J. S., . . . Maris, J. M. (2015). Relapsed neuroblastomas show frequent RAS-MAPK pathway mutations. *Nat Genet*, *47*(8), 864-871. https://doi.org/10.1038/ng.3333

Fasullo, M., & Endres, L. (2015). Nucleotide salvage deficiencies, DNA damage and neurodegeneration. *Int J Mol Sci*, *16*(5), 9431-9449. https://doi.org/10.3390/ijms16059431

Floros, K. V., Cai, J., Jacob, S., Kurupi, R., Fairchild, C. K., Shende, M., Coon, C. M., Powell, K. M., Belvin, B. R., Hu, B., Puchalapalli, M., Ramamoorthy, S., Swift, K., Lewis, J. P., Dozmorov, M. G., Glod, J., Koblinski, J. E., Boikos, S. A., & Faber, A. C. (2021). MYCN-Amplified Neuroblastoma Is Addicted to Iron and Vulnerable to Inhibition of the System Xc-/Glutathione Axis. *Cancer Res*, *81*(7), 1896-1908. https://doi.org/10.1158/0008-5472.CAN-20-1641

Foroutan, M., Bhuva, D. D., Lyu, R., Horan, K., Cursons, J., & Davis, M. J. (2018). Single sample scoring of molecular phenotypes. *BMC Bioinformatics*, *19*(1), 404. https://doi.org/10.1186/s12859-018-2435-4

Furman, W. L., Federico, S. M., McCarville, M. B., Shulkin, B. L., Davidoff, A. M., Krasin, M. J., Sahr, N., Sykes, A., Wu, J., Brennan, R. C., Bishop, M. W., Helmig, S., Stewart, E., Navid, F., Triplett, B., Santana, V. M., Bahrami, A., Anthony, G., Yu, A. L., . . . Pappo, A. S. (2019). A Phase II Trial of Hu14.18K322A in Combination with Induction Chemotherapy in Children with Newly Diagnosed High-Risk Neuroblastoma. *Clin Cancer Res*, *25*(21), 6320-6328. https://doi.org/10.1158/1078-0432.CCR-19-1452

Gagliardi, M., Cotella, D., Santoro, C., Cora, D., Barlev, N. A., Piacentini, M., & Corazzari, M. (2019). Aldo-keto reductases protect metastatic melanoma from ER stress-independent ferroptosis. *Cell Death Dis*, *10*(12), 902. https://doi.org/10.1038/s41419-019-2143-7

Garnett, M. J., Edelman, E. J., Heidorn, S. J., Greenman, C. D., Dastur, A., Lau, K. W., Greninger, P., Thompson, I. R., Luo, X., Soares, J., Liu, Q., Iorio, F., Surdez, D., Chen, L., Milano, R. J., Bignell, G. R., Tam, A. T., Davies, H., Stevenson, J. A., . . . Benes, C. H. (2012). Systematic identification of genomic markers of drug sensitivity in cancer cells. *Nature*, *483*(7391), 570-575. https://doi.org/10.1038/nature11005

Gartlgruber, M., Sharma, A. K., Quintero, A., Dreidax, D., Jansky, S., Park, Y. G., Kreth, S., Meder, J., Doncevic, D., Saary, P., Toprak, U. H., Ishaque, N., Afanasyeva, E., Wecht, E., Koster, J., Versteeg, R., Grunewald, T. G. P., Jones, D. T. W., Pfister, S. M., . . . Westermann, F. (2021). Super enhancers define regulatory subtypes and cell identity in neuroblastoma. *Nat Cancer*, *2*(1), 114-128. https://doi.org/10.1038/s43018-020-00145-w

Geeleher, P., Zhang, Z., Wang, F., Gruener, R. F., Nath, A., Morrison, G., Bhutra, S., Grossman, R. L., & Huang, R. S. (2017). Discovering novel pharmacogenomic

References

biomarkers by imputing drug response in cancer patients from large genomics studies. *Genome Res*, *27*(10), 1743-1751. https://doi.org/10.1101/gr.221077.117

George, R. E., Sanda, T., Hanna, M., Frohling, S., Luther, W., 2nd, Zhang, J., Ahn, Y., Zhou, W., London, W. B., McGrady, P., Xue, L., Zozulya, S., Gregor, V. E., Webb, T. R., Gray, N. S., Gilliland, D. G., Diller, L., Greulich, H., Morris, S. W., . . . Look, A. T. (2008). Activating mutations in ALK provide a therapeutic target in neuroblastoma. *Nature*, *455*(7215), 975-978. https://doi.org/10.1038/nature07397

Hanigan, M. H., & Ricketts, W. A. (1993). Extracellular glutathione is a source of cysteine for cells that express gamma-glutamyl transpeptidase. *Biochemistry*, *32*(24), 6302-6306. https://doi.org/10.1021/bi00075a026

Harding, H. P., Zhang, Y., Zeng, H., Novoa, I., Lu, P. D., Calfon, M., Sadri, N., Yun, C., Popko, B., Paules, R., Stojdl, D. F., Bell, J. C., Hettmann, T., Leiden, J. M., & Ron, D. (2003). An integrated stress response regulates amino acid metabolism and resistance to oxidative stress. *Mol Cell*, *11*(3), 619-633. https://doi.org/10.1016/s1097-2765(03)00105-9

Harris, I. S., Treloar, A. E., Inoue, S., Sasaki, M., Gorrini, C., Lee, K. C., Yung, K. Y., Brenner, D., Knobbe-Thomsen, C. B., Cox, M. A., Elia, A., Berger, T., Cescon, D. W., Adeoye, A., Brustle, A., Molyneux, S. D., Mason, J. M., Li, W. Y., Yamamoto, K., . . . Mak, T. W. (2015). Glutathione and thioredoxin antioxidant pathways synergize to drive cancer initiation and progression. *Cancer Cell*, *27*(2), 211-222. https://doi.org/10.1016/j.ccell.2014.11.019

Hartlieb, S. A., Sieverling, L., Nadler-Holly, M., Ziehm, M., Toprak, U. H., Herrmann, C., Ishaque, N., Okonechnikov, K., Gartlgruber, M., Park, Y. G., Wecht, E. M., Savelyeva, L., Henrich, K. O., Rosswog, C., Fischer, M., Hero, B., Jones, D. T. W., Pfaff, E., Witt, O., . . . Westermann, F. (2021). Alternative lengthening of telomeres in childhood neuroblastoma from genome to proteome. *Nat Commun*, *12*(1), 1269. https://doi.org/10.1038/s41467-021-21247-8

Hertwig, F., Peifer, M., & Fischer, M. (2016). Telomere maintenance is pivotal for high-risk neuroblastoma. *Cell Cycle*, *15*(3), 311-312. https://doi.org/10.1080/15384101.2015.1125243

Hosoki, R., Matsuki, N., & Kimura, H. (1997). The possible role of hydrogen sulfide as an endogenous smooth muscle relaxant in synergy with nitric oxide. *Biochem Biophys Res Commun*, *237*(3), 527-531. https://doi.org/10.1006/bbrc.1997.6878

Hu, W., Zhou, C., Jing, Q., Li, Y., Yang, J., Yang, C., Wang, L., Hu, J., Li, H., Wang, H., Yuan, C., Zhou, Y., Ren, X., Tong, X., Du, J., & Wang, Y. (2021). FTH promotes the proliferation and renders the HCC cells specifically resist to ferroptosis by maintaining iron homeostasis. *Cancer Cell Int*, *21*(1), 709. https://doi.org/10.1186/s12935-021-02420-x

Imamura, J., Bartram, C. R., Berthold, F., Harms, D., Nakamura, H., & Koeffler, H. P. (1993). Mutation of the p53 gene in neuroblastoma and its relationship with N-myc amplification. *Cancer Res*, *53*(17), 4053-4058. https://www.ncbi.nlm.nih.gov/pubmed/8358734

Irwin, M. S., Naranjo, A., Zhang, F. F., Cohn, S. L., London, W. B., Gastier-Foster, J. M., Ramirez, N. C., Pfau, R., Reshmi, S., Wagner, E., Nuchtern, J., Asgharzadeh, S., Shimada, H., Maris, J. M., Bagatell, R., Park, J. R., & Hogarty, M. D. (2021). Revised Neuroblastoma Risk Classification System: A Report From the Children's Oncology Group. *J Clin Oncol*, *39*(29), 3229-3241. https://doi.org/10.1200/JCO.21.00278

Janoueix-Lerosey, I., Lopez-Delisle, L., Delattre, O., & Rohrer, H. (2018). The ALK receptor in sympathetic neuron development and neuroblastoma. *Cell Tissue Res*, *372*(2), 325-337. https://doi.org/10.1007/s00441-017-2784-8

Janoueix-Lerosey, I., Schleiermacher, G., Michels, E., Mosseri, V., Ribeiro, A., Lequin, D., Vermeulen, J., Couturier, J., Peuchmaur, M., Valent, A., Plantaz, D., Rubie, H., Valteau-Couanet, D., Thomas, C., Combaret, V., Rousseau, R., Eggert, A., Michon, J., Speleman, F., & Delattre, O. (2009). Overall genomic pattern is a predictor of outcome in neuroblastoma. *J Clin Oncol*, *27*(7), 1026-1033. https://doi.org/10.1200/JCO.2008.16.0630

Jansky, S., Sharma, A. K., Korber, V., Quintero, A., Toprak, U. H., Wecht, E. M., Gartlgruber, M., Greco, A., Chomsky, E., Grunewald, T. G. P., Henrich, K. O., Tanay, A., Herrmann, C., Hofer, T., & Westermann, F. (2021). Single-cell transcriptomic analyses provide insights into the developmental origins of neuroblastoma. *Nat Genet*, *53*(5), 683-693. https://doi.org/10.1038/s41588-021-00806-1

Jones, D. T. W., Banito, A., Grunewald, T. G. P., Haber, M., Jager, N., Kool, M., Milde, T., Molenaar, J. J., Nabbi, A., Pugh, T. J., Schleiermacher, G., Smith, M. A., Westermann, F., & Pfister, S. M. (2019). Molecular characteristics and therapeutic vulnerabilities across paediatric solid tumours. *Nat Rev Cancer*, *19*(8), 420-438. https://doi.org/10.1038/s41568-019-0169-x

Kaczor-Kaminska, M., Sura, P., & Wrobel, M. (2020). Multidirectional Changes in Parameters related to Sulfur Metabolism in Frog Tissues exposed to Heavy Metal-related Stress. *Biomolecules*, *10*(4). https://doi.org/10.3390/biom10040574

Keshelava, N., Seeger, R. C., Groshen, S., & Reynolds, C. P. (1998). Drug resistance patterns of human neuroblastoma cell lines derived from patients at different phases of therapy. *Cancer Res*, *58*(23), 5396-5405. https://www.ncbi.nlm.nih.gov/pubmed/9850071

Kilberg, M. S., Shan, J., & Su, N. (2009). ATF4-dependent transcription mediates signaling of amino acid limitation. *Trends Endocrinol Metab*, *20*(9), 436-443. https://doi.org/10.1016/j.tem.2009.05.008

Koppula, P., Zhang, Y., Shi, J., Li, W., & Gan, B. (2017). The glutamate/cystine antiporter SLC7A11/xCT enhances cancer cell dependency on glucose by exporting glutamate. *J Biol Chem*, *292*(34), 14240-14249. https://doi.org/10.1074/jbc.M117.798405

Kovacevic, Z., & McGivan, J. D. (1983). Mitochondrial metabolism of glutamine and glutamate and its physiological significance. *Physiol Rev*, *63*(2), 547-605. https://doi.org/10.1152/physrev.1983.63.2.547

Kraft, V. A. N., Bezjian, C. T., Pfeiffer, S., Ringelstetter, L., Muller, C., Zandkarimi, F., Merl-Pham, J., Bao, X., Anastasov, N., Kossl, J., Brandner, S., Daniels, J. D., Schmitt-Kopplin, P., Hauck, S. M., Stockwell, B. R., Hadian, K., & Schick, J. A. (2020). GTP Cyclohydrolase 1/Tetrahydrobiopterin Counteract Ferroptosis through Lipid Remodeling. *ACS Cent Sci*, *6*(1), 41-53. https://doi.org/10.1021/acscentsci.9b01063

Laherty, C. D., Yang, W. M., Sun, J. M., Davie, J. R., Seto, E., & Eisenman, R. N. (1997). Histone deacetylases associated with the mSin3 corepressor mediate mad transcriptional repression. *Cell*, *89*(3), 349-356. https://doi.org/10.1016/s0092-8674(00)80215-9

Lane, A. N., & Fan, T. W. (2015). Regulation of mammalian nucleotide metabolism and biosynthesis. *Nucleic Acids Res*, *43*(4), 2466-2485. https://doi.org/10.1093/nar/gkv047

References

Langner, M., Mateska, I., Bechmann, N., Wielockx, B., Chavakis, T., Alexaki, V. I., & Peitzsch, M. (2022). Liquid chromatography-tandem mass spectrometry based quantification of arginine metabolites including polyamines in different sample matrices. *J Chromatogr A*, *1671*, 463021. https://doi.org/10.1016/j.chroma.2022.463021

Le Grand, M., Mukha, A., Puschel, J., Valli, E., Kamili, A., Vittorio, O., Dubrovska, A., & Kavallaris, M. (2020). Interplay between MycN and c-Myc regulates radioresistance and cancer stem cell phenotype in neuroblastoma upon glutamine deprivation. *Theranostics*, *10*(14), 6411-6429. https://doi.org/10.7150/thno.42602

Levy, A. G., Zage, P. E., Akers, L. J., Ghisoli, M. L., Chen, Z., Fang, W., Kannan, S., Graham, T., Zeng, L., Franklin, A. R., Huang, P., & Zweidler-McKay, P. A. (2012). The combination of the novel glycolysis inhibitor 3-BrOP and rapamycin is effective against neuroblastoma. *Invest New Drugs*, *30*(1), 191-199. https://doi.org/10.1007/s10637-010-9551-y

Lewis, E. C., Kraveka, J. M., Ferguson, W., Eslin, D., Brown, V. I., Bergendahl, G., Roberts, W., Wada, R. K., Oesterheld, J., Mitchell, D., Foley, J., Zage, P., Rawwas, J., Rich, M., Lorenzi, E., Broglio, K., Berry, D., & Saulnier Sholler, G. L. (2020). A subset analysis of a phase II trial evaluating the use of DFMO as maintenance therapy for high-risk neuroblastoma. *Int J Cancer*, *147*(11), 3152-3159. https://doi.org/10.1002/ijc.33044

Li, J., Cao, F., Yin, H. L., Huang, Z. J., Lin, Z. T., Mao, N., Sun, B., & Wang, G. (2020). Ferroptosis: past, present and future. *Cell Death Dis*, *11*(2), 88. https://doi.org/10.1038/s41419-020-2298-2

Li, Y., Umbach, D. M., Krahn, J. M., Shats, I., Li, X., & Li, L. (2021). Predicting tumor response to drugs based on gene-expression biomarkers of sensitivity learned from cancer cell lines. *BMC Genomics*, *22*(1), 272. https://doi.org/10.1186/s12864-021-07581-7

Liberzon, A., Birger, C., Thorvaldsdottir, H., Ghandi, M., Mesirov, J. P., & Tamayo, P. (2015). The Molecular Signatures Database (MSigDB) hallmark gene set collection. *Cell Syst*, *1*(6), 417-425. https://doi.org/10.1016/j.cels.2015.12.004

Liu, M., Xia, Y., Ding, J., Ye, B., Zhao, E., Choi, J. H., Alptekin, A., Yan, C., Dong, Z., Huang, S., Yang, L., Cui, H., Zha, Y., & Ding, H. F. (2016). Transcriptional Profiling Reveals a Common Metabolic Program in High-Risk Human Neuroblastoma and Mouse Neuroblastoma Sphere-Forming Cells. *Cell Rep*, *17*(2), 609-623. https://doi.org/10.1016/j.celrep.2016.09.021

Liu, X., Olszewski, K., Zhang, Y., Lim, E. W., Shi, J., Zhang, X., Zhang, J., Lee, H., Koppula, P., Lei, G., Zhuang, L., You, M. J., Fang, B., Li, W., Metallo, C. M., Poyurovsky, M. V., & Gan, B. (2020). Cystine transporter regulation of pentose phosphate pathway dependency and disulfide stress exposes a targetable metabolic vulnerability in cancer. *Nat Cell Biol*, *22*(4), 476-486. https://doi.org/10.1038/s41556-020-0496-x

Liu, Z., Chen, S. S., Clarke, S., Veschi, V., & Thiele, C. J. (2020). Targeting MYCN in Pediatric and Adult Cancers. *Front Oncol*, *10*, 623679. https://doi.org/10.3389/fonc.2020.623679

Locasale, J. W. (2013). Serine, glycine and one-carbon units: cancer metabolism in full circle. *Nat Rev Cancer*, *13*(8), 572-583. https://doi.org/10.1038/nrc3557

London, W. B., Castleberry, R. P., Matthay, K. K., Look, A. T., Seeger, R. C., Shimada, H., Thorner, P., Brodeur, G., Maris, J. M., Reynolds, C. P., & Cohn, S. L. (2005). Evidence for an age cutoff greater than 365 days for neuroblastoma risk group stratification in the Children's Oncology Group. *J Clin Oncol*, *23*(27), 6459-6465. https://doi.org/10.1200/JCO.2005.05.571

Lu, Y., Yang, Q., Su, Y., Ji, Y., Li, G., Yang, X., Xu, L., Lu, Z., Dong, J., Wu, Y., Bei, J. X., Pan, C., Gu, X., & Li, B. (2021). MYCN mediates TFRC-dependent ferroptosis and reveals vulnerabilities in neuroblastoma. *Cell Death Dis*, *12*(6), 511. https://doi.org/10.1038/s41419-021-03790-w

Maiorino, M., Conrad, M., & Ursini, F. (2018). GPx4, Lipid Peroxidation, and Cell Death: Discoveries, Rediscoveries, and Open Issues. *Antioxid Redox Signal*, *29*(1), 61-74. https://doi.org/10.1089/ars.2017.7115

Malynn, B. A., de Alboran, I. M., O'Hagan, R. C., Bronson, R., Davidson, L., DePinho, R. A., & Alt, F. W. (2000). N-myc can functionally replace c-myc in murine development, cellular growth, and differentiation. *Genes Dev*, *14*(11), 1390-1399. https://www.ncbi.nlm.nih.gov/pubmed/10837031

Marini, P., MacLeod, R. A., Treuner, C., Bruchelt, G., Bohm, W., Wolburg, H., Schweizer, P., & Girgert, R. (1999). SiMa, a new neuroblastoma cell line combining poor prognostic cytogenetic markers with high adrenergic differentiation. *Cancer Genet Cytogenet*, *112*(2), 161-164. https://doi.org/10.1016/s0165-4608(98)00269-6

Maris, J. M., Hogarty, M. D., Bagatell, R., & Cohn, S. L. (2007). Neuroblastoma. *Lancet*, *369*(9579), 2106-2120. https://doi.org/10.1016/S0140-6736(07)60983-0

Martinez-Reyes, I., & Chandel, N. S. (2021). Cancer metabolism: looking forward. *Nat Rev Cancer*, *21*(10), 669-680. https://doi.org/10.1038/s41568-021-00378-6

Matsushita, Y., Nakagawa, H., & Koike, K. (2021). Lipid Metabolism in Oncology: Why It Matters, How to Research, and How to Treat. *Cancers (Basel)*, *13*(3). https://doi.org/10.3390/cancers13030474

Matthay, K. K., Villablanca, J. G., Seeger, R. C., Stram, D. O., Harris, R. E., Ramsay, N. K., Swift, P., Shimada, H., Black, C. T., Brodeur, G. M., Gerbing, R. B., & Reynolds, C. P. (1999). Treatment of high-risk neuroblastoma with intensive chemotherapy, radiotherapy, autologous bone marrow transplantation, and 13-cis-retinoic acid. Children's Cancer Group. *N Engl J Med*, *341*(16), 1165-1173. https://doi.org/10.1056/NEJM199910143411601

McBean, G. J. (2017). Cysteine, Glutathione, and Thiol Redox Balance in Astrocytes. *Antioxidants (Basel)*, *6*(3). https://doi.org/10.3390/antiox6030062

McCarthy, D. J., Chen, Y., & Smyth, G. K. (2012). Differential expression analysis of multifactor RNA-Seq experiments with respect to biological variation. *Nucleic Acids Res*, *40*(10), 4288-4297. https://doi.org/10.1093/nar/gks042

Melino, G., Knight, R. A., & Thiele, C. J. (1993). New insight on the biology of neuroectodermal tumors. Workshop report from the University of Rome Tor Vergata and the IDI-IRCCS on the genetics and control of growth, differentiation, and programmed cell death. *Cancer Res*, *53*(4), 926-928. https://www.ncbi.nlm.nih.gov/pubmed/8428371

Mena, M. A., Garcia de Yebenes, J., Dwork, A., Fahn, S., Latov, N., Herbert, J., Flaster, E., & Slonim, D. (1989). Biochemical properties of monoamine-rich human neuroblastoma cells. *Brain Res*, *486*(2), 286-296. https://doi.org/10.1016/0006-8993(89)90514-3

Mendes, C., & Serpa, J. (2019). Metabolic Remodelling: An Accomplice for New Therapeutic Strategies to Fight Lung Cancer. *Antioxidants (Basel)*, *8*(12). https://doi.org/10.3390/antiox8120603

Minturn, J. E., Evans, A. E., Villablanca, J. G., Yanik, G. A., Park, J. R., Shusterman, S., Groshen, S., Hellriegel, E. T., Bensen-Kennedy, D., Matthay, K. K., Brodeur, G. M., & Maris, J. M. (2011). Phase I trial of lestaurtinib for children with refractory neuroblastoma: a new

approaches to neuroblastoma therapy consortium study. *Cancer Chemother Pharmacol*, *68*(4), 1057-1065. https://doi.org/10.1007/s00280-011-1581-4

Molenaar, J. J., Koster, J., Zwijnenburg, D. A., van Sluis, P., Valentijn, L. J., van der Ploeg, I., Hamdi, M., van Nes, J., Westerman, B. A., van Arkel, J., Ebus, M. E., Haneveld, F., Lakeman, A., Schild, L., Molenaar, P., Stroeken, P., van Noesel, M. M., Ora, I., Santo, E. E., . . . Versteeg, R. (2012). Sequencing of neuroblastoma identifies chromothripsis and defects in neuritogenesis genes. *Nature*, *483*(7391), 589-593. https://doi.org/10.1038/nature10910

Morales-Loredo, H., Barrera, A., Garcia, J. M., Pace, C. E., Naik, J. S., Gonzalez Bosc, L. V., & Kanagy, N. L. (2019). Hydrogen sulfide regulation of renal and mesenteric blood flow. *Am J Physiol Heart Circ Physiol*, *317*(5), H1157-H1165. https://doi.org/10.1152/ajpheart.00303.2019

Mosharov, E., Cranford, M. R., & Banerjee, R. (2000). The quantitatively important relationship between homocysteine metabolism and glutathione synthesis by the transsulfuration pathway and its regulation by redox changes. *Biochemistry*, *39*(42), 13005-13011. https://doi.org/10.1021/bi001088w

Muller, I., Larsson, K., Frenzel, A., Oliynyk, G., Zirath, H., Prochownik, E. V., Westwood, N. J., & Henriksson, M. A. (2014). Targeting of the MYCN protein with small molecule c-MYC inhibitors. *PLoS One*, *9*(5), e97285. https://doi.org/10.1371/journal.pone.0097285

Murray, M. R., & Stout, A. P. (1947). Distinctive Characteristics of the Sympathicoblastoma Cultivated in Vitro: A Method for Prompt Diagnosis. *Am J Pathol*, *23*(3), 429-441. https://www.ncbi.nlm.nih.gov/pubmed/19970938

Murre, C., McCaw, P. S., & Baltimore, D. (1989). A new DNA binding and dimerization motif in immunoglobulin enhancer binding, daughterless, MyoD, and myc proteins. *Cell*, *56*(5), 777-783. https://doi.org/10.1016/0092-8674(89)90682-x

Murre, C., McCaw, P. S., Vaessin, H., Caudy, M., Jan, L. Y., Jan, Y. N., Cabrera, C. V., Buskin, J. N., Hauschka, S. D., Lassar, A. B., & et al. (1989). Interactions between heterologous helix-loop-helix proteins generate complexes that bind specifically to a common DNA sequence. *Cell*, *58*(3), 537-544. https://doi.org/10.1016/0092-8674(89)90434-0

Muth, D., Ghazaryan, S., Eckerle, I., Beckett, E., Pohler, C., Batzler, J., Beisel, C., Gogolin, S., Fischer, M., Henrich, K. O., Ehemann, V., Gillespie, P., Schwab, M., & Westermann, F. (2010). Transcriptional repression of SKP2 is impaired in MYCN-amplified neuroblastoma. *Cancer Res*, *70*(9), 3791-3802. https://doi.org/10.1158/0008-5472.CAN-09-1245

Neuroblastoma Treatment (PDQ(R)): Health Professional Version. (2002). In *PDQ Cancer Information Summaries*. https://www.ncbi.nlm.nih.gov/pubmed/26389190

Nguyen, L., Dang, C. C., & Ballester, P. J. (2016). Systematic assessment of multi-gene predictors of pan-cancer cell line sensitivity to drugs exploiting gene expression data. *F1000Res*, *5*. https://doi.org/10.12688/f1000research.10529.2

Nie, Q., Hu, Y., Yu, X., Li, X., & Fang, X. (2022). Induction and application of ferroptosis in cancer therapy. *Cancer Cell Int*, *22*(1), 12. https://doi.org/10.1186/s12935-021-02366-0

Nile, D. L., Rae, C., Walker, D. J., Waddington, J. C., Vincent, I., Burgess, K., Gaze, M. N., Mairs, R. J., & Chalmers, A. J. (2021). Inhibition of glycolysis and mitochondrial respiration promotes radiosensitisation of neuroblastoma and glioma cells. *Cancer Metab*, *9*(1), 24. https://doi.org/10.1186/s40170-021-00258-5

Novoa, I., Zhang, Y., Zeng, H., Jungreis, R., Harding, H. P., & Ron, D. (2003). Stress-induced gene expression requires programmed recovery from translational repression. *EMBO J*, *22*(5), 1180-1187. https://doi.org/10.1093/emboj/cdg112

Oberthuer, A., Theissen, J., Westermann, F., Hero, B., & Fischer, M. (2009). Molecular characterization and classification of neuroblastoma. *Future Oncol*, *5*(5), 625-639. https://doi.org/10.2217/fon.09.41

Oliynyk, G., Ruiz-Perez, M. V., Sainero-Alcolado, L., Dzieran, J., Zirath, H., Gallart-Ayala, H., Wheelock, C. E., Johansson, H. J., Nilsson, R., Lehtio, J., & Arsenian-Henriksson, M. (2019). MYCN-enhanced Oxidative and Glycolytic Metabolism Reveals Vulnerabilities for Targeting Neuroblastoma. *iScience*, *21*, 188-204. https://doi.org/10.1016/j.isci.2019.10.020

Pacenta, H. L., & Macy, M. E. (2018). Entrectinib and other ALK/TRK inhibitors for the treatment of neuroblastoma. *Drug Des Devel Ther*, *12*, 3549-3561. https://doi.org/10.2147/DDDT.S147384

Pakos-Zebrucka, K., Koryga, I., Mnich, K., Ljujic, M., Samali, A., & Gorman, A. M. (2016). The integrated stress response. *EMBO Rep*, *17*(10), 1374-1395. https://doi.org/10.15252/embr.201642195

Patel, J. H., Loboda, A. P., Showe, M. K., Showe, L. C., & McMahon, S. B. (2004). Analysis of genomic targets reveals complex functions of MYC. *Nat Rev Cancer*, *4*(7), 562-568. https://doi.org/10.1038/nrc1393

Pavlova, N. N., Zhu, J., & Thompson, C. B. (2022). The hallmarks of cancer metabolism: Still emerging. *Cell Metab*, *34*(3), 355-377. https://doi.org/10.1016/j.cmet.2022.01.007

Pedley, A. M., & Benkovic, S. J. (2017). A New View into the Regulation of Purine Metabolism: The Purinosome. *Trends Biochem Sci*, *42*(2), 141-154. https://doi.org/10.1016/j.tibs.2016.09.009

Peifer, M., Hertwig, F., Roels, F., Dreidax, D., Gartlgruber, M., Menon, R., Kramer, A., Roncaioli, J. L., Sand, F., Heuckmann, J. M., Ikram, F., Schmidt, R., Ackermann, S., Engesser, A., Kahlert, Y., Vogel, W., Altmuller, J., Nurnberg, P., Thierry-Mieg, J., . . . Fischer, M. (2015). Telomerase activation by genomic rearrangements in high-risk neuroblastoma. *Nature*, *526*(7575), 700-704. https://doi.org/10.1038/nature14980

Petroni, M., Veschi, V., Gulino, A., & Giannini, G. (2012). Molecular mechanisms of MYCN-dependent apoptosis and the MDM2-p53 pathway: an Achille's heel to be exploited for the therapy of MYCN-amplified neuroblastoma. *Front Oncol*, *2*, 141. https://doi.org/10.3389/fonc.2012.00141

Petroni, M., Veschi, V., Prodosmo, A., Rinaldo, C., Massimi, I., Carbonari, M., Dominici, C., McDowell, H. P., Rinaldi, C., Screpanti, I., Frati, L., Bartolazzi, A., Gulino, A., Soddu, S., & Giannini, G. (2011). MYCN sensitizes human neuroblastoma to apoptosis by HIPK2 activation through a DNA damage response. *Mol Cancer Res*, *9*(1), 67-77. https://doi.org/10.1158/1541-7786.MCR-10-0227

Pietsch, T., Gottert, E., Meese, E., Blin, N., Feickert, H. J., Riehm, H., & Kovacs, G. (1988). Characterization of a continuous cell line (MHH-NB-11) derived from advanced neuroblastoma. *Anticancer Res*, *8*(6), 1329-1333. https://www.ncbi.nlm.nih.gov/pubmed/3218965

Pugh, T. J., Morozova, O., Attiyeh, E. F., Asgharzadeh, S., Wei, J. S., Auclair, D., Carter, S. L., Cibulskis, K., Hanna, M., Kiezun, A., Kim, J., Lawrence, M. S., Lichenstein, L., McKenna, A., Pedamallu, C. S., Ramos, A. H., Shefler, E., Sivachenko, A., Sougnez, C., .

References

. . Maris, J. M. (2013). The genetic landscape of high-risk neuroblastoma. *Nat Genet*, *45*(3), 279-284. https://doi.org/10.1038/ng.2529

Qing, G., Li, B., Vu, A., Skuli, N., Walton, Z. E., Liu, X., Mayes, P. A., Wise, D. R., Thompson, C. B., Maris, J. M., Hogarty, M. D., & Simon, M. C. (2012). ATF4 regulates MYC-mediated neuroblastoma cell death upon glutamine deprivation. *Cancer Cell*, *22*(5), 631-644. https://doi.org/10.1016/j.ccr.2012.09.021

Qing, G., Skuli, N., Mayes, P. A., Pawel, B., Martinez, D., Maris, J. M., & Simon, M. C. (2010). Combinatorial regulation of neuroblastoma tumor progression by N-Myc and hypoxia inducible factor HIF-1alpha. *Cancer Res*, *70*(24), 10351-10361. https://doi.org/10.1158/0008-5472.CAN-10-0740

Rees, M. G., Seashore-Ludlow, B., Cheah, J. H., Adams, D. J., Price, E. V., Gill, S., Javaid, S., Coletti, M. E., Jones, V. L., Bodycombe, N. E., Soule, C. K., Alexander, B., Li, A., Montgomery, P., Kotz, J. D., Hon, C. S., Munoz, B., Liefeld, T., Dancik, V., . . . Schreiber, S. L. (2016). Correlating chemical sensitivity and basal gene expression reveals mechanism of action. *Nat Chem Biol*, *12*(2), 109-116. https://doi.org/10.1038/nchembio.1986

Reina-Campos, M., Diaz-Meco, M. T., & Moscat, J. (2020). The complexity of the serine glycine one-carbon pathway in cancer. *J Cell Biol*, *219*(1). https://doi.org/10.1083/jcb.201907022

Reinhold, W. C., Sunshine, M., Liu, H., Varma, S., Kohn, K. W., Morris, J., Doroshow, J., & Pommier, Y. (2012). CellMiner: a web-based suite of genomic and pharmacologic tools to explore transcript and drug patterns in the NCI-60 cell line set. *Cancer Res*, *72*(14), 3499-3511. https://doi.org/10.1158/0008-5472.CAN-12-1370

Reisinger, E., Genthner, L., Kerssemakers, J., Kensche, P., Borufka, S., Jugold, A., Kling, A., Prinz, M., Scholz, I., Zipprich, G., Eils, R., Lawerenz, C., & Eils, J. (2017). OTP: An automatized system for managing and processing NGS data. *J Biotechnol*, *261*, 53-62. https://doi.org/10.1016/j.jbiotec.2017.08.006

Ren, P., Yue, M., Xiao, D., Xiu, R., Gan, L., Liu, H., & Qing, G. (2015). ATF4 and N-Myc coordinate glutamine metabolism in MYCN-amplified neuroblastoma cells through ASCT2 activation. *J Pathol*, *235*(1), 90-100. https://doi.org/10.1002/path.4429

Reynolds, C. P., Biedler, J. L., Spengler, B. A., Reynolds, D. A., Ross, R. A., Frenkel, E. P., & Smith, R. G. (1986). Characterization of human neuroblastoma cell lines established before and after therapy. *J Natl Cancer Inst*, *76*(3), 375-387. https://www.ncbi.nlm.nih.gov/pubmed/3456456

Richter, S., Gieldon, L., Pang, Y., Peitzsch, M., Huynh, T., Leton, R., Viana, B., Ercolino, T., Mangelis, A., Rapizzi, E., Menschikowski, M., Aust, D., Kroiss, M., Beuschlein, F., Gudziol, V., Timmers, H. J., Lenders, J., Mannelli, M., Cascon, A., . . . Klink, B. (2019). Metabolome-guided genomics to identify pathogenic variants in isocitrate dehydrogenase, fumarate hydratase, and succinate dehydrogenase genes in pheochromocytoma and paraganglioma. *Genet Med*, *21*(3), 705-717. https://doi.org/10.1038/s41436-018-0106-5

Robinson, M. D., McCarthy, D. J., & Smyth, G. K. (2010). edgeR: a Bioconductor package for differential expression analysis of digital gene expression data. *Bioinformatics*, *26*(1), 139-140. https://doi.org/10.1093/bioinformatics/btp616

Ross, R. A., Spengler, B. A., & Biedler, J. L. (1983). Coordinate morphological and biochemical interconversion of human neuroblastoma cells. *J Natl Cancer Inst*, *71*(4), 741-747. https://www.ncbi.nlm.nih.gov/pubmed/6137586

Rudolph, G., Schilbach-Stuckle, K., Handgretinger, R., Kaiser, P., & Hameister, H. (1991). Cytogenetic and molecular characterization of a newly established neuroblastoma cell line LS. *Hum Genet*, *86*(6), 562-566. https://doi.org/10.1007/BF00201542

Santos, C. R., & Schulze, A. (2012). Lipid metabolism in cancer. *FEBS J*, *279*(15), 2610-2623. https://doi.org/10.1111/j.1742-4658.2012.08644.x

Sausen, M., Leary, R. J., Jones, S., Wu, J., Reynolds, C. P., Liu, X., Blackford, A., Parmigiani, G., Diaz, L. A., Jr., Papadopoulos, N., Vogelstein, B., Kinzler, K. W., Velculescu, V. E., & Hogarty, M. D. (2013). Integrated genomic analyses identify ARID1A and ARID1B alterations in the childhood cancer neuroblastoma. *Nat Genet*, *45*(1), 12-17. https://doi.org/10.1038/ng.2493

Savino, M., Annibali, D., Carucci, N., Favuzzi, E., Cole, M. D., Evan, G. I., Soucek, L., & Nasi, S. (2011). The action mechanism of the Myc inhibitor termed Omomyc may give clues on how to target Myc for cancer therapy. *PLoS One*, *6*(7), e22284. https://doi.org/10.1371/journal.pone.0022284

Sbodio, J. I., Snyder, S. H., & Paul, B. D. (2019). Regulators of the transsulfuration pathway. *Br J Pharmacol*, *176*(4), 583-593. https://doi.org/10.1111/bph.14446

Schleiermacher, G., Janoueix-Lerosey, I., Ribeiro, A., Klijanienko, J., Couturier, J., Pierron, G., Mosseri, V., Valent, A., Auger, N., Plantaz, D., Rubie, H., Valteau-Couanet, D., Bourdeaut, F., Combaret, V., Bergeron, C., Michon, J., & Delattre, O. (2010). Accumulation of segmental alterations determines progression in neuroblastoma. *J Clin Oncol*, *28*(19), 3122-3130. https://doi.org/10.1200/JCO.2009.26.7955

Schleiermacher, G., Michon, J., Ribeiro, A., Pierron, G., Mosseri, V., Rubie, H., Munzer, C., Benard, J., Auger, N., Combaret, V., Janoueix-Lerosey, I., Pearson, A., Tweddle, D. A., Bown, N., Gerrard, M., Wheeler, K., Noguera, R., Villamon, E., Canete, A., . . . Couturier, J. (2011). Segmental chromosomal alterations lead to a higher risk of relapse in infants with MYCN-non-amplified localised unresectable/disseminated neuroblastoma (a SIOPEN collaborative study). *Br J Cancer*, *105*(12), 1940-1948. https://doi.org/10.1038/bjc.2011.472

Schlesinger, H. R., Gerson, J. M., Moorhead, P. S., Maguire, H., & Hummeler, K. (1976). Establishment and characterization of human neuroblastoma cell lines. *Cancer Res*, *36*(9 pt.1), 3094-3100. https://www.ncbi.nlm.nih.gov/pubmed/10079

Schulte, J. H., Lindner, S., Bohrer, A., Maurer, J., De Preter, K., Lefever, S., Heukamp, L., Schulte, S., Molenaar, J., Versteeg, R., Thor, T., Kunkele, A., Vandesompele, J., Speleman, F., Schorle, H., Eggert, A., & Schramm, A. (2013). MYCN and ALKF1174L are sufficient to drive neuroblastoma development from neural crest progenitor cells. *Oncogene*, *32*(8), 1059-1065. https://doi.org/10.1038/onc.2012.106

Schulze, A., & Harris, A. L. (2012). How cancer metabolism is tuned for proliferation and vulnerable to disruption. *Nature*, *491*(7424), 364-373. https://doi.org/10.1038/nature11706

Schwab, M., Alitalo, K., Klempnauer, K. H., Varmus, H. E., Bishop, J. M., Gilbert, F., Brodeur, G., Goldstein, M., & Trent, J. (1983). Amplified DNA with limited homology to myc cellular oncogene is shared by human neuroblastoma cell lines and a neuroblastoma tumour. *Nature*, *305*(5931), 245-248. https://doi.org/10.1038/305245a0

Seeger, R. C., Brodeur, G. M., Sather, H., Dalton, A., Siegel, S. E., Wong, K. Y., & Hammond, D. (1985). Association of multiple copies of the N-myc oncogene with rapid progression of neuroblastomas. *N Engl J Med*, *313*(18), 1111-1116. https://doi.org/10.1056/NEJM198510313131802

References

Seeger, R. C., Danon, Y. L., Rayner, S. A., & Hoover, F. (1982). Definition of a Thy-1 determinant on human neuroblastoma, glioma, sarcoma, and teratoma cells with a monoclonal antibody. *J Immunol*, *128*(2), 983-989. https://www.ncbi.nlm.nih.gov/pubmed/6172518

Seeger, R. C., Rayner, S. A., Banerjee, A., Chung, H., Laug, W. E., Neustein, H. B., & Benedict, W. F. (1977). Morphology, growth, chromosomal pattern and fibrinolytic activity of two new human neuroblastoma cell lines. *Cancer Res*, *37*(5), 1364-1371. https://www.ncbi.nlm.nih.gov/pubmed/856461

Seibt, T. M., Proneth, B., & Conrad, M. (2019). Role of GPX4 in ferroptosis and its pharmacological implication. *Free Radic Biol Med*, *133*, 144-152. https://doi.org/10.1016/j.freeradbiomed.2018.09.014

Shin, H. Y. (2018). Targeting Super-Enhancers for Disease Treatment and Diagnosis. *Mol Cells*, *41*(6), 506-514. https://doi.org/10.14348/molcells.2018.2297

Sholler, G. L. S., Ferguson, W., Bergendahl, G., Bond, J. P., Neville, K., Eslin, D., Brown, V., Roberts, W., Wada, R. K., Oesterheld, J., Mitchell, D., Foley, J., Parikh, N. S., Eshun, F., Zage, P., Rawwas, J., Sencer, S., Pankiewicz, D., Quinn, M., . . . Kraveka, J. M. (2018). Maintenance DFMO Increases Survival in High Risk Neuroblastoma. *Sci Rep*, *8*(1), 14445. https://doi.org/10.1038/s41598-018-32659-w

Stipanuk, M. H., Dominy, J. E., Jr., Lee, J. I., & Coloso, R. M. (2006). Mammalian cysteine metabolism: new insights into regulation of cysteine metabolism. *J Nutr*, *136*(6 Suppl), 1652S-1659S. https://doi.org/10.1093/jn/136.6.1652S

Sugimoto, T., Tatsumi, E., Kemshead, J. T., Helson, L., Green, A. A., & Minowada, J. (1984). Determination of cell surface membrane antigens common to both human neuroblastoma and leukemia-lymphoma cell lines by a panel of 38 monoclonal antibodies. *J Natl Cancer Inst*, *73*(1), 51-57. https://www.ncbi.nlm.nih.gov/pubmed/6610792

Sugimoto, T., Ueyama, H., Hosoi, H., Inazawa, J., Kato, T., Kemshead, J. T., Reynolds, C. P., Gown, A. M., Mine, H., & Sawada, T. (1991). Alpha-smooth-muscle actin and desmin expressions in human neuroblastoma cell lines. *Int J Cancer*, *48*(2), 277-283. https://doi.org/10.1002/ijc.2910480221

Tao, L., Mohammad, M. A., Milazzo, G., Moreno-Smith, M., Patel, T. D., Zorman, B., Badachhape, A., Hernandez, B. E., Wolf, A. B., Zeng, Z., Foster, J. H., Aloisi, S., Sumazin, P., Zu, Y., Hicks, J., Ghaghada, K. B., Putluri, N., Perini, G., Coarfa, C., & Barbieri, E. (2022). MYCN-driven fatty acid uptake is a metabolic vulnerability in neuroblastoma. *Nat Commun*, *13*(1), 3728. https://doi.org/10.1038/s41467-022-31331-2

Tjaden, B., Baum, K., Marquardt, V., Simon, M., Trajkovic-Arsic, M., Kouril, T., Siebers, B., Lisec, J., Siveke, J. T., Schulte, J. H., Benary, U., Remke, M., Wolf, J., & Schramm, A. (2020). N-Myc-induced metabolic rewiring creates novel therapeutic vulnerabilities in neuroblastoma. *Sci Rep*, *10*(1), 7157. https://doi.org/10.1038/s41598-020-64040-1

Trachootham, D., Alexandre, J., & Huang, P. (2009). Targeting cancer cells by ROS-mediated mechanisms: a radical therapeutic approach? *Nat Rev Drug Discov*, *8*(7), 579-591. https://doi.org/10.1038/nrd2803

Trigg, R. M., & Turner, S. D. (2018). ALK in Neuroblastoma: Biological and Therapeutic Implications. *Cancers (Basel)*, *10*(4). https://doi.org/10.3390/cancers10040113

Tsherniak, A., Vazquez, F., Montgomery, P. G., Weir, B. A., Kryukov, G., Cowley, G. S., Gill, S., Harrington, W. F., Pantel, S., Krill-Burger, J. M., Meyers, R. M., Ali, L., Goodale, A.,

Lee, Y., Jiang, G., Hsiao, J., Gerath, W. F. J., Howell, S., Merkel, E., . . . Hahn, W. C. (2017). Defining a Cancer Dependency Map. *Cell*, *170*(3), 564-576 e516. https://doi.org/10.1016/j.cell.2017.06.010

Tumilowicz, J. J., Nichols, W. W., Cholon, J. J., & Greene, A. E. (1970). Definition of a continuous human cell line derived from neuroblastoma. *Cancer Res*, *30*(8), 2110-2118. https://www.ncbi.nlm.nih.gov/pubmed/5459762

Turner, M. A., Yuan, C. S., Borchardt, R. T., Hershfield, M. S., Smith, G. D., & Howell, P. L. (1998). Structure determination of selenomethionyl S-adenosylhomocysteine hydrolase using data at a single wavelength. *Nat Struct Biol*, *5*(5), 369-376. https://doi.org/10.1038/nsb0598-369

Tweddle, D. A., Malcolm, A. J., Cole, M., Pearson, A. D., & Lunec, J. (2001). p53 cellular localization and function in neuroblastoma: evidence for defective G(1) arrest despite WAF1 induction in MYCN-amplified cells. *Am J Pathol*, *158*(6), 2067-2077. https://doi.org/10.1016/S0002-9440(10)64678-0

Twist, C. J., Schmidt, M. L., Naranjo, A., London, W. B., Tenney, S. C., Marachelian, A., Shimada, H., Collins, M. H., Esiashvili, N., Adkins, E. S., Mattei, P., Handler, M., Katzenstein, H., Attiyeh, E., Hogarty, M. D., Gastier-Foster, J., Wagner, E., Matthay, K. K., Park, J. R., . . . Cohn, S. L. (2019). Maintaining Outstanding Outcomes Using Response- and Biology-Based Therapy for Intermediate-Risk Neuroblastoma: A Report From the Children's Oncology Group Study ANBL0531. *J Clin Oncol*, *37*(34), 3243-3255. https://doi.org/10.1200/JCO.19.00919

Valentijn, L. J., Koster, J., Zwijnenburg, D. A., Hasselt, N. E., van Sluis, P., Volckmann, R., van Noesel, M. M., George, R. E., Tytgat, G. A., Molenaar, J. J., & Versteeg, R. (2015). TERT rearrangements are frequent in neuroblastoma and identify aggressive tumors. *Nat Genet*, *47*(12), 1411-1414. https://doi.org/10.1038/ng.3438

van de Wetering, M., Oving, I., Muncan, V., Pon Fong, M. T., Brantjes, H., van Leenen, D., Holstege, F. C., Brummelkamp, T. R., Agami, R., & Clevers, H. (2003). Specific inhibition of gene expression using a stably integrated, inducible small-interfering-RNA vector. *EMBO Rep*, *4*(6), 609-615. https://doi.org/10.1038/sj.embor.embor865

van den Berg, M. P., Almomani, R., Biaggioni, I., van Faassen, M., van der Harst, P., Sillje, H. H. W., Mateo Leach, I., Hemmelder, M. H., Navis, G., Luijckx, G. J., de Brouwer, A. P. M., Venselaar, H., Verbeek, M. M., van der Zwaag, P. A., Jongbloed, J. D. H., van Tintelen, J. P., Wevers, R. A., & Kema, I. P. (2018). Mutations in CYB561 Causing a Novel Orthostatic Hypotension Syndrome. *Circ Res*, *122*(6), 846-854. https://doi.org/10.1161/CIRCRESAHA.117.311949

van Groningen, T., Koster, J., Valentijn, L. J., Zwijnenburg, D. A., Akogul, N., Hasselt, N. E., Broekmans, M., Haneveld, F., Nowakowska, N. E., Bras, J., van Noesel, C. J. M., Jongejan, A., van Kampen, A. H., Koster, L., Baas, F., van Dijk-Kerkhoven, L., Huizer-Smit, M., Lecca, M. C., Chan, A., . . . Versteeg, R. (2017). Neuroblastoma is composed of two super-enhancer-associated differentiation states. *Nat Genet*, *49*(8), 1261-1266. https://doi.org/10.1038/ng.3899

Van Maerken, T., Ferdinande, L., Taildeman, J., Lambertz, I., Yigit, N., Vercruysse, L., Rihani, A., Michaelis, M., Cinatl, J., Jr., Cuvelier, C. A., Marine, J. C., De Paepe, A., Bracke, M., Speleman, F., & Vandesompele, J. (2009). Antitumor activity of the selective MDM2 antagonist nutlin-3 against chemoresistant neuroblastoma with wild-type p53. *J Natl Cancer Inst*, *101*(22), 1562-1574. https://doi.org/10.1093/jnci/djp355

References

Van Roy, N., Vandesompele, J., Menten, B., Nilsson, H., De Smet, E., Rocchi, M., De Paepe, A., Pahlman, S., & Speleman, F. (2006). Translocation-excision-deletion-amplification mechanism leading to nonsyntenic coamplification of MYC and ATBF1. *Genes Chromosomes Cancer*, *45*(2), 107-117. https://doi.org/10.1002/gcc.20272

Vander Heiden, M. G., Cantley, L. C., & Thompson, C. B. (2009). Understanding the Warburg effect: the metabolic requirements of cell proliferation. *Science*, *324*(5930), 1029-1033. https://doi.org/10.1126/science.1160809

Veschi, V., Petroni, M., Cardinali, B., Dominici, C., Screpanti, I., Frati, L., Bartolazzi, A., Gulino, A., & Giannini, G. (2012). Galectin-3 impairment of MYCN-dependent apoptosis-sensitive phenotype is antagonized by nutlin-3 in neuroblastoma cells. *PLoS One*, *7*(11), e49139. https://doi.org/10.1371/journal.pone.0049139

Vizan, P., Di Croce, L., & Aranda, S. (2021). Functional and Pathological Roles of AHCY. *Front Cell Dev Biol*, *9*, 654344. https://doi.org/10.3389/fcell.2021.654344

Wada, R. K., Seeger, R. C., Brodeur, G. M., Einhorn, P. A., Rayner, S. A., Tomayko, M. M., & Reynolds, C. P. (1993). Human neuroblastoma cell lines that express N-myc without gene amplification. *Cancer*, *72*(11), 3346-3354. https://doi.org/10.1002/1097-0142(19931201)72:11<3346::aid-cncr2820721134>3.0.co;2-e

Wahlstrom, T., & Henriksson, M. A. (2015). Impact of MYC in regulation of tumor cell metabolism. *Biochim Biophys Acta*, *1849*(5), 563-569. https://doi.org/10.1016/j.bbagrm.2014.07.004

Wakamatsu, Y., Watanabe, Y., Nakamura, H., & Kondoh, H. (1997). Regulation of the neural crest cell fate by N-myc: promotion of ventral migration and neuronal differentiation. *Development*, *124*(10), 1953-1962. https://doi.org/10.1242/dev.124.10.1953

Wang, C., Liu, Z., Woo, C. W., Li, Z., Wang, L., Wei, J. S., Marquez, V. E., Bates, S. E., Jin, Q., Khan, J., Ge, K., & Thiele, C. J. (2012). EZH2 Mediates epigenetic silencing of neuroblastoma suppressor genes CASZ1, CLU, RUNX3, and NGFR. *Cancer Res*, *72*(1), 315-324. https://doi.org/10.1158/0008-5472.CAN-11-0961

Wang, H., Hammoudeh, D. I., Follis, A. V., Reese, B. E., Lazo, J. S., Metallo, S. J., & Prochownik, E. V. (2007). Improved low molecular weight Myc-Max inhibitors. *Mol Cancer Ther*, *6*(9), 2399-2408. https://doi.org/10.1158/1535-7163.MCT-07-0005

Wang, T., Liu, L., Chen, X., Shen, Y., Lian, G., Shah, N., Davidoff, A. M., Yang, J., & Wang, R. (2018). MYCN drives glutaminolysis in neuroblastoma and confers sensitivity to an ROS augmenting agent. *Cell Death Dis*, *9*(2), 220. https://doi.org/10.1038/s41419-018-0295-5

Warburg, O. (1956). On respiratory impairment in cancer cells. *Science*, *124*(3215), 269-270. https://www.ncbi.nlm.nih.gov/pubmed/13351639

Westermann, F., Muth, D., Benner, A., Bauer, T., Henrich, K. O., Oberthuer, A., Brors, B., Beissbarth, T., Vandesompele, J., Pattyn, F., Hero, B., Konig, R., Fischer, M., & Schwab, M. (2008). Distinct transcriptional MYCN/c-MYC activities are associated with spontaneous regression or malignant progression in neuroblastomas. *Genome Biol*, *9*(10), R150. https://doi.org/10.1186/gb-2008-9-10-r150

White, P. S., Maris, J. M., Beltinger, C., Sulman, E., Marshall, H. N., Fujimori, M., Kaufman, B. A., Biegel, J. A., Allen, C., Hilliard, C., Valentine, M. B., Look, A. T., Enomoto, H., Sakiyama, S., & Brodeur, G. M. (1995). A region of consistent deletion in neuroblastoma maps within human chromosome 1p36.2-36.3. *Proc Natl Acad Sci U S A*, *92*(12), 5520-5524. https://doi.org/10.1073/pnas.92.12.5520

Wirtz, M., Droux, M., & Hell, R. (2004). O-acetylserine (thiol) lyase: an enigmatic enzyme of plant cysteine biosynthesis revisited in Arabidopsis thaliana. *J Exp Bot*, *55*(404), 1785-1798. https://doi.org/10.1093/jxb/erh201

Wortel, I. M. N., van der Meer, L. T., Kilberg, M. S., & van Leeuwen, F. N. (2017). Surviving Stress: Modulation of ATF4-Mediated Stress Responses in Normal and Malignant Cells. *Trends Endocrinol Metab*, *28*(11), 794-806. https://doi.org/10.1016/j.tem.2017.07.003

Xia, Y., Ye, B., Ding, J., Yu, Y., Alptekin, A., Thangaraju, M., Prasad, P. D., Ding, Z. C., Park, E. J., Choi, J. H., Gao, B., Fiehn, O., Yan, C., Dong, Z., Zha, Y., & Ding, H. F. (2019). Metabolic Reprogramming by MYCN Confers Dependence on the Serine-Glycine-One-Carbon Biosynthetic Pathway. *Cancer Res*, *79*(15), 3837-3850. https://doi.org/10.1158/0008-5472.CAN-18-3541

Xiao, D., Ren, P., Su, H., Yue, M., Xiu, R., Hu, Y., Liu, H., & Qing, G. (2015). Myc promotes glutaminolysis in human neuroblastoma through direct activation of glutaminase 2. *Oncotarget*, *6*(38), 40655-40666. https://doi.org/10.18632/oncotarget.5821

Xiao, Q., Ying, J., Xiang, L., & Zhang, C. (2018). The biologic effect of hydrogen sulfide and its function in various diseases. *Medicine (Baltimore)*, *97*(44), e13065. https://doi.org/10.1097/MD.0000000000013065

Yang, M., & Vousden, K. H. (2016). Serine and one-carbon metabolism in cancer. *Nat Rev Cancer*, *16*(10), 650-662. https://doi.org/10.1038/nrc.2016.81

Yang, W. S., SriRamaratnam, R., Welsch, M. E., Shimada, K., Skouta, R., Viswanathan, V. S., Cheah, J. H., Clemons, P. A., Shamji, A. F., Clish, C. B., Brown, L. M., Girotti, A. W., Cornish, V. W., Schreiber, S. L., & Stockwell, B. R. (2014). Regulation of ferroptotic cancer cell death by GPX4. *Cell*, *156*(1-2), 317-331. https://doi.org/10.1016/j.cell.2013.12.010

Yi, H., Talmon, G., & Wang, J. (2019). Glutamate in cancers: from metabolism to signaling. *J Biomed Res*, *34*(4), 260-270. https://doi.org/10.7555/JBR.34.20190037

Yu, Y., Ding, J., Zhu, S., Alptekin, A., Dong, Z., Yan, C., Zha, Y., & Ding, H. F. (2021). Therapeutic targeting of both dihydroorotate dehydrogenase and nucleoside transport in MYCN-amplified neuroblastoma. *Cell Death Dis*, *12*(9), 821. https://doi.org/10.1038/s41419-021-04120-w

Yue, M., Jiang, J., Gao, P., Liu, H., & Qing, G. (2017). Oncogenic MYC Activates a Feedforward Regulatory Loop Promoting Essential Amino Acid Metabolism and Tumorigenesis. *Cell Rep*, *21*(13), 3819-3832. https://doi.org/10.1016/j.celrep.2017.12.002

Zeid, R., Lawlor, M. A., Poon, E., Reyes, J. M., Fulciniti, M., Lopez, M. A., Scott, T. G., Nabet, B., Erb, M. A., Winter, G. E., Jacobson, Z., Polaski, D. R., Karlin, K. L., Hirsch, R. A., Munshi, N. P., Westbrook, T. F., Chesler, L., Lin, C. Y., & Bradner, J. E. (2018). Enhancer invasion shapes MYCN-dependent transcriptional amplification in neuroblastoma. *Nat Genet*, *50*(4), 515-523. https://doi.org/10.1038/s41588-018-0044-9

Zeineldin, M., Federico, S., Chen, X., Fan, Y., Xu, B., Stewart, E., Zhou, X., Jeon, J., Griffiths, L., Nguyen, R., Norrie, J., Easton, J., Mulder, H., Yergeau, D., Liu, Y., Wu, J., Van Ryn, C., Naranjo, A., Hogarty, M. D., . . . Dyer, M. A. (2020). MYCN amplification and ATRX mutations are incompatible in neuroblastoma. *Nat Commun*, *11*(1), 913. https://doi.org/10.1038/s41467-020-14682-6

Zhang, Y., Tan, H., Daniels, J. D., Zandkarimi, F., Liu, H., Brown, L. M., Uchida, K., O'Connor, O. A., & Stockwell, B. R. (2019). Imidazole Ketone Erastin Induces Ferroptosis and

References

Slows Tumor Growth in a Mouse Lymphoma Model. *Cell Chem Biol*, *26*(5), 623-633 e629. https://doi.org/10.1016/j.chembiol.2019.01.008

Zhao, E., Ding, J., Xia, Y., Liu, M., Ye, B., Choi, J. H., Yan, C., Dong, Z., Huang, S., Zha, Y., Yang, L., Cui, H., & Ding, H. F. (2016). KDM4C and ATF4 Cooperate in Transcriptional Control of Amino Acid Metabolism. *Cell Rep*, *14*(3), 506-519. https://doi.org/10.1016/j.celrep.2015.12.053

Zhao, Y., Li, Y., Zhang, R., Wang, F., Wang, T., & Jiao, Y. (2020). The Role of Erastin in Ferroptosis and Its Prospects in Cancer Therapy. *Onco Targets Ther*, *13*, 5429-5441. https://doi.org/10.2147/OTT.S254995

Zheng, J., Sato, M., Mishima, E., Sato, H., Proneth, B., & Conrad, M. (2021). Sorafenib fails to trigger ferroptosis across a wide range of cancer cell lines. *Cell Death Dis*, *12*(7), 698. https://doi.org/10.1038/s41419-021-03998-w

Zhou, X., Hao, Q., Liao, P., Luo, S., Zhang, M., Hu, G., Liu, H., Zhang, Y., Cao, B., Baddoo, M., Flemington, E. K., Zeng, S. X., & Lu, H. (2016). Nerve growth factor receptor negates the tumor suppressor p53 as a feedback regulator. *Elife*, *5*. https://doi.org/10.7554/eLife.15099

Zhu, S., Lee, J. S., Guo, F., Shin, J., Perez-Atayde, A. R., Kutok, J. L., Rodig, S. J., Neuberg, D. S., Helman, D., Feng, H., Stewart, R. A., Wang, W., George, R. E., Kanki, J. P., & Look, A. T. (2012). Activated ALK collaborates with MYCN in neuroblastoma pathogenesis. *Cancer Cell*, *21*(3), 362-373. https://doi.org/10.1016/j.ccr.2012.02.010

Zimmerman, K. A., Yancopoulos, G. D., Collum, R. G., Smith, R. K., Kohl, N. E., Denis, K. A., Nau, M. M., Witte, O. N., Toran-Allerand, D., Gee, C. E., & et al. (1986). Differential expression of myc family genes during murine development. *Nature*, *319*(6056), 780-783. https://doi.org/10.1038/319780a0

Zimmerman, M. W., Liu, Y., He, S., Durbin, A. D., Abraham, B. J., Easton, J., Shao, Y., Xu, B., Zhu, S., Zhang, X., Li, Z., Weichert-Leahey, N., Young, R. A., Zhang, J., & Look, A. T. (2018). MYC Drives a Subset of High-Risk Pediatric Neuroblastomas and Is Activated through Mechanisms Including Enhancer Hijacking and Focal Enhancer Amplification. *Cancer Discov*, *8*(3), 320-335. https://doi.org/10.1158/2159-8290.CD-17-0993

Zirath, H., Frenzel, A., Oliynyk, G., Segerstrom, L., Westermark, U. K., Larsson, K., Munksgaard Persson, M., Hultenby, K., Lehtio, J., Einvik, C., Pahlman, S., Kogner, P., Jakobsson, P. J., & Henriksson, M. A. (2013). MYC inhibition induces metabolic changes leading to accumulation of lipid droplets in tumor cells. *Proc Natl Acad Sci U S A*, *110*(25), 10258-10263. https://doi.org/10.1073/pnas.1222404110

10 Appendix

Appendix

10.1. Supplementary Figures

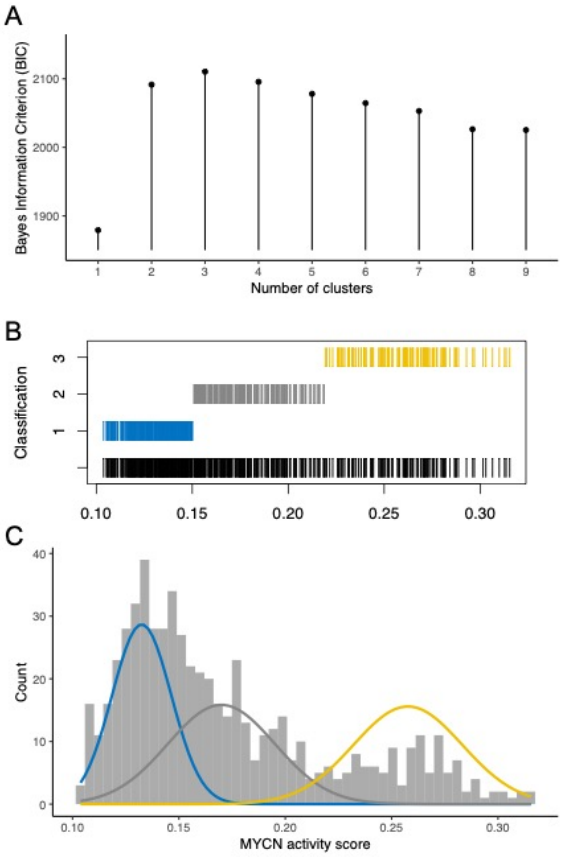

Supplementary Figure 1: Clustering of NB tumors based on their MYC(N) transcriptional activity. (**A**) Bayesian information criterion used to define number of clusters that best describes the data, suggesting the presence of three clusters. (**B** and **C**) Classification of tumors into different groups based on MYC(N) activity scores. Tumors with the lowest MYC(N)-activity (n = 266) are colored in blue, tumors with moderate MYC(N) activity (n = 221) in grey, and tumors with the highest MYC(N)-activity (n = 113) are shown in yellow.

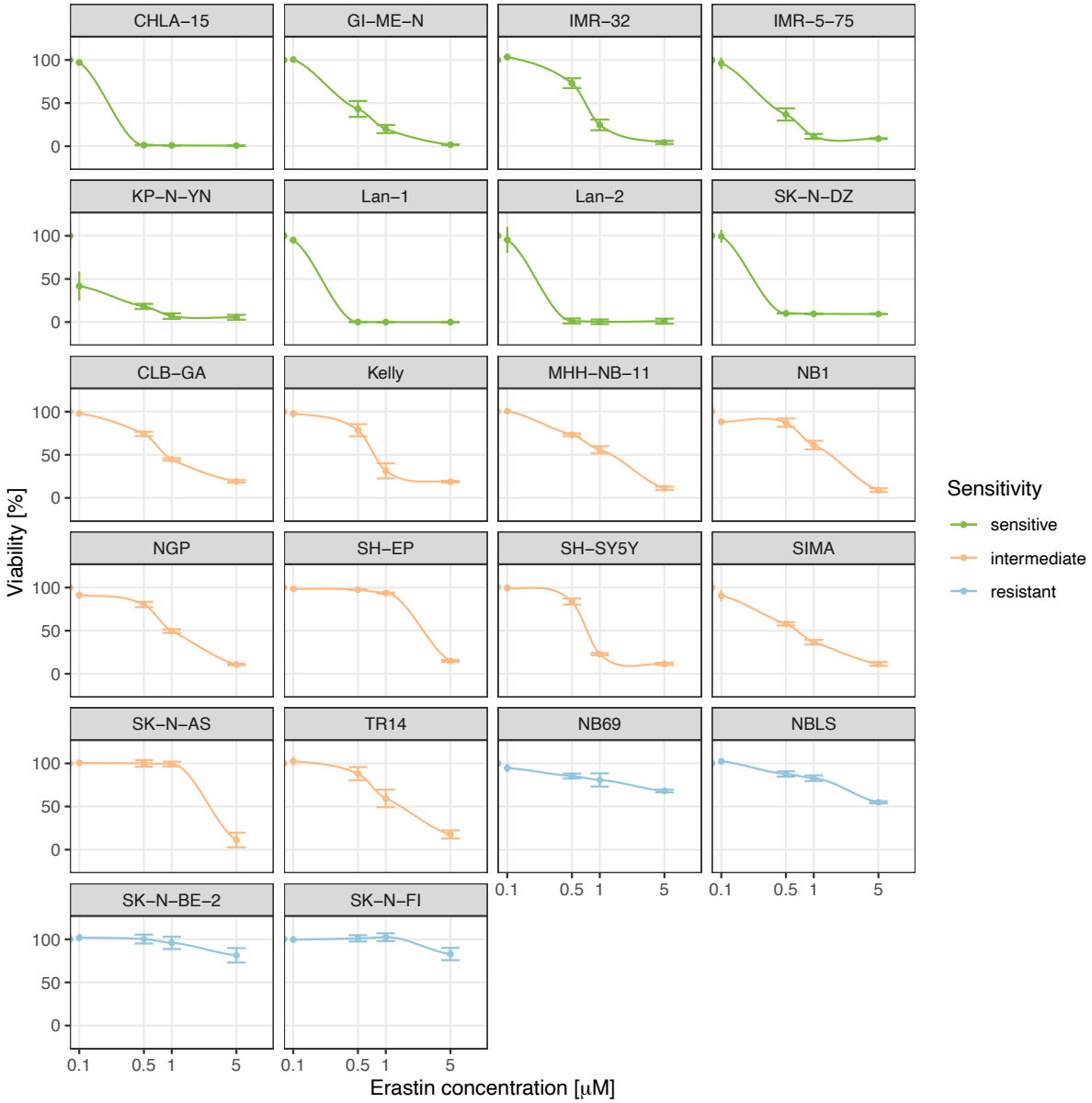

Supplementary Figure 2: Viability curves obtained from erastin titration expriments performed for a large panel of NB cell lines.
The plots display the viability of different cell lines under varying concentrations of erastin, with each cell line represented by a separate plot. The x-axis represents the concentration of erastin and the y-axis represents the viability of the cells after 1 hour. Cell lines are color-coded based on their sensitivity to erastin as indicated in the legend. $n_{biol.rep.} = 3$.

Appendix

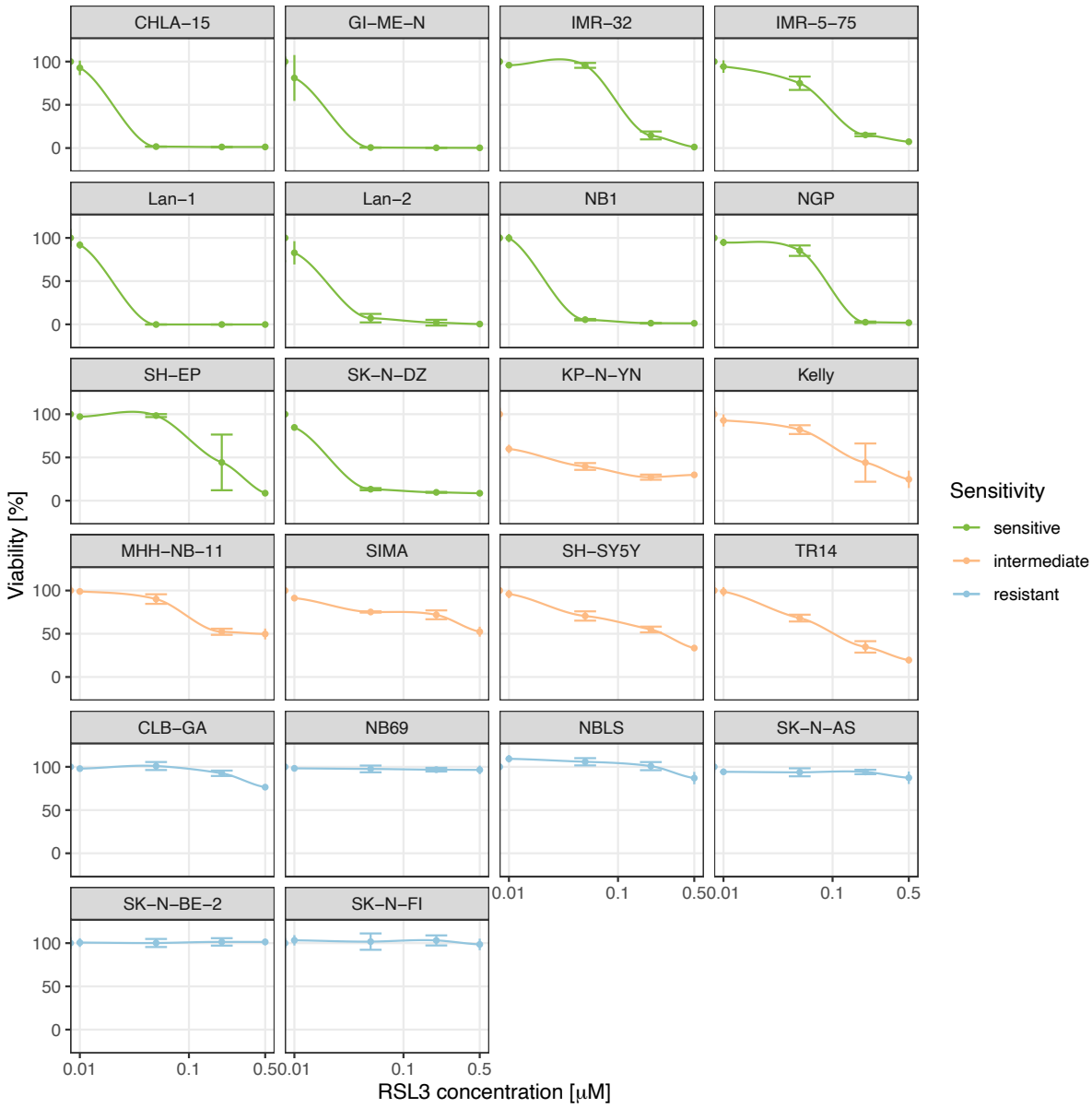

Supplementary Figure 3: Viability curves obtained from RSL3 titration expriments performed for a large panel of NB cell lines.
The plots display the viability of different cell lines under varying concentrations of RSL3, with each cell line represented by a separate plot. The x-axis represents the concentration of RSL3 and the y-axis represents the viability of the cells after 1 hour. Cell lines are color-coded based on their sensitivity to RSL3 as indicated in the legend. $n_{biol.rep.} = 3$.

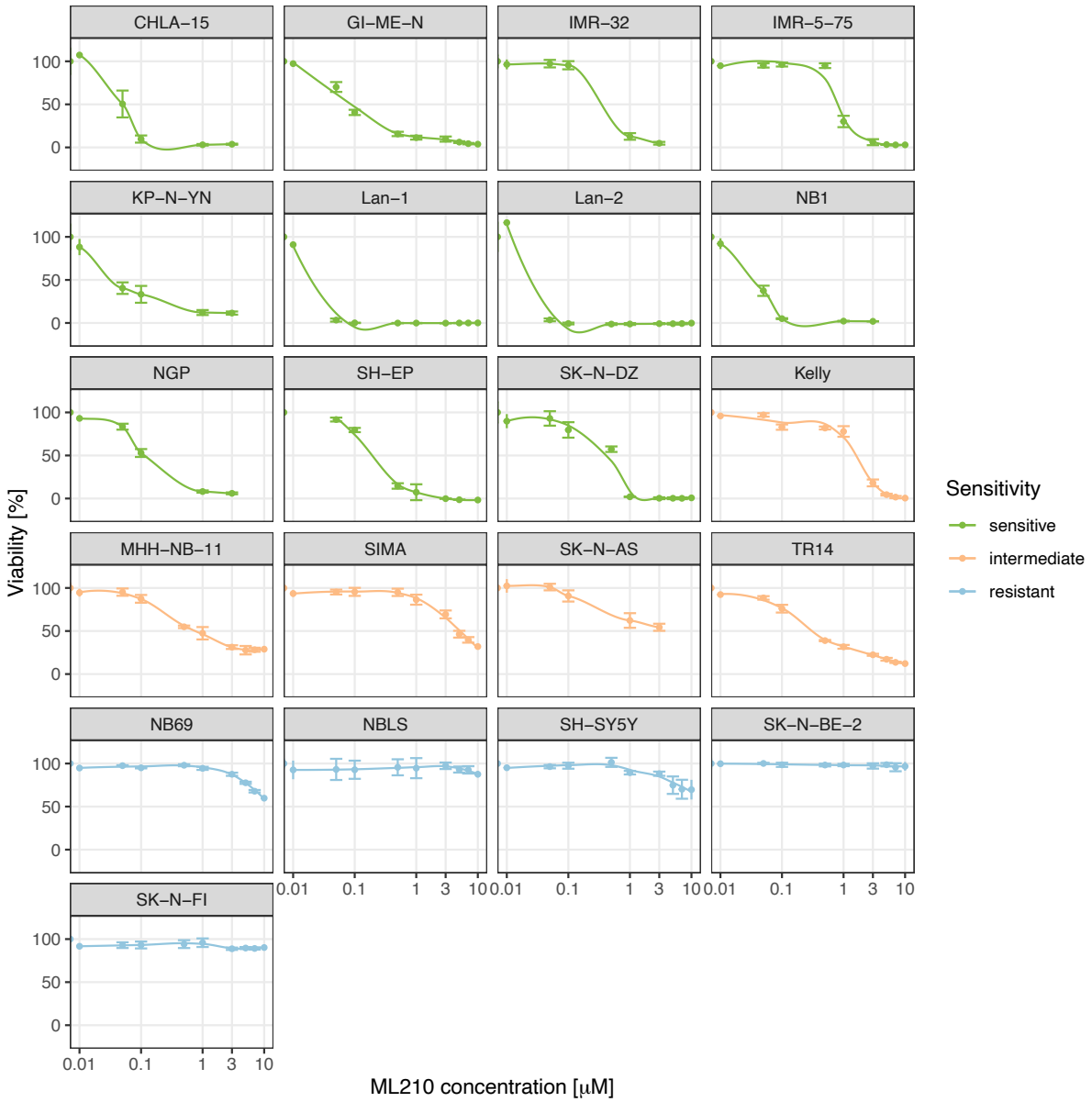

Supplementary Figure 4: Viability curves obtained from ML210 titration expriments performed for a large panel of NB cell lines.
The plots display the viability of different cell lines under varying concentrations of ML210, with each cell line represented by a separate plot. The x-axis represents the concentration of ML210 and the y-axis represents the viability of the cells after 1 hour. Cell lines are color-coded based on their sensitivity to ML210 as indicated in the legend. $n_{biol.rep.} = 3$.

Appendix

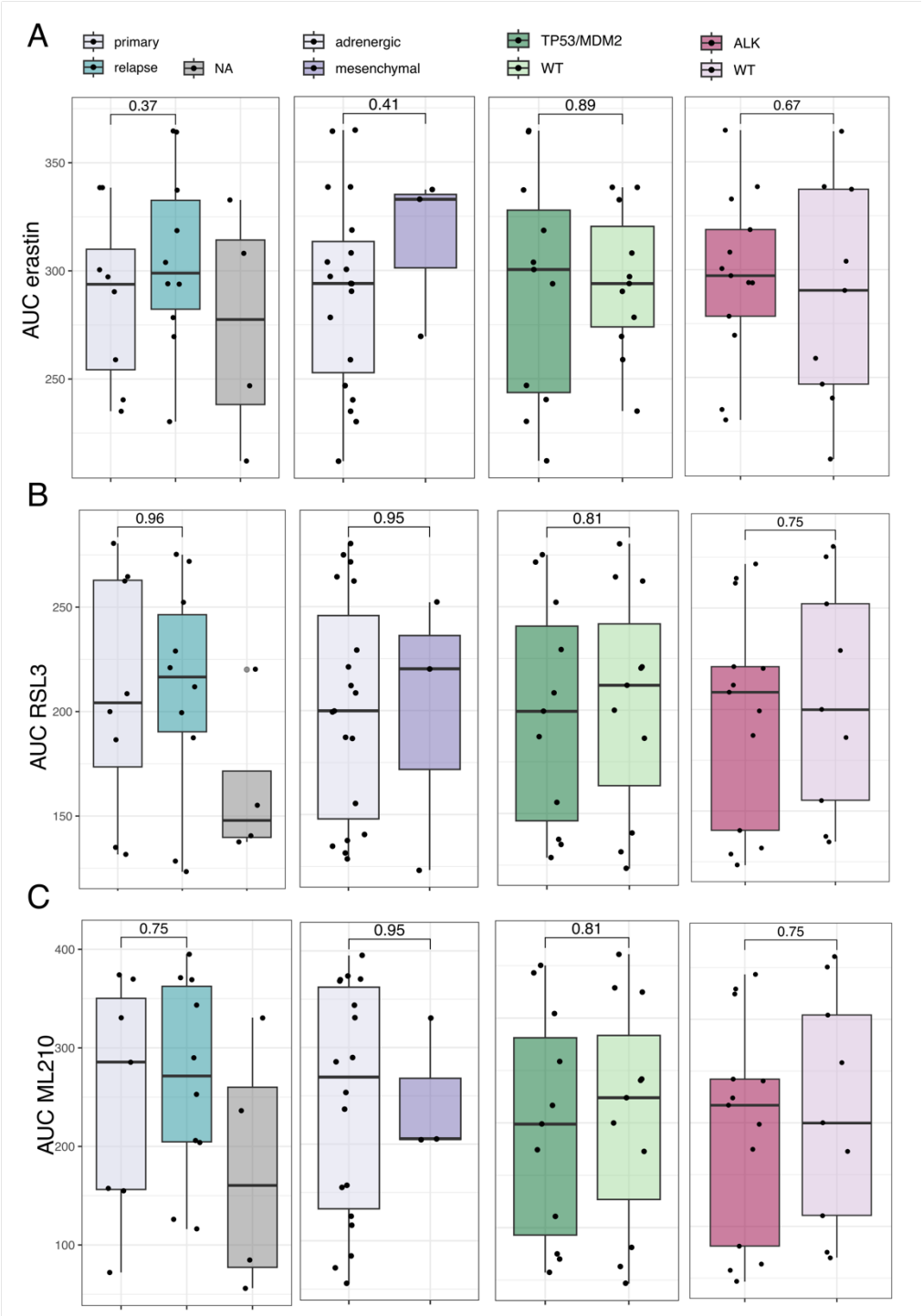

Supplementary Figure 5: Impact of various NB markers on ferroptosis sensitivity induces by FINs.
The impact of the status of the tumor treatment at the time of the cell line establishment, cell identity and the mutation status in *TP53*/*ALK* pathways on sensitivity to (A) erastin, (B) RSL3 and (C) ML210. Primary ($n_{erastin}$ = 8, n_{RSL3} = 8, n_{ML210} = 7) cell lines are presented in blue, relapse (n = 10) cell lines in light grey. NA (n = 4) – status unknown. Adrenergic ($n_{erastin}$ = 19, n_{RSL3} = 19, n_{ML210} = 19) cells are presented in light violet, and mesenchymal (n = 3) in dark violet. Cell lines with *TP53*/*MDM2* mutations (n=11) are shown in dark green, and WT (n in light green and *ALK* status on ML210 sensitivity. *TP53/MDM2* altered (n = 11) cell lines are presented in dark green, while wild-type ($n_{erastin}$ = 9, n_{RSL3} = 9, n_{ML210} = 10) in light green. *ALK*-mutated/ amplified (n = 12, $n_{erastin}$ = 13, n_{RSL3} = 13) cell lines are colored in dark pink, while wild-type (n = 9) in light pink. The statical significance was assessed using un unpaired t-test.

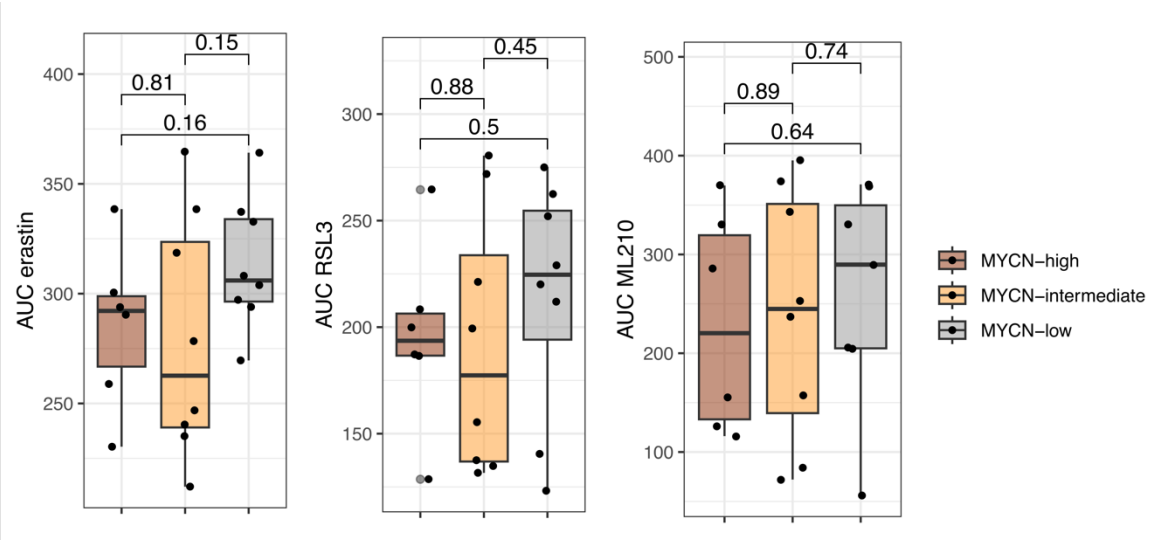

Supplementary Figure 6: Analysis of cell line's sensitivity to FINs with respect to MYC(N) activity.
Cell lines were classified into two groups based on their MYC(N) activity scores. Cell lines (n = 6) with high-MYCN activity are shown in brown, cell lines (n = 8) are colored in orange, and cell lines (n = 7) with the low-MYC(N) activity are colored in grey. The significance was tested using an unpaired t-test.

Appendix

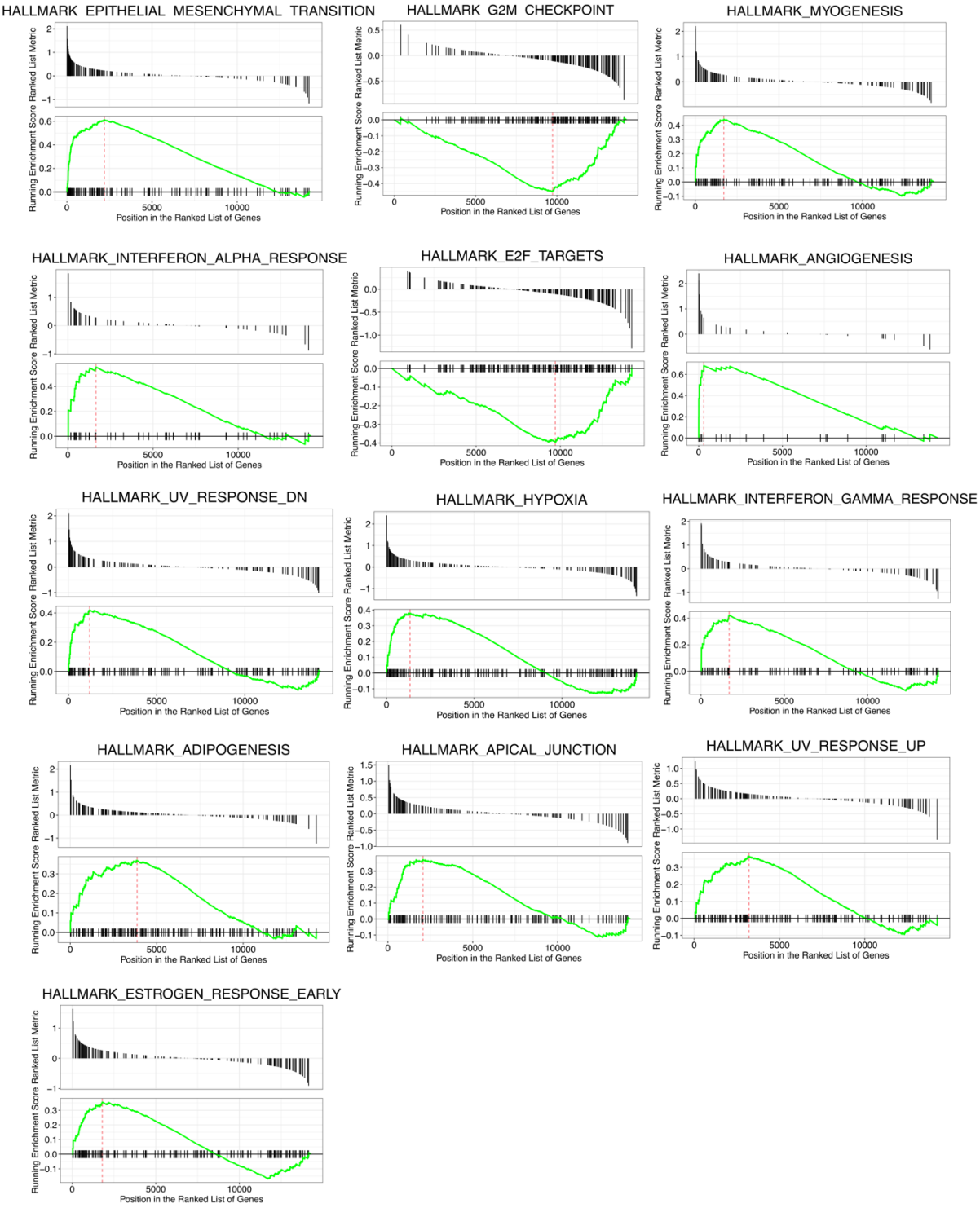

Supplementary Figure 7: Graphical representation of the enrichment scores for each significantly enriched gene set upon *CTH* knockdown.
A red line indicates the location of the maximum enrichment score, while the black lines in the Running Enrichment Score indicate the location of the gene set's members in the ranked list of genes, highlighting the leading-edge subset. The Ranked list metric is also shown, representing the value of the ranking metric (log2 fold change) as the analysis moves down the list of ranked genes, and it measures a correlation between a gene and a phenotype.

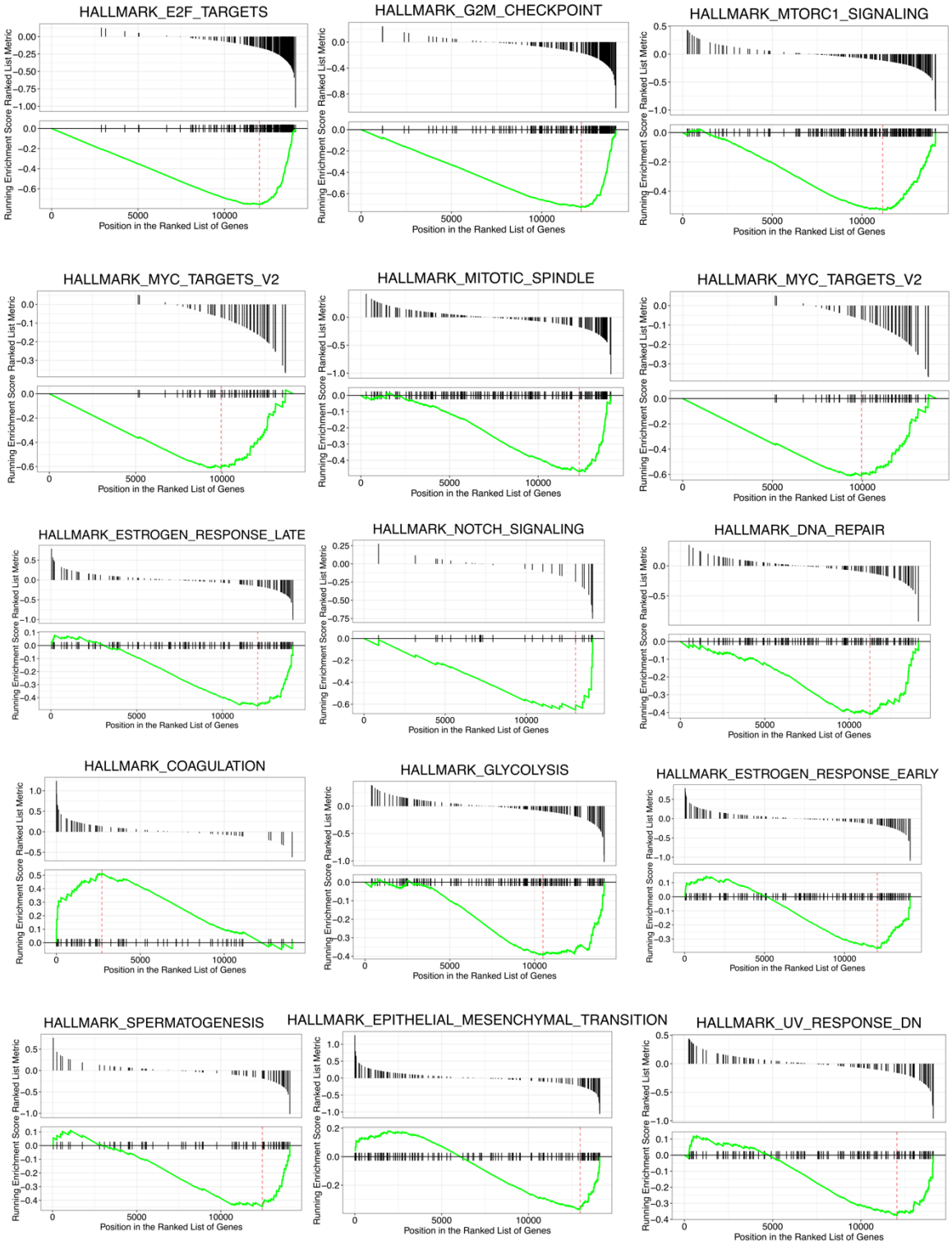

Supplementary Figure 8: Graphical representation of the enrichment scores for each significantly enriched gene set upon *AHCY* knockdown.
A red line indicates the location of the maximum enrichment score, while the black lines in the Running Enrichment Score indicate the location of the gene set's members in the ranked list of genes, highlighting the leading-edge subset. The Ranked list metric is also shown, representing the value of the ranking metric (log2 fold change) as the analysis moves down the list of ranked genes, and it measures a correlation between a gene and a phenotype.

Appendix

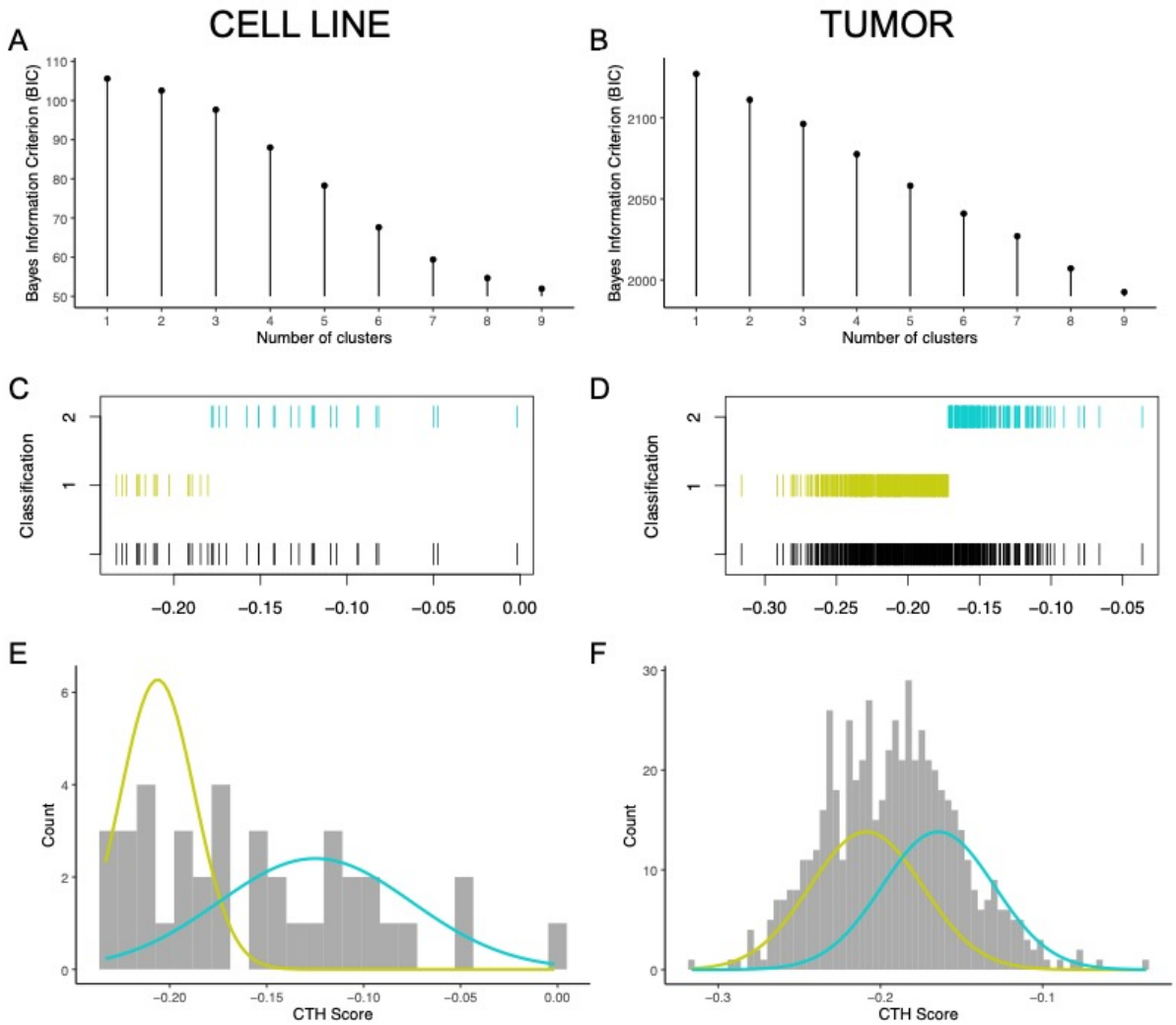

Supplementary Figure 9: Classification of NB cell line and tumor samples based on their CTH knockdown signature score.
(**A** and **B**) Bayesian information criterion used to define number of clusters that best describes the cell line (A) and (B) tumor data. (**C - F**) Classification of cell lines (C, E) and tumors (D, F) into different groups based on CTH knockdown signature scores. Cell lines (n = 11) and tumors (n = 420) with low CTH knockdown signature scores (CTH-high) are colored in green, while cell lines (n = 20) and tumors (n = 180) with the high CTH knockdown signature scores (CTH-low) are shown in yellow.

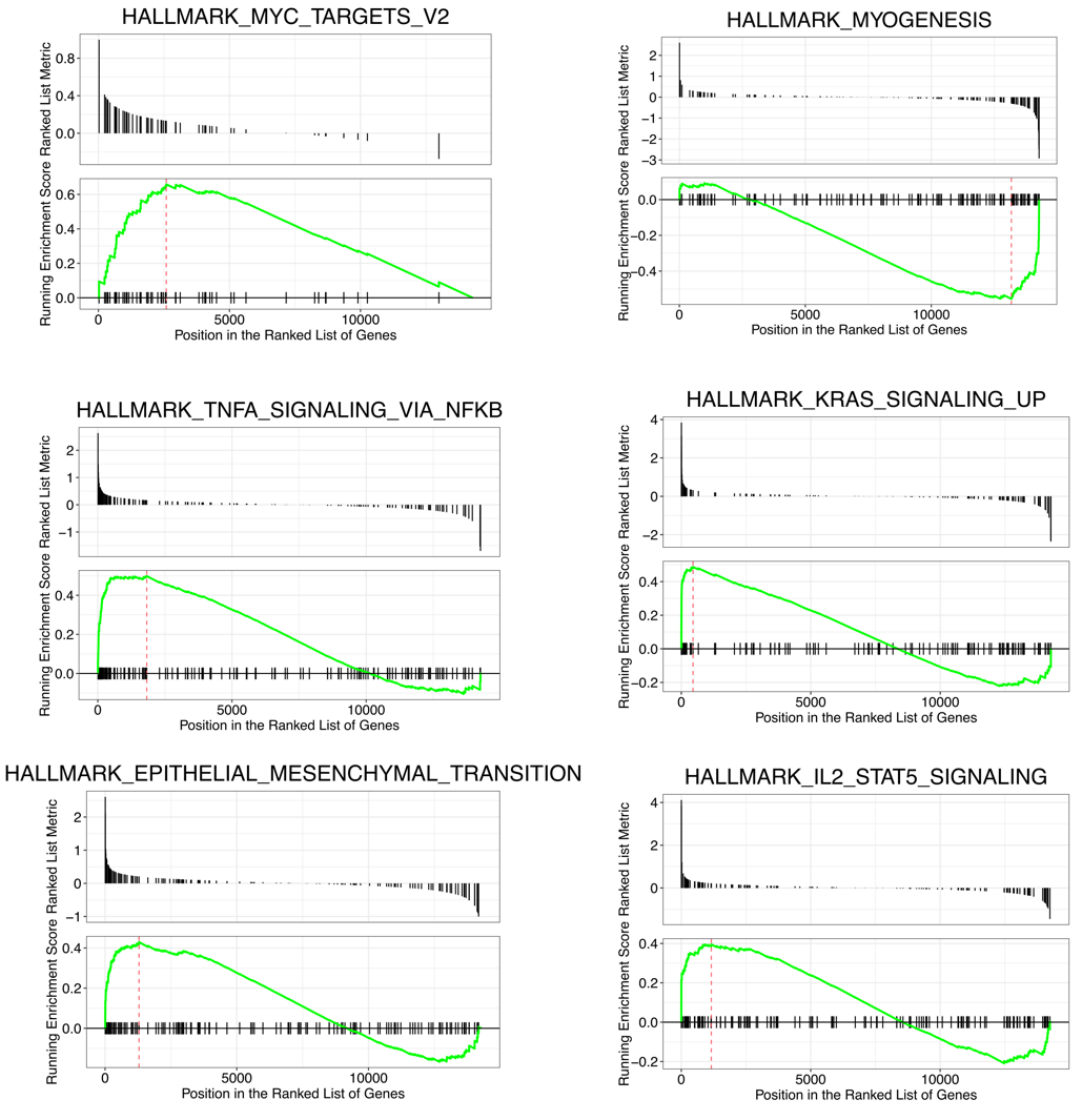

Supplementary Figure 10: Graphical view of the enrichment scores for each significantly enriched gene set upon *GPX4* knockdown.
A red line indicates the location of the maximum enrichment score, while the black lines in the Running Enrichment Score indicate the location of the gene set's members in the ranked list of genes, highlighting the leading-edge subset. The Ranked list metric is also shown, representing the value of the ranking metric (log2 fold change) as the analysis moves down the list of ranked genes, and it measures a correlation between a gene and a phenotype.

Appendix

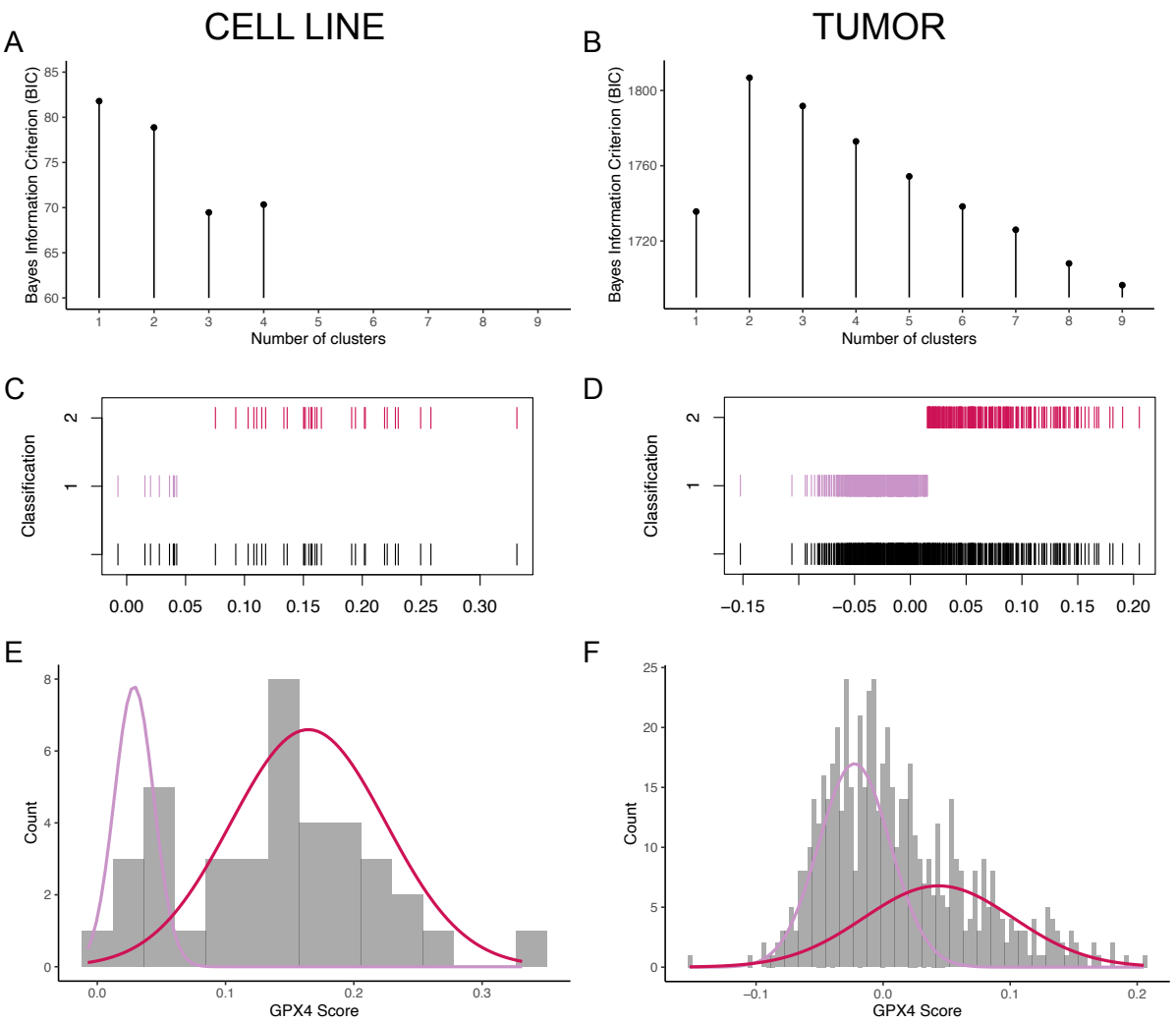

Supplementary Figure 11: Classification of NB cell line and tumor samples based on their GPX4 knockdown signature score.
(**A** and **B**) Bayesian information criterion used to define number of clusters that best describes the cell line (A) and (B) tumor data. (**C - F**) Classification of cell lines (C, E) and tumors (D, F) into different groups based on GPX4 knockdown signature scores. Cell lines (n = 7) and tumors (n = 368) with low GPX4 knockdown signature scores (GPX4-high) are colored in light pink, while cell lines (n = 24) and tumors (n = 232) with high GPX4 knockdown signature scores (GPX4-low) are shown in dark pink.

10.2. Supplementary Tables

Supplementary Table 1: Overview of NB cell lines used in this study.
Genetic description, type, cell line status at the time of establishment, TP53/MDM2 and ALK pathways status, as well as AUC values derived from cystine deprivation and FINs treatment experiments. AUC values were calculated using pROC R package. Primary – pre-treatment, relapse – post-treatment, WT-wilde-type, mut – mutation/amplification., AUC – area under the curve.

Cell line	Genetic description	Type	Treatment	TP53 MDM2	ALK	AUC erastin	AUC RSL3	AUC ML210	AUC cys
CHLA-15	c-$MYC_{amplified}$	adrenergic	primary	WT	mut	235.1	131.6	72.13	208.9
CHLA-20	c-$MYC_{amplified}$	adrenergic	relapse	WT	mut	NA	NA	NA	612.9
CHP-126	$MYCN_{amplified}$	adrenergic	primary	WT	WT	NA	NA	NA	346
CHP-134	$MYCN_{amplified}$	adrenergic	relapse	WT	WT	NA	NA	NA	482.1
CLB-GA	$TERT_{pos}$	adrenergic	primary	WT	mut	297.2	262.3	NA	535.7
GI-ME-N	$TERT_{pos}$	mesenchymal	relapse	WT	mut	269.6	123.3	205.6	154.2
HD-N-33	$TERT_{pos}$	mesenchymal	NA	WT	WT	NA	NA	NA	478.5
IMR-32	$MYCN_{amplified}$	adrenergic	primary	WT	WT	290.4	199.9	155	412.6
IMR-5-75	$MYCN_{amplified}$	adrenergic	primary	WT	WT	258.9	186.4	285.6	166.9
Kelly	$MYCN_{amplified}$	adrenergic	primary	mut	mut	300.5	208.5	330.7	487.5
KP-N-YN	$MYCN_{amplified}$	adrenergic	NA	mut	WT	212.1	155.3	84.36	483.6
Lan-1	$MYCN_{amplified}$	adrenergic	relapse	mut	mut	230.3	128.6	125.8	93.94
Lan-2	$MYCN_{amplified}$	adrenergic	primary	mut	WT	240.4	134.9	157.7	NA
Lan-5	$MYCN_{amplified}$	adrenergic	primary	WT	mut	NA	NA	NA	534.5
Lan-6	ALT_{pos}	adrenergic	relapse	WT	mut	NA	NA	NA	184.4
LS	$MYCN_{amplified}$	adrenergic	relapse	mut	WT	NA	NA	NA	185.5
MHH-NB-11	$MYCN_{amplified}$	adrenergic	relapse	mut	WT	303.9	229.1	289.7	NA
NB1	$MYCN_{amplified}$	adrenergic	NA	WT	mut	308.1	140.5	56.15	436.6
NB69	c-$MYC_{translocated}$	adrenergic	primary	WT	mut	338.5	264.5	369.8	380.7
NBLS	$MYCN_{translocated}$	adrenergic	primary	WT	WT	338.5	280.5	374.4	456.6
NGP	$MYCN_{amplified}$	adrenergic	relapse	mut	mut	293.9	187.3	116.1	240.1
SH-EP	c-$MYC_{translocated}$	mesenchymal	NA	WT	mut	332.8	220.1	330.7	273.9
SH-SY5Y	c-$MYC_{translocated}$	adrenergic	relapse	WT	mut	294	212	370.9	558.5
Sima	$MYCN_{amplified}$	adrenergic	relapse	WT	mut	278.4	221.1	343.4	597.1
SK-N-AS	c-$MYC_{translocated}$	mesenchymal	relapse	mut	WT	337.3	252.1	204.3	526.5
SK-N-BE-2	$MYCN_{amplified}$	adrenergic	relapse	mut	mut	364.7	271.7	395.2	524.5
SK-N-DZ	$MYCN_{amplified}$	adrenergic	NA	mut	WT	246.9	137.6	236.5	174.7
SK-N-FI	ALT_{pos}	adrenergic	relapse	mut	WT	364.2	275.1	368.8	450.2
SK-N-SH	c-$MYC_{translocated}$	dual	relapse	WT	mut	NA	NA	NA	501.1
SMS-KCNR	$MYCN_{amplified}$	adrenergic	relapse	WT	mut	NA	NA	NA	514.2
TR14	$MYCN_{amplified}$	adrenergic	relapse	mut	mut	318.6	199.4	253.2	475.3

Supplementary Table 2: Correlation of gene expression to ferroptosis induction.
Results of Pearson's correlation analysis between normalized gene expression data and cell lines' sensitivity to FINs treatment containing only significant results overlapping across all the treatments. Official gene symbol annotation was not aviable for gene *ENSG00000261254*.

ENSEMBL ID	Gene Symbol	AUC RSL3	AUC ML210	AUC Cys	AUC Erastin
ENSG00000265282	*AC005828.4*	0.70	0.64	0.47	0.64
ENSG00000159640	*ACE*	0.65	0.60	0.52	0.56
ENSG00000184378	*ACTRT3*	0.70	0.50	0.45	0.71
ENSG00000148848	*ADAM12*	0.79	0.62	0.61	0.64
ENSG00000157510	*AFAP1L1*	0.73	0.79	0.52	0.72
ENSG00000042286	*AIFM2*	0.65	0.47	0.40	0.73
ENSG00000234944	*AL365199.1*	0.59	0.53	0.49	0.52

Appendix

ENSG00000156966	*B3GNT7*	0.57	0.61	0.40	0.44
ENSG00000164619	*BMPER*	0.57	0.59	0.40	0.62
ENSG00000118004	*COLEC11*	0.52	0.60	0.42	0.49
ENSG00000008283	*CYB561*	0.73	0.70	0.47	0.69
ENSG00000107984	*DKK1*	0.71	0.47	0.44	0.50
ENSG00000150672	*DLG2*	0.72	0.54	0.48	0.54
ENSG00000188522	*FAM83G*	0.45	0.47	0.39	0.46
ENSG00000064763	*FAR2*	0.55	0.51	0.47	0.45
ENSG00000131979	*GCH1*	0.70	0.46	0.54	0.49
ENSG00000127920	*GNG11*	0.50	0.50	0.46	0.56
ENSG00000119669	*IRF2BPL*	0.64	0.63	0.38	0.52
ENSG00000112769	*LAMA4*	0.69	0.66	0.47	0.51
ENSG00000104903	*LYL1*	0.52	0.54	0.45	0.51
ENSG00000254087	*LYN*	0.61	0.46	0.39	0.44
ENSG00000101460	*MAP1LC3A*	0.54	0.50	0.44	0.51
ENSG00000166823	*MESP1*	0.60	0.49	0.39	0.53
ENSG00000224287	*MSL3P1*	0.82	0.57	0.44	0.61
ENSG00000172936	*MYD88*	0.53	0.51	0.43	0.52
ENSG00000116981	*NT5C1A*	0.61	0.70	0.44	0.45
ENSG00000089127	*OAS1*	0.74	0.67	0.43	0.66
ENSG00000177989	*ODF3B*	0.52	0.50	0.40	0.46
ENSG00000112038	*OPRM1*	0.69	0.63	0.45	0.55
ENSG00000171631	*P2RY6*	0.70	0.63	0.45	0.63
ENSG00000236671	*PRKG1-AS1*	0.74	0.50	0.52	0.52
ENSG00000129667	*RHBDF2*	0.50	0.53	0.46	0.59
ENSG00000187994	*RINL*	0.52	0.56	0.47	0.46
ENSG00000164403	*SHROOM1*	0.51	0.48	0.39	0.52
ENSG00000149577	*SIDT2*	0.53	0.54	0.39	0.70
ENSG00000036565	*SLC18A1*	0.63	0.59	0.38	0.43
ENSG00000160326	*SLC2A6*	0.58	0.49	0.41	0.60
ENSG00000170921	*TANC2*	0.58	0.48	0.45	0.54
ENSG00000234224	*TMEM229A*	0.53	0.52	0.48	0.48
ENSG00000056558	*TRAF1*	0.62	0.62	0.52	0.56
ENSG00000183696	*UPP1*	0.57	0.46	0.39	0.65
ENSG00000179403	*VWA1*	0.49	0.55	0.39	0.48
ENSG00000260855	*AL591848.4*	-0.61	-0.63	-0.39	-0.49
ENSG00000065243	*PKN2*	-0.57	-0.47	-0.41	-0.56
ENSG00000144283	*PKP4*	-0.58	-0.49	-0.40	-0.50
ENSG00000153201	*RANBP2*	-0.49	-0.53	-0.40	-0.56
ENSG00000133104	*SPART*	-0.55	-0.66	-0.39	-0.58
ENSG00000136111	*TBC1D4*	-0.62	-0.49	-0.39	-0.60
ENSG00000187187	*ZNF546*	-0.48	-0.54	-0.46	-0.52
ENSG00000261254		-0.73	-0.58	-0.47	-0.69

Supplementary Table 3: Differentially expressed genes upon CTH downregulation.
Log-fold-change (logFC), log-counts-per-milion (logCPM), p-values and FDR-corrected p-values are depicted. Only significant results are included.

Gene symbol	logFC	logCPM	PValue	FDR
DUSP27	4.03	-1.47	3.11E-109	5.56E-106
STRA6	2.51	2.93	2.35E-113	5.59E-110
AGT	2.44	-0.94	1.70E-47	8.99E-45
S100A4	2.40	2.20	2.21E-94	2.86E-91
TYRP1	2.27	0.01	4.15E-47	2.12E-44
HRC	2.21	2.23	8.93E-76	8.51E-73
ENPP2	2.17	1.16	9.16E-29	2.26E-26
COL3A1	2.12	6.52	1.13E-135	5.37E-132
CCDC80	2.07	0.60	1.03E-94	1.47E-91
BMP5	2.03	-0.66	1.07E-09	8.90E-08
MGAM	1.99	-1.40	4.50E-25	1.05E-22
COL26A1	1.97	-0.65	5.04E-08	3.48E-06
PCDH7	1.94	2.46	3.08E-78	3.38E-75
SAMD5	1.94	-0.41	1.55E-06	9.05E-05
ZNF467	1.92	0.31	1.22E-15	1.71E-13
ARID5B	1.92	1.34	1.01E-59	6.56E-57
CAMK2A	1.90	-0.84	4.37E-10	3.85E-08
LINC00890	1.88	0.48	7.08E-11	6.57E-09
IFI44L	1.85	3.55	1.15E-101	1.82E-98
GABRG1	1.84	-0.88	6.52E-18	1.08E-15
IFI44	1.82	0.62	1.44E-37	5.27E-35
SMTNL2	1.81	1.35	8.01E-56	4.97E-53
PALMD	1.69	2.98	8.41E-89	1.00E-85
TMEM100	1.67	-0.71	2.14E-16	3.21E-14
ADRA1A	1.66	0.14	5.81E-17	9.11E-15
RARG	1.66	2.79	1.27E-43	5.85E-41
CNTN6	1.66	-0.88	2.66E-07	1.74E-05
FAM198B	1.65	-0.28	2.96E-13	3.32E-11
OLFML3	1.64	3.93	1.50E-138	1.07E-134
ETV5	1.63	2.26	6.54E-33	1.95E-30
TLL1	1.59	1.12	1.58E-38	6.10E-36
C1QTNF1	1.59	-1.00	0.00012588	0.00549679
LUM	1.57	2.75	2.91E-19	5.13E-17
GALNT5	1.56	0.78	1.44E-23	3.07E-21
SNCG	1.53	2.17	2.04E-15	2.80E-13
SPRY4	1.52	0.97	1.63E-11	1.59E-09
TTC24	1.51	0.03	6.02E-20	1.10E-17
PRICKLE2	1.50	0.15	3.19E-15	4.34E-13
NEXN	1.50	1.34	5.94E-33	1.81E-30

CHAC1	1.48	1.41	5.07E-07	3.19E-05
TGFBR2	1.46	2.96	2.83E-55	1.69E-52
GAS2	1.45	1.65	8.61E-45	4.10E-42
ABHD12B	1.45	-0.62	1.28E-13	1.48E-11
PYGL	1.41	5.83	4.71E-114	1.35E-110
MTUS1	1.40	3.30	5.36E-68	4.03E-65
HTR1E	1.36	-0.64	3.96E-14	4.83E-12
RPL22L1	1.34	5.33	8.61E-46	4.24E-43
RP11-145O15.2	1.30	0.37	1.29E-13	1.48E-11
CA10	1.30	1.08	1.11E-16	1.72E-14
SDC1	1.27	4.86	2.85E-19	5.09E-17
CPS1	1.27	0.87	3.61E-13	4.02E-11
DNAI1	1.26	-0.03	6.53E-10	5.52E-08
MLIP	1.26	-0.78	1.95E-09	1.57E-07
SLC6A9	1.24	3.23	3.93E-15	5.30E-13
POU6F2	1.20	0.76	8.35E-11	7.60E-09
STC2	1.20	2.38	7.31E-11	6.73E-09
CNDP1	1.20	-0.28	4.58E-10	3.98E-08
RIMS4	1.19	4.61	1.16E-42	5.19E-40
LEPREL1	1.19	2.18	7.95E-34	2.64E-31
NDST4	1.18	-0.08	2.02E-16	3.08E-14
HOPX	1.18	1.02	5.92E-14	7.16E-12
KAZALD1	1.18	0.35	8.03E-11	7.35E-09
SEMA3C	1.17	2.53	3.61E-33	1.14E-30
FAM47E-STBD1	1.16	-0.03	0.00012122	0.00532575
SGCZ	1.16	-0.06	1.87E-11	1.80E-09
COL1A1	1.15	4.90	6.72E-07	4.15E-05
PRR16	1.14	1.66	4.56E-15	6.09E-13
LPPR4	1.13	5.17	1.29E-41	5.40E-39
RP11-101E14.2	1.13	2.14	1.99E-06	0.00011461
MATN2	1.13	2.22	1.47E-18	2.47E-16
AMPD3	1.13	0.60	5.79E-17	9.11E-15
AP000221.1	1.09	-0.70	0.00055223	0.02119697
PCOLCE	1.08	5.96	1.50E-12	1.60E-10
CSMD3	1.08	1.05	4.74E-09	3.64E-07
ABCA9	1.07	2.50	2.57E-07	1.68E-05
TNFRSF19	1.07	-0.13	6.39E-07	3.96E-05
SLC7A11	1.06	1.66	0.00064658	0.02448929
PKDREJ	1.06	0.06	5.26E-05	0.00246207
PKNOX2	1.06	1.42	1.00E-14	1.28E-12
LIX1	1.05	0.35	6.73E-05	0.00306869
LUZP2	1.05	0.63	5.93E-10	5.07E-08
RMST	1.05	-0.01	0.0007983	0.02968468

ASIC4	1.04	1.19	0.0001113	0.00495104
CDH6	1.04	4.69	2.85E-21	5.70E-19
RP11-449D8.1	1.04	-0.09	4.59E-09	3.54E-07
SEMA3D	1.03	3.25	5.40E-15	7.07E-13
SRCRB4D	1.03	-0.42	0.00020531	0.00854681
RGS4	1.02	4.96	5.19E-07	3.25E-05
IGSF10	1.01	0.60	1.18E-09	9.68E-08
ARSJ	1.01	3.79	5.11E-25	1.18E-22
PDGFRB	1.01	3.09	7.27E-14	8.73E-12
ALPK2	1.01	1.01	1.07E-11	1.08E-09
C11orf96	1.01	1.59	0.00048498	0.01881804
FAM110D	1.01	-0.17	0.0001784	0.00760414
CKMT1A	1.01	3.19	3.85E-19	6.70E-17
FAM196A	1.00	0.55	1.80E-08	1.29E-06
ANO3	1.00	-0.87	6.95E-07	4.28E-05
SYTL1	1.00	0.48	0.00073636	0.02752473
CKMT1B	1.00	4.05	1.84E-23	3.87E-21
C10orf10	1.00	2.00	4.51E-12	4.67E-10
MAP7	1.00	-0.47	1.44E-06	8.50E-05
NTNG1	1.00	3.55	1.28E-14	1.62E-12
JAZF1	0.99	1.36	4.63E-07	2.94E-05
MT-TF	0.99	-0.42	0.00022398	0.0092166
CDH18	0.99	0.62	3.85E-09	3.01E-07
ZNF705E	0.98	-0.35	8.21E-05	0.00372041
SLITRK6	0.98	3.67	7.91E-14	9.41E-12
TRIM54	0.98	-0.14	0.00014373	0.00621899
CD248	0.98	2.67	1.07E-05	0.00055307
TUBA4A	0.97	4.59	4.38E-16	6.38E-14
CGNL1	0.97	1.63	8.58E-10	7.16E-08
GJA3	0.96	1.81	2.28E-09	1.81E-07
LRRC10B	0.96	0.24	4.99E-05	0.00234591
TMEM119	0.96	2.13	1.02E-06	6.22E-05
OSTN	0.95	2.40	7.92E-06	0.0004173
ZCCHC24	0.95	3.38	6.12E-15	7.87E-13
MSX1	0.94	1.46	4.32E-05	0.00204144
RP11-405A12.1	0.94	-0.95	0.00010293	0.00462197
ANKFN1	0.94	0.96	3.38E-05	0.00162992
CNN2	0.94	3.32	1.80E-09	1.46E-07
B3GNT9	0.94	1.91	1.97E-06	0.00011381
SH3RF2	0.94	0.11	2.72E-06	0.0001553
FAAH	0.93	0.51	0.00032083	0.01279633
GRM5	0.93	0.06	0.00032059	0.01279633
BCAN	0.93	1.91	2.98E-07	1.93E-05

PHF15	0.93	3.70	1.41E-11	1.39E-09
SULF1	0.92	2.01	1.24E-10	1.11E-08
NCAM2	0.92	3.32	1.34E-11	1.34E-09
MYLIP	0.92	2.11	4.92E-10	4.26E-08
SCN1A	0.91	2.13	0.00013227	0.00574081
PCDH9	0.91	3.70	8.85E-08	5.99E-06
CTB-158E9.1	0.91	-0.58	0.00021001	0.00871745
COL6A6	0.90	0.57	5.64E-05	0.00263042
ANKRD34A	0.90	1.81	6.01E-06	0.00032484
MOXD1	0.89	0.90	4.76E-06	0.00026266
KAL1	0.89	3.27	8.80E-08	5.98E-06
BTN3A3	0.88	1.96	5.35E-07	3.33E-05
SOBP	0.87	3.16	5.51E-10	4.74E-08
CHRNG	0.87	0.62	0.00038026	0.0149993
ZNF385A	0.87	4.90	2.09E-07	1.37E-05
TGFBR3	0.86	2.48	7.20E-08	4.92E-06
UPK1B	0.86	-0.79	0.00120085	0.04276052
FGF10	0.86	0.38	0.00023914	0.00975621
GLI1	0.85	1.68	4.54E-06	0.00025116
ETS1	0.85	3.19	1.87E-10	1.66E-08
FABP3	0.84	2.72	9.27E-07	5.68E-05
ALPK1	0.84	1.87	2.64E-05	0.00129767
ST6GALNAC2	0.84	1.87	3.82E-05	0.00182606
STRCP1	0.83	0.17	0.0011511	0.04119427
MMP2	0.83	6.16	2.55E-14	3.14E-12
WNT5A	0.83	2.83	2.75E-07	1.79E-05
RAB38	0.83	0.95	7.70E-06	0.00040738
FZD6	0.82	1.28	0.00026417	0.01071603
HEATR4	0.82	0.54	0.00084435	0.03131553
TNFAIP2	0.82	1.89	0.00026711	0.01080463
STEAP3	0.81	3.78	4.00E-07	2.56E-05
PLCH1	0.80	4.21	3.30E-08	2.33E-06
TMEM255A	0.80	3.50	1.02E-05	0.00052965
CNTN3	0.80	1.54	0.00028155	0.0113565
ANO4	0.80	2.14	0.00010785	0.00481265
BHLHE40	0.80	3.32	6.64E-05	0.00304088
CDS1	0.79	1.88	0.00010349	0.00463261
DDR1	0.78	4.96	3.76E-05	0.00180362
PCDH10	0.77	3.75	9.26E-06	0.0004808
LHFP	0.77	2.48	4.48E-05	0.00211185
PCDHAC2	0.76	2.90	1.46E-05	0.00074517
ARHGAP31	0.76	1.78	0.00011432	0.00504169
VEGFC	0.76	2.69	0.00047824	0.01860701

THBS4	0.75	1.46	0.00113584	0.04075039
F3	0.75	2.57	0.00010072	0.0045368
KAZN	0.75	4.11	0.00020299	0.00852508
MAML2	0.74	2.48	0.00044956	0.01763527
DACT3	0.74	2.65	0.00127457	0.04527255
SCG2	0.74	5.16	0.00065234	0.02464214
BCHE	0.74	4.02	5.99E-05	0.00278655
GDF11	0.74	5.68	4.98E-08	3.45E-06
METTL12	0.74	2.63	0.00109818	0.03949868
NID2	0.73	2.70	0.00017378	0.00742939
RP11-512M8.3	0.73	2.88	0.0001144	0.00504169
MFAP4	0.73	7.30	0.00072926	0.02733102
PRSS35	0.73	2.62	0.00133553	0.0473203
KIAA1671	0.72	2.82	9.61E-05	0.00434229
PTGFRN	0.72	6.90	4.15E-11	3.92E-09
EDA	0.72	2.56	0.00094028	0.03425077
FRZB	0.72	3.91	3.14E-06	0.00017658
SIX1	0.72	3.97	0.0002049	0.00854681
PPM1H	0.72	4.37	0.00018558	0.00786302
INPP1	0.71	2.63	0.00118507	0.04230398
PVR	0.70	4.43	6.15E-05	0.00284089
UNC5C	0.69	6.44	0.00037922	0.0149993
KIRREL	0.67	6.96	0.00086804	0.03194528
LRRN1	-0.68	7.71	0.00079667	0.02968468
EGFLAM	-0.69	5.90	1.12E-05	0.00057544
CREB3L4	-0.69	5.64	0.00019763	0.00832444
ELAVL4	-0.69	8.04	0.00047748	0.01860701
C16orf45	-0.69	4.13	0.00068867	0.02594589
KLF7	-0.69	6.66	0.00106731	0.03848532
MTSS1	-0.70	4.37	0.0001604	0.0069193
MTMR12	-0.70	4.82	0.00018665	0.00788513
SATB2	-0.70	5.42	0.00039124	0.01538982
ATL3	-0.70	3.62	0.00101319	0.03671916
DYNC1I2	-0.71	7.07	0.00033418	0.01329161
KIT	-0.71	5.02	0.00087693	0.03218944
C5orf30	-0.71	4.24	6.43E-05	0.0029608
SH3RF1	-0.71	3.47	0.00064505	0.02448929
ST6GAL1	-0.72	6.43	1.86E-05	0.00093667
MBTPS2	-0.72	5.06	0.000221	0.00912048
SULT1C4	-0.72	5.16	0.00021564	0.00892503
RP11-143K11.1	-0.72	5.33	0.00016387	0.00704771
USP14	-0.73	7.61	3.03E-05	0.00147386
NLGN4X	-0.73	5.68	8.02E-09	6.06E-07

Appendix

DCK	-0.73	4.33	0.0008475	0.03135093
FAM188A	-0.74	4.03	2.60E-05	0.00128666
ITGB1	-0.74	7.52	7.03E-06	0.00037614
GLUL	-0.75	7.61	4.54E-08	3.16E-06
KCTD20	-0.75	7.42	3.05E-06	0.00017225
STX7	-0.75	3.87	2.48E-05	0.00122786
HRK	-0.75	2.49	0.00058994	0.02252353
FABP5	-0.76	6.93	1.90E-05	0.00095202
GLOD4	-0.76	6.47	3.77E-07	2.42E-05
VSTM2A	-0.77	4.49	2.85E-06	0.00016231
CADM4	-0.77	3.34	0.00045337	0.01773597
SBK1	-0.77	6.71	0.00054625	0.02102397
TMEM170B	-0.77	4.10	0.00093084	0.0339937
OPA1	-0.78	6.98	1.23E-08	9.07E-07
ST8SIA2	-0.78	6.36	2.44E-14	3.03E-12
PELI2	-0.78	5.16	1.88E-06	0.00010939
KIF21B	-0.78	5.75	0.00059602	0.02269488
MAPK8	-0.78	6.31	2.48E-09	1.96E-07
TGFBR1	-0.78	5.68	5.91E-06	0.00032063
GSTCD	-0.78	4.76	1.14E-06	6.81E-05
NAPB	-0.78	4.61	4.05E-08	2.84E-06
MYT1	-0.79	5.16	2.68E-05	0.00131722
SLC35A3	-0.79	4.57	3.90E-05	0.00185829
AC013394.2	-0.79	4.61	2.97E-06	0.00016822
CD63	-0.79	6.72	3.82E-09	3.00E-07
LYPD6	-0.79	3.45	3.03E-05	0.00147386
BLOC1S6	-0.79	5.89	1.94E-07	1.28E-05
AC023115.4	-0.79	1.55	0.00020448	0.00854681
PGM2L1	-0.79	4.30	0.00012172	0.00533154
KRAS	-0.80	5.83	6.48E-06	0.00034915
TCEA1	-0.80	6.09	2.09E-06	0.00011979
ELAVL3	-0.80	6.11	1.12E-05	0.00057544
TUBA1A	-0.80	10.18	1.15E-09	9.49E-08
LRP6	-0.80	5.98	4.04E-07	2.58E-05
SSTR2	-0.80	7.26	1.39E-08	1.02E-06
RP11-363E7.4	-0.80	1.51	0.0005404	0.02091142
ZMAT3	-0.81	4.72	2.16E-05	0.00107755
MAPK10	-0.81	4.83	1.39E-11	1.37E-09
TAF13	-0.82	4.46	3.60E-05	0.00173095
FRK	-0.82	0.75	0.00086229	0.03181548
AP1S2	-0.82	4.89	0.00056101	0.02147634
COQ7	-0.83	3.73	1.53E-09	1.25E-07
FRMD5	-0.83	2.79	7.76E-05	0.00353098

TOX3	-0.83	3.28	8.43E-06	0.00044247
TTC33	-0.83	3.66	5.52E-06	0.00030076
SOX4	-0.83	7.05	1.34E-08	9.90E-07
C9orf9	-0.84	1.74	0.00011193	0.00496331
LHX9	-0.84	4.55	4.07E-09	3.16E-07
MTFR1	-0.84	5.30	1.81E-10	1.61E-08
THSD7B	-0.84	7.14	5.77E-16	8.24E-14
BHLHE22	-0.85	1.05	1.61E-05	0.00081754
YPEL1	-0.86	3.17	9.77E-08	6.58E-06
DEPDC1	-0.86	5.88	6.36E-09	4.83E-07
RNGTT	-0.86	5.10	1.50E-11	1.46E-09
FSD1L	-0.86	3.66	0.00017325	0.00742882
CLVS2	-0.86	6.27	4.30E-06	0.00023902
ZIC3	-0.86	4.16	1.52E-08	1.10E-06
OSTM1	-0.88	3.68	8.91E-12	9.09E-10
SQLE	-0.88	7.20	2.38E-17	3.90E-15
ERV3-1	-0.88	3.52	0.0001303	0.00567241
CEP97	-0.88	4.72	5.76E-08	3.95E-06
UBE2W	-0.88	4.25	1.51E-06	8.85E-05
TXNIP	-0.88	5.89	1.04E-10	9.39E-09
ZNF654	-0.89	3.05	1.06E-08	7.93E-07
PMEL	-0.89	1.35	5.38E-06	0.00029449
SORT1	-0.90	7.17	4.87E-16	7.03E-14
ALCAM	-0.90	6.09	5.17E-12	5.31E-10
TBL1XR1	-0.90	6.60	1.38E-06	8.15E-05
CACNG4	-0.90	3.17	4.69E-07	2.96E-05
BCL2	-0.91	3.74	3.92E-16	5.77E-14
NR1D2	-0.91	5.50	1.04E-12	1.13E-10
CCKAR	-0.91	1.37	5.93E-11	5.54E-09
CPNE3	-0.91	6.00	3.49E-12	3.64E-10
CCNC	-0.91	5.28	1.92E-09	1.55E-07
YOD1	-0.91	4.68	9.83E-08	6.59E-06
RDX	-0.92	5.74	7.93E-13	8.77E-11
GPR56	-0.92	3.12	1.79E-07	1.19E-05
RTN1	-0.92	6.69	4.20E-29	1.05E-26
B3GAT2	-0.93	3.85	2.88E-12	3.05E-10
PTER	-0.93	1.45	6.55E-05	0.00300628
FAM103A1	-0.93	3.50	2.22E-08	1.58E-06
RASSF2	-0.93	3.73	1.24E-12	1.34E-10
RP11-819C21.1	-0.93	0.22	0.00090424	0.03310677
EFNA2	-0.93	2.55	7.08E-06	0.00037742
SLC6A16	-0.93	4.44	1.08E-06	6.53E-05
PRKAA2	-0.94	5.56	1.32E-06	7.88E-05

ABI2	-0.94	7.06	6.37E-21	1.25E-18
MTMR7	-0.94	3.31	5.19E-11	4.87E-09
ITGB1P1	-0.94	-0.02	0.00022678	0.0093051
GAL3ST4	-0.95	3.94	1.32E-06	7.88E-05
DGKI	-0.95	2.50	3.85E-06	0.00021533
OSGIN2	-0.95	4.62	2.70E-16	4.01E-14
C1QL3	-0.95	1.60	1.05E-06	6.37E-05
CD38	-0.95	1.66	4.54E-10	3.97E-08
AMMECR1	-0.96	4.77	6.10E-19	1.05E-16
NPTX1	-0.97	3.28	2.64E-08	1.88E-06
DLL1	-0.98	4.32	6.67E-06	0.00035821
LINC00939	-0.99	0.62	4.00E-05	0.0018982
NCAN	-0.99	5.49	2.39E-21	4.87E-19
CLTA	-0.99	6.24	7.51E-32	2.10E-29
GNB4	-0.99	5.63	1.31E-19	2.38E-17
MTMR6	-1.00	4.75	1.28E-20	2.43E-18
CLVS1	-1.00	2.10	2.36E-11	2.27E-09
DNM1P47	-1.00	1.58	0.00018314	0.00778289
C1QTNF6	-1.00	1.14	0.00030636	0.01228796
KBTBD11	-1.01	2.73	2.90E-12	3.05E-10
RAB30	-1.02	5.00	5.84E-16	8.25E-14
STS	-1.02	4.42	2.87E-21	5.70E-19
NDUFB2	-1.02	5.35	2.04E-33	6.63E-31
TMEM163	-1.04	0.11	1.89E-05	0.00094936
SMN2	-1.04	1.64	2.03E-09	1.62E-07
PNRC2	-1.04	4.37	7.32E-21	1.41E-18
P2RX3	-1.04	2.04	3.09E-11	2.94E-09
DACH1	-1.04	4.98	2.58E-31	6.96E-29
RAB8B	-1.05	5.43	2.35E-14	2.94E-12
WNT9A	-1.05	0.24	1.08E-06	6.53E-05
SOX11	-1.06	7.51	2.43E-17	3.94E-15
LACC1	-1.07	0.03	1.03E-07	6.85E-06
SESN3	-1.09	6.68	9.43E-14	1.11E-11
SMN1	-1.09	3.20	1.89E-16	2.90E-14
CTD-2611K5.5	-1.09	0.77	0.00034948	0.01386162
CSGALNACT1	-1.10	1.14	1.09E-08	8.10E-07
TMEM178A	-1.11	0.86	1.42E-08	1.03E-06
CBLN1	-1.11	2.23	2.60E-20	4.89E-18
EPHB2	-1.11	4.18	0.00023012	0.00941508
ETNK2	-1.12	2.63	6.02E-05	0.00279009
AMER2	-1.12	0.34	3.54E-08	2.49E-06
MCF2L	-1.12	3.03	1.07E-08	8.01E-07
GS1-18A18.1	-1.13	0.02	2.80E-05	0.00136981

PRODH	-1.13	1.84	8.54E-06	0.00044674
RP11-326E22.1	-1.13	-0.58	3.25E-05	0.00157302
SPOPL	-1.13	4.72	6.63E-24	1.43E-21
NSG1	-1.13	4.95	2.44E-34	8.51E-32
PTBP3	-1.13	5.35	2.43E-24	5.42E-22
NUS1	-1.14	5.57	4.59E-32	1.34E-29
KIAA1239	-1.14	5.31	6.88E-34	2.34E-31
ZBTB41	-1.15	4.14	4.99E-15	6.60E-13
RP11-227F19.1	-1.15	2.10	3.13E-17	5.02E-15
RP11-430C7.5	-1.16	-0.04	0.00025127	0.01022184
SDC4	-1.16	1.07	0.00095494	0.03469615
ADCY8	-1.17	0.85	8.46E-10	7.10E-08
ANKRD24	-1.18	-0.70	0.00030205	0.01214915
LRCH2	-1.18	4.25	1.94E-26	4.69E-24
TMEM56	-1.19	4.21	3.36E-20	6.23E-18
CALB1	-1.19	1.30	1.01E-12	1.11E-10
RP11-1114A5.4	-1.20	0.85	1.15E-11	1.16E-09
GRIK3	-1.20	6.24	0.00069617	0.02615952
LPPR3	-1.20	3.18	2.37E-05	0.00118035
AC007620.3	-1.21	2.69	1.30E-12	1.39E-10
DCHS1	-1.21	5.08	5.88E-24	1.29E-21
ACTR3	-1.22	6.39	1.12E-69	9.37E-67
CCNJ	-1.23	5.74	4.15E-50	2.37E-47
LIFR	-1.24	6.07	8.32E-32	2.29E-29
SYT4	-1.24	3.43	3.99E-22	8.26E-20
JHDM1D	-1.24	4.47	2.58E-38	9.68E-36
PXDNL	-1.28	0.66	1.76E-13	2.01E-11
MTHFD2	-1.29	7.38	2.58E-73	2.31E-70
PHF10	-1.29	6.97	8.02E-61	5.45E-58
ENO1P2	-1.29	-0.07	4.07E-06	0.00022726
CUBN	-1.29	0.01	1.81E-06	0.0001057
C6orf25	-1.31	-0.66	7.57E-06	0.00040157
PPP2CB	-1.31	5.75	3.44E-67	2.45E-64
LINC00682	-1.33	5.09	1.19E-76	1.22E-73
RP11-145M9.4	-1.33	2.95	6.28E-10	5.33E-08
CDKN1C	-1.35	-0.30	0.00105287	0.03806044
AC078941.1	-1.36	5.81	5.70E-48	3.13E-45
DRAXIN	-1.36	3.53	1.15E-13	1.34E-11
CTH	-1.38	3.61	4.61E-40	1.83E-37
FGF9	-1.41	-0.20	1.26E-15	1.74E-13
INSM2	-1.42	4.80	9.06E-19	1.54E-16
GOLT1B	-1.44	4.43	3.25E-26	7.75E-24
RBMS3-AS2	-1.44	3.00	1.62E-69	1.29E-66

AIF1L	-1.44	3.67	7.13E-30	1.85E-27
RHCG	-1.50	-0.88	1.51E-05	0.00076753
MBNL3	-1.51	5.72	1.82E-40	7.43E-38
RNU4-92P	-1.53	-0.36	4.80E-09	3.67E-07
CTD-3193O13.9	-1.55	2.50	2.11E-13	2.40E-11
LIF	-1.56	-0.88	0.00054314	0.02096087
FIGF	-1.57	1.92	6.61E-32	1.89E-29
PLEKHA7	-1.58	1.02	5.19E-06	0.00028497
SMIM14	-1.62	2.77	9.31E-42	4.03E-39
HECW1	-1.70	1.40	3.88E-33	1.20E-30
LPGAT1	-1.80	6.00	3.69E-130	1.32E-126
AC023115.1	-1.83	5.38	4.08E-29	1.04E-26
ECEL1	-1.86	2.19	3.94E-31	1.04E-28
AC008132.13	-1.90	-0.45	8.81E-06	0.00045912
AC023115.2	-1.92	4.94	2.50E-35	8.91E-33
DLK1	-1.94	4.87	1.19E-24	2.71E-22
VSTM2B	-1.98	-0.31	5.54E-15	7.19E-13
ARHGAP36	-2.20	7.83	1.50E-285	2.14E-281
DBH	-2.88	2.61	4.24E-111	8.64E-108
RP11-566J3.4	-3.08	-0.14	1.49E-08	1.08E-06

Supplementary Table 4: Results of a GSEA upon CTH downregulation.
Hallmark gene set from the Human MSigDB Collections was used to determine significantly enriched terms. Term description, enrichment score, adjusted p-value as well as core enrichment genes are depicted.

Description	**Enrichment score**	**p-value$_{adj.}$**	**Core enrichment**
Hallmark EMT	0.61	5.00E-09	*COL3A1, LUM, SDC1, IGFBP3, COL1A1, MATN2, PCOLCE, CDH6, RGS4, PDGFRB, MSX1, TGFBR3, MMP2, WNT5A, BGN, SPP1, VEGFC, SCG2, SNTB1, NID2, PVR, COL5A2, SERPINH1, PLOD1, LAMC1, FBN1, ITGB5, EMP3, SLIT2, SPARC, CXCL12, COL12A1, IGFBP4, FAS, PTX3, NOTCH2, DKK1, THY1, SAT1, ITGA2, SGCD, GAS1, TNFRSF12A, VEGFA, HTRA1, GJA1, COLGALT1, SNAI2, SLC6A8, PLOD2, PLOD3, RHOB, TPM2, FSTL1, FBN2, CD44, GEM, NT5E, APLP1, LOXL1, CD59, FZD8, WIPF1, BMP1, PDLIM4, ACTA2, LGALS1, SFRP1, LAMA1*
Hallmark G2M Checkpoint	-0.45	0.00013	*NASP, MAD2L1, CENPA, POLA2, ILF3, INCENP, CDC6, CCNB2, PLK4, TACC3, SMC2, TOP1, BUB1, RAD21, UBE2C, EFNA5, PBK, SMAD3, MTF2, MCM5, AMD1, ORC6, EXO1, CDC45, ESPL1, ATF5, SRSF10, CDKN1B, LBR, HMGN2, PRMT5, CENPE, KIF11, TTK, MKI67,*

			SMARCC1, CKS2, TRA2B, MYBL2, CCNT1, KATNA1, UBE2S, CASP8AP2, SAP30, KPNB1, FBXO5, RBM14, TOP2A, LMNB1, CCNF, HIF1A, SYNCRIP, KIF5B, MCM2, EZH2, TPX2, CBX1, PDS5B, SRSF2, CCND1, BARD1, SFPQ, NUSAP1, NUMA1, TMPO, HMMR, CTCF, HNRNPU, GSPT1, MEIS2, STMN1, BUB3, CHEK1, KIF15, HMGB3, DMD, PRIM2, NDC80, RACGAP1, CDKN2C, XPO1, CCNA2, ATRX, KIF20B, FANCC, SMC4, E2F2, FOXN3, BRCA2, CENPF, PAFAH1B1, SS18, RASAL2, MARCKS, CDC7, CDC27, SRSF1, SQLE
Hallmark Myogenesis	0.44	0.001	*HRC, COL3A1, STC2, IGFBP3, COL1A1, CHRNG, FABP3, BHLHE40, EPHB3, NQO1, BDKRB2, ITGB5, SPHK1, GPX3, SPARC, KCNH2, KIFC3, PDLIM7, SPEG, CDKN1A, TNNT2, DTNA, MAPK12, SGCD, EIF4A2, BIN1, PFKM, PPP1R3C, MYH3, AEBP1, NAV2, OCEL1, SLC6A8, TPM2, ADCY9, SYNGR2*
Hallmark Interferon alpha response	0.56	0.004	*IFI44L, IFI44, PROCR, IFITM3, GMPR, MOV10, IFITM2, CSF1, PARP9, TRIM14, TRIM25, IFI35, LGALS3BP, LY6E, PSME1, IRF9, B2M, CMPK2*
Hallmark E2F targets	-0.395	0.004	*SPAG5, NASP, MAD2L1, PCNA, MMS22L, POLA2, ILF3, CCNB2, PLK4, TACC3, RNASEH2A, RAD21, SPC24, NAP1L1, MCM7, MCM5, ORC6, CDCA8, TIPIN, ESPL1, RAD1, CDKN1B, LBR, CENPE, MKI67, CKS2, NUDT21, TRA2B, DUT, GINS4, NBN, MYBL2, UBE2S, DLGAP5, RPA3, TOP2A, ASF1A, SMC3, LMNB1, USP1, SYNCRIP, SPC25, DEK, MCM2, EZH2, RFC3, PDS5B, SRSF2, BARD1, TP53, ATAD2, LUC7L3, TMPO, RRM2, POLE4, HMMR, CTCF, GSPT1, STMN1, ING3, CHEK1, HMGB3, PRIM2, PAN2, PPM1D, ANP32E, RACGAP1, MXD3, CDKN2C, BRCA1, XPO1, HMGB2, HELLS, RAD50, SMC4, BRCA2, CCP110, RFC1, SRSF1, DCK, DEPDC1, MTHFD2*
Hallmark Angiogenesis	0.68	0.005	*S100A4, COL3A1, LUM, MSX1, SPP1, COL5A2*
Hallmark UV response DN	0.42	0.006	*COL3A1, TGFBR2, COL1A1, RGS4, PDGFRB, ID1, TGFBR3, BHLHE40, MGLL, F3, COL5A2, LAMC1, INPP4B, ATXN1, NR3C1, GCNT1, PIAS3, LDLR, IRS1, NOTCH2, PRKCA, ADD3, PPARG, FHL2, ANXA2, EFEMP1, LPAR1, SYNE1*
Hallmark Hypoxia	0.38	0.007	*S100A4, STC2, IGFBP3, AMPD3, BCAN, ETS1, BGN, BHLHE40, F3, ATF3, AK4,*

			TMEM45A, ALDOC, ZFP36, MT2A, PGF, CA12, TPST2, GPC3, PGM1, NR3C1, TPBG, SLC37A4, PAM, GPC4, GBE1, PRKCA, CDKN1A, SRPX, DTNA, SCARB1, ANXA2, ADM, PPP1R3C, VEGFA
Hallmark Interferon gamma response	0.42	0.01	*ARID5B, IFI44L, IFI44, NLRC5, IFITM3, TNFAIP2, LYSMD2, MT2A, IFITM2, SOCS3, TAPBP, TRIM14, TRIM25, FAS, IFI35, CDKN1A, LGALS3BP, LY6E, PSME1, IRF9, JAK2, B2M, MVP, CMPK2, ZNFX1, IFNAR2, NOD1*
Hallmark Adipogenesis	0.37	0.01	*ENPP2, SNCG, ABCA1, MGLL, FZD4, DHCR7, ME1, PGM1, GPX3, TOB1, DHRS7, CHCHD10, ECH1, GBE1, REEP5, PPARG, ELOVL6, PEMT, SCARB1, RREB1, AGPAT3, ALDH2, IDH3A, ESRRA, TKT, QDPR, RETSAT, SLC25A10, PFKL, RMDN3, AK2, PREB, COQ5, CMBL, ALDOA, JAGN1, SLC5A6, VEGFB, ARAF, POR, MCCC1, BCL6, GPX4, AIFM1, PHYH, PIM3, SDHB, APLP2, RAB34, SLC19A1, PRDX3, NMT1, APOE, PPP1R15B, MDH2, LPCAT3, NKIRAS1, ACADS, GHITM, DHRS7B, DGAT1, NDUFAB1, ACO2, PEX14, SLC25A1, ATL2, ACLY, PTCD3, SOD1, CYC1*
Hallmark Apical junction	0.37	0.013	*NEXN, CDH6, CNN2, MMP2, CNTN1, FBN1, ITGA9, CLDN11, B4GALT1, SLIT2, KCNH2, ICAM5, CDH8, CDH15, FLNC, AMIGO2, IRS1, PIK3CB, SHROOM2, CERCAM, SPEG, THY1, NLGN3, ITGA2, LDLRAP1, LIMA1, VCL, CLDN18, PKD1, ARHGEF6, ADAM9, MVD, RRAS, SLC30A3, BMP1, NF2*
Hallmark UV response UP	0.37	0.02	*RET, TUBA4A, MSX1, ATF3, AQP3, SHOX2, ABCB1, GPX3, PLCL1, COL2A1, FURIN, KCNH2, BMP2, TYRO3, CDO1, CCNE1, EPHX1, JUNB, PTPRD, SPR, NR4A1, SLC6A8, RHOB, IL6ST, TMBIM6, DLG4, GRINA, PPIF, SIGMAR1, PRKCD, ALDOA, EIF2S3, UROD, BTG2, RAB27A, NAT1, PDLIM3, NPTXR, CREG1, CHKA, CLTB, TGFBRAP1, CYB5R1, AP2S1, HTR7, RPN1, SOD2, BAK1, CYB5B, PPT1, PDAP1, CCND3*
Hallmark Estrogen response early	0.36	0.02	*OLFML3, RET, STC2, BHLHE40, KAZN, AQP3, SLC7A5, ENDOD1, CA12, ASB13, DHCR7, TOB1, B4GALT1, TPBG, CXCL12, IGFBP4, FOXC1, WWC1, BLVRB, SYBU, MREG, ADD3, FHL2, SCARB1, SLC22A5, UNC119, FDFT1, ISG20L2, NAV2, GJA1, JAK2, IL6ST, TSKU, ADCY9, SH3BP5, PAPSS2, CD44, PPIF*

Supplementary Table 5: Differentially expressed genes upon AHCY downregulation.
Log-fold-change (logFC), log-counts-per-milion (logCPM), p-values and FDR-corrected p-values are depicted. Only significant results are included.

Gene symbol	logFC	logCPM	PValue	FDR
NPTX1	-1.80	4.26	2.08E-81	1.47E-77
AHCY	-1.50	7.28	3.08E-87	4.35E-83
PALM3	-1.32	0.85	8.15E-17	8.22E-14
PYY	-1.28	0.93	8.26E-20	1.17E-16
DEPDC1B	-1.23	4.66	7.57E-51	3.56E-47
KANK4	-1.22	0.84	8.39E-16	7.90E-13
CBFA2T3	-1.09	0.10	4.43E-07	0.00018402
CALU	-1.06	7.06	9.84E-43	3.47E-39
KIAA0319	-1.04	0.33	3.80E-07	0.00016751
AURKA	-1.02	5.50	1.68E-30	4.74E-27
SLC7A5	-1.01	6.07	9.90E-16	8.73E-13
TGFBR3	-0.96	1.07	5.97E-08	2.91E-05
EBF2	-0.95	0.04	4.41E-05	0.01270464
SURF1	-0.93	4.64	1.51E-21	2.67E-18
FGFR3	-0.92	1.02	4.33E-05	0.01270464
SLC45A3	-0.90	2.29	6.13E-07	0.00024738
FST	-0.89	1.92	9.96E-07	0.00038684
GNPDA1	-0.89	6.87	6.53E-29	1.54E-25
OPN1SW	-0.89	1.45	2.51E-07	0.00011433
SYNGR2	-0.89	5.04	1.41E-11	9.98E-09
AC005682.5	-0.87	2.03	6.85E-05	0.01933904
EMILIN3	-0.87	2.64	2.54E-06	0.00092004
LDLRAP1	-0.81	2.72	5.06E-06	0.00178473
BCAT1	-0.81	7.40	6.24E-06	0.00209614
NDE1	-0.80	4.05	2.43E-09	1.43E-06
SYBU	0.70	6.30	6.14E-06	0.00209614
ETV4	0.76	4.16	2.84E-05	0.00870009
PARP9	0.77	3.47	1.82E-05	0.00584836
SCG2	0.79	6.64	1.33E-07	6.25E-05
PRCD	0.82	5.36	1.13E-09	7.25E-07
LINC00595	0.85	1.02	4.06E-05	0.01217982
DUSP4	0.87	5.53	3.72E-18	4.04E-15
CFHR1	0.90	2.59	6.36E-09	3.32E-06
CFH	0.92	2.09	3.16E-08	1.59E-05
CSMD3	0.92	1.56	8.36E-06	0.00274494
SPRY4	0.93	1.77	1.01E-06	0.00038684
SYNPO2	0.93	6.26	1.31E-18	1.55E-15
MDGA1	0.93	1.99	4.37E-09	2.37E-06

C1orf137	0.93	0.27	2.58E-05	0.00807807
ASIC4	0.96	1.93	3.92E-07	0.00016751
IFITM2	0.97	0.07	0.0001076	0.02977719
VGF	0.99	5.45	3.22E-10	2.16E-07
PALMD	1.02	3.12	2.79E-15	2.32E-12
KCNJ2	1.03	2.09	2.17E-12	1.70E-09
ETV5	1.04	4.54	2.81E-19	3.61E-16
AQP4	1.06	3.53	5.05E-12	3.75E-09
ABCA12	1.18	-0.21	1.72E-06	0.00063898
PLCL1	1.19	0.15	4.15E-09	2.34E-06
THSD7A	1.22	0.57	2.09E-09	1.28E-06
DUSP6	1.24	2.61	2.14E-21	3.36E-18
LUM	1.26	3.12	9.36E-25	1.89E-21

Supplementary Table 6: Results of a GSEA upon AHCY downregulation.
Hallmark gene set from the Human MSigDB Collections was used to determine significantly enriched terms. Term description, enrichment score, adjusted p-value as well as core enrichment genes are depicted.

Description	Enrichment score	$p\text{-value}_{adj.}$	Core enrichment
Hallmark E2F targets	-0.758	1.25E-09	*DUT, NAP1L1, EXOSC8, NUP205, IPO7, SRSF2, CHEK1, CKS2, RBBP7, MXD3, PSIP1, RFC2, MCM2, NBN, UBE2T, RAD21, XRCC6, UNG, ZW10, TRA2B, MSH2, RAD51C, PHF5A, RPA1, PDS5B, MCM5, RACGAP1, XPO1, WEE1, SSRP1, SMC6, MTHFD2, CHEK2, NUP107, SYNCRIP, MCM3, DDX39A, PSMC3IP, HMGB3, BARD1, STAG1, DCTPP1, CCNE1, EZH2, LYAR, RFC1, CIT, KIF22, SUV39H1, CTCF, EED, HNRNPD, WDR90, SLBP, KPNA2, MCM7, CSE1L, DONSON, DCK, TRIP13, HMMR, UBE2S, BIRC5, TIMELESS, RRM2, ORC6, CCNB2, DEPDC1, RPA3, PCNA, RANBP1, LIG1, CENPM, TCF19, TOP2A, LMNB1, RNASEH2A, BUB1B, NCAPD2, KIF4A, DNMT1, NASP, MAD2L1, POLD1, SPAG5, POLE, E2F8, POLD3, MCM4, MKI67, TACC3, CDC25A, HELLS, PRIM2, ASF1B, ASF1A, HMGB2, SHMT1, PTTG1, KIF2C, PLK4, GINS4, SPC24, PLK1, POLA2, DEK, CDKN3, ATAD2, BRCA1, TMPO, CENPE, MMS22L, CDCA8, CDCA3, AURKB, LBR, CDK1, TIPIN, DCLRE1B, KIF18B, DLGAP5, ANP32E, MCM6, ESPL1, SMC4, BRCA2, USP1, CDC20, STMN1, MYBL2, RAD51AP1, MELK, SPC25,*

			DSCC1, GINS1, DIAPH3, TK1, AURKA
Hallmark G2M Checkpoint	-0.731	1.25E-09	*SRSF2, CHEK1, CKS2, TRAIP, MCM2, TLE3, KATNA1, RAD21, NUP98, TRA2B, SNRPD1, PDS5B, MCM5, CBX1, RACGAP1, XPO1, SMC2, KIF5B, TFDP1, SYNCRIP, SQLE, MCM3, DDX39A, HMGB3, MEIS2, BARD1, STAG1, EZH2, AMD1, DTYMK, KIF22, SUV39H1, CTCF, HNRNPD, CASP8AP2, KPNA2, CDC7, HMMR, FBXO5, UBE2S, CHAF1A, BIRC5, KPNB1, EXO1, DBF4, ORC6, CCNB2, E2F2, POLQ, CENPA, UBE2C, TOP2A, LMNB1, INCENP, KIF4A, CDC6, NASP, TTK, SMAD3, TOP1, MAD2L1, POLE, MKI67, TACC3, CDC25A, TPX2, STIL, PRIM2, PRC1, RAD54L, GINS2, CCNF, PTTG1, CENPF, CDC45, KIF2C, KIF23, NDC80, PLK4, MT2A, CCNA2, PLK1, POLA2, CDKN3, TMPO, CENPE, BUB1, TROAP, AURKB, LBR, KIF20B, KIF11, CDK1, KIF15, E2F1, CCND1, MCM6, ESPL1, NEK2, SMC4, NUSAP1, BRCA2, CDC20, STMN1, MYBL2, ODC1, HMGN2, PBK, NOTCH2, SLC7A5, AURKA*
Hallmark mTORC1 signaling	-0.528	1.25E-09	*EBP, CTSC, UCHL5, TPI1, TCEA1, HPRT1, ACACA, EGLN3, ENO1, TUBG1, GAPDH, TMEM97, STIP1, TFRC, TOMM40, HMGCR, SLC6A6, TBK1, EEF1E1, PPIA, SHMT2, NUFIP1, PSMA3, HMBS, CYP51A1, ELOVL5, NUP205, PSMC4, IGFBP5, SLC1A4, SLC1A5, EIF2S2, PSMC2, MCM2, GMPS, BHLHE40, PPA1, RRP9, ME1, ALDOA, UNG, SLC9A3R1, ACSL3, PSMA4, FADS1, RPA1, CORO1A, HSPD1, GGA2, P4HA1, MTHFD2, PSMD12, DHCR7, SQLE, DDX39A, ADIPOR2, SCD, LDLR, DHFR, CACYBP, HSPE1, PSMG1, CYB5B, SLC2A1, IDH1, PSMD14, GSR, SLC37A4, HMGCS1, RRM2, DHCR24, CCNG1, CTH, MCM4, CDC25A, LDHA, INSIG1, PHGDH, CCNF, PLK1, IDI1, BUB1, POLR3G, PRDX1, MAP2K3, FADS2, PLOD2, BCAT1, SLC7A5, AURKA*
Hallmark MYC Targets V1	-0.635	1.25E-09	*SF3B3, UBE2E1, NOP56, NDUFAB1, PRPF31, ORC2, HSP90AB1, RAD23B, COX5A, EIF2S1, MRPL9, EIF4G2, SNRPB2, PA2G4, PGK1, PCBP1, EIF3J, CLNS1A, CYC1,*

			SSBP1, YWHAQ, DDX21, SERBP1, XPOT, APEX1, PSMC6, SSB, HDAC2, RUVBL2, UBE2L3, C1QBP, UBA2, RAN, CAD, SNRPD3, HPRT1, HNRNPA3, SNRPA, NME1, HNRNPR, FBL, PSMD7, CCT5, HNRNPC, ABCE1, CUL1, SRSF1, PHB, ERH, PSMA2, ILF2, DHX15, PSMD3, YWHAE, TCP1, TARDBP, PPIA, POLD2, VDAC3, G3BP1, HNRNPU, SRSF7, LSM2, DUT, NAP1L1, U2AF1, SNRPA1, HDGF, PSMC4, PSMA7, IMPDH2, HNRNPA1, SRSF2, SRSF3, EIF2S2, PPM1G, SNRPG, PRDX3, PSMA1, AP3S1, EIF1AX, MCM2, RRP9, PSMB3, PSMA6, POLE3, XRCC6, SET, PSMA4, TRA2B, SNRPD2, SNRPD1, MCM5, HSPD1, XPO1, TRIM28, CSTF2, NPM1, EIF4E, PSMD1, TFDP1, SYNCRIP, PSMB2, VBP1, STARD7, GLO1, HNRNPD, KPNA2, HSPE1, MCM7, HNRNPA2B1, PSMD14, PTGES3, KPNB1, PCNA, RANBP1, RRM1, MAD2L1, RFC4, MCM4, LDHA, CDK2, PRPS2, CDC45, CCNA2, DEK, TYMS, SRPK1, MCM6, USP1, CDC20, ODC1
Hallmark Mitotic Spindle	-0.471	2.90E-08	*GEMIN4, EPB41L2, KATNA1, OPHN1, SASS6, ARHGAP5, RACGAP1, MAP3K11, SHROOM1, KIF5B, NET1, ALMS1, NIN, SYNPO, RFC1, CEP72, KIF22, ARHGAP10, PIF1, CENPJ, FBXO5, BIRC5, ECT2, CCNB2, TOP2A, LMNB1, INCENP, KIF4A, TTK, KNTC1, TPX2, PRC1, CENPF, KIF2C, KIF23, NDC80, PLK1, ANLN, PCGF5, CENPE, BUB1, KIF20B, KIF11, CDK1, KIF15, DLGAP5, CD2AP, ESPL1, NEK2, SMC4, NUSAP1, BRCA2, NOTCH2, AURKA*
Hallmark MYC Targets V2	-0.613	8.69E-06	*NOP16, CDK4, PRMT3, RCL1, PES1, MYBBP1A, GNL3, DDX18, NOP56, IMP4, PA2G4, NIP7, EXOSC5, MPHOSPH10, HK2, TCOF1, WDR43, PPRC1, TFB2M, SLC19A1, RABEPK, WDR74, BYSL, PHB, TMEM97, SUPV3L1, NDUFAF4, MRTO4, NOC4L, NOP2, RRP9, GRWD1, UNG, PUS1, SLC29A2, MCM5, HSPD1, NPM1, DCTPP1, UTP20, HSPE1, MCM4, PLK4, PLK1*
Hallmark Estrogen Response Late	-0.466	2.75E-05	*ELOVL5, PDZK1, XRCC3, SLC1A4, ID2, SIAH2, RBBP8, IL17RB, SLC9A3R1, FKBP5, CELSR2, NXT1, CHPT1, BLVRB, FABP5, DHCR7,*

			SLC29A1, FDFT1, IGFBP4, SLC22A5, TOP2A, RNASEH2A, PDLIM3, KIF20A, CDC6, CD44, RABEP1, STIL, ITPK1, GINS2, KCNK5, PLK4, MYB, LLGL2, ASCL1, MEST, CCND1, CDC20, EMP2, KLF4, CXCL12, TPBG, NMU, FGFR3, SLC7A5
Hallmark KRAS Signaling UP	0.461	0.0008	*DUSP6, ETV5, CFH, TMEM100, ETV4, SPRY2, MAP3K1, GALNT3, CPE, JUP, ETV1, ABCB1, GLRX, SNAP91, RABGAP1L, SEMA3B, RGS16, MAFB, TMEM176B, CXCR4, RELN, SCN1B, TSPAN7, SNAP25, GABRA3, PPP1R15A, FBXO4*
Hallmark NOTCH Signaling	-0.653	0.0009	*FZD5, FZD7, TCF7L2, WNT5A, FZD1, CCND1, NOTCH3, NOTCH1, NOTCH2, LFNG*
Hallmark DNA Rapair	-0.411	0.0009	*RPA2, NELFB, POLR2H, HPRT1, NME1, POLR2J, POLR2A, TAF6, POLH, ARL6IP1, POLR2C, GTF2H5, RFC3, GTF2A2, DUT, IMPDH2, TAF9, CETN2, RFC2, ADRM1, NME4, SSRP1, DDB2, POLR2D, ADA, ALYREF, RFC5, POLA1, RPA3, PCNA, LIG1, POLD1, FEN1, RFC4, POLD3, RAD51, ZWINT, CLP1, POLA2, TYMS, PRIM1, ELL, SURF1*
Hallmark Coagulation	0.514	0.001	*DUSP6, CFH, MMP2, KLKB1, CTSO, CLU, S100A13, CSRP1, CTSK, SERPING1, S100A1, TIMP3, MSRB2, SIRT2, GSN, SPARC, FBN1, SH2B2, CTSB, F8, BMP1, ISCU, MST1, CAPN5, HTRA1, USP11, PROS1*
Hallmark Glycolysis	-0.395	0.001	*ARPP19, AKR1A1, PGK1, PRPS1, GALK1, SRD5A3, PGM2, ME2, CITED2, HK2, GUSB, PAXIP1, IER3, GALE, PPP2CB, SLC25A13, DPYSL4, TPI1, EGLN3, ENO1, CASP6, NSDHL, ALDH9A1, RPE, POLR3K, TXN, PPIA, KIF2A, GPC1, PSMC4, SLC25A10, ME1, P4HA2, ALDOA, PKM, TALDO1, SOD1, GLCE, LHX9, P4HA1, HOMER1, IDH1, HMMR, NANP, SLC37A4, EGFR, DEPDC1, SDC2, CENPA, KIF20A, CTH, NASP, CD44, CHST2, LDHA, KDELR3, CDK1, CYB5A, PYGL, STMN1, PLOD2, SLC35A3, GPC4, SOX9, TPBG, GNPDA1, AURKA*
Hallmark Estrogen Response Early	-0.370	0.008	*ELOVL5, PDZK1, SLC1A4, ADCY1, SIAH2, TGM2, RBBP8, ELOVL2, BHLHE40, SLC7A2, IL17RB, SLC9A3R1, FKBP5, RARA, CELSR2, NXT1, CHPT1, BLVRB, DHCR7,*

			MYBL1, RASGRP1, ASB13, PMAIP1, FASN, FDFT1, KAZN, IGFBP4, SLC22A5, SLC2A1, ENDOD1, PDLIM3, CD44, ITPK1, REEP1, KCNK5, MYB, CCND1, KLF4, CXCL12, TPBG, CELSR1, SLC7A5, CBFA2T3
Hallmark Spermatogenesis	-0.447	0.01	*TALDO1, CLPB, GMCL1, MLF1, GRM8, EZH2, PSMG1, IDE, DBF4, CCNB2, TTK, RFC4, ARL4A, KIF2C, CDKN3, BUB1, CDK1, NEK2, NCAPH, TEKT2, AURKA*
Hallmark EMT	-0.372	0.01	*FBLN1, PMP22, COL3A1, COL4A1, SNTB1, MCM7, IGFBP4, OXTR, COL12A1, FBN2, VIM, CDH11, VEGFC, WNT5A, TNFRSF12A, CD44, TNC, PLAUR, SERPINE2, LAMA1, LOX, GAS1, MEST, PDGFRB, PLOD2, SDC4, FZD8, CXCL12, NOTCH2, RGS4, TGFBR3, CALU*
Hallmark UV Response DN	-0.377	0.01	*TJP1, BCKDHB, DDAH1, IGFBP5, RBPMS, BHLHE40, ANXA2, SMAD7, F3, LTBP1, IRS1, PMP22, COL3A1, SYNJ2, LDLR, CELF2, PPARG, SDC2, SMAD3, AMPH, INSIG1, FZD2, ID1, GCNT1, SFMBT1, PDGFRB, RXRA, KIT, NOTCH2, NR3C1, RGS4, TGFBR3*

Supplementary Table 7: Differentially expressed genes upon GPX4 downregulation.
Log-fold-change (logFC), log-counts-per-milion (logCPM), p-values and FDR-corrected p-values are depicted. Only significant results are included.

Gene symbol	logFC	logCPM	PValue	FDR
LINC00473	4.90	0.30	8.31E-266	3.96E-262
SPRY4	4.12	0.97	0	0
ETV4	3.84	2.69	0	0
ETV5	3.15	2.26	1.16E-152	3.33E-149
EGR3	2.63	-0.21	3.11E-89	4.45E-86
IGFBP3	2.61	2.08	8.42E-106	1.50E-102
VGF	2.42	3.44	8.97E-28	4.00E-25
DUSP6	2.32	0.59	1.69E-100	2.68E-97
DKK1	2.11	-1.03	1.45E-34	8.61E-32
SPRY2	2.10	3.05	7.22E-189	2.58E-185
GPR3	1.67	1.81	1.48E-59	1.41E-56
LINC00890	1.57	0.48	2.03E-21	7.06E-19
DUSP4	1.48	3.15	9.24E-69	9.43E-66
MAFB	1.47	2.87	9.34E-35	5.80E-32

SAMD5	1.41	-0.41	3.17E-09	4.57E-07
RET	1.34	-0.21	6.58E-10	1.06E-07
PLCL1	1.24	-0.19	4.43E-08	5.65E-06
MAFF	1.20	0.97	3.18E-19	9.67E-17
LONRF2	1.16	0.49	5.49E-10	9.01E-08
MAP3K1	1.13	4.54	7.75E-38	5.27E-35
SYNPO2	1.05	2.71	1.19E-09	1.81E-07
SNAI2	1.03	3.46	2.38E-08	3.17E-06
DUSP2	1.00	0.19	0.00021549	0.01645452
EPHA2	0.99	3.31	7.00E-09	9.70E-07
DUSP5	0.97	2.26	2.07E-09	3.02E-07
ALS2CL	0.97	1.26	4.52E-05	0.00400699
LGR5	0.91	3.57	6.67E-14	1.34E-11
LUM	0.91	2.75	2.93E-06	0.00029876
TMEM108	0.90	4.54	5.09E-18	1.42E-15
ID4	0.88	1.54	2.66E-05	0.00246613
ASS1	0.87	8.96	5.18E-15	1.14E-12
KCNJ6	0.86	4.13	7.53E-05	0.00655516
CXCR4	0.86	2.47	3.85E-05	0.00345577
MAN1A1	0.85	5.37	1.56E-07	1.81E-05
RP11-101E14.2	0.85	2.14	4.95E-07	5.39E-05
TRABD2A	0.84	1.31	7.03E-05	0.00616208
SHC3	0.83	3.87	5.80E-09	8.12E-07
CHGA	0.81	7.14	1.21E-05	0.00118715
PER2	0.80	4.17	4.75E-08	6.00E-06
PDE3A	0.78	4.04	7.92E-05	0.00685472
RP11-82L18.4	0.77	1.87	0.00036671	0.02605087
PDZD2	0.76	1.40	0.00073902	0.04977586
LRRC2	0.76	2.07	0.00072649	0.04916353
RP11-82L18.2	0.75	2.46	0.00023362	0.01765017
PALMD	0.74	2.98	0.00021547	0.01645452
KANK4	0.74	3.22	0.00015011	0.01217835
EMILIN2	0.74	2.78	0.00017413	0.01381349
SPRED2	0.68	5.37	0.00012606	0.0104651
MCC	-0.66	8.03	0.00059137	0.04079328
RIMS3	-0.69	7.44	1.37E-05	0.00131035
MEIS1	-0.72	7.83	2.58E-05	0.00241139
STAC2	-0.74	2.50	0.00025267	0.01888973
ENO3	-0.74	6.16	3.90E-07	4.32E-05
ZNF395	-0.75	5.31	1.60E-06	0.00016811
EYA2	-0.75	6.10	1.26E-07	1.50E-05
TUBA4A	-0.75	4.59	0.00013094	0.01080713
NOVA2	-0.77	4.61	5.20E-06	0.00052282

CHRND	-0.78	2.92	9.60E-05	0.0081592
POU2F2	-0.79	3.37	0.00013541	0.01111227
DACT3	-0.80	2.65	2.12E-05	0.00198953
LYN	-0.80	4.99	3.33E-08	4.32E-06
GRASP	-0.81	2.30	0.00027265	0.02017177
TOX3	-0.81	3.28	1.87E-05	0.00177213
STON1	-0.81	2.66	2.83E-05	0.00260611
GDF11	-0.81	5.68	3.49E-14	7.23E-12
HAND1	-0.82	4.10	0.00034277	0.02482765
ZNF385A	-0.82	4.90	1.39E-05	0.00132634
CXXC4	-0.83	3.33	8.90E-07	9.55E-05
SLC8A3	-0.83	0.29	0.00039541	0.02795066
BAIAP2-AS1	-0.84	6.67	2.24E-15	5.07E-13
SFXN3	-0.84	3.95	7.60E-09	1.04E-06
SCUBE1	-0.85	4.27	3.31E-05	0.00301097
CHPT1	-0.85	5.29	9.49E-10	1.49E-07
CBLN2	-0.85	1.48	0.00034427	0.02482765
INSM2	-0.85	4.80	0.00027051	0.02011779
DLL1	-0.85	4.32	0.00072637	0.04916353
LHX9	-0.86	4.55	1.75E-09	2.61E-07
PIM1	-0.86	3.46	1.33E-12	2.50E-10
FMNL1	-0.87	2.09	0.00032929	0.02398948
TESC	-0.87	2.21	1.44E-06	0.0001522
RND2	-0.87	3.99	4.07E-09	5.75E-07
DRD2	-0.87	2.54	0.000184	0.01451551
PGM5	-0.87	-0.39	0.00011461	0.00957088
PSTPIP1	-0.88	2.41	9.90E-05	0.00836816
TMEM130	-0.88	2.99	9.87E-08	1.18E-05
ACOT11	-0.88	2.74	4.36E-05	0.00389541
GIPR	-0.88	4.13	8.56E-05	0.00736649
RPRM	-0.89	5.37	7.42E-06	0.00074065
POU3F1	-0.89	1.04	0.00021429	0.01645452
TMEM255A	-0.89	3.50	2.96E-08	3.88E-06
SLC44A3	-0.89	2.98	1.37E-07	1.61E-05
SLC24A2	-0.89	1.63	0.00051236	0.03568773
SPP1	-0.89	1.04	0.00030607	0.02252802
SPEG	-0.89	4.22	0.00017156	0.01368528
FRMPD1	-0.89	4.34	8.67E-16	2.03E-13
C20orf166-AS1	-0.90	0.85	0.0005609	0.03887876
ABCC8	-0.90	5.33	3.04E-07	3.42E-05
SMIM18	-0.91	0.91	0.00022825	0.01733606
SEZ6	-0.92	4.56	9.51E-12	1.70E-09
CRB1	-0.92	3.28	4.19E-07	4.61E-05

ZBTB42	-0.92	1.57	0.00019348	0.0151797
P2RX3	-0.93	2.04	4.16E-08	5.35E-06
SH3RF2	-0.94	0.11	0.00031758	0.02325484
CGNL1	-0.94	1.63	3.21E-07	3.58E-05
RBMS3-AS2	-0.94	3.00	6.25E-12	1.13E-09
IGSF10	-0.95	0.60	0.00016619	0.01340719
BMF	-0.95	2.18	5.78E-10	9.38E-08
PEG10	-0.95	4.41	9.88E-08	1.18E-05
WDFY3-AS2	-0.95	1.90	2.90E-07	3.29E-05
ABCA12	-0.95	-0.34	0.00035267	0.0253056
PPFIA4	-0.96	5.50	2.99E-05	0.00273699
CDKN1C	-0.96	-0.30	0.00019918	0.0155415
ADM	-0.96	1.53	1.43E-06	0.0001522
KLHDC8A	-0.97	2.74	1.74E-09	2.61E-07
NUAK1	-0.97	4.60	5.26E-18	1.45E-15
KCNK3	-0.97	1.93	2.48E-08	3.28E-06
C1QL1	-0.99	5.11	0.00063403	0.04334548
CBFA2T3	-0.99	1.60	2.07E-06	0.0002143
RGS4	-1.00	4.96	6.33E-08	7.86E-06
NTNG2	-1.01	0.25	0.00025044	0.01882157
VSTM2B	-1.01	-0.31	1.23E-05	0.00119471
ATP1B2	-1.02	-0.52	0.00020336	0.01578156
PKNOX2	-1.03	1.42	2.39E-07	2.76E-05
IGFBP5	-1.03	6.66	9.14E-39	6.52E-36
CASQ1	-1.04	-0.65	3.61E-05	0.00326127
TMEM119	-1.04	2.13	1.74E-08	2.36E-06
CCM2L	-1.04	0.74	6.69E-08	8.24E-06
PLEKHA6	-1.04	3.04	9.91E-13	1.91E-10
CD248	-1.05	2.67	3.30E-06	0.0003344
RAB26	-1.05	3.69	5.56E-07	6.01E-05
PEAR1	-1.06	0.72	1.27E-05	0.00122379
TMEM51-AS1	-1.07	-0.60	9.38E-05	0.00801878
SPATA42	-1.08	-0.15	0.00063444	0.04334548
FGF7	-1.09	-1.03	1.81E-06	0.00018905
KIRREL2	-1.09	3.69	9.77E-16	2.25E-13
ANKFN1	-1.10	0.96	4.80E-05	0.00422663
RPP25	-1.10	0.39	1.37E-07	1.61E-05
CNTNAP2	-1.11	7.51	4.79E-21	1.59E-18
HDAC9	-1.11	4.23	1.45E-16	3.52E-14
CDH18	-1.12	0.62	9.59E-08	1.17E-05
CSDC2	-1.12	2.18	9.25E-06	0.00091052
NHLH1	-1.13	4.38	2.41E-34	1.37E-31
SULF1	-1.14	2.01	4.13E-10	6.86E-08

FOXO6	-1.15	3.73	1.83E-09	2.70E-07
MAFA	-1.16	-0.42	0.00035657	0.02545721
PRPH	-1.16	4.88	4.76E-25	1.84E-22
GRM4	-1.17	3.81	4.93E-12	9.02E-10
AKNAD1	-1.17	4.54	3.68E-29	1.75E-26
WFIKKN2	-1.17	5.40	1.95E-25	7.96E-23
NDST4	-1.18	-0.08	0.00047906	0.0335317
ELFN1	-1.19	-1.11	0.00017043	0.01367151
ARSI	-1.20	-0.39	0.00013726	0.01119959
APOBEC2	-1.25	-0.19	1.13E-12	2.15E-10
CD82	-1.26	1.43	5.77E-14	1.18E-11
RHBDL3	-1.26	3.11	6.53E-20	2.12E-17
RNU5A-1	-1.26	-0.76	9.28E-11	1.56E-08
MLIP	-1.27	-0.78	2.42E-06	0.00024881
SYNPO	-1.28	-0.16	1.17E-09	1.80E-07
HIF3A	-1.29	1.05	2.90E-25	1.15E-22
SLC17A7	-1.29	2.65	6.92E-23	2.53E-20
COL6A6	-1.30	0.57	2.57E-13	5.02E-11
KCNJ11	-1.30	3.53	3.75E-12	6.96E-10
ABCD2	-1.31	1.87	3.79E-15	8.45E-13
ADAMTS4	-1.32	1.13	3.03E-11	5.28E-09
INSRR	-1.33	1.19	3.68E-09	5.26E-07
PXDNL	-1.34	0.66	5.08E-17	1.29E-14
C10orf10	-1.34	2.00	4.15E-21	1.41E-18
ASIC4	-1.34	1.19	7.56E-11	1.29E-08
LINC00470	-1.35	-0.43	2.77E-07	3.16E-05
FIGF	-1.36	1.92	1.95E-16	4.64E-14
SMTNL2	-1.39	1.35	4.06E-31	2.00E-28
AQP4	-1.41	-0.35	1.98E-08	2.67E-06
RAB27B	-1.42	0.09	9.87E-10	1.53E-07
PRSS35	-1.43	2.62	9.47E-32	4.83E-29
TRANK1	-1.43	-0.23	8.02E-10	1.27E-07
PYY	-1.43	1.98	5.03E-08	6.30E-06
GPX4	-1.45	6.45	1.62E-33	8.57E-31
DBH	-1.51	2.61	2.91E-24	1.09E-21
PODN	-1.51	0.80	7.55E-26	3.17E-23
CTCFL	-1.54	-1.09	2.00E-11	3.52E-09
S100A4	-1.54	2.20	3.78E-28	1.74E-25
HTR3A	-1.55	4.14	3.75E-80	4.86E-77
NTRK1	-1.55	4.98	4.19E-22	1.50E-19
CHRNA1	-1.55	5.46	1.30E-45	1.03E-42
ENPP2	-1.56	1.16	3.02E-17	7.85E-15
RNF17	-1.57	0.27	9.16E-06	0.00090814

OLFML3	-1.60	3.93	1.35E-112	2.75E-109
CTB-158E9.1	-1.61	-0.58	8.92E-14	1.77E-11
CRB2	-1.62	2.11	4.25E-19	1.25E-16
PPP1R17	-1.65	5.11	1.04E-71	1.23E-68
MAMDC2	-1.65	1.60	1.09E-52	9.20E-50
LDB3	-1.65	2.41	1.34E-39	1.01E-36
AFP	-1.66	-0.91	0.00039942	0.02809499
FOSB	-1.70	1.15	0.00011462	0.00957088
SNCG	-1.71	2.17	7.92E-20	2.51E-17
GPR4	-1.73	-0.49	6.46E-11	1.11E-08
CDH15	-1.75	0.78	1.40E-16	3.45E-14
ZNF467	-1.75	0.31	4.29E-19	1.25E-16
LIX1	-1.75	0.35	2.28E-17	6.03E-15
ALPK2	-1.76	1.01	9.14E-15	1.98E-12
RP11-286N22.10	-1.77	-0.48	3.37E-14	7.07E-12
TNNI1	-1.79	1.66	9.81E-36	6.36E-33
PLP1	-1.84	-0.86	2.96E-14	6.31E-12
RP11-453M23.1	-1.97	1.22	5.15E-17	1.29E-14
CAMK2A	-2.19	-0.84	6.90E-18	1.86E-15
TNNT2	-2.28	-0.70	9.90E-34	5.44E-31
SRL	-2.29	1.62	2.26E-27	9.77E-25
NGF	-2.36	1.98	8.98E-20	2.79E-17
HRC	-2.48	2.23	8.07E-57	7.20E-54
NGFR	-2.67	2.24	2.74E-71	3.00E-68
MYOG	-2.93	2.90	1.00E-112	2.39E-109
CCDC129	-3.14	-0.08	2.44E-18	6.98E-16

Supplementary Table 8: Results of a GSEA upon GPX4 downregulation.
Hallmark gene set from the Human MSigDB Collections was used to determine significantly enriched terms. Term description, enrichment score, adjusted p-value as well as core enrichment genes are depicted.

Description	Enrichment score	$p\text{-value}_{adj.}$	Core enrichment
Hallmark MYC targets V2	0.66	8.04E-05	*DUSP2, RRP12, RRP9, HK2, PPAN, MYBBP1A, MAP3K6, IPO4, NOP2, UTP20, PES1, NIP7, WDR74, WDR43, UNG, IMP4, SLC19A1, NOP16, PPRC1, NOC4L, TBRG4, RCL1, EXOSC5, SRM, GRWD1, SUPV3L1, NDUFAF4, NOLC1, SORD, TFB2M, MCM5, BYSL, FARSA, DCTPP1, PHB*
Hallmark Myogenesis	-0.56	0.00017	*NCAM1, GSN, MAPRE3, KCNH2, CAMK2B, DAPK2, REEP1, DMD, FKBP1B, MYO1C, FST, CKM, KLF5, SORBS1, MEF2D, OCEL1, SPARC, KCNH1, FOXO4, BDKRB2, NOTCH1,*

			HDAC5, CRAT, CHRNB1, TNNT1, FABP3, ENO3, COL1A1, CHRNG, SPEG, PPFIA4, CASQ1, CHRNA1, LDB3, TNNI1, TNNT2, HRC, MYOG
Hallmark TNFA signaling via NFKB	0.498	0.00017	*EGR3, DUSP4, MAFF, DUSP2, DUSP5, PTPRE, HES1, RELB, SGK1, NR4A3, PDE4B, FOSL2, CSF1, SERPINB8, LIF, NR4A2, PER1, CD44, IRF1, SIK1, PLK2, IRS2, F3, SAT1, ID2, GEM, NR4A1, DRAM1, YRDC, IER3, ZFP36, TNC, SQSTM1, SPHK1, EGR1, EHD1, RHOB, KLF10, FUT4, JUNB, TNFAIP8, ATP2B1, SMAD3, KLF6, NFKB1, TGIF1, TNIP2, KDM6B*
Hallmark KRAS signaling up	0.49	0.0025	*ETV4, ETV5, IGFBP3, DUSP6, SPRY2, MAFB, MAP3K1, CXCR4, ETV1, GALNT3, FBXO4, LIF, RGS16, MYCN, ID2, ALDH1A3, CROT, YRDC*
Hallmark EMT	0.43	0.007	*IGFBP3, DKK1, SNAI2, LUM, COL12A1, SERPINH1, MSX1, FAS, NOTCH2, SCG2, CD44, CDH6, PLOD3, HTRA1, TNFRSF12A, SAT1, ID2, GEM, QSOX1, TPM2, PMP22, COL3A1, ACTA2, TNC, FGF2, FERMT2, FBLN2, SGCD, OXTR, GJA1, RHOB, SDC1, VCAN, FUCA1, MYLK*
Hallmark IL-2 STAT5 signaling	0.3955	0.019	*SPRY4, ETV4, MAFF, SPRED2, CSF1, LIF, RGS16, CD44, BATF3, CCNE1, ITGA6, ALCAM, HK2, PLAGL1, COCH, IFITM3, NFKBIZ, NOP2, TNFRSF21, LCLAT1, IL4R, SLC39A8, S100A1, CISH, CCND3, RHOB, PDCD2L*

10.3. List of Figures

Appendix

Appendix

Appendix

10.4. List of Tables

Appendix

10.5. Abbreviations

ALT	Alternative lengthening of telomeres
AMT	Adrenergic-to-mesenchymal transition
AUC	Area under the curve
bHLH-Zip	Basic helix-loop-helix leucine zipper domain
BIC	Bayesian information criterion
cDNA	complementary DNA
CRISPR	Clustered regularly interspaced short palindromic repeats
Cysta	Cystathionine
DEG	Differentially expressed genes
DM	Double minutes
EDTA	Ethylen diamine tetra acetic acid
EMT	Epithelial-to-mesenchymal transition
et al.	et alii (and others)
FIN	Ferroptosis-inducing agent
FPKM	Fragments per kilobase of transcript per million mapped reads
GPX4	Glutathione Peroxidase 4
GSEA	Gene set enrichment analysis
H3K27ac	Acetylation of histone 3 at lysine residue 27
H3K27me3	Trimethylation of histone 3 at lysine residue 27
H3K4me3	Trimethylation of histone 3 at lysine residue 4
HAT	Histone acetylase
HDAC	Histone deacteylase
hg19	Human genome 19
HSPB1	Heat Shock Protein Family B Member 1
INSS	International neuroblastoma staging system
IPP	Isopentenyl Pyrophosphate
IREB2	Iron Responsive Element Binding Protein 2
kDa	Kilodalton
LOF	Loss-of-function
Mito	Mitochondria
MTHFD 1/2	Methylenetetrahydrofolate dehydrogenase 1/2
MTs	Methyltransferases
MYC(N)	MYCN/ c-MYC
NB	Neuroblastoma
OS	Overall survival
OXPHOS	Oxidative Phosphorylation
PCA	Principle component analysis
PCR	Polymerase chain reaction
pH	*potentia Hydrogenii*
Pro	Proline

Appendix

PUFA	Polyunsaturated Fatty Acids
PUFA-PE	Phosphatidylethanolamine containing PUFA
RNA	Ribonucleic acid
RNAseq	RNA sequencing
ROS	Reactive Oxygen Species
rpm	Rotation per minute
SGOC	Serine-glycine-one-carbon
shRNA	Short hairpin RNA
TBS-T	Tris-buffered saline with Tween 20
TCA	The tricarboxylic acid cycle
TMM	Telomere maintenance mechanism
WGS	Whole genome sequencing

Appendix

10.6. Publication

Alborzinia, H., Flórez, AF., Kreth, S., Brückner, LM., Yildiz, U., Gartlgruber, M., Odoni, DI., Poschet, G., **Garbowicz, K.**, Shao, C., Klein, C., Meier, J., Zeisberger, P., Nadler-Holly, M., Ziehm, M., Paul, F., Burhenne, J., Bell, E., Shaikhkarami, M., Würth, R., Stainczyk, SA., Wecht, EM., Kreth, J., Büttner, M., Ishaque, N., Schlesner, M., Nicke, B., Stresemann, C., Llamazares-Prada, M., Reiling, JH., Fischer, M., Amit, I., Selbach, M., Herrmann, C., Wölfl, S., Henrich, KO., Höfer, T., Trumpp, A., Westermann, F. **MYCN mediates cysteine addiction and sensitizes neuroblastoma to ferroptosis.** *Nat Cancer*, *3*(4), 471-485 (2022). https://doi.org/10.1038/s43018-022-00355-4. PubMed ID: 35484422

Appendix

10.7. Acknowledgments

I would like to express my sincerest appreciation to all those who have contributed to the successful completion of my doctoral thesis.

To Frank Westermann, for his invaluable scientific input and unwavering supervision, without which this research project would not have been possible. I am particularly grateful for your flexibility in allowing me to shift the project towards the bioinformatics side due to the challenges posed by the COVID-19 pandemic.

To Prof. Tobias Dick and Prof. Stefan Wölfl, who provided excellent guidance and feedback, and helped to steer the project in the right direction during the Thesis Advisory Committee meetings. Additionally, I would like to thank them and Prof. Ursula Klingmüller for their thoughtful evaluation as members of the examination committee.

To the B087 team, who has provided me with indispensable support throughout this journey. I would like to thank Dr. Sina Kreth for her scientific advice and enormous emotional support during this challenging period. My gratitude also extends to Diana, Elisa, and Young-Gyu from our technical team for their tireless assistance with various technical issues in the lab. Special thanks are also due to Dr. Sabine Stainczyk and Dr. Kai-Oliver Henrich for their help with data acquisition and valuable scientific input.

I am also grateful to former lab members, especially Dr. Lea and Dr. Ines, for making my PhD time much more enjoyable with our endless conversations in the lab and fun moments outside of it. Without you it would have not been the same ☺.

I also owe a significant debt of gratitude to Dr. Dorett Odoni, whose contributions, particularly her ideas and foundational knowledge of bioinformatics, have been invaluable in shaping this project.

My great appreciation also goes to the PhD Resistance team for making my time in Heidelberg unforgettable. Your emotional support and the fun experiences we shared helped me navigate the challenging times during my research.

And finally, to my best support team, THANK YOU. Beginning with Alessio, whose scientific expertise and unwavering emotional support were critical in helping me

achieve my goals, I am deeply grateful. Without you it would have not been possible to complete this project.

Beata, Monika, Natalia, Kuba, Kasia, Asia, Ola, Jagoda and Nastia, you offered enormous mental support throughout the great period of my life, but especially through the pandemic and other challenging moments. It really made a significant difference in my life. You provided me with the encouragement, advice, and strength that I needed to persevere. I cannot thank each and every one of you enough for your firm dedication. I feel incredibly lucky to have such amazing people around me.

To my cousin Karola, thank you for keeping me entertained and uplifted through your thoughtful phone calls during the entire process.

Finally, to my parents, who instilled in me a belief in myself and gave me the foundation to pursue a scientific career. To my mom, whose support and encouragement have been a constant throughout my life, thank you. To my dad, thank you for believing in me and providing me with a great start in life. You will always be in my heart.

Appendix

Drodzy Mamo i Tato,

Nie jestem w stanie wyrazić w słowach, jak bardzo jestem wdzięczna za Wasze nieustanne wsparcie, motywację oraz wiarę, jaką mnie darzycie. Bez Waszej pomocy i zachęty, nigdy nie byłabym w stanie dotrzeć tak daleko.

Tato, Twoje wartości, mądrość i poświęcenie nauczyły mnie, co to znaczy być twardą i zdeterminowaną w dążeniu do celów. Twoja obecność i przykład na zawsze pozostaną ze mną w sercu.

Mamo, Twoje nieograniczone wsparcie, ciepło i miłość pozwoliły mi przezwyciężyć trudne momenty i osiągać cele, których wcześniej nie byłabym w stanie sobie wyobrazić. Twoja niezłomna siła i determinacja zawsze motywowały mnie do działania, nawet w najtrudniejszych momentach.

Dziękuję Wam z całego serca za to, że zawsze byliście przy mnie, a także za to, że nauczyliście mnie, jak być dobrą osobą i walczyć o swoje marzenia. Doceniam Waszą miłość i poświęcenie bardziej, niż kiedykolwiek będziecie w stanie to sobie wyobrazić.